Studies of the Evolution and Stability of the Thin Film Equation for Externally Modulated Control of Electrohydrodynamic and Thermocapillary Patterning

Thesis by
Yi Hua Chang

In Partial Fulfillment of the Requirements for the
Degree of
Doctor of Philosophy

CALIFORNIA INSTITUTE OF TECHNOLOGY
Pasadena, California

2024
Defended May 28 2024

Yi Hua Chang
ORCID: 0000-0003-0112-4139

ACKNOWLEDGEMENTS

First and foremost, I would like to thank my advisor Professor Sandra Troian for her guidance, support, and encouragement throughout my graduate studies. I have learnt to approach different scientific problems critically, and I believe that the skills I have acquired will be invaluable not just in my future career but also in my personal life.

I would also like to thank other members of the group: Peter for setting up the computational infrastructure and providing technical support for my research, Chengzhe and Nicholas for sharing their physical insights, and Cheolmin and Hiroki for their support and camaraderie.

I also want to thank my family for enabling what I achieve: my parents for giving me the freedom to explore my interests, my brother James for pushing me to be better, my grandparents for their care and love, and the extended Chang family in the US for helping me settle in a new country.

I am grateful to all the teachers and mentors from my high school St. Joseph's College in Hong Kong and my undergraduate university Imperial College London who have instilled in me a love for learning and a desire to understand the world around me. I would like to thank my friends, classmates, lab mates for making a positive impact on my life.

I also want to acknowledge all the support personnel and medical practitioners during the difficult times in the past few years. When we are hiking in the mountains and get lost, we remember the people who give us directions and point us to the right path, but we often forget the people who build the paths and maintain the trails. My research would not be possible without the sacrifice and dedication of the people who work behind the scenes, and I am grateful for their hard work.

Finally, it has been a difficult few years for my hometown Hong Kong. I have learnt through countless stories and people's sacrifice that the freedom to pursue knowledge is not something to be taken for granted. It is a privilege to be able to study, learn and conduct research in a free and open society, and I am grateful for the opportunities that I have been given. Light will always shine through the darkness.

ABSTRACT

It has been known for a couple decades, based on extensive experimental, theoretical and numerical studies, that a flat slender nanoscale viscous film in the absence of gravity always undergoes early time linear instability when subject to electrical or thermocapillary forces. The patterns resulting from a uniform transverse electric or thermal field resemble clusters of small rounded protrusions whose early time dynamics have been described by linear stability analysis of the governing fourth-order nonlinear interface equation – the so-called thin film equation. However, the pattern formation process beyond early times generates larger amplitude protrusions prone to coalescence or an Oswald-like ripening of adjacent formations which destroy the pattern uniformity. Introduction of film interface modulation by external spatially periodic modulation offers a superior method for this type of lithographic patterning. The resulting linear and nonlinear response of the liquid layer can be tuned to corral the evolution of the liquid interface into periodic arrays containing identical components in certain parameter range. Conditions for achieving high-fidelity patterns are still not fully understood, however, rendering such technique not yet fully utilized in practical applications.

To that end, we have conducted a number of analytical and numerical studies which elucidate various regimes leading to high-fidelity patterning by external spatial and temporal modulation. We focus on a single layer of viscous liquid film on a solid substrate which is described by the thin film equation derived under the long wavelength approximation. We first study the linear stability of periodic non-uniform stationary states subject to electrostatic stress and find that the necessary conditions for achieving stable states in 1D are the mass-limitation or saturation with a system-confining boundary (touching the mask) in order to suppress the coalescence and Ostwald-like-ripening modes. In 2D, stationary ridges are only achieved by saturation with a system-confining boundary in order to suppress its breakup. Time-dependent simulations further reveal inaccessible stationary states due to large electrode separation or large applied voltage. Exploratory studies on system subject to temperature gradient shows that the coalescence mode becomes unstable over a wider range of parameters due to thermocapillary stress. These findings result in phase diagrams relating the spatial modulation amplitude and electric Weber number or Marangoni number to the conditions for high-fidelity patterns which cannot be explained simply by matching the patterning and intrinsic instability wavelengths as previously claimed in literature.

We then turn to the optimal control of electrohydrodynamic thin film patterning where the optimal strategy in deforming a flat film toward a desired shape is determined. A computational framework is derived which allows us to study the open-loop terminal control problem for thin liquid film. The approach allows us to quantify the best-

possible outcome only constrained by the underlying physical mechanisms, and better understand the limitations of thin film patterning in relation to the choice of target shapes and system parameters. The impact of imperfect engineering and methods of mitigations are also discussed, which should prove useful to soft lithography and other applications.

PUBLISHED CONTENT AND CONTRIBUTIONS

1. **Chang, Yi Hua**, and Sandra M. Troian. "Thermocapillary Patterning of Highly Uniform Microarrays by Resonant Wavelength Excitation". Physical Review Applied 18.6 (2022): 064090. URL: 10.1103/PhysRevApplied.18.064090

   Basis: Published article is based on material in Chapter 6.

   Contribution: YHC extended the original analysis, conducted numerical simulations, collected the data, prepared figures and movies for distribution and participated in the writing of the final publication.

NOMENCLATURE AND NOTATIONS

List of Acronyms

c.c.: complex conjugate

h.o.t.: higher-order terms

ss (as subscript): stationary state

vdw (as subscript): van der Waals

DFT: discrete Fourier transform

EHD: electrohydrodynamic

FDM: finite difference method

FEM: finite element method

LSA: linear stability analysis

LWA: long-wave(length) approximation

ODE: ordinary differential equation

PDE: partial differential equation

TC: thermocapillary

WNA: weakly-nonlinear analysis

List of Nomenclature

free surface: the interface between the liquid and the passive gas (typically air) mathematically denotes as $h(\mathbf{x}, t)$ or $H(\mathbf{X}, \tau)$

in-plane: the 'horizontal' (or $x - y$) direction of the system parallel to the substrate

out-of-plane: the 'vertical' (or z) direction of the system perpendicular to the substrate

(un-)modulated: experimental configuration with constant separation between mask and substrate, temperature and applied voltage

mask: plate above the air and liquid, also referred to as 'bottom plate' or 'bottom electrode'

substrate: supporting plate below the liquid, also referred to as 'bottom plate' or 'bottom electrode'

List of Commonly Used Symbols

β: growth rate (of a particular mode)

d_0 (D_0): mean separation between the mask and substrate in dimensional (dimensionless) unit

$\epsilon = h_0/h_0$: small aspect ratio parameter used in LWA

ε: (relative) electric permittivity

γ: surface tension of the liquid

Γ: dimensionless surface tension variation

k_c (K_c): critical wave number from linear stability analysis in dimensional (dimensionless) unit

k_m (K_m): fastest-growing wave number from linear stability analysis in dimensional (dimensionless) unit

k_p (K_p): patterning wave number in dimensional (dimensionless) unit

λ_m (Λ_m): fastest-growing wavelength in dimensional (dimensionless) unit

λ_p (Λ_p): patterning wavelength in dimensional (dimensionless) unit

Π: dimensionless external pressure (e.g., disjoining pressure, electrostatic stress, etc.)

ϱ: modulation amplitude

ρ: liquid density

τ: dimensionless time

τ_f: final or terminal time for numerical simulation

Υ: regularization parameter for optimal control (in Chapter 7)

ξ: system or control variable to be modulated (e.g., mask topography, applied voltage, imposed temperatures, etc.)

TABLE OF CONTENTS

Chapter 1

INTRODUCTION

1.1 Thin Film Flows

Thin film flows are ubiquitous in nature and industry. For example, in biology they manifest as the spreading and evaporation of blood [1]. In geophysics, many phenomena ranging from the transport of oil and gas, rock formation to the storage of CO_2 can be modeled as gravity-driven thin film flows [144]. Other examples include the (de)wetting of liquid films and droplets [9], spin coating in micro/nano-fabrication, the sliding motion of droplets on a window pane [89], or even the mathematical modeling of making pancakes [10]. All these examples feature a freely deformable interface separating the liquid from the surrounding medium, and are capable of displaying complex nonlinear behavior and many interesting pattern formation phenomena.

On the most exciting applications involving thin film flows is the patterning of thin polymer films for micro/nano-fabrication. Chou and coworkers [16, 17] first reported the experimental observation of the spontaneous formation of periodic pillar arrays in a thin layer of heated polymer film, using an experimental setup similar to the schematic shown in Fig. 1.1 where a polymer film is situated between two parallel plates. It inspired many subsequent studies to investigate the patterning of submicron film with external forces using a similar configuration, and two common approaches involve the use of electric or thermal fields as the driving force to deform the liquid film.

Consider a liquid film situated between two parallel plates bounded by air from above as shown in Fig. 1.1. If the two parallel plates are held at different voltages as shown in Fig. 1.1(a), an electric field is created, and the electrostatic force acting on the bound charge or free charge at the free surface of the liquid film can deform the liquid film to develop peak-like structures. This forms the basis of electrohydrodynamic (EHD) patterning first experimentally demonstrated by Schäffer et al. [103]. Similarly, when the two parallel plates are held at different temperatures as shown in Fig. 1.1(b), a temperature gradient is present at the free surface of the liquid film. This results in a surface tension gradient due to the temperature-dependence of surface tension, which then deforms the liquid film via a shear stress. This forms the basis of thermocapillary (TC) patterning first experimentally demonstrated by Schäffer et al. [100]. Experimental demonstrations of EHD or TC patterning typically use melted layer of polymer film with submicron thickness, and the resulting patterns typical exhibit lateral feature size of the order of microns or tens of microns, though submicron feature size has also been demonstrated. The typical scales and experimental parameters for EHD and TC

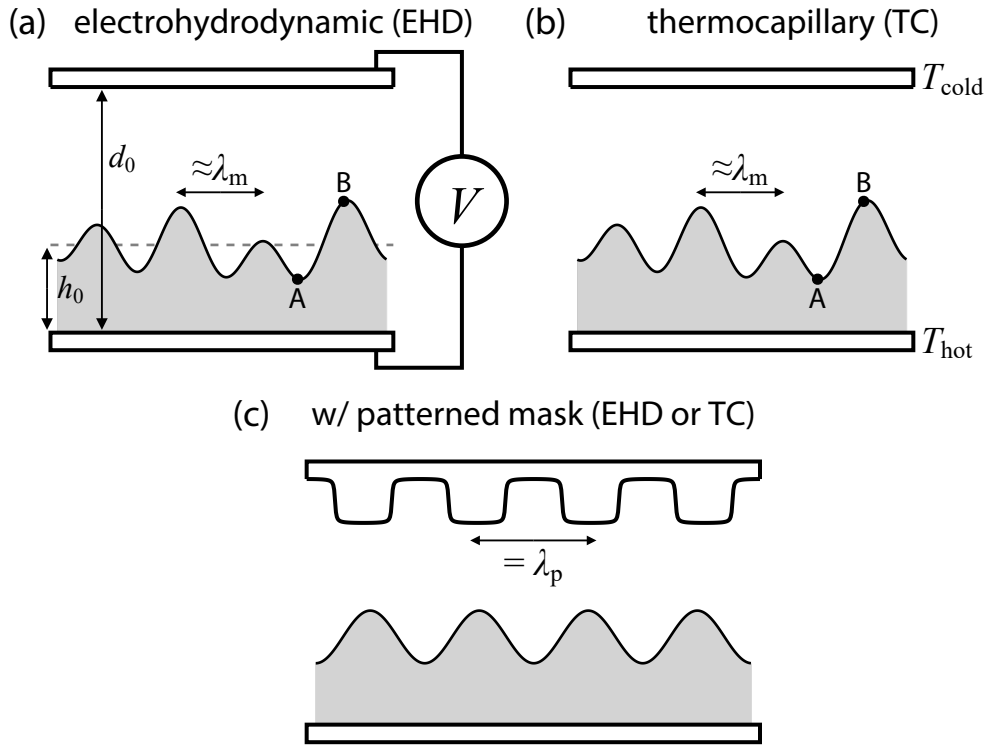

Figure 1.1: Schematic of liquid thin film patterning. A liquid film (typically polymer film) shown as gray region is placed between two parallel plates with an air layer above it. (a) In electrohydrodynamic (EHD) patterning, a thin liquid film is subject to an external electric field generated by two electrodes held at different electric potentials with potential difference V, and the free surface is deformed by the resulting electrostatic stress. Point A of the liquid film is closer to the top plate and experiences a larger electrostatic stress than point B which leads to subsequent runaway growth of the protrusion. (b) In thermocapillary (TC) patterning, the top and bottom plates are kept at temperature $T_{\rm hot}$ and $T_{\rm cold}$, respectively, where $T_{\rm hot} > T_{\rm cold}$. Point B has a lower temperature than point A because it is closer to the top cold plate. Due to thermocapillary effect, the surface tension at point B is larger than at point A which drives fluid flow toward that region. The initial length scale of the developed patterns is the fastest growing wavelength λ_m predicted by linear stability analysis. (c) In both EHD and TC patterning, a patterned mask with a periodicity of λ_p is typically employed to impose a spatially inhomogeneous external fields to control the pattern formation in the liquid film. The mean film thickness h_0, mean separation between the plates d_0 are indicated in (a).

Table 1.1: Typical values of the experimental parameters extracted from selected studies in EHD/TC patterning: (1) Figure 2, 3 and Table 1 in [104]; (2) Figure 1, 5, 6, 7, 9 and 10 in [128]; (3) Table 1 and 2 in [52]; (4) Table I in [36].

Physical quantity	Symbol	Unit	Values
Mean film thickness	h_0	nm	$93-125$ [104] $78-125$ [128] $140-400$ [52] $95-390$ [36]
Mean separation between top plate (mask) and bottom electrode (substrate)	d_0	μm	$0.23-1.73$ [104] $0.2-0.5$ [128] $1.1-1.8$ [52] $0.6-2.2$ [36]
Mean separation between top plate (mask) and bottom electrode (substrate) (dimensionless)	$D_0 = d_0/h_0$	–	$2.3-14.4$ [104] $1.67-4.00$ [128] $2.7-10.8$ [52] $2.0-14.1$ [36]
Applied voltage	V	V	$30-50$ [104] $10-80$ [128] $40-100$ [52]
Temperature of hot substrate	T_{hot}	°C	$90-100$ [36]
Temperature of cold substrate	T_{cold}	°C	$69-89$ [36]
Temperature difference	ΔT	°C	$9.8-25.8$ [36]
Fastest-growing wavelength (predicted from linear stability analysis)	λ_m	μm	$1.5-37$ [104] $1.5-7.9$ [128] $8.2-36.5$ [52] $29.1-73.2$ [36]
Patterning wavelength	λ_p	μm	$1.2-5.3$ [128] $6-15$ [52]
Modulation strength	ϱ	–	$0-0.37$ [52]

patterning are summarized in Table 1.1. Other mechanisms for deforming the liquid film, such as the combination of both electrostatics and thermocapillarity [21], and solutal-Marangoni effect where the surface tension of a photosensitive polymer is varied from exposure to UV light [58], have also been studied for patterning liquid film.

Both electrohydrodynamics and thermocapillarity have been studied for decades, and their earliest manifestations can be traced back to more than a century ago. Taylor [115] pointed out that Gilbert was likely the first to demonstrate an EHD instability in his work *De Magnete* in 1600, while Taylor himself also contributed many pioneering studies on electrified liquid [114]. Bénard's original experiment on heated liquid film in

1900 showed the pattern formation of convection cells, and subsequent analysis showed that this effect, which was originally attributed to buoyancy-driven convection in what is known as Rayleigh-Bénard convection, was likely due to thermocapillary effect in what is known as the Bénard-Marangoni instability [63, Section 12.H]. The utilization of these hydrodynamic instabilities for thin film patterning and micro/nano-fabrication only become feasible and widespread since the early 2000s, decades after their initial discovery, thanks to the advancement in experimental techniques that allow access to thin films with submicron thickness. At the submicron scale, gravitational force which is usually stabilizing becomes negligible compared to surface forces due to the large surface-area-to-volume ratio. For the configuration shown in Fig. 1.1, the close proximity of the two plates also allows the creation of very large electric or thermal fields, resulting in very large surface forces which can overcome the stabilizing effect of surface tension. This results in an instability where noise present in the system leads to a spatially varying surface force (e.g., electrostatics or thermocapillarity) which deforms the liquid film. Variation in local film thickness further enhances the effect of the surface force, leading to a runaway process where the peak-like structures formed by the liquid film keep growing until terminated by other processes like contact with the top plate. The initial length scale of the patterns is found to agree with the fastest growing wavelength λ_m predicted from linear stability analysis, and λ_m reflects the competition between the stabilizing capillarity and destabilizing external forces due to electrostatics or thermocapillarity. Since λ_m depends on the physical properties of the liquid film as well as other adjustable process parameters like the applied voltage or temperature difference, the length scale of the patterns becomes controllable.

The thin film used in experiments is usually polymer film (e.g., Polystyrene or PMMA) heated above the glass transition temperature. This polymer melt, once deformed to certain shape by the external forces, can be solidified *in-situ* by removal of heating or photochemical process, resulting in patterned micro structures as solid at the end. This type of 'soft' lithographic techniques offer many advantages compared to conventional techniques such as photolithography as it only involves one single step, is contactless, and is capable of making molecularly smooth and curved surfaces, making it a particularly attractive technique in the broader field of soft lithography [12, 25, 27, 135]. Proof-of-concept studies using EHD patterning for device fabrication include the fabrication of microlens arrays [55, 64–67, 69], optical waveguides [67, 70, 71] and cell substrates [122], as well as in sensing [46, 72], microfiltration [61] and fog collection [87]. Fabrication of microlens arrays using TC patterning have also been demonstrated [30, 75], see, for example, Fig. 1.2(b).

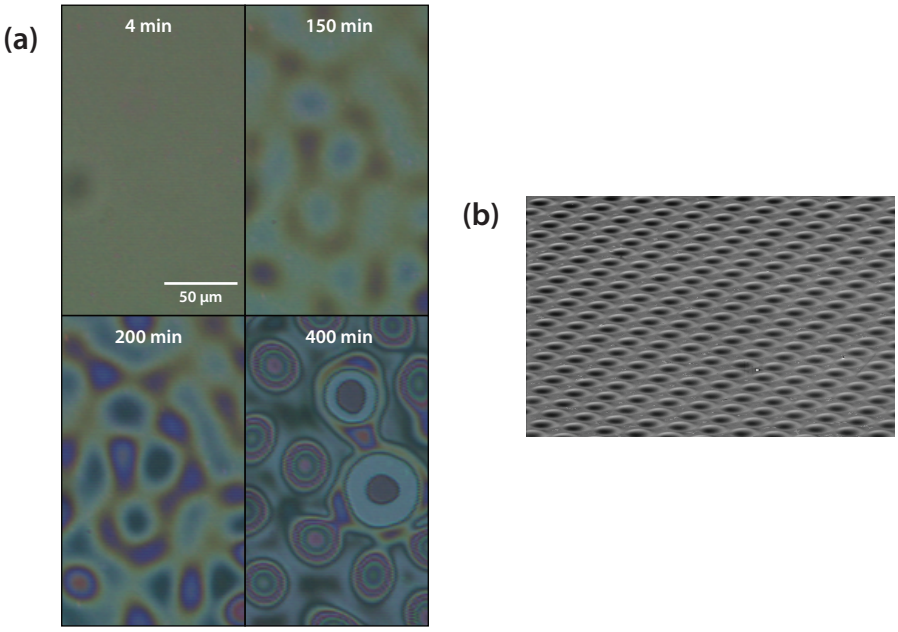

Figure 1.2: Images showing the pattern formation in thermocapillary (TC) patterning. (a) Optical images showing variation in surface reflectivity due to emergent fluid protrusions in TC patterning with flat plates. Images demonstrate significant nonuniformity in pattern pitch, shape, and height. (b) Scanning electron micrograph showing a solidified square microlens array resulting from a spatially periodically modulated thermal field enforced by a patterned colder substrate. Here, an initial 150-nm polymer melt film is exposed to an upper thin cold disk patterned by a square array of cylindrical pins with pitch 50 μm, pin diameter 5 μm and pin length 1.6 μm. Published as Fig. 1(b) and (c) in Ref [15] courtesy of S. M. Troian and E. McLeod.

1.2 Challenges of Thin Liquid Film Patterning

1.2.1 Limitations of relying on instability

Despite the seeming elegance of relying on an intrinsic hydrodynamic instability to generate periodic arrays, there remain notable challenges for both EHD and TC patterning. The first difficulty stems from the very mechanism sustaining protrusion growth. Since taller peaks always advance more rapidly toward the upper plate, initial configurations marked by any disparities in film thickness, however small, will rapidly incur disparities in peak heights, shape and pitch. Non-uniformities, such as those shown in Fig. 1.2(a), are traceable to variations in initial film thickness incurred either during initial film preparation, deposition and annealing or dewetting and pooling events which can be difficult to control experimentally [15].

A second difficulty is related to achieving a reduction in the array pitch. For EHD patterning, while λ_m can be reduced by increasing the applied voltage, dielectric breakdown limits the maximum dielectric field strength achievable, and hence the extent of which λ_m can be reduced [62]. In TC patterning, λ_m scales with $\Delta T^{-1/2}$ where ΔT is the

applied temperature difference. Generation of large vertical thermal gradient requires the parallel plates to be placed in very close proximity (few microns or fewer), but such close proximity causes effective cooling of the warmer substrate which tends to diminish the temperature difference ΔT. These limitations restrict the typical length scale to the orders of micron or even tens of micron, which are too large for applications requiring sub-micron resolution.

1.2.2 High-fidelity patterns with external spatial modulation

In order to improve pattern uniformity, reduce feature size, or even achieve patterns with specific morphology such as stripes or Cartesian arrays, researchers commonly design a heterogeneous external fields with an imposed patterning wavelength λ_p which is most often achieved by the use of patterned mask as shown in Fig. 1.1(c). The spatially periodic modulation of the external electric or thermal field increases the surface forces for deforming the liquid film, and can potentially lead to rapid and synchronous formation of highly uniform periodic arrays.

However, whether the liquid film develops high-fidelity patterns conforming to the external spatial modulation still depends on how various system parameters are chosen. An example can be seen from numerical simulation in Fig. 1.3 showing how a liquid film develops ridges which later break up under the use of topographically patterned mask with stripe-like patterns. Despite numerous studies in literature addressing the use of spatial modulation into the pattern formation of liquid film, the conditions for developing high-fidelity patterns are not fully understood beyond the simple matching of $\lambda_p \approx \lambda_m$ which only works for a limited range of system parameters.

1.2.3 Needs for optimal control

Even if high fidelity patterns can reliably be formed, for example, the liquid film develops patterns matching that imprinted on the patterned mask or the spatially modulated external fields, the precise control of the out-of-plane profile of the liquid film is still required for application purposes. For example, the curvature of the lenses in a microlens array (e.g. see Fig. 1.2(b)) affects the focal length and other focusing properties of the lenses. The ridges shown in Fig. 1.3 can also be used as optical waveguides, in which case the light confinement strongly depends on the cross sections of the ridges. However, such control remains difficult to achieve, and there is a lack of studies in literature which address the optimal control of thin film patterning.

1.3 Objectives

The objective of this thesis is to address these two fundamental challenges in the patterning of thin liquid film with electric and thermal fields. The first part of the thesis addresses the so-called 'forward problem' where the response of the liquid film to an

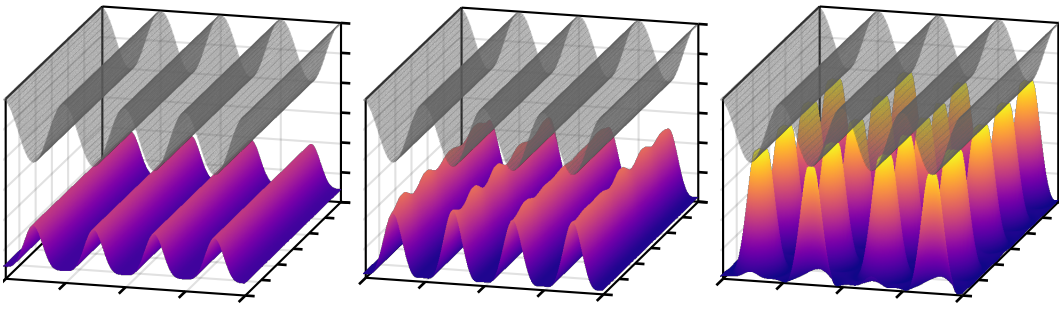

Figure 1.3: Schematic showing the evolution of a liquid film in EHD patterning under topographically patterned mask (top electrode). The liquid film initially develops ridges (left subplot) that follow the shape of the mask. As time progresses (left to right), the ridges break up into column-like structures that have different morphology compared to the top electrode. Studying the conditions for forming high-fidelity patterns, in this case ridges that sustain for a sufficiently long time, is a key challenge in thin film patterning and is one of the objectives of this thesis.

externally imposed periodic modulation, e.g., a spatially inhomogeneous external fields due to topographically patterned top plate, is studied in detail. Specifically, we study how the shapes and stability of non-uniform stationary states depend on the spatial dimension of the system and different keys system parameters, as well as the dynamics of the liquid film in the presence of external modulation. The second part of the thesis addresses the so-called 'inverse problem' where the objective is to find the optimal control strategies to achieve a specific shape with the liquid film, and the fundamental limitations in liquid film patterning under an optimal control framework.

The studies presented in this thesis are conducted mainly through numerical simulations of the so-called 'thin film equation', which is an evolution type nonlinear partial differential equation (PDE) governing the local film thickness, derived under long wavelength approximation [85]. Analytical study of the thin film equation subject to external spatial modulation is also carried out whenever possible under certain limit of small modulation amplitude. The aim of the present study is to employ various well-developed techniques in dynamical systems to study the spatiotemporal response of a pattern-forming system with huge potential applications yet with limited studies on how the underlying physics mechanisms can be fully harnessed to achieve high-fidelity patterns needed for actual adoption. The results presented in this thesis will provide a more intuitive understanding regarding the destabilization mechanism, as well as more quantitative design principles in the selection of system parameters in achieving high-fidelity patterns in liquid thin film patterning which should be of interest to the broader community of both theorists and experimentalists.

1.4 Outline and Key Findings

In Chapter 2, we provide the derivation of the governing thin film equation from first principles, and discuss how various physical effects are coupled to the hydrodynamics of the liquid film.

In Chapter 3, we introduce the linear stability analysis (LSA), which is a widely used technique for studying the stability of dynamical systems.

In Chapter 4, we discuss the numerical methods, especially the spatial discretization of the thin film equation, the time stepping scheme for solving time-dependent simulations, and the pseudo-arclength continuation method for solving non-linear equations. These numerical tools will be used throughout the thesis.

In Chapter 5, we study the forward problem of EHD patterning under the so-called perfect dielectric model. Since shear stress is absent in the problem, it simplifies the governing equation for stationary state, and we specifically focus on the role of *normal* stress on the free surface of the liquid. The results in this chapter lead to the following key findings:

- The Ostwald ripening mode is the dominant destabilization mechanism in EHD patterning when electrode separation is not to small.
- The Ostwald ripening mode can be suppressed by the presence of thin precursor film which leads to quasi-stationary states, and can only be truly stabilized via contact with the patterned mask.
- The stable stationary states for ridges may not be accessible for an initially flat liquid film for sufficiently large electrode separation or applied voltage.

In Chapter 6, we study the forward problem of TC patterning. Specifically, we focus on the role of shear stress and how different phenomena are brought about compared to the case of EHD patterning without shear stress. The results in this chapter show that for TC patterning, the protrusions mainly destabilize via the coalescence mode whose stability appear to depend sensitively on the topography of the patterned mask when contact is established.

In Chapter 7, we introduce the general mathematical formulation for solving the inverse problem in liquid thin film patterning. Numerical results are presented for the terminal control problem in EHD patterning, focusing on the following areas regarding the realization of high-fidelity patterns:

- How the minimum achievable deviation representing the best case scenario depends on different system parameters and the target shapes.

- How imperfect control in the form of fabrication imperfection for the patterned mask affects the final liquid film shape and the methods of mitigations.

Finally, in Chapter 8, we summarize the main findings of the thesis.

Chapter 2

GOVERNING EQUATIONS

In this section, the derivation of the governing thin film equation is derived from first principle under the so-called long wavelength approximation (LWA). Note that the derivation presented here rely on techniques which have been covered in many standard texts such as Leal [63], Deen [26] and Oron et al. [85], and have been applied to study many problems involving thin liquid films in the literature. See the reviews by Oron et al. [85] and Craster and Matar [22] for an extensive list of studies utilizing LWA. The aim of presenting the derivation in full is for completeness and to address the specific choice of scalings and non-dimensionalization adopted in this thesis which may be different from other similar studies. Symbols, notations and terminology are also introduced along the derivation.

The system under investigation is shown in Fig. 2.1 where a single layer of thin viscous Newtonian fluid is supported from below by a substrate, confined from above by an inviscid fluid layer (typically air) and a mask. Throughout this thesis, the substrate is also referred to as 'bottom plate' or 'bottom electrode' interchangeably, while the mask is also referred to as 'top plate' or 'top electrode'. Note that the mask may be featureless or topographically patterned.

Section 2.1 presents the derivation leading up to Eq. (2.49) which governs the hydrodynamics of the thin liquid film irrespective of the presence of other external physical effects which are studied in this thesis. Section 2.2 provides a short discussion of the gradient flow formulation of Eq. (2.49). Finally, the coupling of the hydrodynamics to different physical effects, including electrostatics and thermocapillarity, is discussed in Section 2.3. This completes the full derivation of the relevant governing equation used throughout this thesis.

2.1 Hydrodynamics

2.1.1 Dimensional governing equations

Table 2.1 summarizes the typical values of different material constants relevant to thin film patterning for polystyrene and air.

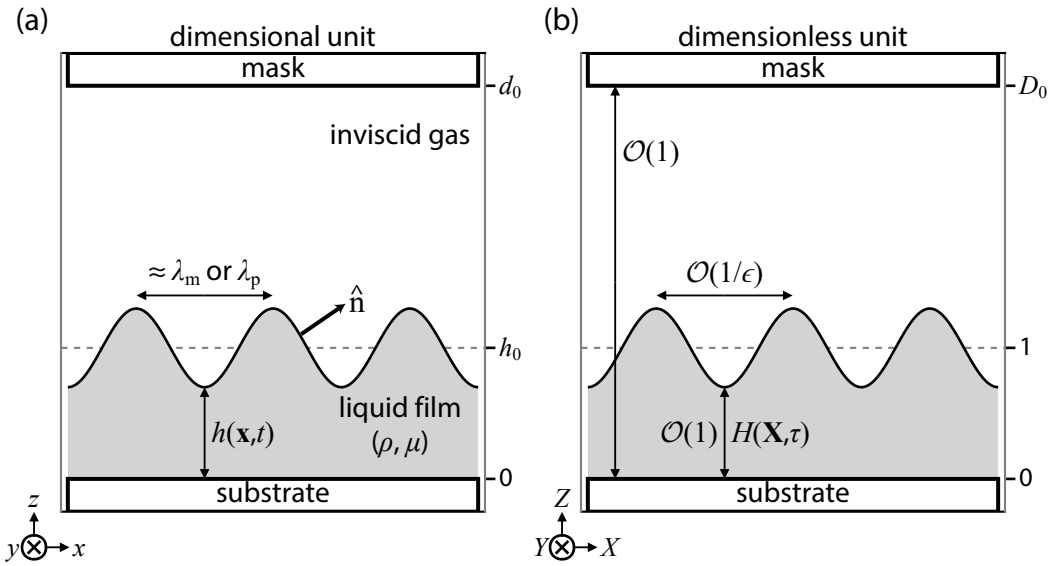

Figure 2.1: Schematic of a thin film patterning system. Notations are labeled in (a) dimensional and (b) dimensionless units. Gray shaded region denotes the liquid film with density ρ and dynamic viscosity μ. The mean film thickness is h_0 and mean separation between mask and substrate is d_0. Local film thickness is $h(\mathbf{x}, t)$. The initial corrugation developed by the liquid film has length scale equal to either fastest-growing wavelength λ_m or imposed patterning wavelength λ_p. The unit vector normal to the free surface of the liquid film is denoted by $\hat{\mathbf{n}}$. Uppercase letters shown in (b) denote dimensionless quantities whose definitions and scalings are described in section 2.1.2 and summarized in Table 2.2.

Table 2.1: Typical values of material properties relevant to EHD/TC patterning for polystyrene and air.

Property	Symbol	Unit	Polystyrene	Air $(350\ \mathrm{K})$ [a]	Air $(400\ \mathrm{K})$ [a]
Density	ρ	$\mathrm{kg/m^3}$	1040 – 1065 [b]	0.5664	0.5243
Dynamic viscosity	μ	$\mathrm{Pa \cdot s}$	1 – 8000 [c]	3.101×10^{-5}	3.261×10^{-5}
Relative Permittivity	ε_r	–	2.49 – 2.55 [b]	≈ 1	≈ 1
Thermal conductivity	$\hat{k}$	$\mathrm{W/(m \cdot K)}$	0.128 [d]	0.04721	0.05015
Specific heat capacity	c_p	$\mathrm{J/(kg \cdot K)}$	1720 [e]	1056	1069
Prandtl Number	$\mathrm{Pr} = c_p\mu/\hat{k}$	–	$10^4 - 10^8$	0.6937	0.6948
Surface tension	γ	$\mathrm{N/m}$	0.0292 – 0.0314 [f]	–	–
Thermocapillary coefficient	γ_T	$\mathrm{N/(m \cdot K)}$	$(6.5 - 7.7) \times 10^{-5}$ [g]	–	–
Hamaker constant	A	J	2.2×10^{-20} [h]	–	–
Glass transition temperature	T_g	K	373 [b]	–	–

[a] Table A–9 in [14].
[b] Page 830 in [73] for amorphous polystyrene.
[c] Estimated from Figure 7 in [124] for temperature between $64°\mathrm{C} - 167°\mathrm{C}$ where $\mu/(\mathrm{Pa \cdot s})$ spans between $\exp(0)$ and $\exp(9)$.
[d] Page 834 in [73] for $T = 373\ \mathrm{K}$.
[e] Table 5.2 in [125] for 'liquid' polystyrene.
[f] Page 834 in [73] for polystyrene at $T = 423\ \mathrm{K}$ with molecular weights between 1700 and 44000 $\mathrm{g/mol}$.
[g] Page 834 in [73].
[h] From measurement in [105] for air/polystyrene/SiO system assuming the dimensional disjoining pressure is defined as $\varpi_{\mathrm{vdw}} = A/6\pi h^3$. The annealing temperature was reported to be between $50°\mathrm{C}$ and $100°\mathrm{C}$.

2.1.1.1 Equations in the Bulk

The hydrodynamics in the bulk of an incompressible liquid film is governed by the continuity equation [1] enforcing mass conservation

$$\nabla \cdot \mathbf{u} = \nabla_{\parallel} \cdot \mathbf{u}_{\parallel} + \frac{\partial w}{\partial z} = \frac{\partial u}{\partial x} + \frac{\partial v}{\partial y} + \frac{\partial w}{\partial z} = 0, \tag{2.1}$$

and the Navier-Stokes equation [2] enforcing momentum conservation

$$\rho \left(\frac{\partial \mathbf{u}}{\partial t} + \mathbf{u} \cdot \nabla \mathbf{u} \right) = \nabla \cdot \overleftrightarrow{\mathbf{T}} - \nabla \varpi_{\text{ext}}, \tag{2.2}$$

where ρ is the density of the liquid film, ϖ_{ext} is the body force potential in unit of energy per unit volume which can represent contribution from gravity (see Section 2.3.4) or intermolecular interactions (see Section 2.3.3), $\mathbf{u}(x, y, z, t)$ is the velocity vector defined as

$$\mathbf{u} = u(x, y, z, t)\hat{\mathbf{e}}_x + v(x, y, z, t)\hat{\mathbf{e}}_y + w(x, y, z, t)\hat{\mathbf{e}}_z = \mathbf{u}_{\parallel} + w\hat{\mathbf{e}}_z, \tag{2.3a}$$

$$\mathbf{u}_{\parallel} = u(x, y, z, t)\hat{\mathbf{e}}_x + v(x, y, z, t)\hat{\mathbf{e}}_y, \tag{2.3b}$$

and the gradient operator ∇ is defined as

$$\nabla = \frac{\partial}{\partial x}\hat{\mathbf{e}}_x + \frac{\partial}{\partial y}\hat{\mathbf{e}}_y + \frac{\partial}{\partial z}\hat{\mathbf{e}}_z, \qquad \nabla_{\parallel} = \frac{\partial}{\partial x}\hat{\mathbf{e}}_x + \frac{\partial}{\partial y}\hat{\mathbf{e}}_y, \tag{2.4}$$

Note that the notation $\hat{\mathbf{e}}_i$ denotes unit vector along the i direction, and the subscript '$\parallel$' in both $\mathbf{u}_{\parallel}$ and $\nabla_{\parallel}$ denote the $x - y$ or 'in-plane' direction. The stress tensor $\overleftrightarrow{\mathbf{T}}$ is given by

$$\overleftrightarrow{\mathbf{T}} = -p\,\overleftrightarrow{\mathbf{I}} + 2\mu\,\overleftrightarrow{\mathbf{E}} + \overleftrightarrow{\mathbf{M}}, \qquad \overleftrightarrow{\mathbf{E}} = \frac{1}{2}\left[\nabla\mathbf{u} + (\nabla\mathbf{u})^T\right], \tag{2.5}$$

where $p(x, y, z, t)$ is the fluid pressure, $\overleftrightarrow{\mathbf{I}}$ is the identity matrix, μ is the viscosity of the liquid film, $\overleftrightarrow{\mathbf{E}}$ is the rate-of-strain tensor and $\overleftrightarrow{\mathbf{M}}$ is the Maxwell stress tensor [3]. Note that

[1] The general continuity equation is $\partial\rho/\partial t + \nabla \cdot (\rho\mathbf{u}) = 0$, which reduces to Eq. (2.1) for incompressible fluid where ρ is a constant.

[2] The derivation of the Navier-Stokes equation can be found in textbooks such as [63, Chapter 2C, 2H, 2I] and [26, Chapter 5.3].

[3] The derivation presented in the rest of this chapter still holds even when the stress tensor $\overleftrightarrow{\mathbf{M}}$ represents other physical effects not related to electromagnetic phenomena, as long as the condition $\nabla \cdot \overleftrightarrow{\mathbf{M}} = 0$ holds.

the constitutive relation given by Eq. (2.5) holds for a Newtonian fluid, which is local, instantaneous, isotropic, homogeneous and has a local viscous stress which is a linear function of the local rate of strain [4]. For a fluid with a constant relative permittivity in the absence of free charge, it can be shown that $\nabla\cdot \overleftrightarrow{\mathbf{M}}= 0$ (see Section 2.3.2.2), i.e., electrostatic effects are absent in the governing equations in the bulk, though the coupling with hydrodynamics still occurs through the interfacial boundary conditions. Eq. (2.2) is then simplified to

$$\rho\left(\frac{\partial \mathbf{u}}{\partial t}+\mathbf{u}\cdot\nabla\mathbf{u}\right)=-\nabla p+\mu\nabla^2\mathbf{u}-\nabla\varpi_{\text{ext}}. \tag{2.6}$$

2.1.1.2 Boundary Conditions

For the boundary conditions, we first consider the velocity at the substrate (i.e., bottom plate) at $z = 0$. Imposing the usual no-slip and no-penetration conditions at the substrate, we have

$$\text{no-slip:} \qquad \mathbf{u}_{\parallel}=(u,v)=0, \qquad \text{at } z=0, \tag{2.7}$$

$$\text{no-penetration:} \qquad \mathbf{u}\cdot\hat{\mathbf{e}}_z=w=0, \qquad \text{at } z=0. \tag{2.8}$$

At the free surface $z = h(x, y, t)$ separating the liquid film and ambient gas, we have the stress balance condition [5]

$$\hat{\mathbf{n}}\cdot(\overleftrightarrow{\mathbf{T}}_a-\overleftrightarrow{\mathbf{T}}_b)+\nabla_s\gamma-\gamma(\nabla\cdot\hat{\mathbf{n}})\hat{\mathbf{n}}=0 \qquad \text{at } z=h(x,y,t). \tag{2.9}$$

Here, $\overleftrightarrow{\mathbf{T}}_a$ and $\overleftrightarrow{\mathbf{T}}_b$ denote the stress tensor associated with the upper gas layer ('a' for 'air' or 'above') and the bottom liquid film ('b' for 'bottom') respectively, $\hat{\mathbf{n}}$ is the unit normal vector pointing outward from the liquid film toward the ambient gas (from 'b' to 'a') as shown in Fig. 2.1(a), ∇_s is the surface gradient (see Appendix A.3.2), γ is the surface tension, and $\nabla\cdot\hat{\mathbf{n}}$ is the curvature (see Appendix A.3.3).

In this thesis, the hydrodynamics of the ambient gas is neglected, i.e., $\overleftrightarrow{\mathbf{E}}_a= 0$. To simplify notations, we introduce the stress vector $\boldsymbol{\varpi}_{\text{M}}$ associated with the (Maxwell) stress tensor $\overleftrightarrow{\mathbf{M}}$ defined as:

[4] It can be shown that the most general form of stress tensor for a Newtonian fluid (neglecting the contribution from external field) is $\overleftrightarrow{\mathbf{T}}= (-p+\lambda\ \text{tr}\ \overleftrightarrow{\mathbf{E}})\mathbf{I}+2\mu\ \overleftrightarrow{\mathbf{E}}$, where $\lambda+(2/3)$ is the bulk viscosity. For an incompressible fluid, $\text{tr}\ \overleftrightarrow{\mathbf{E}}= \nabla\cdot\mathbf{u}=0$. See Chapter 2H of [63] or Chapter 5.6 of [26] for a more in-depth discussion on the viscous stress tensor.

[5] Eq. (2.9) appears as Eq. (2-134) in [63] with the substitution $\mathbf{T}\rightarrow\overleftrightarrow{\mathbf{T}}_a$ and $\overleftrightarrow{\mathbf{T}}\rightarrow\overleftrightarrow{\mathbf{T}}_b$, as well as Eq. (5.7-8) in [26] with the substitution $\mathbf{s}(\hat{\mathbf{n}})|_2\rightarrow\hat{\mathbf{n}}\cdot\overleftrightarrow{\mathbf{T}}_a$ and $\mathbf{s}(\hat{\mathbf{n}})|_1\rightarrow\hat{\mathbf{n}}\cdot\overleftrightarrow{\mathbf{T}}_b$. Note that Leal is not consistent with convention of $\mathbf{T}\cdot\hat{\mathbf{n}}$ versus $\hat{\mathbf{n}}\cdot\mathbf{T}$.

$$\boldsymbol{\varpi}_{\mathrm{M}} = \hat{\mathbf{n}} \cdot (\overleftrightarrow{\mathbf{M}}_a - \overleftrightarrow{\mathbf{M}}_b) = \varpi_{\mathrm{M}}^{(n)} \hat{\mathbf{n}} + \boldsymbol{\varpi}_{\mathrm{M}}^{(t)}, \tag{2.10a}$$

$$\varpi_{\mathrm{M}}^{(n)} = \boldsymbol{\varpi}_{\mathrm{M}} \cdot \hat{\mathbf{n}}, \tag{2.10b}$$

$$\boldsymbol{\varpi}_{\mathrm{M}}^{(t)} = \sum_i \varpi_{\mathrm{M}}^{(t_i)} \hat{\mathbf{t}}_i, \qquad \varpi_{\mathrm{M}}^{(t_i)} = \boldsymbol{\varpi}_{\mathrm{M}} \cdot \hat{\mathbf{t}}_i, \tag{2.10c}$$

where $\hat{\mathbf{t}}_i$ (with $i = 1$ or 2) is the unit tangent vector orthogonal to $\hat{\mathbf{n}}$ (see Appendix A.3.1). Further dropping the subscript 'b' in $\overleftrightarrow{\mathbf{E}}_b$ for brevity, the stress balance in the direction normal to the free surface is given by

$$p - 2\mu\ \hat{\mathbf{n}} \cdot \overleftrightarrow{\mathbf{E}} \cdot \hat{\mathbf{n}} + \varpi_{\mathrm{M}}^{(n)} - \gamma \nabla \cdot \hat{\mathbf{n}} = 0 \qquad \text{at } z = h(x, y, t), \tag{2.11}$$

and the stress balance in the direction tangent to the free surface is given by

$$-2\mu\ \hat{\mathbf{n}} \cdot \overleftrightarrow{\mathbf{E}} \cdot \hat{\mathbf{t}}_i + \varpi_{\mathrm{M}}^{(t_i)} + \hat{\mathbf{t}}_i \cdot \nabla_s \gamma = 0 \qquad \text{at } z = h(x, y, t). \tag{2.12}$$

The curvature term in Eq. (2.11) represents surface tension effect, while the $\nabla_s \gamma$ term in Eq. (2.12) represents shear flow driven by surface tension gradient known as Marangoni effect. We assume the liquid film is a perfect dielectric and there is no free charge residing at the free surface at $z = h$. As shown in Section 2.3.2.3, $\varpi_{\mathrm{M}}^{(t_i)} = \hat{\mathbf{n}} \cdot (\overleftrightarrow{\mathbf{M}}_a - \overleftrightarrow{\mathbf{M}}_b) \cdot \hat{\mathbf{t}}_i = 0$ for perfect dielectric, but we retain $\varpi_{\mathrm{M}}^{(t_i)}$ for the sake of completeness and only drop the term at the very end.

Finally, we have the kinematic condition [6]

$$\frac{\partial h}{\partial t} + \mathbf{u}_{\parallel} \cdot \nabla_{\parallel} h = w \qquad \text{at } z = h(x, y, t). \tag{2.13}$$

2.1.1.3 Derivation of the $\partial h/\partial t$ Conservation Equation

To obtain a more tractable equation for describing the free surface $h(x, y, t)$ from the full sets of governing equations and boundary conditions, we first perform the following algebraic manipulations:

$$w|_{z=h} = w|_{z=h} - w|_{z=0} = \int_{z=0}^{z=h} \frac{\partial w}{\partial z} \mathrm{d}z = -\int_{z=0}^{z=h} \nabla_{\parallel} \cdot \mathbf{u}_{\parallel}\ \mathrm{d}z. \tag{2.14}$$

[6] Following the discussion in Chapter 2M in [63], consider a scalar function $F(x, y, z, t) = z - h(x, y, t)$. In the absence of interfacial mass transfer, the time derivative following any material point on the free surface is zero, which gives $\partial F/\partial t + \mathbf{u} \cdot \nabla F = 0$. Using the relations $\partial F/\partial t = -\partial h/\partial t$ and $\nabla F = -\partial h/\partial x\ \hat{\mathbf{e}}_x - \partial h/\partial y\ \hat{\mathbf{e}}_y + \hat{\mathbf{e}}_z$ gives Eq. (2.13).

The first and third equality result from the use of no-penetration condition given by Eq. (2.8) and the continuity equation given by Eq. (2.1), respectively.

Using the Leibniz integral rule which in 1D is given by [26, Eq. (A.5-8)]

$$\frac{\partial}{\partial x}\int_{a(x)}^{b(x)} f(x,t)\mathrm{d}t = f(x,b(x))\frac{\partial b}{\partial x} - f(x,a(x))\frac{\partial a}{\partial x} + \int_{a(x)}^{b(x)} \frac{\partial f}{\partial x}\mathrm{d}t, \tag{2.15}$$

we can re-write the last term of Eq. (2.14) (with $x \to \mathbf{x}$, $t \to z$, $a(x) \to 0$, $b(x) \to h(\mathbf{x})$, $f(x,t) \to \mathbf{u}_{\parallel}(\mathbf{x},z)$) as

$$\int_{z=0}^{z=h} \nabla_{\parallel}\cdot\mathbf{u}_{\parallel}\ \mathrm{d}z = \nabla_{\parallel}\cdot\int_{z=0}^{z=h}\mathbf{u}_{\parallel}\ \mathrm{d}z - \nabla_{\parallel}h\cdot\mathbf{u}_{\parallel}|_{z=h}. \tag{2.16}$$

Finally, using the kinematic equation given by Eq. (2.13), we arrive at the following general equation

$$\frac{\partial h}{\partial t} + \nabla_{\parallel}\cdot\left(\int_{z=0}^{z=h}\mathbf{u}_{\parallel}\mathrm{d}z\right) = 0, \tag{2.17}$$

which is simply a kinematic condition with mass conservation enforced for a domain with a free boundary at $z = h(x,y,t)$ and holds under fairly general conditions [7].

To gain more intuition of Eq. (2.17), consider a short time interval Δt and a short segment of length Δx in 1D. Suppose the local film thickness changes by Δh due to incoming flux, then the change in mass equals $\Delta m = \rho\Delta x\Delta h$. The incoming fluid at x equals $\rho(\bar{u}h)|_x\Delta t$, where $\bar{u} = \int u\mathrm{d}z$ is the height-averaged velocity, while the outgoing fluid at $x+\Delta x$ equals $\rho(\bar{u}h)|_{x+\Delta x}\Delta t$. Equating the change in mass to the incoming/outgoing fluid gives $\rho\Delta x\Delta h = \rho\left[(\bar{u}h)|_x - (\bar{u}h)|_{x+\Delta x}\right]\Delta t$. As $(\Delta t, \Delta x, \Delta h) \to 0$, we recover the 1D version of Eq. (2.17).

The problem has now been turned into the determination of $\mathbf{u}_{\parallel}$, which in general requires solving the full Navier-Stokes equation with the appropriate boundary conditions, but can be simplified for liquid thin film patterning by using the long wavelength approximation to be discussed next.

2.1.2 Dimensionless governing equations

Here, we derive the dimensionless governing equation used for modeling liquid thin film phenomena throughout this thesis. The final equation given by Eq. (2.49) is summarized at the end of this subsection along with some general discussions of the assumptions and limitations. Table 2.2 summarizes all the dimensional and dimensionless

[7] Eq. (2.17) is derived by only assuming mass conservation (for an incompressible fluid), no-penetration condition at the substrate and no mass loss at the free surface. It also holds for the more general Navier slip boundary condition.

variables used in this thesis, Table 2.3 summarizes the characteristic scales used for non-dimensionalization, and Table 2.4 summarizes different dimensionless groups and quantities which appear after non-dimensionalization.

Table 2.2: Dimensional and dimensionless variables for different physical quantities.

Variable	Dimensional Symbol	Dimensionless Symbol
Local film thickness	h	$H = h/h_0$
Vertical coordinate	z	$Z = z/h_0$
Horizontal coordinate	(x, y)	$(X, Y) = (x, y)/l_0$
	$\mathbf{x} = x\ \hat{\mathbf{e}}_x + y\ \hat{\mathbf{e}}_y$	$\mathbf{X} = X\hat{\mathbf{e}}_x + Y\hat{\mathbf{e}}_y$
Spatial derivatives	$\nabla = \nabla_\parallel + \frac{\partial}{\partial z}\hat{\mathbf{e}}_z$	$\nabla^* = \nabla^*_\parallel + \frac{\partial}{\partial Z}\hat{\mathbf{e}}_z$
	$\nabla_\parallel = \frac{\partial}{\partial x}\hat{\mathbf{e}}_x + \frac{\partial}{\partial y}\hat{\mathbf{e}}_y$	$\nabla^*_\parallel = \frac{\partial}{\partial X}\hat{\mathbf{e}}_x + \frac{\partial}{\partial Y}\hat{\mathbf{e}}_y$
		$\nabla^*_\parallel = \frac{h_0}{\epsilon}\nabla_\parallel, \quad \frac{\partial}{\partial Z} = h_0\frac{\partial}{\partial z}$
Voltage	V	$\Psi = V/V_0$
Temperature	T	$\Theta = (T - T_{\text{cold}})/\Delta T$
Lateral velocity	(u, v)	$(U, V) = (u, v)/u_0$
	$\mathbf{u}_\parallel = u\hat{\mathbf{e}}_x + v\hat{\mathbf{e}}_y$	$\mathbf{U}_\parallel = U\hat{\mathbf{e}}_x + V\hat{\mathbf{e}}_y$
Vertical velocity	w	$W = w/\epsilon u_0$
Time	t	$\tau = t/t_0$
Pressure	p	$P = p/p_0$
Surface tension variation	$\gamma - \gamma_0$	$\Gamma = (\gamma - \gamma_0)/\Delta\gamma$

2.1.2.1 Non-dimensionalization using Long Wavelength Approximation

The variables and governing equations introduced in the previous section are non-dimensionalized under the assumption of long wavelength approximation (LWA) [8] that the typical length scale in the horizontal or 'in-plane' direction is much longer than that in the vertical or 'out-of-plane' direction. The derivation presented in this section closely follows the review by Oron et al. [85]. Additional references can be found in the more recent review by Craster and Matar [22] or the textbook by Leal [63, Chapter 6A].

Uppercase letters and symbols are used to denote dimensionless quantities, and the subscript '0' (e.g., h_0, l_0, t_0, etc.) is used to denote dimensional quantities for non-

[8] It is also known as lubrication approximation, long wavelength approximation or slender-gap approximation in the literature.

Table 2.3: Typical values of the characteristic scales used in non-dimensionalization. Each data entry reported in the studies quoted in Table 1.1 to used to estimate the characteristic scales, and the resulting spread of the characteristic scales are reported in this table.

Variable	Symbol	Unit	Typical Values
Vertical coordinate	h_0	nm	$78 - 400$
Lateral coordinate	l_0 $(= \lambda_m/2$ or $\lambda_p/2)$	μm	$0.6 - 36.6$
Voltage	V_0	V	$10 - 100$
Temperature	$\Delta T = T_{\text{hot}} - T_{\text{cold}}$	K	$9.8 - 25.8$
Time	$t_0 = \frac{l_0}{u_0} = \frac{\mu l_0^4}{h_0^3 \gamma_0}$	s	$7500 - 3 \times 10^5$
Lateral velocity[a]	$u_0 = \frac{\epsilon^3 \gamma_0}{\mu} = \frac{h_0^3 \gamma_0}{l_0^3 \mu}$	m/s	$8 \times 10^{-11} - 2 \times 10^{-9}$
Pressure[b]	$p_0 = \frac{\mu u_0}{\epsilon h_0} = \frac{h_0 \gamma_0}{l_0^2}$	Pa	$5 - 33$
Surface tension	γ_0	N/m	$0.03 - 0.036$
Surface tension variation[c]	$\Delta\gamma = \frac{\mu u_0}{\epsilon} = \frac{h_0^2 \gamma_0}{l_0^2}$	N/m	$0.0006 - 0.002$

Expressions highlighted in blue are typical scalings employed under LWA [85], while those highlighted in red are obtained after substituting the specific choice of $u_0 = \epsilon^3 \gamma_0 / \mu$, see Chapter 2.1.2.3.

[a] Velocity scale u_0 is obtained by balancing capillary and viscous stress in normal stress boundary condition.

[b] Pressure scale p_0 is obtained by balancing the viscous term and pressure gradient term in the Navier-Stokes equation along the horizontal direction.

[c] Surface tension variation scale $\Delta\gamma$ is obtained by balancing the Marangoni term and the viscous shear stress term in the tangential stress boundary condition.

Table 2.4: Typical values of the dimensionless numbers relevant to EHD/TC patterning under LWA. Each data entry reported in the studies quoted in Table 1.1 to used to estimate the dimensionless numbers, and the resulting spread of the dimensionless numbers are reported in this table.

Name	Physical meaning	Expression	Values
Lubrication		$\epsilon = h_0/l_0$	$0.005 - 0.2$
Reynolds	$\frac{\text{inertial force}}{\text{viscous force}}$	$\text{Re} = \frac{\rho u_0 h_0}{\mu}$	$\mathcal{O}(10^{-16} - 10^{-8})$
Capillary	$\frac{\text{viscous forces}}{\text{capillary force}}$	$\overline{\text{Ca}} = \frac{\mu u_0}{\epsilon^3 \gamma_0}$	1 [a]
Marangoni Marangoni [a]	$\frac{\text{thermocapillary force}}{\text{viscous force}}$ $\frac{\text{thermocapillary force}}{\text{capillary force}}$	$\overline{\text{Ma}} = \frac{\epsilon \gamma_T \Delta T}{\mu u_0}$ $\mathcal{M} = \overline{\text{Ma}} \times \overline{\text{Ca}} = \frac{\gamma_T \Delta T}{\epsilon^2 \gamma_0}$	$\mathcal{O}(10^1 - 10^4)$
Electric Weber Electric Weber [a]	$\frac{\text{electrostatic force}}{\text{viscous force}}$ $\frac{\text{electrostatic force}}{\text{capillary force}}$	$\overline{\text{We}} = \frac{\epsilon \varepsilon_0 V_0^2}{\mu u_0 h_0}$ $\mathcal{W} = \overline{\text{We}} \times \overline{\text{Ca}} = \frac{\varepsilon_0 V_0^2}{\epsilon^2 \gamma_0 h_0}$	$\mathcal{O}(10^2 - 10^5)$
Bond	$\frac{\text{gravitational force}}{\text{capillary force}}$	$\mathcal{B} = \frac{\rho g h_0^2}{\epsilon^2 \gamma_0} = \frac{\rho g l_0^2}{\gamma_0}$	$\mathcal{O}(10^{-7} - 10^{-4})$
Hamaker	$\frac{\text{intermolecular force}}{\text{capillary force}}$	$\mathcal{A} = \frac{A}{\epsilon^2 6\pi \gamma_0 h_0^2}$	$\mathcal{O}(10^{-5} - 10^{-1})$
Prandtl	$\frac{\text{momentum diffusivity}}{\text{thermal diffusivity}}$	$\text{Pr} = \frac{\mu/\rho}{\hat{k}/c_p \rho} = \frac{c_p \mu}{\hat{k}}$	$\mathcal{O}(10^0 - 10^8)$ [b]

[a] After substitution of u_0 given by Eq. (2.48).
[b] Air: $0.69 - 0.72$ for temperature between $50°$C and $200°$C; Polystyrene: $\mathcal{O}(10^4 - 10^8)$, see footnote in Table 2.1 for details on estimation of viscosity.

dimensionalization.

The mean film thickness h_0 is used as the characteristic vertical scale and can be experimentally measured. The symbol l_0 is used to denote the characteristic horizontal scale, which is either the fastest-growing wavelength λ_m [9] in the absence of any spatial modulation as shown in Fig. 1.1(a)-(b), or the externally imposed patterning wavelength λ_p which is assumed to be known. The dimensionless coordinates are

$$(X, Y) = \frac{(x, y)}{l_0} = \epsilon \frac{(x, y)}{h_0}, \qquad (Z, H) = \frac{(z, h)}{h_0}, \tag{2.18}$$

while the dimensionless gradient operators denoted by the asterisk $(*)$ is

[9] In both EHD and TC patterning, λ_m is determined by the mean film thickness h_0, material's properties and other adjustable experimental parameters (see section 3.1.3), and is therefore assumed to be a known quantity for a given set of parameters.

$$\nabla^* = \left(\frac{\partial}{\partial X}, \frac{\partial}{\partial Y}, \frac{\partial}{\partial Z}\right) = \left(l_0\frac{\partial}{\partial x}, l_0\frac{\partial}{\partial y}, h_0\frac{\partial}{\partial z}\right) = h_0\left(\frac{1}{\epsilon}\frac{\partial}{\partial x}, \frac{1}{\epsilon}\frac{\partial}{\partial y}, \frac{\partial}{\partial z}\right), \tag{2.19}$$

The symbol $\epsilon = h_0/l_0$ is reserved to denote the small aspect ratio in LWA. It will be shown later that $\epsilon^2 \ll 1$ is required for LWA to hold. Referring to Fig. 2.1, the vertical lengths scale as $\mathcal{O}(1)$, while the horizontal lengths scale as $\mathcal{O}(1/\epsilon)$.

Let u_0 and w_0 denote the characteristic horizontal and vertical velocity scale which will be specified later in Section 2.1.2.3. The dimensionless velocity is

$$\mathbf{U} = \mathbf{U}_\parallel + W\hat{\mathbf{e}}_z, \quad \mathbf{U}_\parallel = U\hat{\mathbf{e}}_x + V\hat{\mathbf{e}}_y, \quad \mathbf{U}_\parallel = \frac{\mathbf{u}_\parallel}{u_0}, \quad W = \frac{w}{u_0}. \tag{2.20}$$

The continuity equation given by Eq. (2.1) is non-dimensionalized to

$$\frac{u_0}{l_0}\nabla_\parallel^*\mathbf{U}_\parallel + \frac{w_0}{h_0}\frac{\partial W}{\partial Z} = 0. \tag{2.21}$$

Since both terms should be of the same order, and $\nabla_\parallel^*\mathbf{U}_\parallel$ and $\partial W/\partial Z$ are assumed to be $\mathcal{O}(1)$ after non-dimensionalization, we can fix the vertical velocity scale w_0 as follow:

$$w_0 = \frac{h_0}{l_0}u_0 = \epsilon u_0. \tag{2.22}$$

The characteristic time t_0 is determined from the lateral fluidic motion, i.e., $t_0 = l_0/u_0$, and so the dimensionless time τ and the time derivative $\partial/\partial\tau$ are

$$\tau = \frac{t}{l_0/u_0} = \frac{\epsilon u_0 t}{h_0}, \qquad \frac{\partial}{\partial\tau} = \frac{h_0}{\epsilon u_0}\frac{\partial}{\partial t}. \tag{2.23}$$

The characteristic pressure scale p_0 is used to non-dimensionalize the pressure p and external body force potential ϖ_{ext}. Introducing the notation $\bar{P} = P + \Pi_{\text{ext}} = p_0(p + \varpi_{\text{ext}})$, the Navier-Stokes equation given by Eq. (2.6) becomes

$$\epsilon\frac{\rho u_0^2}{h_0}\left(\frac{\partial\mathbf{U}_\parallel}{\partial\tau} + \mathbf{U}_\parallel\cdot\nabla_\parallel^*\mathbf{U}_\parallel + W\frac{\partial\mathbf{U}_\parallel}{\partial Z}\right) = -\frac{\epsilon p_0}{h_0}\nabla_\parallel^*\bar{P} + \frac{\mu u_0}{h_0^2}\left[\epsilon^2\nabla_\parallel^{*2}\mathbf{U}_\parallel + \frac{\partial^2\mathbf{U}_\parallel}{\partial Z^2}\right], \tag{2.24}$$

$$\epsilon^3\frac{\rho u_0^2}{h_0}\left(\frac{\partial W}{\partial\tau} + \mathbf{U}_\parallel\cdot\nabla_\parallel^* W + W\frac{\partial W}{\partial Z}\right) = -\frac{p_0}{h_0}\frac{\partial\bar{P}}{\partial Z} + \frac{\epsilon^2\mu u_0}{h_0^2}\left(\epsilon^2\nabla_\parallel^{*2}W + \frac{\partial^2 W}{\partial Z^2}\right), \tag{2.25}$$

On the left-hand side, we can identify the Reynolds number as $\mathrm{Re} = \rho u_0 h_0/\mu$, and for typical experimental conditions applicable to thin film patterning, $\mathrm{Re} \ll 1$ (see Table 2.4 on page 19). The inertial term of the left-hand side can thus be safely neglected. On the right-hand side, balancing horizontal pressure gradient $\nabla^*_{\parallel}\bar{P}$ and the dominant viscous stress term $\partial^2 \mathbf{U}_{\parallel}/\partial Z^2$ leads to

$$\mathcal{O}\left(\frac{\epsilon p_0}{h_0}\right) = \mathcal{O}\left(\frac{\mu u_0}{h_0^2}\right) \implies p_0 = \frac{\mu u_0}{\epsilon h_0}. \tag{2.26}$$

Note that the pressure should be retained in either Eq. (2.24) or Eq. (2.25) whatever the scaling turns out to be. The other alternative would be choosing p_0 such that the pressure gradient $\partial\bar{P}/\partial Z$ and viscous term $\partial^2 W/\partial Z^2$ is balanced instead. However, this leads to an inconsistency [63] in the resulting equations, and hence Eq. (2.26) is the only appropriate choice for choosing the pressure scale. Assuming $\epsilon^2 \ll 1$, the dimensionless Navier-Stokes equation becomes

$$\boxed{\nabla^*_{\parallel}\bar{P} = \frac{\partial^2 \mathbf{U}_{\parallel}}{\partial Z^2},} \tag{2.27}$$

$$\boxed{\frac{\partial \bar{P}}{\partial Z} = 0,} \tag{2.28}$$

which together with the continuity equation

$$\boxed{\nabla^*_{\parallel}\mathbf{U}_{\parallel} + \frac{\partial W}{\partial Z} = 0} \tag{2.29}$$

govern the hydrodynamics in the bulk of the liquid film. The dimensionless pressure and body force potential can also be written as

$$(P, \Pi_{\mathrm{ext}}) = \frac{(p, \varpi_{\mathrm{ext}})}{p_0} = \frac{\epsilon h_0}{\mu u_0}(p, \varpi_{\mathrm{ext}}). \tag{2.30}$$

Next, we begin to non-dimensionalize the boundary conditions. The no-slip (Eq. (2.7)) and no-penetration (Eq. (2.8)) conditions are non-dimensionalized to

$$\boxed{\mathbf{U} = (U, V, W) = 0, \qquad \text{at } Z = 0.} \tag{2.31}$$

For the stress balance condition, we first simplify the unit normal and tangent vectors $\hat{\mathbf{n}}$ and $\hat{\mathbf{t}}$:

$$\hat{\mathbf{n}} = \frac{-\epsilon\nabla_{\parallel}^{*}H + \hat{\mathbf{e}}_z}{\sqrt{1+\left|\epsilon\nabla_{\parallel}^{*}H\right|^2}} = \left(-\epsilon\frac{\partial H}{\partial X}\hat{\mathbf{e}}_x - \epsilon\frac{\partial H}{\partial Y}\hat{\mathbf{e}}_y + \hat{\mathbf{e}}_z\right)\left[1+\mathcal{O}(\epsilon^2)\right], \tag{2.32a}$$

$$\hat{\mathbf{t}}_x = \left(\hat{\mathbf{e}}_x + \epsilon\frac{\partial H}{\partial X}\hat{\mathbf{e}}_z\right)\left[1+\mathcal{O}(\epsilon^2)\right], \tag{2.32b}$$

$$\hat{\mathbf{t}}_y = \left(\hat{\mathbf{e}}_y + \epsilon\frac{\partial H}{\partial Y}\hat{\mathbf{e}}_z\right)\left[1+\mathcal{O}(\epsilon^2)\right], \tag{2.32c}$$

and the rate-of-strain tensor $\overset{\leftrightarrow}{\mathbf{E}}$:

$$2\overset{\leftrightarrow}{\mathbf{E}} = \frac{u_0}{h_0}\begin{pmatrix} 2\epsilon\dfrac{\partial U}{\partial X} & \epsilon\left(\dfrac{\partial U}{\partial Y}+\dfrac{\partial V}{\partial X}\right) & \dfrac{\partial U}{\partial Z}+\epsilon^2\dfrac{\partial W}{\partial X} \\ \epsilon\left(\dfrac{\partial U}{\partial Y}+\dfrac{\partial V}{\partial X}\right) & 2\epsilon\dfrac{\partial V}{\partial Y} & \dfrac{\partial V}{\partial Z}+\epsilon^2\dfrac{\partial W}{\partial Y} \\ \dfrac{\partial U}{\partial Z}+\epsilon^2\dfrac{\partial W}{\partial X} & \dfrac{\partial V}{\partial Z}+\epsilon^2\dfrac{\partial W}{\partial Y} & 2\epsilon\dfrac{\partial W}{\partial Z} \end{pmatrix}. \tag{2.33}$$

We also assume the surface tension can be expressed as

$$\gamma = \gamma_0 + \gamma_\Delta\Gamma, \tag{2.34}$$

where γ_0 and γ_Δ represent the typical values of the *total* surface tension and the *change* in surface tension due to Marangoni effect, respectively. Note that the dimensionless surface tension variation is Γ, and the dimensional surface tension variation $|\gamma_\Delta\Gamma|$ is typically much smaller than γ_0.

The stress balance conditions given in Eq. (2.11) are (2.12) are non-dimensionalized to

$$P + \frac{\epsilon h_0}{\mu u_0}\varpi_{\mathrm{M}}^{(n)} - 2\epsilon^2\left[\frac{\partial W}{\partial Z} - \nabla_{\parallel}^{*}H\cdot\frac{\partial \mathbf{U}_{\parallel}}{\partial Z} + \mathcal{O}(\epsilon^2)\right] + \frac{\epsilon^3\gamma_0}{\mu u_0}\left(1+\frac{\gamma_\Delta}{\gamma_0}\Gamma\right)\nabla_{\parallel}^{*2}H\left[1+\mathcal{O}(\epsilon^2)\right] = 0. \qquad \text{at } Z=H \tag{2.35}$$

$$-\left[\frac{\partial \mathbf{U}_{\parallel}}{\partial Z} + \mathcal{O}(\epsilon^2)\right] + \frac{h_0}{\mu u_0}\boldsymbol{\varpi}_{\mathrm{M}}^{(t)} + \frac{\epsilon\gamma_\Delta}{\mu u_0}\nabla_{\parallel}^{*}\Gamma = 0. \qquad \text{at } Z=H \tag{2.36}$$

Appropriate scalings need to be chosen in order to retain the relevant terms to leading order. For the external forcing associated with the stress tensor $\overset{\leftrightarrow}{\mathbf{M}}$, balancing the P term and $\varpi_{\mathrm{M}}^{(n)}$ term in Eq. (2.35) and the $\partial\mathbf{U}_{\parallel}/\partial Z$ term and $\boldsymbol{\varpi}_{\mathrm{M}}^{(t)}$ term in Eq. (2.36) give the following scalings [85]:

$$(\Pi_{\mathrm{M}}^{(n)}, \mathbf{\Pi}_{\mathrm{M}}^{(t)}) = \frac{h_0}{\mu u_0}(\epsilon \varpi_{\mathrm{M}}^{(n)}, \boldsymbol{\varpi}_{\mathrm{M}}^{(t)}). \tag{2.37}$$

Note that $\varpi_{\mathrm{M}}^{(n)}$ and $\boldsymbol{\varpi}_{\mathrm{M}}^{(t)}$ are scaled differently by a factor of ϵ under LWA. In order to retain the surface tension effect in Eq. (2.35), we assume $\mathcal{O}(\epsilon^3 \gamma_0/\mu u_0) = 1$. Similarly, to retain the Marangoni effect in Eq. (2.36), we assume $\mathcal{O}(\epsilon \gamma_\Delta/\mu u_0) = 1$.

The dimensionless surface tension variation Γ and the characteristic scale γ_Δ are then given by

$$\gamma_\Delta = \frac{\mu u_0}{\epsilon}, \qquad \Gamma = \frac{\epsilon(\gamma - \gamma_0)}{\mu u_0}, \tag{2.38}$$

We introduce the capillary number Ca, the Marangoni number Ma, and the corresponding rescaled numbers denoted by an overhead bar which are assumed to be $\mathcal{O}(1)$:

$$\mathsf{Ca} = \frac{\mu u_0}{\gamma_0}, \qquad \mathsf{Ma} = \frac{\gamma_\Delta}{\mu u_0}, \qquad \overline{\mathsf{Ca}} = \frac{\mathsf{Ca}}{\epsilon^3} = \frac{\mu u_0}{\epsilon^3 \gamma_0}, \qquad \overline{\mathsf{Ma}} = \epsilon \mathsf{Ma} = \frac{\epsilon \gamma_\Delta}{\mu u_0}. \tag{2.39}$$

Note that the Γ term in Eq. (2.35) (highlighted in red) becomes $\gamma_\Delta/\gamma_0 = \epsilon^2 \overline{\mathsf{Ca}}$ and hence can be neglected. Dropping other $\mathcal{O}(\epsilon^2)$ terms (highlighted in red) in the viscous stress and curvature, Eq. (2.35) and (2.36) become

$$\boxed{\begin{aligned} P + \Pi_{\mathrm{M}}^{(n)} + \frac{1}{\overline{\mathsf{Ca}}} \nabla_\parallel^* H = 0, \qquad & \text{at } Z = H, \qquad (2.40) \\ -\frac{\partial \mathbf{U}_\parallel}{\partial Z} + \mathbf{\Pi}_{\mathrm{M}}^{(t)} + \overline{\mathsf{Ma}}\ \nabla_\parallel^* \Gamma = 0, \qquad & \text{at } Z = H. \qquad (2.41) \end{aligned}}$$

Finally, Eq. (2.17) is non-dimensionalized to

$$\boxed{\frac{\partial H}{\partial \tau} + \nabla_\parallel^* \cdot \left[\int_0^H \mathbf{U}_\parallel \mathrm{d}Z \right] = 0,} \tag{2.42}$$

which is exact and always holds regardless of whether LWA is used.

2.1.2.2 Determination of $\mathbf{U}_\parallel$

We are now ready to solve the boxed governing equations to obtain an approximate expression for $\mathbf{U}_\parallel$ under LWA. First, Eq. (2.28) implies $\bar{P} = \bar{P}(\mathbf{X})$ is independent of Z. We can therefore integrate Eq. (2.27) along Z twice to obtain

$$\mathbf{U}_\parallel = \frac{1}{2} \nabla_\parallel^* \bar{P}\ Z^2 + \alpha_1 Z + \alpha_0, \tag{2.43}$$

where $\alpha_i(X,Y)$ $(i=0,1)$ are integration constants which are determined by the boundary conditions given in Eq. (2.41) and (2.31). We can then solve for $\mathbf{U}_\parallel$ to obtain

$$\mathbf{U}_\parallel = Z\left[\frac{1}{2}\nabla_\parallel^* P(Z-2H) + \overline{\mathrm{Ma}}\nabla_\parallel^*\Gamma + \mathbf{\Pi}_{\mathrm{M}}^{(t)}\right]. \tag{2.44}$$

While not necessary for the subsequent derivation, here we provide the expression for the vertical velocity W for completeness by using the continuity equation:

$$\begin{aligned} W &= -\int_0^Z \nabla_\parallel^* \cdot \mathbf{U}_\parallel \mathrm{d}Z \\ &= \frac{Z^2}{6}\left[\nabla_\parallel^{*2} P(3H-Z) + 3\nabla_\parallel^* P\cdot\nabla_\parallel H - 3\nabla_\parallel^*\cdot\left(\overline{\mathrm{Ma}}\nabla_\parallel^*\Gamma + \mathbf{\Pi}_{\mathrm{M}}^{(t)}\right)\right]. \end{aligned} \tag{2.45}$$

Finally, Eq. (2.44) is integrated from $Z=0$ to $Z=H$ and then substituted into Eq. (2.42), giving

$$\boxed{\frac{\partial H}{\partial \tau} + \nabla_\parallel^*\cdot\left[-\frac{H^3}{3}\nabla_\parallel^*\bar{P} + \frac{H^2}{2}\left(\nabla_\parallel^*\Gamma + \mathbf{\Pi}_{\mathrm{M}}^{(t)}\right)\right] = 0,} \tag{2.46}$$

where $\bar{P}$ is obtained from Eq. (2.40):

$$\boxed{\bar{P} = P + \Pi_{\mathrm{ext}} = (P+\Pi_{\mathrm{ext}})|_{Z=H} = -\frac{1}{\overline{\mathrm{Ca}}}\nabla_\parallel^{*2} H - \Pi_{\mathrm{M}}^{(n)} + \Pi_{\mathrm{ext}}|_{Z=H}.} \tag{2.47}$$

2.1.2.3 Choice of horizontal velocity scale u_0

In order to maintain consistent form of the governing equation regardless of the dominant physical effects (electrostatics for EHD pattering or thermocapillarity for TC patterning), we scale the velocity by balancing the viscous force and the surface tension force, both of which are always present for the parameters of interest in this thesis. This amounts to setting the rescaled Capillary number, which is simply the ratio of viscous force and surface tension force under LWA, to unity, i.e., $\overline{\mathrm{Ca}} = 1$. This gives the following expression of u_0

$$u_0 = \frac{\epsilon^3\gamma_0}{\mu} = \frac{h_0^3\gamma_0}{l_0^3\mu}. \tag{2.48}$$

This choice of u_0 is also mathematically equivalent to rescaling the dimensionless time by absorbing $\overline{\mathrm{Ca}}$ into the definition of τ in Eq. (2.46), thus reducing the number of dimensionless groups by one. The other dimensionless groups which enter Eq. (2.46) through $\Phi|_{Z=H}$, $\mathbf{\Pi}_{\mathrm{M}}$ and Γ become the ratio of the corresponding physical force to surface tension force under this specific choice of u_0.

2.1.3 Summary of governing thin film equation

The governing thin film equation for a single viscous incompressible Newtonian liquid layer on a flat substrate used throughout this thesis can be expressed as

$$\boxed{\begin{aligned} \frac{\partial H}{\partial \tau} &= \nabla_{\parallel}^{*} \cdot \left[M_{\perp}(H) \nabla_{\parallel}^{*} \bar{P} - M_{\parallel}(H) \nabla_{\parallel}^{*} \Gamma \right], \\ \bar{P} &= -\nabla_{\parallel}^{*2} H - \Pi, \\ M_{\perp}(H) &= \frac{H^3}{3}, \qquad M_{\parallel}(H) = \frac{H^2}{2}, \end{aligned}} \tag{2.49}$$

where $M_{\perp}(H)$ and $M_{\parallel}(H)$ are the two mobility factors associated with the normal (subscript '$\perp$') and tangential (subscript '$\parallel$') direction with respect to the free surface. The specific forms of the two mobility factors are derived assuming no-slip conditions hold at the bottom substrate and neglecting the hydrodynamics in the upper gas layer.

Additional physical phenomena enter Eq. (2.49) through the external pressure term Π or the Marangoni term Γ, and we will consider electrostatics Π_{EM} under perfect dielectric model (Section 2.3.2), thermocapillarity Π_{TC} with thermal conduction (Section 2.3.1), van-der Waals interaction Π_{vdw} (Section 2.3.3) and gravity Π_{gravity} (Section 2.3.4) which are given by

$$\Pi = \Pi_{\mathrm{EM}} + \Pi_{\mathrm{vdw}} + \Pi_{\mathrm{gravity}}, \qquad \Gamma = \Gamma_{\mathrm{TC}}$$

$$\Pi_{\mathrm{EM}} = \frac{\mathcal{W}\varepsilon_r(\varepsilon_r - 1)\Psi_{\Delta}^2}{2\left[H + \varepsilon_r(D - H)\right]^2}, \tag{2.50a}$$

$$\Pi_{\mathrm{vdw}} = \mathcal{A}\left(\frac{1}{H^3} - \frac{1}{(D - H)^3}\right), \tag{2.50b}$$

$$\Pi_{\mathrm{gravity}} = -\mathcal{B}H, \tag{2.50c}$$

$$\Gamma_{\mathrm{TC}} = -\frac{\mathcal{M}\left[\kappa H \Theta_{\mathrm{cold}} + (D - H)\Theta_{\mathrm{hot}}\right]}{D - (1 - \kappa)H}. \tag{2.50d}$$

The derivations of Eq. (2.50) and the physical meanings of different symbols and terms are discussed in Section 2.3. Note that since pressure arising from both body force (e.g., gravity) and surface force (electrostatics) can be treated similarly inside $\bar{P}$, we no longer distinguish between the two and simply use the general symbol Π to represent external pressure acting on the free surface which is not due to capillarity.

Certain assumptions can be relaxed, or more complicated physical phenomena can be considered, if appropriate modifications to Eq. (2.49) are made. Here we briefly discuss a few common cases:

1. Navier-slip at $z = 0$: If we allow a slip length at the bottom substrate such that $\mathbf{u}_\parallel \propto \partial \mathbf{u}_\parallel / \partial z$ at $z = 0$, both mobility factors $M_\perp(H)$ and $M_\parallel(H)$ are modified to the form $M_\perp(H) = H^3/3 + \beta_{\text{slip}} H^2$ and $M_\parallel(H) = H^2/2 + \beta_{\text{slip}} H$ where β_{slip} is the slip coefficient [85].

2. Temperature dependent viscosity $\mu = \mu(T)$: The viscosity of polymers, which are the fluids commonly used in EHD and TC patterning, is highly temperature dependent. Its effect can be incorporated which results in more complicated forms for the mobility factors, see, for example, Ref [85, Section G].

3. Viscous fluid in the upper layer: If the passive gas layer is replaced by a viscous fluid such that its hydrodynamics cannot be ignored, the mobility factors become a function of H, D and the viscosities of the two fluids.

4. Topographically patterned substrate: If the bottom substrate is not flat but topographically patterned with shape given by $Z = S(\mathbf{X})$, and the free surface position is $Z = H(\mathbf{X}, \tau) + S(\mathbf{X})$, then $\bar{P}$ contains an additional term $\nabla_\parallel^{*2} S$ which is the pressure gradient caused by the uneven substrate profile.

5. Electric or/and thermal fields generated from different configurations: If we have a different system configuration, such as the absence of the top plate, Π_{EM} and Γ_{TC} will have different expressions depending on the actual physics. For example, if a liquid film is subject to convective cooling, then Γ_{TC} is derived with Newton's law of cooling as the boundary condition. Eq. (2.49) still holds as long as individual terms in Π and Γ only depend on H, other systems' variables such as $D(\mathbf{X})$ and materials' constants.

It can be seen that more general conditions or additional physical phenomena can be handled in a relatively straightforward manner despite the focus of this thesis being EHD and TC patterning. One main requirement is that $H(\mathbf{X}, \tau)$ is the *only* state variable describing the system, and additional state variables such as the electric potential and temperature have to be expressed in terms of H via some sort of approximations. Examples where additional state variables are required, including multi-layer films, or the presence of particles like surfactants or free charges, cannot be handled by simple modification of terms in Eq. (2.49) and so fall outside the scope of this thesis.

2.2 Gradient Flow Formulation

Mitlin [76] first showed that the interface equation describing thin film dewetting, which has the same form as Eq. (2.49) without shear stress, can be expressed in the following form

$$\frac{\partial H}{\partial \tau} = \nabla_{\parallel} \cdot \left[M_{\perp}(H) \nabla_{\parallel} \left(\frac{\delta \mathcal{F}[H]}{\delta H} \right) \right], \tag{2.51}$$

where $\mathcal{F}[H]$ is an energy functional defined as

$$\mathcal{F}[H] = \int_{\Omega} \left[\frac{1}{2} \left| \nabla_{\parallel} H \right|^2 + \Phi(H) \right] \mathrm{d}\mathbf{X}. \tag{2.52}$$

Eq. (2.51) is known as the gradient flow, and offers some advantages from a modeling perspective: it may offer better flexibility in incorporating energy functional to represent additional physical effects and it can be obtained via the Onsager variational principle [116]. Here, Eq. (2.51) is used to demonstrate an important fact that the free energy is a non-increasing function with time, and lay the foundation for latter discussion from an energy perspective.

Expand $H = H + \delta H_1$ where $\delta \ll 1$, the energy functional becomes

$$\begin{aligned}
\mathcal{F}[H + \delta H_1] &= \int_{\Omega} \frac{1}{2} \left[\nabla_{\parallel} (H + \delta H_1) \right]^2 + \Phi(H + \delta H_1) \mathrm{d}\mathbf{X} \\
&= \int_{\Omega} \left[\frac{1}{2} \left(\left| \nabla_{\parallel} H \right|^2 + 2\delta \nabla_{\parallel} H \cdot \nabla_{\parallel} H_1 + \Phi(H) + \frac{\mathrm{d}\Phi}{\mathrm{d}H} \delta H_1 \right) \right] \mathrm{d}\mathbf{X} + \mathcal{O}(\delta^2) \\
&= \mathcal{F}[H] + \delta \int_{\Omega} \left(-\nabla_{\parallel}^2 H + \frac{\mathrm{d}\Phi}{\mathrm{d}H} \right) H_1 \, \mathrm{d}\mathbf{X} + \mathcal{O}(\delta^2).
\end{aligned} \tag{2.53}$$

The functional derivative of $\mathcal{F}$ is

$$\frac{\delta \mathcal{F}[H]}{\delta H} = -\nabla_{\parallel}^{*2} H + \frac{\mathrm{d}\Phi}{\mathrm{d}H} = -\nabla_{\parallel}^{*2} H - \Pi, \tag{2.54}$$

where the $\Pi = -\mathrm{d}\Phi/\mathrm{d}H$ is the generalized external pressure, and Φ can be interpreted as the energy density (energy per unit area). The form of Φ depends on the specific physical effects and are discussed in Section 2.3. Inspection of Eq. (2.49) shows that it automatically satisfies the form of Eq. (2.51) and (2.54) when there is no shear stress, i.e., $\nabla_{\parallel}^{*} \Gamma = 0$. For the case of TC patterning where the Marangoni term is present, expressing Eq. (2.49) in the form of Eq. (2.51) is possible when the system is not spatially modulated (see Section 2.3.1.3).

Suppose the governing thin film equation can indeed be cast in the form of Eq. (2.51). We first investigate the time evolution of the free energy, i.e., $\mathrm{d}\mathcal{F}/\mathrm{d}\tau$. When the only time-dependent quantity of the system is the shape of the liquid film $H(\mathbf{X}, \tau)$, we have

$$\begin{aligned}\frac{\mathrm{d}\mathcal{F}[H]}{\mathrm{d}\tau} &= \frac{\mathrm{d}}{\mathrm{d}\tau}\int_\Omega \left[\frac{1}{2}|\nabla_\parallel H|^2 + \Phi(H)\right]\mathrm{d}\mathbf{X} \\ &= \int_\Omega \left[\nabla_\parallel H \cdot \frac{\mathrm{d}}{\mathrm{d}\tau}(\nabla_\parallel H) + \frac{\mathrm{d}\Phi}{\mathrm{d}H}\frac{\partial H}{\partial \tau}\right]\mathrm{d}\mathbf{X}. \end{aligned} \tag{2.55}$$

Using Green's first identity which is given by

$$\int_\Omega \left(\nabla\psi\cdot\nabla\phi + \psi\nabla^2\phi\right) dV = \int_{\partial\Omega} \psi\left(\nabla\phi\cdot\hat{\mathbf{n}}\right) dS \tag{2.56}$$

for any general vector fields $\phi(\vec{x})$ and $\psi(\vec{x})$ (not to be confused with the $\Phi(H)$ we have above).

Exchange the order of $\nabla_\parallel$ and $\mathrm{d}/\mathrm{d}\tau$ in the first term, and apply the Green's first identity with $\phi = H$ and $\psi = \partial H/\partial\tau$, we have

$$\int_\Omega \nabla_\parallel H\cdot\frac{\mathrm{d}}{\mathrm{d}\tau}(\nabla_\parallel H)\mathrm{d}\mathbf{X} = \int_\Omega \nabla_\parallel H\cdot\nabla_\parallel\left(\frac{\partial H}{\partial\tau}\right)\mathrm{d}\mathbf{X} = -\int_\Omega\left(\frac{\partial H}{\partial\tau}\nabla_\parallel^2 H\right)\mathrm{d}\mathbf{X} \tag{2.57}$$

where the boundary term vanishes if we impose periodic boundary condition or the Neumann boundary condition ($\nabla_\parallel H = 0$ along $\partial\Omega$).

Therefore, we have

$$\begin{aligned}\frac{\mathrm{d}\mathcal{F}[H]}{\mathrm{d}\tau} &= \int_\Omega\left(-\nabla_\parallel^2 H + \frac{\partial\Phi}{\partial H}\right)\frac{\partial H}{\partial\tau}\mathrm{d}\mathbf{X} \\ &= \int_\Omega\left(-\nabla_\parallel^2 H + \frac{\partial\Phi}{\partial H}\right)\nabla_\parallel\cdot\left[M(H)\left(-\nabla_\parallel^2 H + \frac{\partial\Phi}{\partial H}\right)\right]\mathrm{d}\mathbf{X} \\ &= -\int_\Omega M(H)\left|\nabla_\parallel\left(-\nabla_\parallel^2 H + \frac{\mathrm{d}\Phi}{\mathrm{d}H}\right)\right|^2\mathrm{d}\mathbf{X} \le 0. \end{aligned} \tag{2.58}$$

The last line is obtained via integration by parts. The boundary term vanishes if we impose the periodic boundary condition or the no flux boundary condition. Hence, the Lyapunov free energy functional is a non-increasing function with time.

2.3 Coupling with Other Physical Effects

In this section, we discuss how different physical phenomena relevant to EHD or TC patterning can be incorporated into Eq. (2.49) through the external pressure Π or the surface tension variation Γ.

2.3.1 Thermocapillarity

Since surface tension varies with temperature, the Marangoni term $\nabla^*_{\parallel}\Gamma$ in Eq. (2.46) can become significant when there is a temperature gradient along the free surface. Here we follow the derivation in Dietzel and Troian [29] to arrive at dimensionless Marangoni term $\nabla^*_{\parallel}\Gamma$ given by Eq. (2.72).

2.3.1.1 Dimensional Governing Equations

The temperature T is governed by the energy equation given by [85]

$$\rho_\alpha \; c_{p,\alpha} \left(\frac{\partial T_\alpha}{\partial t} + \mathbf{u}_i \cdot \nabla T_\alpha \right) = \hat{k}_\alpha \nabla^2 T_\alpha, \qquad \alpha = a \text{ (air)}, b \text{ (liquid)}, \tag{2.59}$$

where ρ_α is the density, $c_{p,\alpha}$ is the specific heat capacity at constant pressure, and $\hat{k}_\alpha$ is the thermal conductivity [10] of the fluid α where $\alpha = a$ refers to the upper layer of passive gas and $\alpha = b$ refers to the bottom layer of fluid. Note that while hydrodynamics is neglected in the passive gas layer, i.e., $\mathbf{u}_\alpha = 0$ for $\alpha = a$, heat transfer still occurs in both top and bottom layers. The boundary conditions are

$$T_a(z = d) = T_{\text{cold}}(\mathbf{x}), \tag{2.60}$$

$$T_b(z = 0) = T_{\text{hot}}(\mathbf{x}), \tag{2.61}$$

$$T_a(z = h) = T_b(z = h), \tag{2.62}$$

$$\hat{k}_a \; \hat{\mathbf{n}} \cdot \nabla T_a(z = h) = \hat{k}_b \; \hat{\mathbf{n}} \cdot \nabla T_b(z = h), \tag{2.63}$$

where $\hat{\mathbf{n}}$ is again the unit vector normal to the free surface at $z = h$. We allow the mask topography d and both T_{cold} and T_{hot} to be functions of the horizontal coordinates $\mathbf{x}$ to take into account spatially modulated mask topography and temperatures of the plates.

2.3.1.2 Dimensionless Governing Equations

Defining the dimensionless temperature Θ as

$$\Theta = \frac{T - T_{\text{cold}}}{T_{\text{hot}} - T_{\text{cold}}} = \frac{T - T_{\text{cold}}}{\Delta T}, \tag{2.64}$$

where $\Delta T \equiv \text{mean}(T_{\text{hot}} - T_{\text{cold}})$ is the mean temperature difference, and non-dimensionalizing the spatial scales through the LWA given by Eq. (2.18), Eq. (2.59) becomes

[10] In this thesis, k (with and without subscripts) generally refers to wave number except in this section where $\hat{k}$ refers to thermal conductivity. $\hat{k}_\alpha$ does not appear in the rest of this thesis where dimensionless quantities are mostly used.

$$\epsilon \text{Re Pr}_a \left(\frac{\partial \Theta_a}{\partial \tau} + \mathbf{U}_\parallel \cdot \nabla_\parallel^* \Theta_a + W \frac{\partial \Theta_a}{\partial Z} \right) = \epsilon^2 \nabla_\parallel^{*2} \Theta_a + \frac{\partial^2 \Theta_a}{\partial Z^2}, \tag{2.65a}$$

$$\epsilon \text{Re Pr}_b \frac{\rho_a}{\rho_b} \frac{\mu_b}{\mu_a} \frac{\partial \Theta_b}{\partial \tau} = \epsilon^2 \nabla_\parallel^{*2} \Theta_b + \frac{\partial^2 \Theta_b}{\partial Z^2}, \tag{2.65b}$$

where $\text{Pr}_\alpha = (\mu_\alpha c_{p,\alpha} / \hat{k}_\alpha)$ is the Prandtl number for fluid α and is a material constant. As shown in Table 2.1 and 2.4, $\text{Pr}_a = \mathcal{O}(1)$, $\text{Pr}_b = \mathcal{O}(10^4 - 10^8)$, $\text{Re} = \mathcal{O}(10^{-16} - 10^{-8})$, $\epsilon = \mathcal{O}(10^{-3} - 10^{-1})$, $\rho_a / \rho_b = \mathcal{O}(10^{-3})$ and $\mu_b / \mu_a = \mathcal{O}(10^5 - 10^8)$. Therefore, the left-hand side of both Eq. (2.65) can be neglected under typical conditions for TC patterning. The energy equation can then be simplified to a 1D Laplace equation

$$\frac{\partial^2 \Theta_\alpha}{\partial Z^2} = 0, \qquad \alpha = a, b, \tag{2.66}$$

with the boundary conditions

$$\Theta_a(Z = D) = \Theta_{\text{cold}}, \tag{2.67a}$$

$$\Theta_a(Z = 0) = \Theta_{\text{hot}}, \tag{2.67b}$$

$$\Theta_a(Z = H) = \Theta_b(Z = H), \tag{2.67c}$$

$$\kappa \frac{\partial \Theta_a(Z = H)}{\partial Z} = \frac{\partial \Theta_b(Z = H)}{\partial Z}, \tag{2.67d}$$

where $\kappa = \hat{k}_a / \hat{k}_b$ is the ratio of thermal conductivity. Using the general solution to 1D Laplace equation given in Appendix A.4, we can solve for the Θ_i:

$$\Theta_a(\mathbf{X}, Z) = \Theta_{\text{cold}} + \frac{\Theta_{\text{hot}} - \Theta_{\text{cold}}}{D - (1 - \kappa)H} (D - Z), \tag{2.68}$$

$$\Theta_b(\mathbf{X}, Z) = \Theta_{\text{hot}} - \frac{\kappa(\Theta_{\text{hot}} - \Theta_{\text{cold}})}{D - (1 - \kappa)H} Z. \tag{2.69}$$

Note that the Z dependence of Θ_i comes directly from the 1D Laplace equation given in Eq. (2.66), while its $\mathbf{X}$ dependence comes from $H(\mathbf{X}, \tau)$, $D(\mathbf{X})$, $\Theta_{\text{hot}}(\mathbf{X})$ and $\Theta_{\text{cold}}(\mathbf{X})$. The temperature at the free surface $Z = H$ (hereafter called 'surface temperature') Θ_s is

$$\Theta_s(\mathbf{X}) \equiv \Theta(\mathbf{X}, Z = H) = \frac{\kappa H \Theta_{\text{cold}} + (D - H)\Theta_{\text{hot}}}{D - (1 - \kappa)H}. \tag{2.70}$$

To relate the temperature to the Marangoni term in Eq. (2.46), we assume the surface tension decreases linearly with temperature as

$$\gamma(T_s) = \gamma_0 - \gamma_T(T_s - T_{\text{cold}}) = \gamma_0 - \gamma_T \Delta T\ \Theta_s, \tag{2.71}$$

where γ_0 is the reference surface tension evaluated at $T = T_{\text{cold}}$, $\gamma_T = |\partial\gamma/\partial T|$, and $\partial\gamma/\partial T < 0$ for most common materials. We can thus identify $\gamma_\Delta = \gamma_T \Delta T$ as the surface tension variation. The Marangoni term in Eq. (2.46) becomes

$$\nabla_\parallel^* \Gamma = -\mathcal{M} \nabla_\parallel^* \Theta_s = -\mathcal{M} \nabla_\parallel^* \left[\frac{\kappa H \Theta_{\text{cold}} + (D - H)\Theta_{\text{hot}}}{D - (1-\kappa)H} \right], \tag{2.72}$$

where the dimensionless number $\mathcal{M}$ is the rescaled Marangoni number with u_0 given by Eq. (2.48):

$$\mathcal{M} = \overline{\text{Ca}} \times \overline{\text{Ma}} = \frac{\mu u_0}{\epsilon^3 \gamma_0} \times \frac{\epsilon \gamma_T \Delta T}{\mu u_0} = \frac{\gamma_T \Delta T}{\epsilon^2 \gamma_0}. \tag{2.73}$$

Throughout the rest of this thesis, $\mathcal{M}$ is simply referred to as the Marangoni number, which is the ratio between the thermocapillary stress and stabilizing capillary stress, and is a key control parameter in TC patterning. Variation in $\mathcal{M}$ corresponds naturally to variation in temperature difference ΔT under fixed material's properties and length scales (h_0 and l_0). If van der Waals' interaction (see Section 2.3.3) is also neglected, then variation in $\mathcal{M}$ can also be achieved by varying the patterning wavelength $l_0 = \lambda_p$ while keeping ΔT and other parameters fixed.

2.3.1.3 Gradient Flow formulation for TC Patterning

It is possible to express Eq. (2.49) with $\nabla_\parallel^* \Gamma$ given by Eq. (2.72) as long as all lateral variation in Γ comes from $H(\mathbf{X}, \tau)$ only, i.e., D, Θ_{hot} and Θ_{cold} are all constants. The derivation given here follows [29, 146] closely.

We need to express the shear stress term as

$$M_\parallel(H) \nabla_\parallel^* \Gamma = M_\perp(H) \left[\frac{M_\parallel(H)}{M_\perp(H)} \nabla_\parallel \Gamma^* \right] = M_\perp(H) \nabla_\parallel \Pi_{\text{TC}}(H), \tag{2.74}$$

where $M_\perp(H) = H^3/3$, $M_\parallel(H) = H^2/2$ and $\Gamma = -\mathcal{M}\Theta_s(H)$ is given by Eq. (2.72) with $D = D_0$, $\Theta_{\text{hot}} = 1$ and $\Theta_{\text{cold}} = 0$. Using the substitution $\chi = (\kappa - 1)/D_0$, Π_{TC} for simplifying expressions, we obtain:

$$\begin{aligned}\frac{M_{\parallel}(H)}{M_{\perp}(H)}\nabla_{\parallel}^{*}\Gamma &= -\frac{3\mathcal{M}}{2H}\frac{\partial\Theta_s}{\partial H}\nabla_{\parallel}H \\ &= \frac{3\mathcal{M}}{2H}\frac{\kappa D_0}{\left[D_0+(\kappa-1)H\right]^2}\nabla_{\parallel}H \\ &= \frac{3\mathcal{M}\kappa}{2D_0}\frac{1}{H(1+\chi H)^2}\nabla_{\parallel}H \\ &= \frac{3\mathcal{M}\kappa}{2D_0}\left[\frac{1}{H}-\frac{\chi}{1+\chi H}-\frac{\chi}{(1+\chi H)^2}\right]\nabla_{\parallel}H \\ &= \frac{3\mathcal{M}\kappa}{2D_0}\nabla_{\parallel}\left[\log\left(\frac{H}{1+\chi H}\right)+\frac{1}{1+\chi H}\right]. \end{aligned} \tag{2.75}$$

Therefore, the governing thin film equation for TC patterning (with constant electrode separation D_0 and temperature difference) can indeed be expressed in the general form of gradient flow given by Eq. (2.49) provided that generalized pressure $\Pi = \Pi_{\mathrm{TC}}$ in Eq. (2.54) is given by

$$\Pi_{\mathrm{TC}} = \frac{3\mathcal{M}\kappa}{2D_0}\left[\log\left(\frac{H}{1+\chi H}\right)+\frac{1}{1+\chi H}\right], \tag{2.76}$$

and the energy density Φ_{TC} is

$$\Phi_{\mathrm{TC}} = -\frac{3\mathcal{M}\kappa}{2D_0}H\log\left(\frac{H}{1+\chi H}\right). \tag{2.77}$$

Note that the expression of Lyapunov energy functional given by Eq. (2.76) was recently used by Yang et al. [138] to deduce the stability of stationary states in TC patterning with patterned mask (i.e., $D = D(\mathbf{X})$). However, recasting the thin film equation into the form of Eq. (2.51) using Eq. (2.77) results in an additional term containing spatial variation in $D(\mathbf{X})$. We have yet to successfully formulate the gradient flow equation for TC patterning with spatially modulated $D(\mathbf{X})$, $\Theta_{\mathrm{hot}}(\mathbf{X})$ or $\Theta_{\mathrm{cold}}(\mathbf{X})$, and are not aware of any rigorous proof in literature whether such formulation is possible.

2.3.1.4 Other temperature models

The governing equations described in this section applies to thermal conduction where the temperature gradient is imposed by maintaining the mask and substrate at different temperatures. In an 'open' configuration where the liquid film is heated from below by the substrate without the top mask, a more appropriate boundary condition is Newton's law of cooling applied at the free surface which has been extensively discussed in literature [85].

2.3.2 Electrostatics

2.3.2.1 Dimensional Governing Equations

In the case of EHD patterning when an external electric field is applied, the 'leaky dielectric model' [99] is commonly used to describe the electrostatics of the system. Under the leaky dielectric model, all charges are depleted from the bulk region along the particle trajectories due to the small charge relaxation time and reside on the fluid-gas interface. In this thesis, we specialize to the case where the fluid and the passive gas are both considered as perfect dielectric with zero electrical conductivity. From here onwards, 'EHD pattering' will be synonymous with the 'perfect dielectric model' which has *no* shear stress as will be demonstrated in Section 2.3.2.3, though it should be stressed that the results presented in this thesis are only special case of the more general leaky dielectric model. Under the 'perfect dielectric model', there is no free charge in the system, and only bound charges reside on the free surface. Gauss' law and Faraday's law for the electric field $\mathbf{E}$ become

$$\nabla \times \mathbf{E} = 0, \qquad \nabla \cdot (\varepsilon \mathbf{E}) = 0, \tag{2.78}$$

where ε [11] is the electrical permittivity. The Maxwell stress tensor $\overset{\leftrightarrow}{\mathbf{M}}$ becomes

$$\overset{\leftrightarrow}{\mathbf{M}} = \varepsilon \left(\mathbf{E}\mathbf{E} - \frac{1}{2}|\mathbf{E}|^2 \overset{\leftrightarrow}{\mathbf{I}} \right). \tag{2.79}$$

To obtain the electric field $\mathbf{E} = -\nabla V$, we need to solve for the electric potential V which is governed by Laplace equation

$$\nabla^2 V_\alpha = 0, \qquad \text{where } \alpha = a, b, \tag{2.80}$$

with the boundary conditions

$$V_a(z = d) = V_\Delta(\mathbf{x}), \tag{2.81a}$$
$$V_b(z = 0) = 0, \tag{2.81b}$$
$$V_a(z = h) = V_b(z = h), \tag{2.81c}$$
$$\varepsilon_a \, \hat{\mathbf{n}} \cdot \nabla V_a(z = h) = \varepsilon_b \, \hat{\mathbf{n}} \cdot \nabla V_b(z = h), \tag{2.81d}$$

As it will become apparent later, it is the *square* of the potential *difference* between the two electrodes that matter, and so without loss of generality we simply ground the

[11] In this thesis, the symbol ε is used exclusively to denote electrical permittivity, while $\epsilon (= h_0/l_0)$ is used to denote the small aspect ratio in LWA. Notice the typographical difference between ε and ϵ.

bottom electrode and set $V = V_\Delta$ (where subscript Δ denotes the *difference*) as the electric potential at the top electrode. Similar to TC patterning, we let both $d(\mathbf{x})$ and $V_\Delta(\mathbf{x})$ be functions of $\mathbf{x}$ to take into account spatially modulated mask topography and voltage difference.

2.3.2.2 Proof of $\nabla\cdot \overleftrightarrow{\mathbf{M}} = 0$ in the bulk

We first show that $\nabla\cdot \overleftrightarrow{\mathbf{M}} = 0$ in the bulk of the medium in the absence of free charge. Using Einstein's notation where M_{ij} and E_j denote the individual component of the Maxwell stress tensor and electric field, we have

$$\begin{aligned}(\nabla\cdot \overleftrightarrow{\mathbf{M}})_j = \partial_i M_{ij} &= \partial_i\left[\varepsilon(E_iE_j - \frac{1}{2}E^2\delta_{ij})\right] \\ &= \cancel{\partial_i(\varepsilon E_i)}E_j + \varepsilon E_i(\partial_i E_j) - \frac{\varepsilon}{2}\partial_j(E_iE_i) \\ &= \varepsilon E_i(\partial_i E_j - \partial_j E_i) = 0,\end{aligned} \tag{2.82}$$

where in the second line $\partial_i(\varepsilon E_i) = \nabla\cdot(\varepsilon\mathbf{E}) = 0$ due to Gauss' law, and in the third line the terms inside the parenthesis is zero due to the cross product in Faraday's law. Therefore, the electrostatic effect does not manifest in the hydrodynamics of the bulk through the Navier-Stokes equation. However, it does couple with the hydrodynamics through the stress boundary condition at $z = h$.

2.3.2.3 Derivation of normal and shear electrostatic stress

To evaluate the electrostatic stress $\varpi_{\mathrm{M}}^{(n)} = \hat{\mathbf{n}}\cdot(\overleftrightarrow{\mathbf{M}}_a - \overleftrightarrow{\mathbf{M}}_b)\cdot\hat{\mathbf{n}}$ in the normal stress balance given by Eq. (2.11), we first evaluate $\hat{\mathbf{n}}\cdot\overleftrightarrow{\mathbf{M}}_\alpha\cdot\hat{\mathbf{n}}$ as follow:

$$\begin{aligned}\hat{\mathbf{n}}\cdot\overleftrightarrow{\mathbf{M}}_\alpha\cdot\hat{\mathbf{n}} &= \varepsilon_\alpha\,\hat{\mathbf{n}}\cdot\left(\mathbf{E}_\alpha\mathbf{E}_\alpha - \frac{1}{2}\mathbf{E}_\alpha\cdot\mathbf{E}_\alpha\right)\cdot\hat{\mathbf{n}} \\ &= \varepsilon_\alpha\left\{(\hat{\mathbf{n}}\cdot\mathbf{E}_\alpha)(\mathbf{E}_\alpha\cdot\hat{\mathbf{n}}) - \frac{1}{2}\left[(\mathbf{E}_\alpha\cdot\hat{\mathbf{n}})^2 + \sum_{i=1,2}(\mathbf{E}_\alpha\cdot\hat{\mathbf{t}}_i)^2\right]\right\} \\ &= \frac{\varepsilon_\alpha}{2}\left[(\mathbf{E}_\alpha\cdot\hat{\mathbf{n}})^2 - \sum_{i=1,2}(\mathbf{E}_\alpha\cdot\hat{\mathbf{t}}_i)^2\right].\end{aligned} \tag{2.83}$$

Across the free surface at $z = h$, the tangential component of the electric field $\mathbf{E}_\alpha\cdot\hat{\mathbf{t}}_i$ is continuous. Using $E_{n,\alpha}$ and $E_{t,\alpha}$ to denote the normal and tangential component of electric field in medium α, $\varpi_{\mathrm{M}}^{(n)}$ becomes

$$\begin{aligned}\varpi_{\mathrm{M}}^{(n)} &= \hat{\mathbf{n}} \cdot (\overleftrightarrow{\mathbf{M}}_a - \overleftrightarrow{\mathbf{M}}_b) \cdot \hat{\mathbf{n}} \\ &= \frac{\varepsilon_a}{2}\left(E_{n,a}^2 - E_{t,a}^2\right) - \frac{\varepsilon_b}{2}\left(E_{n,b}^2 - E_{t,b}^2\right) \\ &= \frac{(\varepsilon_b - \varepsilon_a)}{2}\left(\frac{\varepsilon_b}{\varepsilon_a}E_{t,b}^2 + E_{n,b}^2\right). \end{aligned} \tag{2.84}$$

For the shear stress condition in Eq. (2.12), we first evaluate $\hat{\mathbf{t}} \cdot \overleftrightarrow{\mathbf{M}}_\alpha \cdot \hat{\mathbf{n}}$ as follow:

$$\hat{\mathbf{t}} \cdot \overleftrightarrow{\mathbf{M}}_\alpha \cdot \hat{\mathbf{n}} = \varepsilon_\alpha\, \hat{\mathbf{t}} \cdot \left[\mathbf{E}_\alpha \mathbf{E}_\alpha - \frac{1}{2}(\mathbf{E}_\alpha \cdot \mathbf{E}_\alpha)\, \overleftrightarrow{\mathbf{I}}\right] \cdot \hat{\mathbf{n}} \tag{2.85}$$

$$= \varepsilon_\alpha (\hat{\mathbf{t}} \cdot \mathbf{E}_\alpha)(\mathbf{E}_\alpha \cdot \hat{\mathbf{n}}) - \frac{\varepsilon_\alpha}{2}|\mathbf{E}_\alpha|^2 \cancel{(\hat{\mathbf{t}} \cdot \hat{\mathbf{n}})} = (\hat{\mathbf{t}} \cdot \mathbf{E}_\alpha)(\varepsilon_\alpha \mathbf{E}_\alpha \cdot \hat{\mathbf{n}}). \tag{2.86}$$

Since both $E_{t,\alpha} = \mathbf{E}_\alpha \cdot \hat{\mathbf{t}}$ and $E_{n,\alpha} = \mathbf{E}_\alpha \cdot \hat{\mathbf{n}}$ are continuous across the free surface, electrostatic effects exert no shear stress at the free surface at $z = h$:

$$\varpi_{\mathrm{M}}^{(t_i)} = \hat{\mathbf{t}}_i \cdot (\overleftrightarrow{\mathbf{M}}_a - \overleftrightarrow{\mathbf{M}}_b) \cdot \hat{\mathbf{n}} = E_t(\varepsilon_a E_{n,a} - \varepsilon_b E_{n,b}) = 0. \tag{2.87}$$

In the more general leaky dielectric model where free surface charge resides at $z = h$, the boundary condition for E_n becomes $\varepsilon_a E_{n,a} - \varepsilon_b E_{n,b} = \sigma$ where σ is the free surface charge density. Therefore, $\varpi_{\mathrm{M}}^{(n)}$ in Eq. (2.84) will contain an extra term, and $\boldsymbol{\varpi}_{\mathrm{M}}^{(t)}$ in Eq. (2.87) becomes $\boldsymbol{\varpi}_{\mathrm{M}}^{(t)} = \sigma E_t$.

2.3.2.4 Dimensionless Governing Equations

In order to obtain an analytical expression for the electric potential V, and hence the electrostatic stress $\varpi_{\mathrm{M}}^{(n)}$ given by Eq. (2.84), we again assume the electric potential varies much more slowly along the lateral direction than the vertical direction, and apply LWA. Define the dimensionless electric potential Ψ as

$$\Psi = \frac{V}{V_0}, \tag{2.88}$$

where $V_0 = \mathrm{mean}(V_\Delta)$ is the mean potential difference between the top and bottom electrodes. To leading order in ϵ, the dimensionless Laplace equation is

$$\frac{\partial^2 \Psi_\alpha}{\partial Z^2} = 0, \qquad \alpha = a, b, \tag{2.89}$$

with the boundary conditions

$$\Psi_a(Z=D)=\Psi_\Delta, \tag{2.90a}$$
$$\Psi_a(Z=0)=0, \tag{2.90b}$$
$$\Psi_a(Z=H)=\Psi_b(Z=H), \tag{2.90c}$$
$$\frac{\partial\Psi_a(Z=H)}{\partial Z}=\varepsilon_r\frac{\partial\Psi_b(Z=H)}{\partial Z}, \tag{2.90d}$$

where $\varepsilon_r=\varepsilon_b/\varepsilon_a$ is the ratio of electrical permittivity. When the passive gas layer is air where $\varepsilon_a\approx\varepsilon_0$, ε_r is simply the relative permittivity of the liquid layer.

Using the general solution to 1D Laplace equation given in Appendix A.4, the electric potential in each medium is

$$\Psi_a=\frac{\Psi_\Delta}{H+\varepsilon_r(D-H)}\left[H+\varepsilon_r(Z-H)\right],\qquad \Psi_b=\frac{\Psi_\Delta}{H+\varepsilon_r(D-H)}Z. \tag{2.91}$$

The normal and tangential components of the electric field are

$$E_n=\mathbf{E}\cdot\hat{\mathbf{n}} \qquad =-\frac{V_0}{h_0}\left[\frac{\partial\Psi}{\partial Z}+\mathcal{O}(\epsilon^2)\right], \tag{2.92a}$$
$$E_t=\mathbf{E}\cdot\hat{\mathbf{t}}_i=-\frac{V_0}{h_0}\left[\epsilon\left(\nabla_\parallel^*\Psi+\nabla_\parallel^*H\frac{\partial\Psi}{\partial Z}\right)\cdot\hat{\mathbf{e}}_i+\mathcal{O}(\epsilon^3)\right],\quad i=x,y. \tag{2.92b}$$

Since it is E_n^2 and E_t^2 which enter the normal stress in Eq. (2.84), the tangential term E_t^2 is $\mathcal{O}(\epsilon^2)$ compared to the normal term E_n^2, so only the normal component of the electric field is retained to leading order in Eq. (2.84), and the dimensionless electrostatic stress $\Pi_{\mathrm{M}}^{(n)}$ becomes

$$\Pi_{\mathrm{M}}^{(n)}=\Pi_{\mathrm{EM}}=\frac{\epsilon h_0\varpi_{\mathrm{M}}^{(n)}}{\mu u_0}=\frac{\epsilon\varepsilon_0V_0^2}{2\mu u_0h_0}\left\{\frac{\varepsilon_r(\varepsilon_r-1)\Psi_\Delta^2}{[H+\varepsilon_r(D-H)]^2}+\mathcal{O}(\epsilon^2)\right\}, \tag{2.93}$$

where we assume $\varepsilon_a\approx\varepsilon_0$ which is valid for most gases. Introduce the electric Weber number We and the rescaled electric Weber number $\overline{\mathrm{We}}$ under LWA as follow

$$\mathrm{We}=\frac{\varepsilon_0V_0^2}{\mu u_0h_0},\qquad \overline{\mathrm{We}}=\epsilon\mathrm{We}=\frac{\epsilon\varepsilon_0V_0^2}{\mu u_0h_0}, \tag{2.94}$$

where we assume $\overline{\mathrm{We}}=\mathcal{O}(1)$ such that electrostatic effects are retained in the normal stress condition. After the substitution of u_0 given in Eq. (2.48), $\Pi_{\mathrm{M}}^{(n)}$ becomes

$$\Pi_{\mathrm{M}}^{(n)} = \Pi_{\mathrm{EM}} = \mathcal{W}\frac{\varepsilon_r(\varepsilon_r - 1)\Psi_\Delta^2}{[H + \varepsilon_r(D - H)]^2}, \tag{2.95}$$

where the dimensionless number is

$$\mathcal{W} = \overline{\mathsf{Ca}} \times \overline{\mathsf{We}} = \frac{\varepsilon_0 V_0^2}{\epsilon^2 \gamma_0 h_0}. \tag{2.96}$$

Throughout the rest of this thesis, $\mathcal{W}$ is simply referred to as the Weber number, which is the ratio between the destabilizing electrostatic stress and stabilizing capillary stress, and is a key control parameter in EHD patterning. It is analogous to the Marangoni number $\mathcal{M}$ in TC patterning in that it represents the destabilizing strength to deform the free surface of the liquid film.

Variation in $\mathcal{W}$ corresponds naturally to variation in the applied voltage difference V_0 under fixed material's properties and length scales (h_0 and l_0). If van der Waals' interaction (see Section 2.3.3) is also neglected, then variation in $\mathcal{W}$ can also be achieved by varying the patterning wavelength $l_0 = \lambda_p$ while keeping V_0 and other parameters fixed.

2.3.2.5 Electrostatic energy

The electrostatic energy Φ_{EM} in the gradient flow formulation given by Eq. (2.51) can be obtained via straightforward integration of Π_{EM}:

$$\Phi_{\mathrm{EM}} = -\int \Pi_{\mathrm{EM}}(H)\mathrm{d}H = -\frac{\mathcal{W}}{2}\frac{\varepsilon_r \Psi_\Delta^2}{H + \varepsilon_r(D - H)}. \tag{2.97}$$

Eq. (2.97) can also be obtained by considering the electrostatic energy stored in a system which consists of two capacitors connected in series. As a crude approximation, we assume the free surface at $z = h$ as parallel to the top and bottom electrodes, and treat the liquid film and the air layer as two separate capacitors. The capacitance per unit area of two parallel plates separated by a medium with electric permittivity ε with thickness l is simply ε/l. The capacitance of the air layer and the liquid layer are $C_{\mathrm{air}} = \varepsilon_a/(d-h)$ and $C_{\mathrm{liq}} = \varepsilon_b\varepsilon_r/h$, respectively. The total capacitance of the system C_{total} is

$$\frac{1}{C_{\mathrm{total}}} = \frac{1}{C_{\mathrm{air}}} + \frac{1}{C_{\mathrm{liq}}} \implies C_{\mathrm{total}} = \frac{\varepsilon_a\varepsilon_b}{\varepsilon_a h + \varepsilon_b(d-h)}. \tag{2.98}$$

Using the expression of the electrostatic energy $\phi_{\mathrm{EM}} = CV_0^2/2$ and non-dimensionalizing the resulting expression gives Eq. (2.97).

2.3.2.6 Other models for electrostatics

The results presented in this section LWA is satisfied in *both* the liquid layer and the air gap. When the top electrode is very far away and the air gap distance is comparable to the characteristic lateral scale, i.e., $(d_0 - h_0)/l_0 = \mathcal{O}(1)$, LWA can no longer be applied to the air layer. This case was studied in [121] in detail, and the electrostatic stress involves the Hilbert transform of $\nabla_{\parallel}^{*} H$. Under LSA, this gives rise to a destabilizing term $|K|^2 K$ in the dispersion relation (see Section 3.1), instead of the K^2 term for the present case of thin air gap.

2.3.3 Intermolecular interactions

Intermolecular interactions typically become important when the film thickness is smaller than about 100 nm. For a polymer thin film on top of a solid substrate, the van der Waals' interaction is often the dominant intermolecular interaction. Although it is a body force in nature, it appears only when materials are separated by at least two interfaces, and is therefore often treated as an interfacial effect [63]. Van der Waals' interaction can be incorporated into the pressure balance condition given by Eq. (2.11) via the (dimensional) disjoining pressure φ_{vdw}

$$\varphi_{\mathrm{vdw}}(h) = \frac{A}{6\pi h^3}, \tag{2.99}$$

where A is the Hamaker constant with a typical magnitude of about $10^{-20}\mathrm{J}$. Positive A denotes repelling surfaces or thin film wetting, while negative A denotes attracting surfaces or thin film dewetting [12]. Non-dimensionalizing Eq. (2.99) using the characteristic pressure scale p_0, and including an additional term for modeling the van der Waals' interaction between the liquid-air interface and the air-solid interface at the top mask, gives the following dimensionless disjoining pressure

$$\Pi_{\mathrm{vdw}}(H) = \mathcal{A}\left[\frac{1}{H^3} - \frac{1}{(D-H)^3}\right], \tag{2.100}$$

where $\mathcal{A}$ is the dimensionless Hamaker constant representing the ratio of van der Waals' force to capillary force given by

$$\mathcal{A} = \frac{A}{6\pi h_0^3 p_0} = \frac{A}{6\pi h_0^3}\frac{\epsilon h_0}{\mu u_0} = \frac{A}{6\pi\epsilon^2\gamma_0 h_0^2} = \frac{A l_0^2}{6\pi\gamma_0 h_0^4}. \tag{2.101}$$

In general, the Hamaker constants for the mask and substrate need not be the same, but they are assumed to be equal due to a lack of accurate measurement in literature,

[12] Note that the sign convention for the disjoining pressure varies between different studies. Here we adopt the sign convention used in Ref [9, 22].

and their specific values do not affect the general dynamics of the liquid film [132]. A positive $\mathcal{A}$ is chosen for both interactions at the mask and substrate, because under many experimental conditions the mask is dewetting to the polymer while the substrate is wetting to the hydrophobic polymer [132]. The inclusion of repulsive intermolecular interaction also prevents liquid film rupture at the substrate $H \to 0$ and contact with the mask ($H \to D$). This is known as the 'precursor film' model is also one of the common methods in literature to relieve the dynamical singularity near moving contact line [9].

While other forms of intermolecular interactions are possible and may be more appropriate for certain materials, they are outside the scope of this thesis. Interested readers can consult the review [9] and references therein for a more detailed discussion.

Similar to Φ_{EM}, the energy functional associated to van der Waals' interaction Φ_{vdw} can be obtained via integration of Eq. (2.100):

$$\Phi_{\mathrm{vdw}} = -\int \Pi_{\mathrm{vdw}}(H)\mathrm{d}H = \frac{\mathcal{A}}{2}\left[\frac{1}{H^2} + \frac{1}{(D-H)^2}\right]. \tag{2.102}$$

2.3.4 Gravity

Suppose gravity points vertically downward, i.e., $\varpi_{\mathrm{ext}} = \varpi_{\mathrm{gravity}} = \rho g z$, such that $-\nabla\varpi_{\mathrm{gravity}} = -\rho g \hat{\mathbf{e}}_z$.

The dimensionless stress is

$$\Pi_{\mathrm{gravity}}(Z) = \frac{-\varpi_{\mathrm{gravity}}(z)}{p_0} = -\frac{\rho g z}{\mu u_0/\epsilon h_0} = -\frac{\epsilon\rho g h_0^2 Z}{\mu u_0} \xrightarrow{\text{Eq.(2.48)}} \frac{\rho g h_0^2}{\epsilon^2\gamma_0} Z = -\mathcal{B}Z, \tag{2.103}$$

where the rescaled Bond number is given by

$$\mathcal{B} = \frac{\rho g h_0^2}{\epsilon^2\gamma_0} = \frac{\rho g l_0^2}{\gamma_0}, \tag{2.104}$$

and the minus sign comes from the definition of $\bar{\Pi}$ in Eq. (2.47). Gravity is always stabilizing when it points downward, and destabilizing (the pressure becomes $\Pi_{\mathrm{gravity}}(Z) = \mathcal{B}H$) when it points upward which is the case of free-hanging film.

As shown in Appendix 2.4, $\mathcal{B} \sim \mathcal{O}(10^{-7} - 10^{-4})$ for typical experimental parameters with polystyrene. Since $\Pi_{\mathrm{gravity}}(Z = H) = \mathcal{B}H$, and $H \sim \mathcal{O}(1)$, the gravity term is always much smaller than the destabilizing terms from electrostatics or thermocapillarity as well as the van der Waals' term when $H \to 0$. Therefore, gravity is neglected in the rest of this thesis, and its inclusion is not expected to have any qualitative effects on the stability and dynamics of the liquid film under the regimes of interest.

Chapter 3

LINEAR STABILITY ANALYSIS

In this chapter, we review the basics of linear stability analysis (LSA) which is used to study the stability of stationary states [1]. LSA is covered in many standard texts on dynamical systems, see, for example, Cross and Greenside [24].

The general form of the governing thin film equation derived in chapter 2 is restated below for easier reference:

$$\begin{aligned} \frac{\partial H}{\partial \tau} &= \nabla_{\parallel} \cdot \left[M_{\perp}(H) \nabla_{\parallel} \bar{P} - M_{\parallel}(H) \nabla_{\parallel} \Gamma \right], \\ \bar{P} &= -\nabla_{\parallel}^2 H - \Pi, \\ M_{\perp}(H) = \frac{H^3}{3}, &\qquad M_{\parallel}(H) = \frac{H^2}{2}. \end{aligned} \tag{3.1}$$

Note that the asterisk $(*)$ in the dimensionless gradient operator $\nabla_{\parallel} = (\partial_X, \partial_Y)$ has been dropped for brevity. The external stress in the normal direction Π and the dimensionless surface tension gradient Γ are given in Eq. (2.50), but their exact mathematical expressions do not matter in this chapter except in section 3.1.3 where the fastest-growing wavelengths in dimensional unit for specific systems are derived.

We first discuss the use of LSA to study 'un-modulated' system in section 3.1 where the mask and other system variables (e.g. applied voltage and temperature) are all spatially uniform, and a flat film satisfies the governing equation for stationary state. In section 3.2, we extend the LSA to study 'modulated' system where the mask or other system variables are spatially modulated such that a non-uniform film film is needed to satisfy the stationary state equations. Results presented in chapter 5 and 6 are heavily based on the LSA presented in this chapter.

3.1 Linear Stability Analysis (LSA) of Uniform Stationary States

3.1.1 Basic Theory

In EHD and TC patterning, we refer to the system as 'unmodulated' when the system (excluding the liquid film) is spatially homogeneous without spatial variation – the bottom and top plates have constant separation D_0, and their voltage or temperature are

[1] In this thesis, 'stationary state' simply refers to time-independent liquid-air interface, i.e., $\partial H/\partial \tau = 0$, with no implications on what the underlying physics mechanisms are. Other dependent variables of the actual system such as velocity (which under LWA depend explicitly on H) is not necessarily zero depending on the physical effects involved.

held constant spatially and temporally. Then, both the external stress Π and surface tension variation Γ are only functions of the free surface shape $H(\mathbf{X},\tau)$, i.e., $\Pi = \Pi(H)$ and $\Gamma = \Gamma(H)$, and any spatial variations in Π and Γ are solely due to spatial variation in $H(\mathbf{X},\tau)$. The stationary state $H_{\rm ss}$ (subscript 'ss' stands for **s**tationary state) of the liquid film (i.e., $\partial H_{\rm ss}/\partial\tau = 0$) in the unmodulated case is simply a flat film with constant thickness:

$$H_{\rm ss}(\mathbf{X}) = \text{const.} = 1, \tag{3.2}$$

where the choice of unity reflects the use of mean film thickness h_0 as the characteristic vertical scale.

To investigate whether such a stationary state is stable, i.e., whether infinitesimal perturbation to the stationary state grows or decays, we use the substitution $H(\mathbf{X},\tau) = 1 + \delta H_1(\mathbf{X},\tau)$ where $\delta \ll 1$ to solve Eq. (3.1). Expanding the resulting expression in δ, we obtain the following equation to leading order in δ:

$$\mathcal{O}(\delta): \quad \frac{\partial H_1}{\partial\tau} = -M_\perp(H_{\rm ss})\left[\nabla_\parallel^4 H_1 + \Pi'(H_{\rm ss})\nabla_\parallel^2 H_1\right] - M_\parallel(H_{\rm ss})\Gamma'(H_{\rm ss})\nabla_\parallel^2 H_1, \tag{3.3}$$

where $M_\perp(H_{\rm ss})$, $M_\parallel(H_{\rm ss})$, $\Pi'(H_{\rm ss}) = \mathrm{d}\Pi(H_{\rm ss})/\mathrm{d}H$ and $\Gamma'(H_{\rm ss}) = \mathrm{d}\Gamma(H_{\rm ss})/\mathrm{d}H$ are all evaluated at the base state of $H = H_{\rm ss} = 1$ and are constants in the unmodulated case. Derivatives of Π and Γ with respect to H are listed in Appendix B. Eq. (3.3) can be re-written in the following form for reasons which will become apparent later:

$$\frac{\partial H_1}{\partial\tau} = -M_\perp(H_{\rm ss})\left[\nabla_\parallel^4 H_1 + K_c^2\nabla_\parallel^2 H_1\right], \tag{3.4}$$

where K_c is given by

$$K_c^2 = \Pi'(H_{\rm ss}) + \frac{M_\parallel(H_{\rm ss})}{M_\perp(H_{\rm ss})}\Gamma'(H_{\rm ss}). \tag{3.5}$$

Eq. (3.4) can be solved using separation of variables with the substitution $H_1(\mathbf{X},\tau) = G(\tau)F(\mathbf{X})$, which results in the two ordinary differential equations (ODEs)

$$\frac{\mathrm{d}G}{\mathrm{d}\tau} = \beta, \qquad M_\perp(H_{\rm ss})\left[\nabla_\parallel^4 F + K_c^2\nabla_\parallel^2 F\right] + \beta F = 0, \tag{3.6}$$

where β is a constant to be determined. Solving the first equation gives $G(\tau) \propto e^{\beta\tau}$. The second equation can be solved for F using the trial solution $F(\mathbf{X}) = e^{i\mathbf{K}\cdot\mathbf{X}}$ as long as the following equation known as the 'dispersion relation' is satisfied:

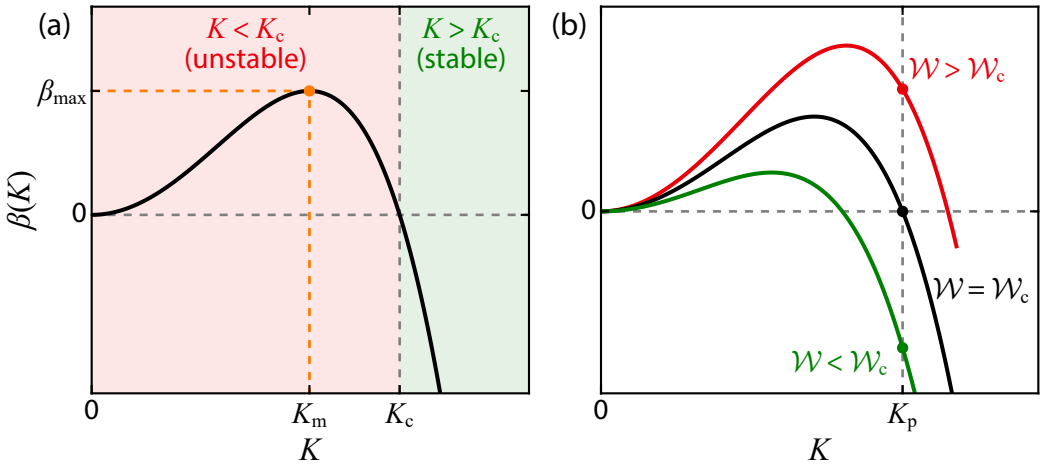

Figure 3.1: Dispersion relation of type II instability described by Eq. (3.7). (a) Dispersion $\beta(K)$ for fixed $\mathcal{W}$. The critical wave number K_c, fastest-growing wave number K_m and the maximum growth rate β_m are indicated. (b) Dispersion $\beta(K)$ for (i) $\mathcal{W} > \mathcal{W}_c$, (ii) $\mathcal{W} = \mathcal{W}_c$ and $\mathcal{W} < \mathcal{W}_c$. The critical electric Weber number $\mathcal{W}_c$ is defined according to Eq. (3.15a) for a given patterning wave number K_p.

$$\beta = M_{\perp}(H_{ss})K^2(K_c^2 - K^2), \tag{3.7}$$

where $\mathbf{K} = (K_x, K_y)$ is the wave vector with magnitude $K = |\mathbf{K}|$. Note that the general solution of $F(\mathbf{X})$ can be written as a linear combination of $e^{\pm i\mathbf{K}\cdot\mathbf{X}}$ and $e^{\pm\mathbf{K}\cdot\mathbf{X}}$ (with four unknown coefficients satisfying the four boundary conditions resulted from the fourth-order derivative). Since we only deal with periodic boundary conditions in the spatial domain for $\mathbf{X}$ in this thesis, $e^{\pm\mathbf{K}\cdot\mathbf{X}}$ is discarded as it does not satisfy the imposed boundary conditions. Therefore, the general solution for $H_1(\mathbf{X}, \tau)$ is $H_1(\mathbf{X}, \tau) = c_1 e^{i\mathbf{K}\cdot\mathbf{X}+\beta(\mathbf{K})\tau} + c_2 e^{-i\mathbf{K}\cdot\mathbf{X}+\beta(\mathbf{K})\tau}$. As customary in literature, we can simply write down the expansion for H as $H(\mathbf{X}, \tau) = 1 + \delta e^{i\mathbf{K}\cdot\mathbf{X}} + \text{c.c.}$ where c.c. denotes complex conjugate since $H(\mathbf{X}, \tau)$ is a real quantity.

We note that the operator in Eq. (3.6) is self-adjoint when periodic boundary condition or Neumann boundary condition is imposed, and so the eigenvalue β given by Eq. (3.7) is real.

The above analysis tells us that around the stationary state of a flat film, infinitesimal perturbation with wave number K have growth rate $\beta(K)$ given by Eq. (3.7), where K_c is the 'critical' or 'cutoff' wave number with $\beta(K_c) = 0$. When $K > K_c$, $\beta(K) < 0$ and so the perturbation decays and vice versa. Dispersion relation given by Eq. (3.7) is known as 'type-II' instability [2] and is shown in Fig. 3.1(a). The quartic term in

[2] This classification of instability into type I, II and III was proposed by Cross and Hohenberg [23].

Eq. (3.7) reflects the contribution of surface tension, which is always negative and hence stabilizing. The quadratic term in Eq. (3.7) is positive (for positive K_c^2 which is satisfied under typical conditions examined in this thesis) and has a destabilizing effect due to the external fields (e.g., electric or thermal fields). At small K, the destabilizing (K^2) term dominates, while at large K the stabilizing capillary (K^4) term dominates. The maximum growth rate $\beta_{\max}$ can be computed by solving $\mathrm{d}\beta(K_m)/\mathrm{d}K = 0$, where K_m is the 'most unstable' or 'fastest-growing' wave number given by

$$K_m = \frac{K_c}{\sqrt{2}} = \frac{1}{\sqrt{2}}\sqrt{\Pi'(H_{\mathrm{ss}}) + \frac{M_{\parallel}(H_{\mathrm{ss}})}{M_{\perp}(H_{\mathrm{ss}})}\Gamma'(H_{\mathrm{ss}})}. \tag{3.8}$$

The smallest possible wave number present in the system is $K_{\min} = 2\pi/L$ where L is the lateral extent of the liquid film, which in dimensional unit is typically of the order $\mathcal{O}(10 - 100\mu\mathrm{m})$ for most experimental studies reported in literature. On the other hand, the dimensional critical wavelength $\lambda_c = 2\pi/k_c$ is typically of the order of $\mathcal{O}(1 - 10\mu\mathrm{m})$. Since $K_{\min} < K_c$, there is always perturbation present in the system which can destabilize the liquid film. Therefore, an initially flat liquid film is said to be always linearly unstable, and develops corrugations with initial characteristic spacing $\Lambda_m = 2\pi/K_m$ (or in dimensional unit $\lambda_m = 2\pi/k_m$) since the mode with $K = K_m$ has the largest growth rate.

3.1.2 Critical wave number K_c for EHD/TC patterning

The dimensionless critical wave number K_c for EHD and TC patterning can be obtained by substituting the appropriate expressions for the normal stress $\Pi(H)$ and surface tension variation $\Gamma(H)$ into Eq. (3.5), evaluated at the base state of the unmodulated system where $H(\mathbf{X}) = 1$, $D(\mathbf{X}) = D_0$, $\Psi_{\Delta}(\mathbf{X}) = 1$, $\Theta_{\mathrm{hot}}(\mathbf{X}) = 1$ and $\Theta_{\mathrm{cold}}(\mathbf{X}) = 0$. The van der Waals' term is negligible compared to either the electrostatic stress or thermocapillary stress when the liquid film free surface is far from the top and bottom plates (because we are interested in the base state of a *flat* film). For EHD patterning where there is no shear stress, K_c is given by

$$\text{EHD:} \quad K_c = \sqrt{\frac{\partial \Pi_{\mathrm{EM}}(H=1)}{\partial H}} = \sqrt{\frac{\mathcal{W}\varepsilon_r(\varepsilon_r - 1)^2}{\left[1 + \varepsilon_r(D_0 - 1)\right]^3}}, \tag{3.9}$$

while for TC patterning which has an additional contribution from shear stress, K_c is given by

Recently Frohoff-Hülsmann and Thiele [40] generalized the classification into eight types based on (i) large-scale vs small-scale instability, (ii) stationary vs oscillatory instability, and (iii) instability with and without conservation laws.

$$\text{TC:} \quad K_c = \sqrt{\frac{M_{\parallel}(H=1)}{M_{\perp}(H=1)} \frac{\partial \Gamma(H=1)_{\text{TC}}}{\partial H}} = \sqrt{\frac{3\mathcal{M}\kappa D_0}{2\left(D_0+\kappa-1\right)^2}}. \tag{3.10}$$

3.1.3 Fastest-growing wavelength in EHD/TC patterning

For the specific case of EHD and TC patterning, the dimensional fastest growing wavelength λ_m can be obtained from Eq. (3.8) by setting λ_m as the characteristic lateral length scale, i.e., $l_0 = \lambda_m$. Under this choice of scaling, $K_m = 2\pi$ and $\epsilon = h_0/l_0 = h_0/\lambda_m$. Using the expressions for $\Pi'(H)$ and $\Gamma'(H)$ given in Appendix B, and the definitions of $\mathcal{W} = \varepsilon_0 V_0^2/\epsilon^2\gamma_0 h_0$ and $\mathcal{M} = \gamma_T \Delta T/\epsilon^2\gamma_0$, we can solve for λ_m:

$$\lambda_m = 2\pi h_0 \left[\frac{2\gamma_0}{\dfrac{\varepsilon_0 V_0^2}{h_0}\dfrac{(\varepsilon_r-1)^2\varepsilon_r}{[1+\varepsilon_r(D_0-1)]^3} + \dfrac{3\gamma_T\Delta T}{2}\dfrac{\kappa_r D_0}{(D_0+\kappa-1)^2}} \right]^{1/2}, \tag{3.11}$$

where the dimensionless version of Eq. (3.11) was first derived in [21]. For the special case when only one of EHD or TC effects are present, Eq. (3.11) is simplified to

$$\text{EHD:} \quad \lambda_m = 2\pi h_0 \sqrt{\frac{2\gamma_0 h_0 [1+\varepsilon_r(d_0/h_0-1)]^3}{\varepsilon_0 V_0^2 \varepsilon_r(\varepsilon_r-1)^2}}, \tag{3.12}$$

for EHD patterning [104], and

$$\text{TC:} \quad \lambda_m = 2\pi h_0 \sqrt{\frac{4\gamma_0 h_0}{3\gamma_T \Delta T \kappa_r d_0}} \left(\frac{d_0}{h_0}+\kappa-1\right). \tag{3.13}$$

for TC patterning [29]. The effects of varying different material constants or experimental parameters can be revealed upon inspection of Eq. (3.12) and (3.13). Increasing the surface tension γ_0 increases λ_m because surface tension is stabilizing. Increasing the destabilizing forces, such as the applied voltage difference V_0 for EHD patterning, or the temperature difference ΔT in TC patterning, decreases λ_m as expected. Notice that $\lambda_m \propto 1/\sqrt{\Delta T}$ and so increasing temperature generally cannot reduce λ_m by a sizeable amount. Increasing V_0 appears to have a more noticeable effect because the electrostatic stress scales as V_0^2. However, it should be aware that dielectric breakdown may occur for sufficiently large electric field strength [62], and the model described by Eq. (3.1) is no longer valid when that happens.

The effects of varying different parameters on λ_m were studied in detail in [104] for EHD patterning and [29] for TC patterning and is not discussed any further here.

3.1.4 Critical bifurcation parameters $\mathcal{W}_c$ and $\mathcal{M}_c$ for fixed patterning wave number $K = K_p$

The critical or cut-off wave number K_c given by Eq. (3.5) determines whether perturbation with a given wave number K grows or decays, and K_c is defined for a given set of parameters appearing in the governing equation including $\mathcal{W}$ and $\mathcal{M}$. In this thesis, we focus on the effects of external spatial modulation in a periodic system. This results in two effects: (1) there is an imposed periodicity on the system with patterning wave number K_p, and (2) the allowable wave numbers in the system are discretized to integer multiples of the smallest wave numbers dictated by the system size. One key objective is to determine how the spatiotemporal dynamics of the liquid film depends on parameters such as $\mathcal{W}$ and $\mathcal{M}$. Therefore, it is more appropriate to define the critical electric Weber number $\mathcal{W}_c$ or Marangoni number $\mathcal{M}_c$ for a given patterning wave number K_p as follow:

$$\text{EHD:} \quad K_p^2 = \frac{\partial \Pi(H_{\text{ss}}; \mathcal{W} = \mathcal{W}_c)}{\partial H}, \tag{3.14a}$$

$$\text{TC:} \quad K_p^2 = \frac{M_{\parallel}(H_{\text{ss}})}{M_{\perp}(H_{\text{ss}})} \frac{\partial \Gamma(H_{\text{ss}}; \mathcal{M} = \mathcal{M}_c)}{\partial H}. \tag{3.14b}$$

Note that van der Waals' forces are neglected, and only and electrostatic stress and the thermocapillary stress terms are kept for EHD and TC patterning, respectively. We can then solve for

$$\text{EHD:} \quad \mathcal{W}_c = K_p^2 \frac{[1 + \varepsilon_r (D_0 - 1)]^3}{\varepsilon_r (\varepsilon_r - 1)^2}, \tag{3.15a}$$

$$\text{TC:} \quad \mathcal{M}_c = \frac{2K_p^2}{3} \frac{(D_0 + \kappa - 1)^2}{\kappa D_0}. \tag{3.15b}$$

Fig. 3.1(b) shows the dispersion relations $\beta(K)$ for three different cases of (i) $\mathcal{W}_c > \mathcal{W}$, (ii) $\mathcal{W}_c = \mathcal{W}$ and (iii) $\mathcal{W}_c < \mathcal{W}$. The case for TC patterning is qualitatively similar with $\mathcal{W}$ and $\mathcal{W}_c$ replaced by $\mathcal{M}$ and $\mathcal{M}_c$ respectively. When $\mathcal{W} > \mathcal{W}_c$, perturbations with wave number $K = K_p$ grow because $\beta(K_p) > 0$ and vice versa for $\mathcal{W} < \mathcal{W}_c$.

Note that Eq. (3.15) only depends on materials' parameters (ε_r or κ) and the mean electrode separation D_0 for fixed K_p, and larger D_0 leads to larger $\mathcal{W}_c$ and $\mathcal{M}_c$. Since both the electric field strength and temperature (both governed by 1D Laplace equation) along the liquid film free surface become weaker as D_0 is increased, in order to maintain the same level of electrostatic or thermocapillary stress, the applied voltage (related to $\mathcal{W}$) or the imposed temperature difference (related to $\mathcal{M}$) must be increased accordingly for larger D_0.

3.2 Linear Stability Analysis of Periodic Non-Uniform Stationary States

When the system is 'modulated', i.e., when the top or bottom plate is topographically (e.g., see Fig. 1.1) or chemically patterned, or the applied voltage or temperature difference across the top and bottom plates are spatially or/and temporally modulated, then the stationary state $H_{\rm ss}(\mathbf{X})$ becomes spatially non-uniform which satisfies the following equation

$$\nabla_{\parallel} \cdot \left\{ M_{\perp}(H_{\rm ss}) \nabla_{\parallel} \left[\nabla_{\parallel}^2 H_{\rm ss} + \Pi(H_{\rm ss}) \right] \right\} = 0, \tag{3.16}$$

subject to the additional constraint $\mathrm{mean}(H_{\rm ss}) = 1$ due to volume conservation. LSA can be done by following the same approach as in the last section except the coefficients in the linearized equation given by Eq. (3.3) also become spatially varying. Using the substitution $H(\mathbf{X}, \tau) = H_{\rm ss}(\mathbf{X}) + \delta H_1(\mathbf{X}) e^{\beta \tau}$, the linearized thin film equation becomes

$$\begin{aligned} \beta H_1 = -\nabla_{\parallel} \cdot \Bigg\{ & M_{\perp}(H_{\rm ss}) \nabla_{\parallel} \left[\nabla_{\parallel}^2 H_1 + \frac{\partial \Pi(H_{\rm ss})}{\partial H} H_1 \right] \\ & + M_{\perp}'(H_{\rm ss}) H_1 \nabla_{\parallel} \left[\nabla_{\parallel}^2 H_{\rm ss} + \Pi(H_{\rm ss}) \right] \\ & + M_{\parallel}(H_{\rm ss}) \nabla_{\parallel} \left[\frac{\partial \Gamma(H_{\rm ss})}{\partial H} H_1 \right] + M_{\parallel}'(H_{\rm ss}) H_1 \nabla_{\parallel} \Gamma(H_{\rm ss}) \Bigg\}. \end{aligned} \tag{3.17}$$

Since $H_{\rm ss}(\mathbf{X})$ and at least one other system variable (e.g., $D(\mathbf{X})$, or $\Psi_{\Delta}(\mathbf{X})$) is spatially non-uniform, the mobility factors $M_{\perp}(H_{\rm ss})$ and $M_{\parallel}(H_{\rm ss})$, the external pressures Π and surface tension Γ, as well as their derivatives with respect to H, all depend on $\mathbf{X}$. Eq. (3.17) is an eigenvalue problem where the eigenvalue β is the growth rate for the corresponding eigenmode $H_1(\mathbf{X})$.

3.2.1 Introduction of auxiliary variable P

In general Eq. (3.17) has to be solved numerically, and the spatial discretization for the all the variables is discussed in details in Chapter 4. We found from numerical experiments that the numerical convergence when solving the system of nonlinear equation is more easily achieved if we introduce the total pressure P as a separate auxiliary variable alongside H. Specifically, the governing equations become

$$f_{s1}(H, P) = \frac{\partial H}{\partial \tau} - \nabla_{\parallel} \cdot \left[M_{\perp}(H) \nabla_{\parallel} P - M_{\parallel}(H) \nabla_{\parallel} \Gamma \right] = 0, \tag{3.18a}$$

$$f_{s2}(H, P) = P + \nabla_{\parallel}^2 H + \Pi = 0. \tag{3.18b}$$

The stationary state equations become

$$f_{s1}(H_{\rm ss}, P_{\rm ss}) = \nabla_{\parallel} \cdot \left[M_{\perp}(H_{\rm ss}) \nabla_{\parallel} P_{\rm ss} - M_{\parallel}(H_{\rm ss}) \nabla_{\parallel} \Gamma \right] = 0, \tag{3.19a}$$

$$f_{s2}(H_{\rm ss}, P_{\rm ss}) = P_{\rm ss} + \nabla_{\parallel}^2 H_{\rm ss} + \Pi(H_{\rm ss}) = 0, \tag{3.19b}$$

and the linearized thin film equation becomes

$$\begin{pmatrix} 1 & 0 \\ 0 & 0 \end{pmatrix} \frac{\partial}{\partial \tau} \begin{pmatrix} H_1 \\ P_1 \end{pmatrix} = \begin{pmatrix} \dfrac{\partial f_{s1}(H_{\rm ss}, P_{\rm ss})}{\partial H} & \dfrac{\partial f_{s1}(H_{\rm ss}, P_{\rm ss})}{\partial P} \\ \dfrac{\partial f_{s2}(H_{\rm ss}, P_{\rm ss})}{\partial H} & \dfrac{\partial f_{s2}(H_{\rm ss}, P_{\rm ss})}{\partial P} \end{pmatrix} \begin{pmatrix} H_1 \\ P_1 \end{pmatrix}, \tag{3.20}$$

where the entries in the Jacobian are given by

$$\begin{aligned} \frac{\partial f_{s1}(H_{\rm ss}, P_{\rm ss})}{\partial H} H_1 = {} & \nabla_{\parallel} \cdot \left\{ \frac{\partial M_{\perp}(H_{\rm ss})}{\partial H} \nabla_{\parallel} P_{\rm ss} - \frac{\partial M_{\parallel}(H_{\rm ss})}{\partial H} \nabla_{\parallel} \Gamma \right\} \\ & - M_{\parallel}(H_{\rm ss}) \nabla_{\parallel} \left[\frac{\partial \Gamma(H_{\rm ss})}{\partial H} H_1 \right] \end{aligned} \tag{3.21a}$$

$$\frac{\partial f_{s1}(H_{\rm ss}, P_{\rm ss})}{\partial P} P_1 = \nabla_{\parallel} \cdot \left[M_{\perp}(H_{\rm ss}) \nabla_{\parallel} P_1 \right] \tag{3.21b}$$

$$\frac{\partial f_{s2}(H_{\rm ss}, P_{\rm ss})}{\partial H} H_1 = \left[\nabla_{\parallel}^2 + \frac{\partial \Pi(H_{\rm ss})}{\partial H} \right] H_1 \tag{3.21c}$$

$$\frac{\partial f_{s2}(H_{\rm ss}, P_{\rm ss})}{\partial P} P_1 = \mathbf{I} P_1. \tag{3.21d}$$

Eq. (3.20) represents a generalized eigenvalue problem with a singular mass matrix on the left hand side. It should be stressed that both Eq. (3.17) and Eq. (3.20) are valid formulations of the LSA for non-uniform stationary states, and Eq. (3.20) is preferred in Chapters 5 and 6 only because of the simpler mathematical expressions and better numerical accuracy. More details regarding the solution procedure for solving the equations are discussed in Chapter 4.

In Chapters 5 and 6, we will study extensively the effects of periodic spatial modulations, and Eq. (3.20) can be simplified to different forms depending on whether the spatial modulation is one-dimensional (e.g. Fig. 3.2(a)) or two-dimensional (e.g., Fig. 3.2(b)) which will be discussed next.

3.2.2 Stripes

When the spatial modulation is one-dimensional, e.g., the patterned mask consists of stripe-like pattern similar to Fig. 3.2(a) with periodicity Λ_p and corresponding wave number $K_p = 2\pi/\Lambda_p$ along the X direction, the stationary states $H_{\rm ss}(\mathbf{X})$ and all the

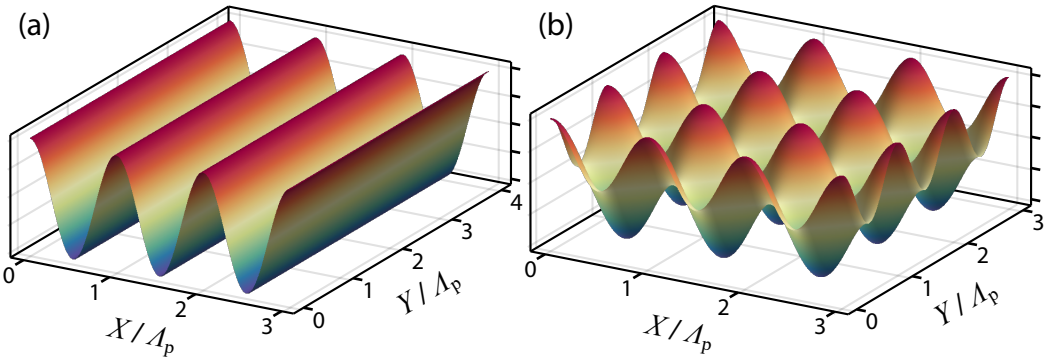

Figure 3.2: Schematic of the form of spatial modulation studied in this thesis. (a) One-dimensional modulation with periodicity Λ_p along the X direction. The spatial profile is sinusoidal. (b) Two-dimensional modulation with periodicity Λ_p along both the X and Y directions. The spatial profile is given by $\cos(2\pi X\Lambda_p) + \cos(2\pi Y/\Lambda_p)$ and looks like an egg carton.

coefficients appearing in the linearized thin film equation become periodic along X, e.g. $H_{\rm ss}(X,Y) = H_{\rm ss}(X+\Lambda_p, Y)$. In order to study the stability against perturbations with arbitrary wavenumber $\mathbf{K} = (K_x, K_y)$, we can apply Bloch's theorem [8] which was first used to study electrons in a spatially periodic crystalline lattice. There is a similar theory commonly known as the Floquet theory [38] in the study of time-periodic states in ODE. From here onwards, we refer to such analysis as Floquet-Bloch (FB) analysis. It turns out the eigenstate H_1 can be expressed as [24, Section 4.2]

$$H_1(\mathbf{X},\tau) = H_1(X)e^{\beta(\mathbf{K})\tau} = \hat{H}_1(X)e^{i\mathbf{K}\cdot\mathbf{X}}e^{\beta(\mathbf{K})\tau}, \tag{3.22}$$

where $\hat{H}_1(X) = \hat{H}_1(X+\Lambda_p)$ has the same periodicity along X. Observe that if $\hat{H}_1(X)$ is periodic in X with wave number K_p, then the function $\hat{H}_1(X)e^{imK_pX}$ is also periodic in X with wave number K_p for any integer m. The Bloch state given in Eq. (3.22) for a given wave number $\mathbf{K} = (K_x, K_y)$ can then be expressed in terms of another Bloch state with wave number $(K_x - mK_p, K_y)$:

$$\hat{H}_1(X)e^{i\mathbf{K}\cdot\mathbf{X}} = \left[\hat{H}_1(X)e^{imK_pX}\right]e^{i[(K_x-mK_p)X+K_yY]}. \tag{3.23}$$

This allows us to restrict the wave number K_x to the following range

$$-\frac{K_p}{2} < K_x \leq \frac{K_p}{2}, \tag{3.24}$$

while the wave number K_y is unrestricted and can take any value. Substituting the expansion given in Eq. (3.22) into Eq. (3.20), and noting that functions of $H_{\rm ss}$ (such as

$M_\perp(H_{\rm ss})$, $\Pi(H_{\rm ss})$) are periodic functions in X with vanishing spatial derivatives along the Y direction, we obtain the following generalized eigenvalue problem for $\hat{H}_1$ and $\hat{P}_1$:

$$\beta \begin{pmatrix} 1 & 0 \\ 0 & 0 \end{pmatrix} \begin{pmatrix} \hat{H}_1 \\ \hat{P}_1 \end{pmatrix} = \begin{pmatrix} f_{1H} & f_{1P} \\ f_{2H} & f_{2P} \end{pmatrix} \begin{pmatrix} \hat{H}_1 \\ \hat{P}_1 \end{pmatrix}, \tag{3.25}$$

where the coefficients of the Jacobian are evaluated at the stationary states of $H = H_{\rm ss}$ and $P = P_{\rm ss}$, and are given by

$$\begin{aligned} f_{1H}\hat{H}_1 = &\left[M'_\perp(H_{\rm ss})\frac{\partial P_{\rm ss}}{\partial X} - M'_\parallel(H_{\rm ss})\frac{\partial \Gamma(H_{\rm ss})}{\partial X} - M_\parallel(H_{\rm ss})\frac{\partial \Gamma'(H_{\rm ss})}{\partial X} \right] \hat{H}_1 \\ &+ \left\{ M'_\perp(H_{\rm ss})\frac{\partial P_{\rm ss}}{\partial X} - M'_\parallel(H_{\rm ss})\frac{\partial \Gamma(H_{\rm ss})}{\partial X} - M_\parallel(H_{\rm ss})\frac{\partial \Gamma(H_{\rm ss})}{\partial X} \right. \\ &\left. - \frac{\partial}{\partial X}\left[M_\parallel(H_{\rm ss})\Gamma'(H_{\rm ss}) \right] \right\} \left(\frac{\partial}{\partial X} + iK_x \right) \hat{H}_1 \\ &- M_\parallel(H_{\rm ss})\Gamma'(H_{\rm ss}) \left(\frac{\partial}{\partial X} + iK_x \right)^2 \hat{H}_1, \end{aligned} \tag{3.26a}$$

$$f_{1P}\hat{P}_1 = \frac{\partial}{\partial X}\left[M_\perp(H_{\rm ss})\frac{\partial \hat{P}_1}{\partial X} \right] - K_y^2 M_\perp(H_{\rm ss})\hat{P}_1, \tag{3.26b}$$

$$f_{2H}\hat{H}_1 = \left[\left(\frac{\partial}{\partial X} + iK_x \right)^2 - K_y^2 \right] \hat{H}_1, \tag{3.26c}$$

$$f_{2P}\hat{P}_1 = \mathbf{I}\hat{P}_1. \tag{3.26d}$$

3.2.3 Cartesian arrays

For 2D periodic patterns arranged in a Cartesian array as shown in Fig. 3.2(b), the above analysis can be extended in a similar way to the Y direction. The eigenstate $\hat{H}_1 = \hat{H}_1(X, Y)$ is now a periodic function of X and Y, and both wave numbers K_x and K_y are restricted to an interval of K_p.

Chapter 4

NUMERICAL METHODS

This chapter provides the implementation details of the two main numerical approaches employed in this thesis – (1) solving the systems of nonlinear equations representing the stationary states and the associated linear stability which will be used in Chapters 5 and 6, and (2) direct numerical simulations of the time-dependent thin film equation which will be used in chapter 5 to 7. The numerical methods covered in this chapter have been well developed, and we simply present the specific technical details relevant to the simulations implemented in this thesis without going to the rigorous theory behind them.

4.1 Spatial Discretization

When solving for the stationary states, the governing equations given by $\partial H/\partial \tau = 0$ are discretized in space, resulting in a system of nonlinear equations to be solved. When solving for the time-dependent evolution of the liquid film, the thin film equation is discretized in space, resulting in a system of coupled ODEs where time τ is the only independent variable. The ODEs can then be solved using different standard ODE solvers implemented in various scientific computing packages. For most numerical results presented in this thesis, the finite difference method (FDM) is used to discretize the spatial derivatives in the governing equations except in Chapter 6.5 where finite element method (FEM) is used to discretize the spatial derivatives of the stationary equations for TC patterning.

A 2D Cartesian domain has size $L_x \times L_y$ such that $0 \leq X \leq L_x$ and $0 \leq Y \leq L_y$. Each dimension is discretized into N_x and N_y uniform intervals with size Δx such that the grid points are located at $X = X_0, X_1, X_2, \ldots X_{N_x-1}, X_{N_x}$ and $Y = Y_0, Y_1, Y_2, \ldots Y_{N_y-1}, Y_{N_y}$. Periodic boundary conditions are imposed so that $X_0 = X_{N_x}$ and $Y_0 = Y_{N_y}$. Introduce the notation $(X_m, Y_n) = (m\Delta X, n\Delta X)$ where $m, n \in \mathbb{N}$. Note that the domain size (L_x, L_y) and the number of grid points (N_x, N_y) are always chosen such the grid size has the same value ΔX along both dimensions unless otherwise specified.

When the system is spatially modulated with dimensionless patterning wavelength Λ_p (e.g., see Fig. 3.2), the domain size (L_x, L_y) is always integer multiples of Λ_p to ensure it can accommodate complete cycles under periodic boundary condition.

4.1.1 Finite difference method (FDM)

Let $u = u(X, Y)$ denote the dependent variable to be solved (not to be confused with horizontal velocity), and define $u_{m,n} = u(X_m, Y_n)$. The following fourth-ordered centered schemes for spatial derivatives are used [39]:

$$\frac{\mathrm{d}u(X_n)}{\mathrm{d}X} = \frac{1}{\Delta X}\left(\frac{1}{12}u_{n-2} - \frac{2}{3}u_{n-1} + \frac{2}{3}u_{n+1} - \frac{1}{12}u_{n+2}\right), \tag{4.1a}$$

$$\frac{\mathrm{d}^2u(X_n)}{\mathrm{d}X^2} = \frac{1}{\Delta X^2}\left(-\frac{1}{12}u_{n-2} + \frac{4}{3}u_{n-1} - \frac{5}{2}u_n + \frac{4}{3}u_{n+1} - \frac{1}{12}u_{n+2}\right), \tag{4.1b}$$

$$\frac{\mathrm{d}^3u(X_n)}{\mathrm{d}X^3} = \frac{1}{\Delta X^3}\left(\frac{1}{8}u_{n-3} - u_{n-2} + \frac{13}{8}u_{n-1} - \frac{13}{8}u_{n+1} + u_{n+2} - \frac{1}{8}u_{n+3}\right), \tag{4.1c}$$

Let $\mathcal{D}_X^{(n)} = \partial^n/\partial X^n$ denotes the finite difference operator for the n^{th} derivatives defined in Eq. (4.1). Define $H_{m,n} = H(X_m, Y_n)$, $P_{m,n} = P(X_m, Y_n) = P(H_{m,n}, \Pi_{m,n})$, $\Pi_{m,n} = \Pi(H_{m,n})$ and $\Gamma_{m,n} = \Gamma(H_{m,n})$. The right hand side of the thin film equation given by Eq. (2.49) can be approximated by the following finite difference scheme in 1D:

$$\frac{\partial H(x_n)}{\partial \tau} \approx -\mathcal{D}_X^{(1)}\left\{M_\perp(H_n)\left(\mathcal{D}_X^{(3)}H_n + \mathcal{D}_X^{(1)}\Pi_n\right) + M_\parallel(H_n)\mathcal{D}_X^{(1)}\Gamma_n\right\}, \tag{4.2}$$

and in 2D:

$$\begin{aligned}\frac{\partial H(X_m, Y_n)}{\partial \tau} \approx{}& \mathcal{D}_X^{(1)}\left[M_\perp(H_n)\mathcal{D}_X^{(1)}P_n + M_\parallel(H_n)\mathcal{D}_X^{(1)}\Gamma_n\right] \\ &+ \mathcal{D}_Y^{(1)}\left[M_\perp(H_n)\mathcal{D}_Y^{(1)}P_n + M_\parallel(H_n)\mathcal{D}_Y^{(1)}\Gamma_n\right], \qquad (4.3a)\\ P_n ={}& -\left(\mathcal{D}_X^{(2)} + \mathcal{D}_Y^{(2)}\right)H_n - \Pi(H_n). \qquad (4.3b)\end{aligned}$$

The stationary equations given by Eq. (3.19) can be discretized similarly. For example, 1D stationary states are given by:

$$\mathcal{D}_X^{(1)}\left[M_\perp(H_n)\mathcal{D}_X^{(1)}P_n + M_\parallel(H_n)\mathcal{D}_X^{(1)}\Gamma_n\right] = 0, \tag{4.4a}$$

$$P_n + \mathcal{D}_X^{(2)}H_n + \Pi(H_n) = 0. \tag{4.4b}$$

Note that after introducing the pressure P as an explicit dependent variable, the maximum order of differentiation becomes two.

The correctness of the implementation of the FDM has been tested in two different ways. First, various periodic test functions are defined using sinusoidal functions. Their

derivatives are computed using FDM using different grid size ΔX, and the results are compared with the exact analytical solutions. Second, the liquid film shape $H(X)$ and the mask topography $D(X)$ are represented by different periodic test functions. The corresponding $\partial H/\partial \tau$ is computed numerically using FDM with different grid size ΔX, and the results are compared with the exact results obtained via automatic differentiation with the Julia package `ForwardDiff.jl`. Both tests show the expected fourth order convergence. The run time of each function call also grows linearly with the number of grid points used as expected.

4.1.2 Finite element method (FEM)

Finite element method (FEM) is an alternative to FDM for spatial discretization. Here we provide a brief overview of the method without going into the technicality with functional analysis. Interested readers can consult standard textbooks such as Ref [123, chapter 4] for more in-depth discussion. Consider the following equation

$$\left[c(x)u'(x)\right]' + a(x)u(x) = f(x) \tag{4.5}$$

defined within an interval given by $0 \leq x \leq L$. Multiplying the equation by a suitable test function $\phi_j(x)$ and integrating the resulting expression using integration by parts, we have

$$[\phi_j(x)c(x)u'(x)]_{x=0}^{x=L} - \langle \phi_j'(x), c(x)u'(x)\rangle + \langle \phi_j(x), a(x)u(x)\rangle = \langle \phi_j(x), f(x)\rangle, \tag{4.6}$$

where the notation $\langle u, v\rangle = \int_0^L u(x)v(x)\mathrm{d}x$ denotes the inner product. Eq. (4.6) is known as the 'weak-form' of Eq. (4.5). If we further suppose $u(x) = \sum_i u_i\phi_i(x)$ and impose periodic boundary conditions on all the variables and test functions (e.g., $u(x=0) = u(x=L)$) such that the boundary term in Eq. (4.6) vanishes, Eq. (4.5) becomes a system of equations given by

$$\sum_i u_i \left[-\langle c(x)\phi_i'(x), \phi_j'(x)\rangle + \langle a(x)\phi_i(x), \phi_j(x)\rangle\right] - \langle f(x), \phi_j(x)\rangle = 0. \tag{4.7}$$

FEM lowers the maximum differentiation order from two to one, so the differentiability requirement for $u(x)$ can be relaxed. Using the expansion $H(X) = \sum_i h_i\phi_i(X)$ and $P(X) = \sum_i p_i\phi_i(X)$, the stationary state equations given by Eq. (3.19) can be discretized using FEM to

$$\sum_i p_i \langle M_\perp(h_i)\phi_i'(X), \phi_j'(X)\rangle + \langle M_\parallel(h_i)\frac{\mathrm{d}\Gamma(h_i)}{\mathrm{d}X}, \phi_j(X)\rangle = 0, \tag{4.8a}$$

$$\sum_i p_i \langle \phi_i(X), \phi_j(X)\rangle - \sum_i h_i \langle \phi_i'(X), \phi_j'(X)\rangle + \Pi(h_i)\phi_j = 0. \tag{4.8b}$$

Note that the coefficients such as $M_\perp(h_i)$, $M_\parallel(h_i)$, $\Pi(h_i)$ and $\Gamma(h_i)$ are all non-linear functions of the dependent variable $H(X)$, and their values at the nodes are estimated by interpolation. Regarding the test functions $\phi_j(X)$, the simplest linear elements are used due to its simpler implementation, and also because it appears slightly more robust to convergence compared to quadratic elements when solving for the stationary states.

4.2 Time-dependent Simulations

4.2.1 Time-stepping

All time-dependent simulations of the thin film equation are carried out using the `DifferentialEquations.jl` package [90] in Julia [5]. FDM is used for spatial discretization (Eq. (4.2) for 1D and (4.3) for 2D), which results in a set of stiff coupled ODEs. Among the recommended stiff ODE solvers provided by `DifferentialEquations.jl`, the `FBDF` solver which is a variant of the well-known backward differentiation formula (BDF) with fixed-leading coefficient is selected for time-stepping, and its specific implementation follows closely the commonly used `ode15i` function in MATLAB [108].

Other solvers supported by the package recommended for solving large stiff ODEs including `QNDF`, `QBDF` and `Kvaerno5` have also been tested on certain custom benchmark tests (see Section 4.2.3), and the results have been compared against each other. The `FBDF` solver was chosen due to its more robust convergence properties as some of the other solvers may occasionally require excessively large number of time steps (and hence long computational time) in certain tests. However, despite the difference in computational time, the numerical solutions obtained with different solvers do agree with each other, i.e., the plots of $H(X, \tau)$ all collapse on the same line.

The volume conservation property is also checked to ensure the accuracy of the numerical results. With the `FBDF` solver, $|\mathrm{mean}[H(\ldots, \tau_f)] - 1| \lesssim 10^{-10}$ for all simulations where τ_f is the simulation end time.

A relative tolerance of 10^{-6} and absolute tolerance of 10^{-9} for time-stepping were found to be sufficient to ensure convergence.

4.2.2 Domain size and initial conditions

Throughout this thesis, two different settings of domain size and initial conditions are commonly used, and they are summarized as follow:

Setting A: Single protrusion with flat initial film

The system size is defined as $-\Lambda_p/2 \leq X \leq +\Lambda_p/2$ in 1D and $-\Lambda_p/2 \leq X, Y \leq +\Lambda_p/2$ in 2D where Λ_p is the dimensionless patterning wavelength (e.g. see Fig. 3.2) such that the spatial domain supports one period of the imposed spatial modulation. The initial condition is a perfectly flat film of $H(\mathbf{X}, \tau = 0) = 1$. This setting can be used to obtain the stationary state from $H(\mathbf{X}, \tau_f)$ via time-dependent simulation by setting a large terminal time τ_f.

Setting B: Multiple protrusions with rough initial film

The system size is $L_x = r_x \Lambda_p$ in 1D and $(L_x, L_y) = (r_x \Lambda_p, r_y \Lambda_p)$ in 2D where r_x and r_y are integers. A larger spatial domain is used since many nonlinear phenomena involve multiple protrusions and ridges, so it is important to have a spatial domain large enough so that long wavelength modes are present. A roughened film described by the following equation is used as the initial condition

$$H_{m,n}(\tau = 0) = H(X_m, Y_n, \tau = 0) = 1 + \sigma_{\text{rand}} \times \text{randn}(m, n), \tag{4.9}$$

where randn(m, n) returns a pseudo-random number drawn from a normal distribution with unit variance and zero mean, and $\sigma_{\text{rand}} \ll 1$ is the random perturbation amplitude. In order to test whether a given stationary state is actually accessible from an initially flat film (but subject to various sources of noise such as thermal fluctuation), and to test the stability of a developed non-uniform stationary state, we add a nonzero random perturbation to the initial condition. This allows different unstable modes to be triggered without relying on numerical noise to be built up, so a smaller simulation time can be used while capturing most phenomena of interest. The noise amplitude is typically set to $\sigma_{\text{rand}} = 10^{-2}$ for the results presented in this thesis. Simulations with different noise amplitude ($10^{-3} \leq \sigma_{\text{rand}} \leq 0.05$) show that unstable stationary states destabilize over a shorter time scale, consistent with the fact that the unstable modes have larger initial amplitudes to begin with. We have also tried using different random initial conditions, such as replacing the normal distribution by a uniform distribution, or using a Fourier series to represent $H(\mathbf{X}, \tau = 0)$ where the Fourier coefficients are drawn from a normal or uniform distribution, and no qualitative difference in the results have been observed. There was also other numerical studies on how using a colored noise spectrum for the initial film roughness affect subsequent dewetting and rupture time of the liquid film [110]. However, a detailed analysis of the effects of the initial condition on the subsequent dynamics is beyond the scope of this work. Eq. (4.9) is used as the initial condition because it is one of the simplest choice possible and is also commonly used in other similar studies in literature.

We also note that the subsequent dynamics of the liquid film is deterministic [1] for a given initial condition given by Eq. (4.9). In order to obtain representative results, multiple time-dependent simulations are typically conducted, each with a different initial condition generated by a random number generator initialized with a different random seed, and quantities averaged across multiple simulations are reported.

4.2.3 Numerical testing

In order to ensure the numerical solutions to $H(\mathbf{X}, \tau)$ converge to the true solutions (which are often unknown) and are accurate, the following tests were carried out to validate the implementation of the time-dependent simulations of the thin film equation:

1. Comparison with LSA with a flat mask (see Section 3.1):

   a) $H(X, \tau)$ is obtained by using a sinusoidal function $H(X, \tau = 0) = 1 + 10^{-3}\cos(2\pi X/L_x)$ as the initial condition, and the simulation is terminated when the change in amplitude $|H(X, \tau) - 1|$ exceeds a certain threshold which is kept very small to ensure the dynamics of the liquid film stays approximately within the linear regime. The growth rate $\beta(K)$ is computed, and K is varied by changing the domain size L_x.

   b) $H(X, \tau)$ is obtained with setting B (large spatial domain with random initial condition) under a flat mask, and the corresponding growth rate is computed from the discrete Fourier transform (DFT) (see Appendix A.5). The averaged growth rate $\beta(K)$ from 50 independent realizations (each seeded with a different random seed to generate different roughened film as initial condition) are computed.

   The numerically computed growth rate $\beta(K)$ from both methods agrees with the theoretical prediction given by Eq. (3.7) up to at least $K \approx 1.3K_c$ for test (a). For test (b), the numerically computed growth rate $\beta(K)$ also agrees with the theoretical prediction up to $K \approx 1.1K_c$ beyond which the (negative) growth rate appears to saturate. This might be related to numerical errors as those stable short wavelength modes with large negative growth rates decay to very small values. They are not expected to significantly affect the results presented in this thesis where we are mostly interested in the unstable long wavelength modes.

2. Different initial conditions $H(X, \tau = 0)$ and mask topography $D(X)$ are used when solving $H(X, \tau)$. The numerical error for the solution $H(X, \tau_f; \Delta X)$ obtained with a particular grid size ΔX is estimated by computing the RMS error $\mathcal{E}_{\text{rms}}$ and maximum error $\mathcal{E}_{\max}$ given by

[1] Studies incorporating thermal fluctuations and other stochastic effects into the thin film equation (resulting in a stochastic PDE) [32, 50, 143] reported qualitative differences due to stochastic effects only for ultra thin films with nanometer thickness which is unusual in the context of EHD or TC patterning.

$$\mathcal{E}_{\text{rms}} = \text{mean}\left[|H(X,\tau_f;\Delta X) - H(X,\tau_f;\Delta X/2)|^2\right], \tag{4.10a}$$

$$\mathcal{E}_{\text{max}} = \max\left[|H(X,\tau_f;\Delta X) - H(X,\tau_f;\Delta X/2)|\right]. \tag{4.10b}$$

Both the RMS and maximum error shows the expected fourth order convergence consistent with the fourth order centered finite difference scheme used.

Regarding numerical accuracy, a grid size of $\Delta X = \Lambda_p/128$ in 1D is sufficient to obtain a numerical solution where both the RMS and maximum errors are $\mathcal{O}(10^{-6} - 10^{-5})$ in most test cases. The actual achievable error is problem-dependent: generally speaking if the liquid film exhibits large deformation where the free surface $H(X,\tau)$ approaches either the substrate or the mask, or when phenomena involving multiple protrusions such as coalescence are involved, the resulting errors are larger. For 2D, a bigger grid size of $\Delta X = \Lambda_p/64$ or $\Lambda_p/32$ is used due to much longer computational time in 2D, and the resulting numerical error is $\mathcal{O}(10^{-5} - 10^{-3})$.

3. The solutions obtained with `DifferentialEquations.jl` using $\Delta X = \Lambda_p/64$ for certain 2D tests showing large liquid film deformation are also benchmarked against solutions obtained with the commercial software COMSOL Multiphysics® v6.0 [20] using finite element method (with quadratic Lagrange element, maximum element size of $\Delta X = \Lambda_p/256$ and PARDISO solver for time-stepping). The results show an RMS deviation of $\mathcal{E}_{\text{rms}} = \mathcal{O}(10^{-5} - 10^{-4})$ between the two.

The largest deviation from the 'true' solution (obtained with finer grid size) usually occurs in the region where the liquid film touches the mask, i.e., when the air gap $\min(D - H)$ is small. Results presented in Section 5.4 show that the smallest vertical length scales in the problem, the air gap $\min(D - H)$ and the precursor film thickness $\min(H)$ when the liquid film exhibits large deformation are both usually of the order of $\mathcal{O}(0.01)$. This is significantly larger than the errors of $\mathcal{O}(10^{-6} - 10^{-4})$ reported above from the numerical benchmark tests, showing that the numerical results presented in this work are accurate enough for the problems of interest.

4.3 Stationary states

When solving for the stationary states (and possibly the associated stability), the discretized equations become a system of nonlinear equations to be solved. The initial guess for the stationary state is obtained by solving the time-dependent thin film equation using setting A described in Section 4.2.2 with a large τ_f so that the liquid film approaches a stationary state. The resulting $H(\mathbf{X},\tau_f)$ is then used as the initial guess for the stationary state, which is solved using standard techniques such as Newton's method coupled to the pseuedo-arclength continuation described below.

4.3.1 Pseudo-arclength continuation (PALC)

Pseudo-arclength continuation is a numerical technique for solving systems of (nonlinear) equations as a function of a specified parameter. This technique is used in Chapter 5 and 6 to study how stationary states and their stability change as a parameter (e.g. D_0 or $\mathcal{W}$) is varied. Here we provide a brief overview of its principles. The presentation follows closely the one given in Ref [123, Chapter 3] and [92, Chapter 5.2].

Let $\mathbf{u} \in \mathbb{R}^n$ denote the vector of the dependent variable to be solved, and λ as a parameter of the governing equation [2]. The discretized stationary state equation is

$$\mathbf{F}(\mathbf{u}, \lambda) = 0, \quad \mathbf{F} : \mathbb{R}^n \times \mathbb{R} \to \mathbb{R}^n, \tag{4.11}$$

Expanding $\mathbf{F}(\mathbf{u}, \lambda)$ around a known solution $(\mathbf{u}_0, \lambda_0)$, we have

$$0 = \mathbf{F}(\mathbf{u}, \lambda) = \underbrace{\mathbf{F}(\mathbf{u}_0, \lambda_0)}_{=0} + \underbrace{\mathbf{F}_\mathbf{u}(\mathbf{u}_0, \lambda_0)}_{=\mathbf{F}_\mathbf{u}^{(0)}}(\mathbf{u} - \mathbf{u}_0) + \underbrace{\mathbf{F}_\lambda(\mathbf{u}_0, \lambda_0)}_{=\mathbf{F}_\lambda^{(0)}}(\lambda - \lambda_0) + \text{h.o.t.} \tag{4.12}$$

where 'h.o.t.' denotes higher order terms in $\mathbf{u} - \mathbf{u}_0$ and $\lambda - \lambda_0$. In a typical parameter sweep, once $\mathbf{F}(\mathbf{u}_0, \lambda_0)$ is solved, the solution $\mathbf{u}$ for the new parameter λ can be obtained by solving Eq. (4.12) using methods such as gradient descent or Newton's method. However, the Jacobian $\mathbf{F}_\mathbf{u}$ becomes singular at the turning point, which corresponds to the point with infinite slope in the $\lambda - u$ plane. Alternative technique such as the pseudo-arclength continuation (PALC) needs to be used in order to trace the full family of solutions beyond the turning point.

PALC works by introducing an additional parameter s that parametrizes the solution branch, i.e., $\mathbf{u} = \mathbf{u}(s)$ and $\lambda = \lambda(s)$, and solve for both $\mathbf{u}$ and λ as s is varied. As λ becomes a new dependent variable, an additional equation is required alongside Eq. (4.11). The tangent vector $\boldsymbol{\tau}^{(0)}$ is defined at $s = s_0$ as follow:

$$\boldsymbol{\tau}^{(0)} = \left(\boldsymbol{\tau}_\mathbf{u}^{(0)}, \boldsymbol{\tau}_\lambda^{(0)}\right) = (\mathbf{u}'(s_0), \lambda'(s_0)) = \frac{\mathrm{d}}{\mathrm{d}s}\left(\mathbf{u}(s), \lambda(s)\right)|_{s=s_0}, \tag{4.13}$$

The projection of the new solution at $(\mathbf{u}(s), \lambda(s))$ along the tangent vector $\boldsymbol{\tau}^{(0)}$ has length $s - s_0$, and can be represented mathematically as follow:

$$\boldsymbol{\tau}^{(0)} \cdot (\mathbf{u} - \mathbf{u}_0, \lambda - \lambda_0) = s - s_0. \tag{4.14}$$

[2] Not to be confused with dimensional wavelength in other parts of this thesis which also uses the symbol λ. The symbol λ represents a general parameter only in this short subsection on PALC.

Eq. (4.14) can now be incorporated with Eq. (4.11) to give the following expanded equation to be solved:

$$\mathbf{G}(\mathbf{u},\lambda;s)=\begin{pmatrix}\mathbf{F}(\mathbf{u},\lambda)\\ \boldsymbol{\tau}_{\mathbf{u}}^{(0)}\cdot(\mathbf{u}-\mathbf{u}_0)+\boldsymbol{\tau}_{\lambda}^{(0)}(\lambda-\lambda_0)-(s-s_0)\end{pmatrix}=\begin{pmatrix}\mathbf{0}\\ 0\end{pmatrix}. \tag{4.15}$$

Differentiating $\mathbf{F}(\mathbf{u},\lambda)=0$ with respect to s gives the following equation for $\boldsymbol{\tau}^{(0)}$:

$$0=\frac{\mathrm{d}}{\mathrm{d}s}\mathbf{F}(\mathbf{u}(s_0),\lambda(s_0))=\mathbf{F}_{\mathbf{u}}^{(0)}\mathbf{u}'(s_0)+\mathbf{F}_{\lambda}^{(0)}\lambda'(s_0)=\left[\mathbf{F}_{\mathbf{u}}^{(0)}|\mathbf{F}_{\lambda}^{(0)}\right]\boldsymbol{\tau}^{(0)}, \tag{4.16}$$

where $\left[\mathbf{F}_{\mathbf{u}}^{(0)}|\mathbf{F}_{\lambda}^{(0)}\right]$ is the extended Jacobian. The tangent vector $\boldsymbol{\tau}^{(0)}$ for the current value of s_0 can be obtained by first solving

$$\mathbf{F}_{\mathbf{u}}^{(0)}\tilde{\mathbf{u}}=-\mathbf{F}_{\lambda}^{(0)}, \tag{4.17}$$

and then setting

$$\boldsymbol{\tau}^{(0)}=\left(\boldsymbol{\tau}_{\mathbf{u}}^{(0)},\boldsymbol{\tau}_{\lambda}^{(0)}\right)=\pm\frac{(\tilde{\mathbf{u}},1)}{\sqrt{\tilde{\mathbf{u}}\cdot\tilde{\mathbf{u}}+1}}, \tag{4.18}$$

where the sign should be chosen by requiring $\boldsymbol{\tau}^{(0)}\cdot\boldsymbol{\tau}_{\mathrm{prev}}^{(0)}>0$ where $\boldsymbol{\tau}_{\mathrm{prev}}^{(0)}$ is the tangent vector at the previous step of s. This allows the parameter λ to pass through a turning point by following the same direction of traversal along the path.

Once $\boldsymbol{\tau}^{(0)}$ is determined, $(\mathbf{u}(s),\lambda(s))$ at the new step $s=s_0+\Delta s$ can be solved iteratively using Newton's method:

$$\left(\mathbf{u}^{(k+1)},\lambda_k\right)=\left(\mathbf{u}^{(k)},\lambda_k\right)+(\Delta\mathbf{u},\Delta\lambda) \tag{4.19}$$

where $(\Delta\mathbf{u},\Delta\lambda)$ is obtained by solving

$$\begin{pmatrix}\mathbf{F}_{\mathbf{u}}(\mathbf{u}^{(k)},\lambda_k) & \mathbf{F}_{\lambda}(\mathbf{u}^{(k)},\lambda_k)\\ \boldsymbol{\tau}_{\mathbf{u}}^{(0)} & \boldsymbol{\tau}_{\lambda}^{(0)}\end{pmatrix}\begin{pmatrix}\Delta\mathbf{u}\\ \Delta\lambda\end{pmatrix}=-\begin{pmatrix}\mathbf{F}(\mathbf{u}^{(k)},\lambda_k)\\ \boldsymbol{\tau}_{\mathbf{u}}^{(0)}\cdot(\mathbf{u}^{(k)}-\mathbf{u}^{(0)})+\boldsymbol{\tau}_{\lambda}^{(0)}(\lambda_k-\lambda_0)-\Delta s\end{pmatrix} \tag{4.20}$$

with $\mathbf{u}^{(0)}=\mathbf{u}(s_0)$ and $\lambda_0=\lambda(s_0)$ as the starting initial guess.

The exact turning point can be further refined by solving the following extended system [123, see Chapter 3.6.1]

$$\begin{pmatrix} \mathbf{F}(\mathbf{u}, \lambda) \\ \mathbf{F}_{\mathbf{u}}(\mathbf{u}, \lambda)\boldsymbol{\phi} \\ \langle \boldsymbol{\phi}, \boldsymbol{\phi} \rangle - 1 \end{pmatrix} = 0, \tag{4.21}$$

where the dependent variable now becomes $(\mathbf{u}, \boldsymbol{\phi}, \lambda) \in \mathbb{R}^{2n+1}$. We can track the locus of the turning point as another parameter different from λ is varied by appending the last equation of Eq. (4.15) into Eq. (4.21). This is known as a codimension two fold point continuation, and will be used in Chapters 5 and 6 to study how the maximum growth rate (represented by a fold point) changes as two parameters are varied.

4.3.2 Computational details

The system of nonlinear equations obtained after discretizing the stationary equations solved numerically using Newton's method implemented in the Julia package `BifurcationKit.jl` [126] with an error tolerance [3] of 10^{-8} as the condition for convergence. Numerical continuation of the solutions is performed using the PALC implemented in `BifurcationKit.jl` where the step size `ds` ($\sim \mathcal{O}(10^{-3} - 10^{-1})$) is chosen based on trial-and-error to ensure a continuous solution branch can be obtained successfully.

As briefly mentioned in the beginning of this chapter, FDM is used for spatial discretization when solving for the stationary states in EHD patterning when shear stress is absent. For the stationary states in TC patterning when shear stress is present, FEM is used for spatial discretization instead for two reasons: (1) fewer difficulties in numerical convergence are encountered using FEM than FDM; (2) FEM appears to give more 'accurate' solutions when comparing certain derived quantities from the numerical solutions. For example, $\mathrm{mean}(H_{\mathrm{ss}}) = 1$ and $\mathrm{mean}(H_1) = 0$ due to volume conservation, and parity of H_1 implies either the real or imaginary part of the complex Fourier coefficients of H_1 (obtained using DFT) should vanish. By checking how close these quantities are to their expected values (either 1 or 0), we can quantify the numerical accuracy achieved with different spatial discretization schemes without knowing the true solution. While the reasons leading to these two observation are not fully understood, we suspect it is due to the lower order of differentiation (one in FEM instead of two in FDM). For stationary states in EHD patterning, however, we find no significant difference in the numerical accuracy and convergence performance between FDM and FEM when solv-

[3] The error tolerance used in the package defaults to the l^2 norm given by $(\sum_i^N r[i]^2)^{1/2}$ where $r[i]$ is the residual vector at index i, and N is the length of the vector.

ing for the stationary states and their stability, and so FDM is used due to its simpler implementation.

The stationary states and the associated eigenvalues and eigenstates computed using `BifurcationKit.jl` with our implemented spatial discretization scheme have been compared to solutions obtained with the commercial software COMSOL Multiphysics® v6.0 [20] using finite element method (with quadratic Lagrange element and maximum element size of $\Delta X = \Lambda_p/256$) for the case where liquid film deformation is not too large (i.e., not touching the substrate or substrate). The results show an RMS deviation of $\mathcal{O}(10^{-4})$ which is order of magnitude smaller than the smallest vertical length scale typically encountered ($\mathcal{O}(10^{-2})$ for minimum film thickness or air gap thickness when the liquid film touches either the mask or substrate). COMSOL is not actually used for computing the numerical solutions presented in this work because of the difficulty in interfacing with external packages for PALC and further analysis.

Chapter 5

HIGH FIDELITY PATTERNS UNDER ELECTROSTATIC STRESS

5.1 Introduction

We begin this chapter by providing a brief overview of the literature on EHD patterning, focusing on the use of external spatial modulation to improve pattern fidelity. We then state the equation and form of spatial modulation to be studied mathematically, and give a brief outline of the chapter.

5.1.1 Literature review

Schäffer et al. [103] first demonstrated that the interface between a polymer and air can be destabilized by an external electric field transverse to the interface. Shortly after this seminal work, subsequent studies focus on understanding the underlying mechanisms of the instability and the initial stage of the pattern formation process. The LSA of the thin film equation (see Section 3.1) has been employed to study the onset of instability [104] under the perfect dielectric model, and its prediction of the fastest growing wavelength λ_m yields quantitative agreement with experimental measurements [104]. Additional physical effects and more complicated models including multiple viscous fluids, non-Newtonian or conducting fluids have also been studied using LSA. Interested readers can consult the extensive list of references in the review by Wu and Russel [134].

As already mentioned in Chapter 1, the patterns formed by the electrostatic instability lack spatial uniformity. This is because according to the dispersion relation given by Eq. (3.7), a range of different modes around $K = K_m$ are excited, so a single well-defined length scale does not necessarily manifest. Besides, predictions of LSA only apply to the early stage of the pattern formation process where the amplitude of the perturbation is small. When the amplitude of the patterns become large, nonlinear terms in the governing thin film equation can no longer be neglected, and subsequent nonlinear processes such as coalescence of neighboring protrusions can ruin the spatial uniformity of the patterns. The initial pattern morphology is also mostly hexagonal, which was explained by Wu et al. [132] using a weakly nonlinear analysis to show that the hexagonal mode has faster initial growth rates than the modes which correspond to Cartesian arrays or stripes.

In order to improve the spatial uniformity, reduce the feature size and to control the morphology of the patterns, researchers typically modulate the electric field, which is most commonly achieved experimentally using a topographically patterned mask (e.g., see Fig. 1.1(c)). Since protrusions are formed in the region of the largest gradient of electrostatic stress, the liquid film is expected to develop protrusions underneath the

regions with smaller electrode separation, resulting in patterns with higher degree of spatial uniformity. Numerous studies have attempted to address how heterogeneous electric field affects the shape of a single layer of viscous thin film, and they are can be classified into two main categories – (1) studying the stationary states and their corresponding stability, and (2) studying the spatiotemporal evolution of the liquid film through direct numerical simulations of an evolution type equation.

The spatial profile and stability of stationary states under a heterogeneous electric field have been studied in Ref [52, 136, 137, 139, 142] numerically. By considering the normal stress balance, Yeoh et al. [142] and Yang et al. [136, 137] observed a critical threshold in the parameters which dictates whether the liquid film developed 'stable' non-uniform patterns without contacting the electrodes. Yeoh et al. [142] specifically studied sinusoidally modulated applied voltage, while Yang et al. [136, 137] studied topographically patterned mask. Yang et al. [139] later applied numerical continuation technique under LWA and discovered hysteresis of the liquid film shape as the applied voltage was varied. Heier et al. [52] also studied the conditions for forming stable stationary states analytically using an energy argument with experimental verification. All these studies [52, 136, 137, 139, 142] focused on a single protrusion or ridge developed by the liquid film, and the 'stability' they considered only refer to whether electrostatic pressure can be balanced by capillarity to form protrusions without touching either the mask or substrate. Stability against other nonlinear phenomena such as coalescence which involves fluid flow between neighboring protrusions and have been observed in experiments [133] or in simulations [131] were not taken into account. Besides, whether an initially flat liquid film does evolve to the predicted stationary state in the first place has also not been addressed in detail.

The other approach involves the direct numerical simulation of the thin film equation derived under LWA [85] for a system with a topographically patterned mask [3, 56, 86, 112, 127, 132]. Studies involving the use of topographically or chemically patterned substrate have also been conducted [3, 112]. Ref [3, 112, 127, 132] have studied the spatiotemporal evolution of the liquid film under selected parameters, and concluded that matching the fastest-growing wavelength λ_m of the system with the externally imposed patterning wavelength λ_p (see Fig. 1.1(c)) is required in order for the liquid film to develop patterns with the same periodicity as the patterns imposed on the patterned mask or substrate, and subsequent experimental studies [127, 133] reported qualitatively similar results. More recently, varying the ratio between the patterning and instability time scales using ultra high voltage was also investigated numerically and experimentally and showed some promising results [56, 86] regarding the formation of high fidelity patterns. However, the simulations conducted in these studies often only cover a small range of parameters out of a large parameter space, so the predictive capability of those results in unexplored parameters is expected to be very limited since the underlying

pattern formation phenomena are highly nonlinear. More in-depth understanding of the pattern formation process, especially the destabilization mechanism and the conditions for achieving stable patterns, are also lacking.

In view of the limitations of prior studies in literature, we aim to provide a more comprehensive understanding of the pattern formation process in viscous liquid film under external periodic spatial modulation in the electric fields. We focus mainly on one-dimensional spatial modulation which results in parallel ridges formed by the liquid film, but also provide preliminary studies on two-dimensional spatial modulation at the end. We first revisit the stationary states of a single ridge and their stability, and demonstrate that the critical threshold separating stationary states with small and large deformation [52, 136, 137, 139, 142] can be be explained analytical by a weakly-nonlinear analysis using multi-scale expansion close to the onset of instability. We then study the stability of the multiple ridges taking into account phenomena such as coalescence and Ostwald ripening using LSA, and present stability phase diagrams showing the parameters for forming stable patterns. Finally, we also investigate the dynamics of liquid film via direct numerical simulation of the thin film equation to corroborate the results on the stability of stationary states, and to determine whether the non-uniform stationary states are accessible for an initially flat liquid film.

5.1.2 Problem statement

The governing equation for EHD patterning is re-stated below for convenience:

$$\frac{\partial H}{\partial \tau} = \nabla_{\parallel} \cdot \left\{ M(H) \nabla_{\parallel} P \right\} = -\nabla_{\parallel} \cdot \left\{ M(H) \nabla_{\parallel} \left[\nabla_{\parallel}^2 H + \Pi(H, \xi) \right] \right\}, \tag{5.1}$$

where $M(H) = H^3/3$ is the mobility factor (the subscript '$\perp$' has been dropped since shear stress is absent and there is only one mobility factor), $P = -\nabla_{\parallel}^2 H - \Pi$ is the total pressure, Π is the external pressure due to electrostatic and van der Waals' effects, and the asterisk $(*)$ for the dimensionless in-plane gradient operator has been dropped for brevity. The symbol ξ is a label which denotes the system variable being spatially modulated from this chapter onwards: for EHD patterning, we focus on either topographically patterning the top electrode, i.e., $\xi = D(\mathbf{X})$, or spatially modulating the applied voltage, i.e., $\xi = \Psi_{\Delta}(\mathbf{X})$. Specifically, we consider the following form of spatial modulation:

$$\xi = D: \qquad D(\mathbf{X}) = D_0 \left[1 + \varrho g(\mathbf{X}) \right], \tag{5.2a}$$

$$\xi = \Psi_{\Delta}: \quad \Psi_{\Delta}(\mathbf{X}) = 1 + \varrho g(\mathbf{X}), \tag{5.2b}$$

where ϱ is the modulation strength [1], D_0 is the mean electrode separation, and $g(\mathbf{X})$ is the patterning function given by

$$\text{1D sinusoidal:} \quad g(X) = \cos(2\pi X/\Lambda_p), \tag{5.3a}$$

$$\text{1D rectangular:} \quad g(X) = \mathrm{rect}(X) = \tanh\left[\frac{X - w_{\mathrm{rect}}}{l_{\mathrm{rect}}}\right] \tanh\left[\frac{X + w_{\mathrm{rect}}}{l_{\mathrm{rect}}}\right], \tag{5.3b}$$

$$\text{2D egg carton:} \quad g(X,Y) = \frac{1}{2}\left[\cos(2\pi X/\Lambda_p) + \cos(2\pi Y/\Lambda_p)\right]. \tag{5.3c}$$

Note that the modulation variable can be expressed in the general form $\xi = \xi_0(1 + \varrho g)$ where $\xi_0 = D_0$ or 1 depending on the actual type of spatial modulation. The patterning wavelength is Λ_p. The parameter w_{rect} in Eq. (5.3b) is the width of rectangular step, while l_{rect} controls how steep the slope of the step is. In actual simulations where the spatial domain $L_x = n\Lambda_p$ spans multiple repetitions of the periodicity (i.e., setting B described in chapter 4.2.2), Eq. (5.3b) is turned to a periodic function by first restricting X to $-\Lambda_p/2 \leq X \leq \Lambda_p/2$ and then repeating the function defined within one unit cell n times periodically.

We are interested in studying how the liquid film responds to external spatial modulation described by Eq. (5.2) and (5.3), including the stationary states and their stability, as well as the dynamic evolution toward the stationary states from an initially flat film.

5.1.3 Outline

In Section 5.2, we study analytically the spatiotemporal dynamics of the liquid film subject to 1D sinusoidal modulation given by Eq. (5.3a) under the limits of small amplitude modulation ($\varrho \ll 1$) using a linear analysis and near the onset of instability ($\mathcal{W} \approx \mathcal{W}_c$) using a weakly-nonlinear analysis. The results from weakly-nonlinear analysis suggest a critical threshold in $\mathcal{W}$ separating small and large deformation of the liquid film, which quantitatively explain previous results in Ref [52, 136, 137, 139, 142]. In Section 5.3, we simplify the equations governing the stationary states and the associated stability first given in Chapter 3 for EHD patterning where the stationary state pressure becomes a constant. In Section 5.4, we present the numerical results for stationary states by successively introducing different physical effects and complexity. We then complete the chapter by discussing the implications of the results in Section 5.5 and summarizing the main findings in Section 5.6. Section 5.7 contains the derivations of a few equations shown in Section 5.2.

[1] Not to be confused with the liquid density ρ in Chapter 2. Notice the typographical difference between ϱ and ρ.

5.2 Analytical Results

We first attempt to study the stationary states and their stability analytically in order to gain more physical insights. Specifically, we look at two cases: when $\varrho \ll 1$ and when $\mathcal{W} \approx \mathcal{W}_c$.

In this chapter, the electric Weber number $\mathcal{W}$ is often presented as the ratio $\mathcal{W}/\mathcal{W}_c$:

$$\mathcal{W}_c = K_p^2 \frac{[1+\varepsilon_r(D_0-1)]^3}{\varepsilon_r(\varepsilon_r-1)^2}, \qquad \mathcal{W}_r \equiv \frac{\mathcal{W}}{\mathcal{W}_c} = \frac{\mathcal{W}\varepsilon_r(\varepsilon_r-1)^2}{K_p^2\,[1+\varepsilon_r(D_0-1)]^3}, \tag{5.4}$$

where $\mathcal{W}_c$ (first introduced in Chapter 3.1.4) is only a function of D_0 when K_p and ε_r are held fixed. The parameters are also often reported using ratios of wavelength or wave number in literature, and they are related to $\mathcal{W}_r$ via

$$\mathcal{W}_r = \frac{\mathcal{W}}{\mathcal{W}_c} = \left(\frac{K_c}{K_p}\right)^2 = \frac{1}{2}\left(\frac{K_m}{K_p}\right)^2 = 2\left(\frac{\lambda_p}{\lambda_m}\right)^2, \tag{5.5}$$

where λ_p is the dimensional patterning wavelength, and λ_m is the dimensional fastest-growing wavelength under LWA given by Eq. (3.12).

5.2.1 Linear theory under small modulation strength ($\varrho \ll 1$)

When the modulation amplitude $\varrho \ll 1$ is small, we can obtain analytical approximation to $H(\mathbf{X},\tau)$. Assume the spatially modulated system variable ξ (representing either D or Ψ_Δ) is given by Eq. (5.3a), i.e., $\xi(X) = \xi_0\,[1+\varrho\cos(K_pX)]$. Using the ansatz $H(\mathbf{X},\tau) = 1 + \varrho H_1(X,\tau) + \mathcal{O}(\varrho^2)$, Eq. (5.1) can be linearized to give

$$\frac{\partial H_1}{\partial \tau} = -M(1)\left[K_c^2\frac{\partial^2 H_1}{\partial X^2} + \frac{\partial^4 H_1}{\partial X^4}\right] + M(1)K_p^2\xi_0\frac{\partial \Pi(1,\xi_0)}{\partial \xi}\cos(K_pX), \tag{5.6}$$

where $M(1) = 1/3$ is the mobility factor evaluated at the base state of a flat film, and $\partial\Pi(1,\xi_0)/\partial\xi$ is given in Appendix B. Periodic boundary conditions $H(-L_x/2,\tau) = H(L_x/2,\tau)$ are imposed, and we assume the spatial domain is $L_x = N\Lambda_p = 2\pi N/K_p$ for integer values of N. The initial condition of H_1 has the following general form

$$H_1(X,\tau=0) = \sum_n \left[a_n\cos(K_nX) + b_n\sin(K_nX)\right], \tag{5.7}$$

where $K_n = 2\pi n/L_x$. As shown in Section 5.7.1, the general solution of $H_1(X,\tau)$ under the given boundary conditions and initial conditions is

$$H_1(X,\tau) = \sum_n \left[a_n \cos(K_n X) + b_n \sin(K_n X)\right] e^{\beta(K_n)\tau} + \frac{\xi_0}{K_p^2 - K_c^2} \frac{\partial \Pi(1,\xi_0)}{\partial \xi} \cos(K_p X) \left[1 - e^{\beta(K_p)\tau}\right], \tag{5.8}$$

where $\beta(K)$ is the dispersion relation for the un-modulated case given by Eq. (3.7). The solution to $H_1(X,\tau)$ consists of the homogeneous solution (first line) due to the intrinsic EHD instability and the particular solution (second line) due to the spatial modulation imposed on the system. If $K_p > K_c$ and $\beta(K_n) < 0$, then the liquid film saturates with deformation amplitude given by

$$\Delta H_{\text{lin}} \equiv \max[H(\tau \to \infty) - 1] = \frac{\varrho \xi_0}{K_p^2 - K_c^2} \left| \frac{\partial \Pi(1,\xi_0)}{\partial \xi} \right| \tag{5.9}$$

$$= \begin{cases} \dfrac{\varrho D_0}{K_p^2 - K_c^2} \dfrac{\mathcal{W} \varepsilon_r^2 (\varepsilon_r - 1)}{\left[1 + \varepsilon_r (D_0 - 1)\right]^3} = \dfrac{\varrho D_0 \mathcal{W} \varepsilon_r}{|\mathcal{W} - \mathcal{W}_c| (\varepsilon_r - 1)}, & \text{if } \xi = D \\ \dfrac{\varrho}{K_p^2 - K_c^2} \dfrac{\mathcal{W} \varepsilon_r (\varepsilon_r - 1)}{\left[1 + \varepsilon_r (D_0 - 1)\right]^2} = \dfrac{\varrho \mathcal{W} \left[1 + \varepsilon_r (D_0 - 1)\right]}{|\mathcal{W} - \mathcal{W}_c| (\varepsilon_r - 1)}, & \text{if } \xi = \Psi_\Delta \end{cases}$$

and the characteristic time scale for achieving the stationary state is given by

$$\tau_p = \frac{1}{|\beta(K_p)|}. \tag{5.10}$$

Note that Eq. (5.9), which has been derived without assuming the specific type of spatial modulation, encompasses previous results in literature studying specific type of spatial modulation [2]. Eq. (5.9) has also been expressed in terms of wave numbers (K_c and K_p) or the electric Weber numbers ($\mathcal{W}$ or $\mathcal{W}_c$) for topographically patterned mask or spatially modulated applied voltage, respectively. The van-der Waals' contribution to Π is assumed to be negligible since the free surface is far from either electrode when the liquid film develops small amplitude deformation.

Since we are interested in large scale periodic patterns, the system size is many times larger than the patterning wave wavelength so that multiple periods of the imposed patterns on the mask are present. Since the smallest wave number allowed in the system is $K_{\min} = 2\pi/L_x$ where $L_x = N\Lambda_p$ for integer values of N, whenever $N > K_p/K_c = \sqrt{\mathcal{W}_c/W}$ which is usually satisfied, then there is at least one mode with

[2] For modulation in applied voltage ($\xi = \Psi_\Delta(X)$), it agrees with Eq. (16) in Yeoh et al. [142] if we take the limit $k \to 0$ under LWA. For modulation in electrode topography ($\xi = D(X)$), it agrees with Eq. (6) in Heier et al. [52] and Eq. (22) in Yang et al. [136] after appropriate algebraic manipulation of the expressions.

positive growth rate (i.e., $\beta(K_{\min}) > 0$). Therefore, in practice an initially flat liquid film subject to random perturbation does not develop stable sinusoidal deformation given by Eq. (5.8). However, the time scale for destabilization which is characterized by $\beta(K)$ for the unstable modes K might be long enough compared to τ_p, and so for practical purposes the patterns developed by the liquid film may still be retained for patterning purposes.

5.2.2 Multi-scale expansion near $\mathcal{W} \approx \mathcal{W}_c$

The linear analysis presented in Section 5.2.1 no longer holds as $K_p \to K_c$, or as $\mathcal{W} \to \mathcal{W}_c$. In order to study the behavior of the liquid film near the critical point where $\mathcal{W} \approx \mathcal{W}_c$, we need to perform a multi-scale expansion around $\mathcal{W}_c$. The multi-scale expansion has been employed to study the rupture of free-standing film [33] and liquid film on patterned substrate [57] near the bifurcation point, and here we apply the multi-scale expansion to study liquid thin film in the context for lithographic patterning. We briefly summarize the scalings employed in the expansion and state the final amplitude equation which is used to obtain various physical insights. Detailed derivation justifying the proposed scalings is provided in Section 5.7.2.

We assume the spatially modulated variable is $\xi(X) = \xi_0 \left[1 + \varrho \cos(K_p X)\right]$, where ξ is a label representing either electrode topography D or the applied voltage difference Ψ_Δ. We expand the liquid film shape as $H(X,\tau) = 1 + \delta H_1(X,\tau) + \delta^2 H_2(X,\tau) + \cdots$ with the scaling $\delta^3 = \varrho \ll 1$. We further expand the electric Weber number as $\mathcal{W} = \mathcal{W}_c + \delta^2 \mathcal{W}_2$, and introduce the slow time $\tau_2 = \delta^2 \tau$. The scalings for $\mathcal{W}$ and τ can be deduced from the multi-scale expansion without spatial modulation, and the scaling $\delta^3 = \varrho$ is required in order for the effect of spatial modulation to appear in the final amplitude equation we seek. From the $\mathcal{O}(\delta)$ expansion, the leading order solution is

$$H_1(X,\tau) = a_1(\tau_2) \cos(K_p X), \tag{5.11}$$

where the amplitude $a_1(\tau_2)$ satisfies the following amplitude equation which comes from the solvability condition in the $\mathcal{O}(\delta^3)$ expansion:

$$\frac{\mathrm{d}a_1}{\mathrm{d}\tau_2} = f_{\mathrm{wnl}}(a_1; \mathcal{W}_2) = c_3 a_1^3 + c_1 \mathcal{W}_2 a_1 + c_0, \tag{5.12}$$

with the coefficients given by

$$c_3 = \frac{1}{24}M(1)\left[\left(\frac{\partial^2\Pi}{\partial H^2}\right)^2 + 3K_p^2\frac{\partial^3\Pi}{\partial H^3}\right] = \frac{15\mathcal{W}_c^2(\varepsilon_r-1)^4(\varepsilon_r-1)^2\varepsilon_r^2}{8\left[1+\varepsilon_r(D_0-1)\right]^8}, \tag{5.13a}$$

$$c_1 = M(1)K_p^2\frac{\partial^2\Pi}{\partial H\partial\mathcal{W}} = K_p^2\frac{\varepsilon_r(\varepsilon_r-1)^2}{\left[1+\varepsilon_r(D_0-1)\right]^3}, \tag{5.13b}$$

$$c_0 = M(1)K_p^2\,\xi_0\frac{\partial\Pi}{\partial\xi}. \tag{5.13c}$$

Note that all derivatives of Π in Eq. (5.13) are evaluated at $H = 1$, $\xi = \xi_0$ and $\mathcal{W} = \mathcal{W}_c$, and their full expressions are given in Appendix B. The expressions after the second equality in Eq. (5.13)(a) and (b) are obtained by neglecting van-der Waals' interactions since their contribution to Π is much smaller than electrostatic stress for a flat liquid film under the parameters investigated. For the case of uniform patterning without spatial modulation, i.e., $\xi(X) = \xi_0 =$ const., we simply set $c_0 = 0$ because the c_0 term arises from spatial modulation in the derivation of Eq. (5.12).

The stationary states can be obtained by solving $f_{\mathrm{wna}}(a1;\mathcal{W}_2) = 0$, while the stability is determined by the sign of the Jacobian (positive for unstable and negative for stable) given by

$$\frac{\partial f_{\mathrm{wna}}}{\partial a_1} = 3c_3a_1^2 + c_1\mathcal{W}_2. \tag{5.14}$$

Fig. 5.2.2 shows the stationary solutions ($\mathrm{d}a_1/\mathrm{d}\tau_2 = 0$) to Eq. (5.12). The unmodulated case (i.e., without spatial modulation) is shown in Fig. 5.2.2(a) which depicts a subcritical pitchfork bifurcation. Solid lines denote the stationary states obtained by solving $\mathrm{d}a_1/\mathrm{d}\tau_2 = 0$ (Eq. (5.12)). When $\mathcal{W}_2 > 0$, i.e., $\mathcal{W} > \mathcal{W}_c$, the trivial stationary state is unstable and no stable non-trivial stationary state can be formed. This is consistent with the LSA carried out in Chapter 3.1 where the growth rate β is positive whenever $\mathcal{W} > \mathcal{W}_c$ (see Fig. 3.1(b)). When $\mathcal{W}_2 < 0$, i.e., $\mathcal{W} < \mathcal{W}_c$, the unstable branch bifurcates into two unstable branch with nonzero amplitude, and a stable branch with zero amplitude. The stable branch represents the parameter range where the electrostatic stress is insufficient to overcome the capillary stress, and so the flat liquid film does not develop any corrugations.

When the mask is topographically patterned (i.e., $\xi = D(X)$), the bifurcation diagram is shown in Fig. 5.2.2(b) which depicts an imperfect supercritical pitchfork bifurcation with two distinct branches. The stable branch with nonzero amplitude only exists when $\mathcal{W}_2 < \mathcal{W}_2^*$, where $\mathcal{W}_2^*$ and the corresponding amplitude a_1^* can be determined by solving $f_{\mathrm{wna}}(a_1^*;\mathcal{W}_2^*) = 0$ and $\partial f_{\mathrm{wna}}(a_1^*;\mathcal{W}_2^*)/\partial a_1 = 0$ simultaneously, giving

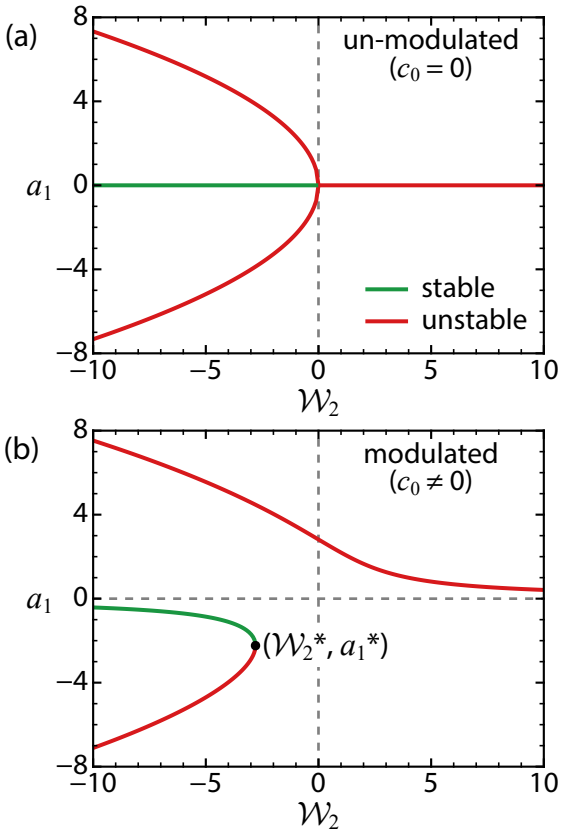

Figure 5.1: Bifurcation diagram under the weakly-nonlinear analysis of a liquid film with (a) flat mask ($c_0 = 0$) and (b) spatially modulated mask ($\xi = D(X)$ and $c_0 \neq 0$). Parameters: $D_0 = 2.5$, $\varepsilon_r = 2.5$, $\xi = D(X)$. Colored lines denote numerical solution to $\mathrm{d}a_1/\mathrm{d}\tau_2 = 0$ given by Eq. (5.12). Green color denotes stable branch while red color denotes unstable branch. The fold point given by Eq. (5.15) which separates the stable and unstable branch in (b) is indicated by the black circle marker.

$$\mathcal{W}_2^* = -\mathrm{sign}(c_1 c_3)\frac{3}{|c_1|}\left(\frac{c_0^2|c_3|}{4}\right)^{1/3}, \qquad a_1^* = \mathrm{sign}(c_0 c_3)\left(\frac{|c_0|}{2|c_3|}\right)^{1/3}. \tag{5.15}$$

This implies $\mathcal{W} = \mathcal{W}_c + \delta^2\mathcal{W}_2$ cannot exceed the threshold $\mathcal{W}_c + \delta^2\mathcal{W}_2^*$ for stable stationary states to form. Physically speaking, the stationary state is stable when capillarity can balance the electrostatic stress. When $\mathcal{W}$ is large enough, the electrostatic stress is too strong for the capillarity to balance if the liquid film deformation is small. In this case, pressure balance can only be satisfied by having large deformation for the liquid film whose shape can no longer be described by a linear or weakly-nonlinear theory [3]. The negative phase for the amplitude of the stable branch is consistent with the fact that the liquid film attains a maximum at the valley of the patterned electrode. If the

[3] This corresponds to the large deformation case when $\mathcal{W} > \mathcal{W}_{\mathrm{f1}}$ described later in Section 5.4.2.

applied voltage Ψ_Δ is modulated instead, then $c_0 \propto \partial\Pi/\partial\xi > 0$, and the bifurcation diagram shown in Fig. 5.2.2(b) is reflected along the horizontal $a_1 = 0$ axis, giving a stable branch with positive amplitude.

Since $\varrho = \delta^3$ and $\mathcal{W} = \mathcal{W}_c + \delta^2\mathcal{W}_2$, we can define the critical modulation strength ϱ^*_{wna} for a given $\mathcal{W}$ as

$$\varrho^*_{\mathrm{wna}} = \left|\frac{\mathcal{W}_c - \mathcal{W}}{\mathcal{W}_2^*}\right|^{3/2}. \tag{5.16}$$

For any given $\mathcal{W} < \mathcal{W}_c$, when $\varrho > \varrho^*_{\mathrm{wna}}$, the stationary state given by solving Eq. (5.12) is unstable under the weakly-nonlinear analysis. On the other hand, when $\varrho < \varrho^*_{\mathrm{wna}}$, the liquid film adopts a stable stationary state with deformation amplitude given by solving $f_{\mathrm{wna}}(a_1) = 0$.

5.3 Numerical Methods for Studying Stability

5.3.1 Stationary state conditions and stability

In EHD patterning under the perfect dielectric model, there is no shear stress or lateral driving force in the system. This simplifies the stationary equations given by Eq. (3.19). Integrating Eq. (3.19)(a) along $\mathbf{X}$ once yields an integration constant which is zero because the net flux into the integration region should vanish when there is no shear stress or lateral driving. Further integration of the resulting expression along $\mathbf{X}$ yields the following equation

$$P_{\mathrm{ss}} = -\nabla_\parallel H_{\mathrm{ss}} - \Pi(H_{\mathrm{ss}}, \xi) = \text{const.} \tag{5.17}$$

where P_{ss} is the second integration constant representing the total pressure at stationary state. Eq. (5.17) is supplemented by another equation enforcing conservation of mass

$$\int_\Omega H_{\mathrm{ss}}(\mathbf{X})\mathrm{d}\mathbf{X} = \int_\Omega \mathrm{d}\mathbf{X} = |\Omega|. \tag{5.18}$$

Note that when the liquid film reaches stationary state in EHD patterning, there is no flow within the liquid film. This can be seen from the horizontal velocity given by Eq. (2.44) where $\nabla_\parallel P_{\mathrm{ss}} = 0$, and $\Gamma = \mathbf{\Pi}^{(t)}_{\mathrm{M}} = 0$. The stationary state is also independent of the mobility factor $M(H)$ since the capillary and electrostatic pressure (as well as disjoining pressure from van der Waals' effect) act in the direction normal to the liquid film surface and no shear is involved. This implies the stationary shapes remain unchanged even when different physics are involved as long as their effects only manifest through the mobility factor, for example, when the upper gas layer become a viscous fluid, or if slip is involved at the fluid-substrate interface.

As discussed out in Chapter 3.2, the stability of an arbitrary non-uniform stationary states can be determined by solving the eigenvalue problem given by Eq. (3.17) with the expansion $H(\mathbf{X},\tau) = H_{\rm ss}(\mathbf{X}) + \delta H_1(\mathbf{X},\tau)$, or the generalized eigenvalue problem given by Eq. (3.20) by introducing an additional auxiliary variable P to solve for alongside H. When shear stress is absent and the stationary state condition is solely determined by Eq. (5.17) and (5.18), we can simplify the expression of the eigenvalue problems using the fact that $\nabla_\parallel \left[\nabla_\parallel^2 H_{\rm ss} + \Pi(H_{\rm ss},\xi)\right] = \nabla_\parallel P_{\rm ss} = 0$ and $\Gamma = 0$. Eq. (3.17) becomes

$$\beta H_1 = -\nabla_\parallel \cdot \left\{ M'_\perp(H_{\rm ss}) H_1 \nabla_\parallel \left[\nabla_\parallel^2 H_{\rm ss} + \Pi(H_{\rm ss})\right]\right\}, \tag{5.19}$$

and similarly Eq. (3.20) becomes

$$\beta H_1 = \nabla_\parallel \cdot \left[M(H_{\rm ss})\nabla_\parallel P_1\right], \tag{5.20a}$$

$$0 = P_1 + \left[\nabla_\parallel^2 + \frac{\partial \Pi(H_{\rm ss})}{\partial H}\right] H_1. \tag{5.20b}$$

The split variable approach given by Eq. (5.20) is chosen for all the numerical results presented in this chapter due to better numerical accuracy as already discussed in chapter 4.1. Note that unlikely the shape of the stationary states, the stability does depend on the mobility factor since it involves fluid flow.

For 1D spatial modulation given by either Eq. (5.3a) or (5.3b), the stability of the stationary states in a 1D system (i.e., invariant along Y direction) defined as $-\Lambda_p/2 \leq X \leq \Lambda_p/2$ can be studied using Bloch analysis introduced in Chapter 3.2 with the substitution $H(X,\tau) = H_{\rm ss}(X) + \delta\hat{H}_1(X)e^{iK_x X + \beta\tau}$ and $P(X,\tau) = P_{\rm ss} + \delta\hat{P}_1(X)e^{iK_x X+\beta\tau}$ where $-K_p/2 < K_x \leq K_p/2$. Eq. (5.20) becomes

$$\beta\hat{H}_1 = \frac{\partial M(H_{\rm ss})}{\partial X}\left(\frac{\partial}{\partial X} + iK_x\right)\hat{P}_1 + M(H_{\rm ss})\left(\frac{\partial}{\partial X} + iK_x\right)^2 \hat{P}_1, \tag{5.21a}$$

$$0 = \hat{P}_1 + \left[\frac{\partial \Pi(H_{\rm ss})}{\partial H} + \left(\frac{\partial}{\partial X} + iK_x\right)^2\right]\hat{H}_1. \tag{5.21b}$$

Eq. (5.21) can also be obtained by setting $K_y = 0$, $\Gamma = 0$ and $P_{\rm ss} =$ const. in Eq. (3.26).

In a 2D system where the liquid film can vary along the Y direction, both K_x and K_y can be nonzero. As it will be shown in Section 5.4, the stability of parallel ridges in 1D is usually determined by the eigenmodes involving two neighboring ridges which correspond to $K_x = K_p/2$. In order to simplify the problem in 2D, we instead consider an enlarged spatial domain with $L_x = 2\Lambda_p$ supporting two parallel ridges, and focus on

the perturbation along the Y direction. Using $H(X,Y,\tau) = H_{\rm ss}(X) + \delta H_1(X) e^{iK_y Y + \beta\tau}$ [13, 117] and $P(X,Y,\tau) = P_{\rm ss} + \delta P_1(X) e^{iK_y Y + \beta\tau}$. Eq. (5.20) becomes

$$\beta H_1 = \frac{\partial M(H_{\rm ss})}{\partial X}\frac{\partial P_1}{\partial X} + M(H_{\rm ss})\left(\frac{\partial^2}{\partial X^2} - K_y^2\right) P_1, \tag{5.22a}$$

$$0 = P_1 + \left[\frac{\partial^2}{\partial X^2} - K_y^2 + \frac{\partial \Pi(H_{\rm ss})}{\partial H}\right] H_1. \tag{5.22b}$$

When solving either Eq. (5.21) or (5.22), either the growth rate β or the wavenumber K_x (or K_y) is held fixed, and the other becomes a dependent variable to be solved. An extra equation is needed, which comes from the constraint of $\int |H_1|^2 \mathrm{d}X$ which fixed the norm of the eigenmodes.

5.3.2 Numerical methods

The numerical methods used for solving the stationary equations and time-dependent thin film equation are discussed in Chapter 4. Below we discuss a few specifics for the EHD patterning problem in this chapter.

5.3.2.1 Stationary states

For a given set of parameters (D_0, ϱ, $\mathcal{W}$), an initial guess for the 1D stationary state $H_{\rm ss}(X)$ is obtained by first solving the time-dependent thin film equation given by Eq. (5.1) with the initial condition $H(X, \tau = 0) = 1$ in a 1D system with $L_x = \Lambda_p = 2$ (see Section 4.2). The final time is fixed at $\tau_f = 10$ such that $\partial H(X,\tau_f)/\partial\tau \approx 0$, so $H(X,\tau_f)$ becomes the initial guess for the numerical solutions to the stationary equations which consist of Eq. (5.17) and (5.18). The discretized nonlinear equations are solved using Newton's method implemented in the Julia package `BifurcationKit.jl` [126]. In order to determine the growth rates β and the eigenmodes $H_1(X)$, Eq. (5.21) and the additional constraint of $\int |H_1|^2 \mathrm{d}X = 1$ are incorporated to the set of nonlinear equations to be solved. Once the stationary solution (and possibly the associated eigenmodes and growth rate) for a given set of parameters is obtained, the PALC implemented in `BifurcationKit.jl` [126] is then employed to obtain the other solutions as one of the parameters (e.g., D_0, ϱ or $\mathcal{W}$) is varied.

5.3.2.2 Time-dependent simulations of Eq. (5.1)

Eq. (5.1) is solved numerically using method of lines as described in Section 4.2. When studying the interactions among the protrusions formed in the liquid film, a large system size is used to ensure long wavelength modes are present. For 1D simulations presented in Section 5.4.3, $L_x = 16\Lambda_p$; for 2D simulations presented in Section 5.4.4, $(L_x, L_y) =$

$(4\Lambda_p, 6\Lambda_p)$ for parallel ridges and $(L_x, L_y) = (4\Lambda_p, 4\Lambda_p)$ for 'egg carton' modulation. The initial condition is $H(\mathbf{X}, \tau) = 1 + 0.01 \times \text{randn}(\mathbf{X})$, where $\text{randn}(\mathbf{X})$ is a random number generator which returns a sample from the standard normal distribution.

To quantify the deviation of the liquid film shape from the stationary state, we introduce the (instantaneous) RMS deviation $\mathcal{E}_{\text{rms}}(\tau)$ and shifted deviation $\mathcal{E}_{\text{shifted}}(\tau)$ defined as

$$\mathcal{E}_{\text{rms}}(\tau) = \frac{1}{|\Omega|} \int_{\Omega} [H(X, Y, \tau) - H_{\text{ss}}(X)]^2 \, \mathrm{d}\mathbf{X}, \tag{5.23a}$$

$$\mathcal{E}_{\text{shifted}}(\tau) = \frac{1}{|\Omega|} \int_{\Omega} [H(X, Y, \tau) - H(X - \Lambda_p, Y, \tau)]^2 \, \mathrm{d}\mathbf{X} \tag{5.23b}$$

The RMS deviation $\mathcal{E}_{\text{rms}}(\tau)$ measures the deviation of the liquid film shape away from the given stationary state $H_{\text{ss}}(X)$, while the shifted deviation $\mathcal{E}_{\text{shifted}}(\tau)$ measures the difference between neighboring ridges. For cases when the liquid film shows relatively large deviation away from the stationary state, if $\mathcal{E}_{\text{shifted}}(\tau)$ remains small, then the liquid film may still exhibit high fidelity patterns which are of practical interests.

The stability of the liquid film can be quantified by $\mathcal{E}_{\text{rms}}(\tau_f)$ and $\mathcal{E}_{\text{shifted}}(\tau_f)$, where the simulation final time τ_f is set to a value much larger than the initial time scale for developing the patterns in the first place. For both 1D and 2D simulations presented in Section 5.4, $\tau_f = 20\tau_{\max}$. Since $\tau_{\max} = 1/\beta(K = K_m)$ is typically larger than the patterning time scale τ_p required to develop non-uniform pattern, $20\tau_{\max}$ is long enough to both ensure the liquid film has reached stationary state if the state is indeed accessible, and if so study the stability of such stationary state.

5.4 Numerical Results

All the numerical results are presented in this section. The parameters are fixed at $\varepsilon_r = 2.5$, $\mathcal{A} = 10^{-3}$ and $\Lambda_p = 2$ $(K_p = \pi)$ [4] unless otherwise specified. For rectangular modulation given by Eq. (5.3b), $w_{\text{rect}} = 0.5$ and $l_{\text{rect}} = 0.02$ unless otherwise specified. The main parameters to be varied are D_0, ϱ and $\mathcal{W}$ [5].

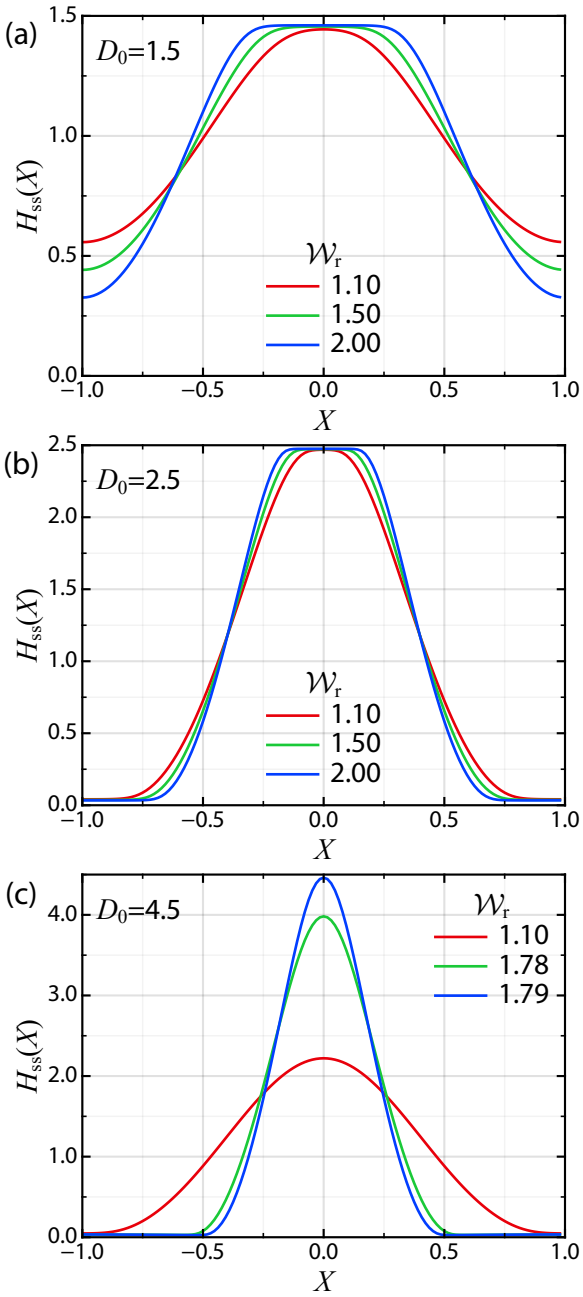

Figure 5.2: Stationary states $H_{\rm ss}(X)$ obtained with flat top electrode ($\varrho = 0$) for (a) $D_0 = 1.5$, (b) $D_0 = 2.5$ and (c) $D_0 = 4.5$. Different colors represent different $\mathcal{W}_r$ indicated in the legend.

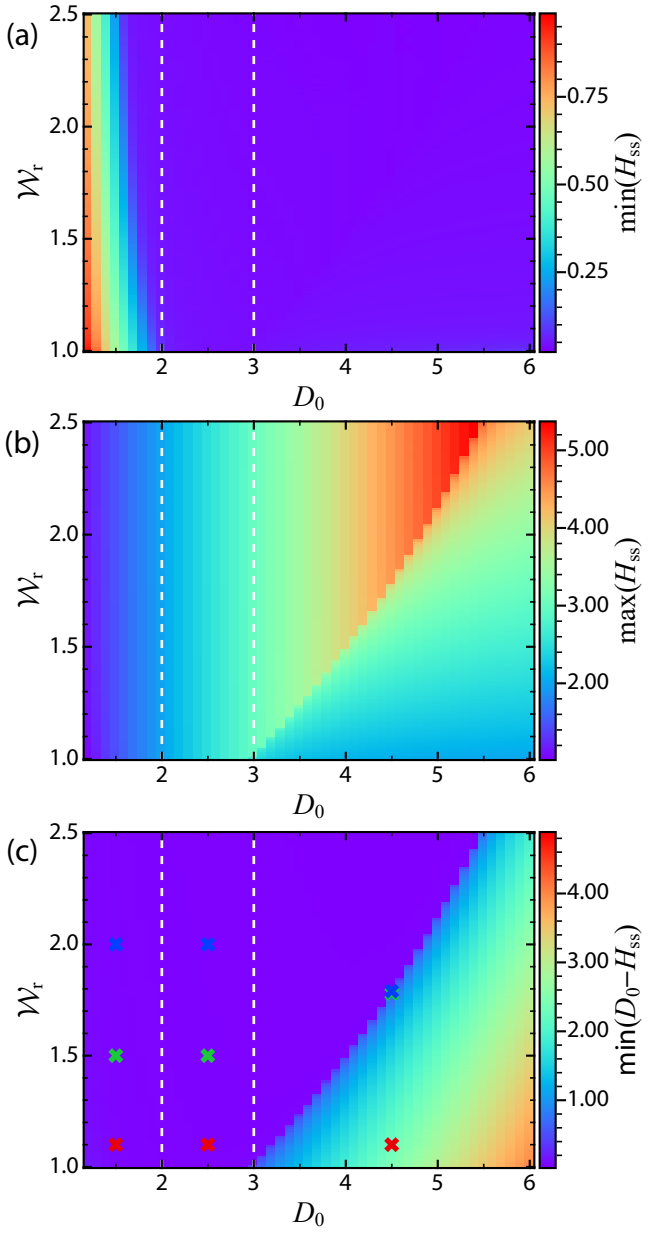

Figure 5.3: Parametric diagram of stationary states $H_{\mathrm{ss}}(X)$ obtained with flat mask ($\varrho = 0$) against different D_0 and $\mathcal{W}_r$. The heat map color represents (a) the minimum liquid film thickness $\min(H_{\mathrm{ss}})$, (b) the maximum liquid film thickness $\max(H_{\mathrm{ss}})$ and (c) the minimum air gap thickness $\min(D_0 - H_{\mathrm{ss}})$. Colored cross symbols in (c) correspond to the parameters of $H_{\mathrm{ss}}(X)$ shown in Fig. 5.2. White vertical dashed lines in all plots separates the three different regimes of stationary states described in the text.

5.4.1 Single ridge with flat electrode ($\varrho = 0$)

We first review the results for un-modulated system (flat mask with $\varrho = 0$) [6] which forms the basis for subsequent discussion on patterned mask ($\varrho > 0$). The two main parameters to be varied are the mean electrode separation D_0 and the electric Weber number $\mathcal{W}$ ($\propto V_0^2$). Results from LSA and weakly-nonlinear analysis show that $H_{\rm ss} = 1$ is stable whenever $\mathcal{W} < \mathcal{W}_c$ ($\mathcal{W}_r < 1$). Therefore, to obtain non-uniform stationary states, we focus on $\mathcal{W} > \mathcal{W}_c$ ($\mathcal{W}_r > 1$).

We can classify the liquid film shape into three different regimes depending on D_0, and the stationary shapes for three different D_0 corresponding to the three regimes are shown in Fig. 5.2. In all three regimes, larger $\mathcal{W}$ results in larger electrostatic stress to deform the liquid film which develops protrusions with taller height (e.g., for $D_0 = 4.5$) or larger contact area with the mask (e.g. for $D_0 = 1.5$ and 2.5) if it touches the top. The three regimes are also separated by the white dashed lines in Fig. 5.3. When the minimum film thickness shown in Fig. 5.3(a) is very small, i.e., $\min(H_{\rm ss}) \sim \mathcal{O}(10^{-2})$, the region between neighboring protrusions or ridges, known as the 'precursor film', is very thin. It does not go to zero due to the repulsive van-der Waals' interaction. On the other hand, when the minimum air gap thickness shown in Fig. 5.3(c) is very small, i.e., $\min(D_0 - H_{\rm ss}) \sim \mathcal{O}(10^{-2})$, the liquid film 'touches' the mask. The separation does not go to zero again due to the repulsive van-der Waals' interaction.

The first regime ($D_0 \lesssim 2.0$) is characterized by a very small minimum air gap thickness $\min(D_0 - H_{\rm ss})$ and relatively large minimum liquid film thickness $\min(H_{\rm ss})$. The stationary state is limited by the geometric constraint imposed by mask, and corresponds to the 'high fill ratio limit' described in Ref [131]. In the second regime ($2.0 \lesssim D_0 \lesssim 3.0$), both $\min(H_{\rm ss})$ and $\min(D_0 - H_{\rm ss})$ are small. The liquid touches the top mask and develops a thin precursor layer near the substrate. In the third regime ($D_0 \gtrsim 3.0$), the liquid film has a thin precursor layer near the substrate, but only touches the top when $\mathcal{W}_r$ exceed a certain threshold for a given D_0. This is apparent from both Fig. 5.3(b) and (c) by the large contrast in color showing the maximum film height and the minimum air gap thickness.

To study the stability of the non-uniform stationary state with a single protrusion against

[4] The characteristic lateral length scale is set at $l_0 = \lambda_p/2$, hence $\Lambda_p = 2$. With this choice of scaling, for a system with $L_x = \Lambda_p$ which consists of a single ridge, the spatial domain varies between $-1 \leq X \leq +1$.

[5] When using PALC to obtain the numerical solutions of the stationary states and eigenmodes, $\mathcal{W}_r$ is the actual variable being varied. For the parameters investigated in this chapter, $0 < \mathcal{W}_r \lesssim 3$. If $\mathcal{W}$ is varied instead, the parameter to be varied can span $\mathcal{O}(10^1 - 10^3)$ which is more challenging for numerical convergence when D_0 is large, and more fine-tuning of the step size in PALC is needed.

[6] Wu et al. [131] first studied the stationary states for EHD patterning *without* spatial modulation where instead of varying the strength of Maxwell stress $\mathcal{W}$ and the electrode separation D_0, they chose the length of the system size as well as the mean film thickness as the parameters to be varied due to a different choice of scalings adopted in that paper.

pressure balance, Eq. (5.21) is solved numerically with $K_x = K_y = 0$. Eq. (5.21) with $K_x = K_y = 0$ always supports a translation mode $H_1 \propto \partial H_{\rm ss}/\partial X$ with zero eigenvalue ($\beta = 0$). This mode is also the eigenmode with the largest growth rate computed numerically, so the system is marginally stable since $\max(\beta) = 0$. When the mask is patterned, the translational symmetry is broken, and β becomes increasingly more negative as ϱ increases.

It can be seen that when stationary state is achieved, the liquid film has to fulfill at least either one of the following conditions: (1) very thin precursor film thickness (small $\min(H_{\rm ss})$) or very thin air gap thickness (small $\min(D_0 - H_{\rm ss})$). For the first condition, the mobility factor $M(H)$ at the precursor film near the substrate is very small, thus fluid flow within the film encounters large resistance. These states can be considered 'mass-limited' as they are unable to grow any further due to difficulty in transporting extra fluid near the precursor film. For the second condition, the liquid film is touching the top, and so further growth of protrusion is suppressed by the geometric confinement of the system. Thus it may be more appropriate to label such states as 'saturated' states since the liquid film has a tendency to grow further if not constrained by the mask.

5.4.2 Single ridge with patterned electrode ($\varrho > 0$)

5.4.2.1 Variation in $\mathcal{W}$

We next study how patterned mask ($\varrho > 0$) affects the non-uniform stationary states in a 1D system with $L_x = \Lambda_p$. Once the stationary solution for one particular set of parameters are obtained, the solutions for other parameters can be obtained efficiently using PALC as described in Section 4.3.1.

It should be pointed out that the stationary states we describe here are not the only possible stationary states. In certain parameter range, other stationary states may exist but those are unstable stables not accessible for a flat liquid film. For example, those states may form protrusions in the region with the largest electrode separation which are unphysical. Those states are not discussed in this chapter.

Fig. 5.4(a) shows the maximum and minimum of the stationary states as a function of $\mathcal{W}_r$ for $D_0 = 2.5$ obtained via PALC. The red dashed line shows the result when $\mathcal{A} = 0$, i.e., no repulsive van-der Waals interaction is present. The deformation amplitude increases with $\mathcal{W}_r$ until $\mathcal{W}_r = \mathcal{W}_{\rm f1}$ when it encounters a fold bifurcation (also known as saddle-node bifurcation), and continuation of the solution branch beyond the fold point becomes possible by using PALC. The solution branch is eventually terminated when either $\min(H_{\rm ss}) \to 0$ for relatively large D_0 or $\max(H_{\rm ss}) \to D_0(1-\varrho)$ for relatively small D_0. The former corresponds to film rupture and the latter corresponds to contact with mask. When repulsive van-der Waals interaction is introduced, i.e., $\mathcal{A} > 0$, then the solution branch can be further continued in PALC beyond the second fold bifurcation

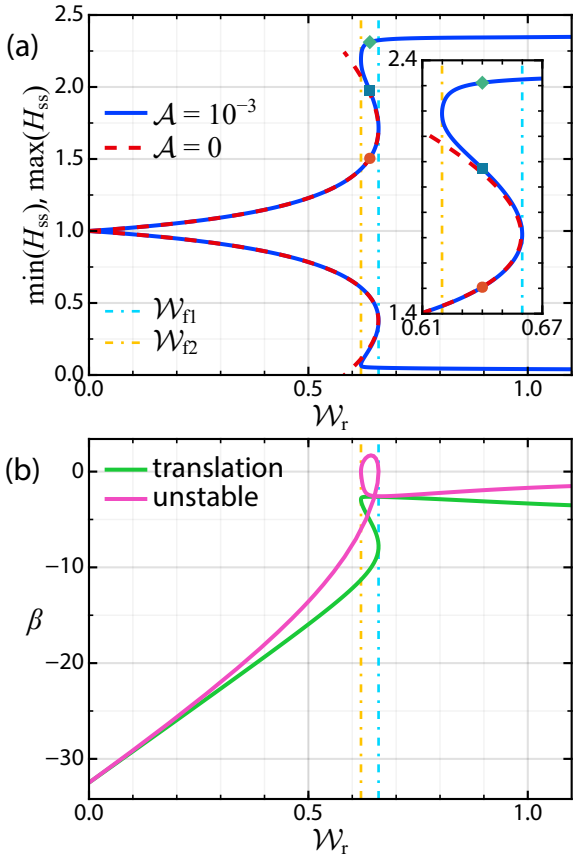

Figure 5.4: Effects of varying $\mathcal{W}_r$ on stationary states' amplitudes and stability for $\varrho = 0.05$ and $D_0 = 2.5$. (a) The maximum and minimum of the liquid film thickness at stationary state ($\max(H_{ss})$ and $\max(H_{ss})$) against $\mathcal{W}_r$ for (i) $\mathcal{A} = 0$ (red dashed lines) and (ii) $\mathcal{A} = 10^{-3}$ (blue solid lines) The two fold points at $\mathcal{W}_r = \mathcal{W}_{f1}$ and $\mathcal{W}_{f2}$ are indicated by vertical dashed lines. The three colored symbols indicate the parameters for the liquid film shapes shown in Fig. 5.5(a). (b) Growth rate β for the (i) translation mode (green) and (ii) unstable mode for vertical growth/shrinkage (pink) against $\mathcal{W}_r$

at $\mathcal{W}_r = \mathcal{W}_{f2}$ to obtain the top solution branch where the liquid film is touching the top mask and form saturated state. It can thus be concluded that the top branch shown in Fig. 5.4(a) for $\mathcal{A} = 10^{-3}$ (blue solid line) can only exist under the presence of intermolecular interaction which prevents film rupture or contact with the substrate and mask. The presence of two fold bifurcations also implies the liquid film develops different stationary states when $\mathcal{W}_{f2} < \mathcal{W}_r < \mathcal{W}_{f1}$ depending on how $\mathcal{W}_r$ is varied. For example, when $\mathcal{W}_r$ is increased from zero, the liquid film likely settles into the small deformation state, while if $\mathcal{W}_r$ is decreased from a large value above $\mathcal{W}_{f1}$, the liquid film likely maintains a large deformation state until $\mathcal{W}_r$ is smaller than $\mathcal{W}_{f2}$. This hysteresis phenomenon was first reported in Ref [139]. From now on we focus solely on the case of $\mathcal{A} > 0$. Detailed parametric studies on how variations in different parameters (e.g.

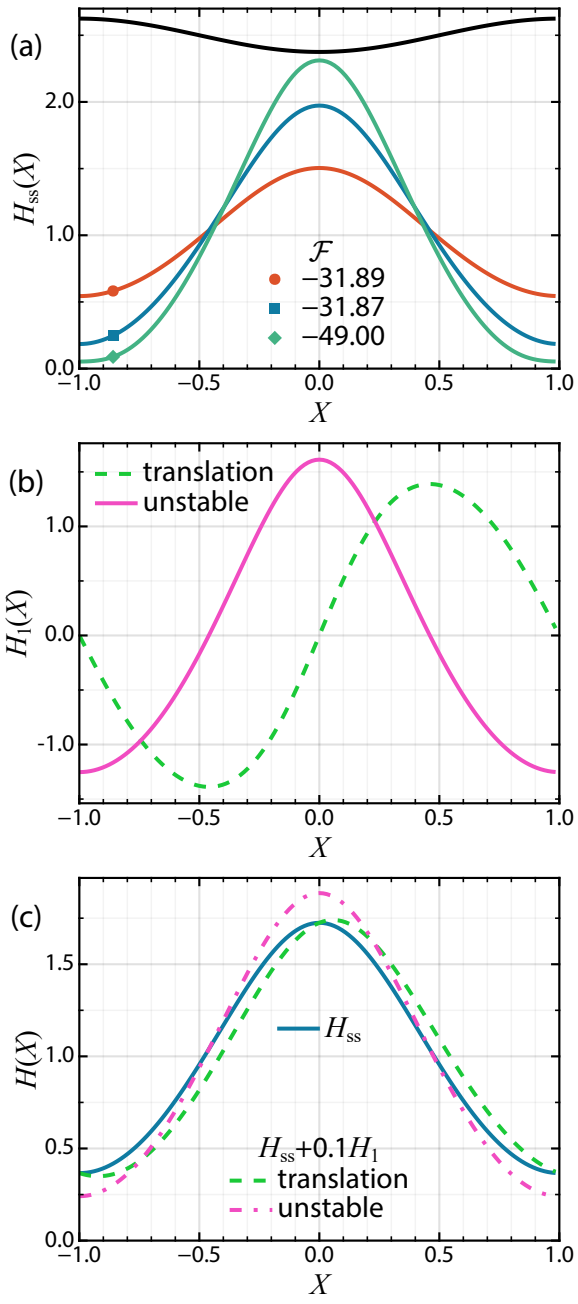

Figure 5.5: Stationary state profiles and corresponding eigenmodes for $D_0 = 2.5$, $\varrho = 0.05$ and $\mathcal{W}_r = 0.64$. (a) The three stationary states $H_{ss}(X)$ for $\mathcal{W}_r = 0.64$. (b) The two most unstable eigenmodes for the stationary state on the unstable branch shown in (a) with blue line. (c) The stationary state superimposed with the eigenmodes to illustrate the fluid flow.

h_0, γ, ε_r) affect the fold bifurcation can be found in Ref [136, 137, 139] and are not discussed any further in this study.

Regarding the stability of stationary states $H_{\mathrm{ss}}(X)$, the translation mode remains stable for all $\mathcal{W}_r$ which can be seen in Fig. 5.4(b). However, another eigenstate representing vertical growth or shrinkage can become unstable in part of the solution branch between $\mathcal{W}_{\mathrm{f2}}$ and $\mathcal{W}_{\mathrm{f1}}$. To further understand the region between $\mathcal{W}_{\mathrm{f2}} < \mathcal{W}_r < \mathcal{W}_{\mathrm{f1}}$, the three stationary states (two stable, one unstable) for $\mathcal{W}_r = 0.64$ are shown in Fig. 5.5(a). The unstable stationary state either grows or decays in amplitude until it reaches one of the other two stable stationary states. The stable translation and unstable growth mode are also shown in Fig. 5.5(b). The unstable stationary state superimposed with the two eigenmodes are shown in Fig. 5.5(c) to better visualize how subsequent fluid flow changes the liquid film shape.

Finally, we also list the Lyapunov free energy $\mathcal{F}$ given by Eq. (2.52) in the figure caption for the three stationary states in Fig. 5.5(a). Notice that the middle unstable stationary state indeed has the largest $\mathcal{F}$ and hence is a local maximum, while the other two stable stationary states have smaller $\mathcal{F}$, and mode showing large deformation and contact with the mask is the global minimum in $\mathcal{F}$. The stability has also been studied in Ref [139] using a heuristic energy argument, and here the same conclusion regarding stability is reached using LSA.

Similar qualitative behaviors, namely the existence of two fold points and a general increase in deformation height against $\mathcal{W}_r$, are also observed for system with larger electrode separation D_0. Larger D_0 requires larger $\mathcal{W}_r$ for the liquid film to approach the patterned mask ($\min(D - H_{\mathrm{ss}}) \to 0$) because more fluid needs to be displaced from the thinned region toward the protrusion tip to reach the patterned mask, which is located further away from the liquid film for large D_0.

5.4.2.2 Variation in ϱ

Next, we investigate the effects of varying the modulation amplitude ϱ. Fig. 5.6(a) shows the structure height $\max(H) - \min(H)$ against $\mathcal{W}_r$ obtained via PALC for different ϱ. As ϱ increases, the interval $\mathcal{W}_{\mathrm{f2}} \leq \mathcal{W} \leq \mathcal{W}_{\mathrm{f1}}$ which supports three stationary states decreases until no fold bifurcations occur. A fold point continuation can be performed at one of the fold points shown in Fig. 5.6(a), with ϱ as the second continuation parameter, and the result is shown in Fig. 5.6(b). The first fold point $\mathcal{W}_{\mathrm{f1}}$ emerges from $\mathcal{W}_r = 1$ at $\varrho = 0$ as expected since $\mathcal{W}_r = 1$ is the bifurcation parameter separating flat and non-uniform stationary states at $\varrho = 0$. As ϱ increases, both fold points approach each other and eventually form a cusp. When ϱ exceeds the value at the cusp, e.g. $\varrho = 0.4$ in Fig. 5.6(a), the structure height always increases with $\mathcal{W}_r$ and no fold bifurcation exists.

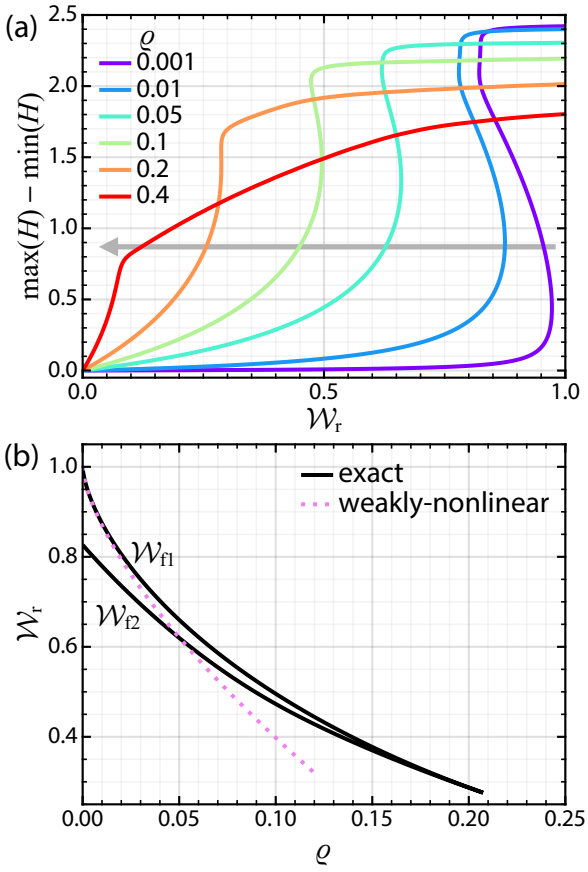

Figure 5.6: Effects of varying the modulation strength ϱ on the amplitudes and bifurcations of the stationary states for $D_0 = 2.5$. (a) Structure height $\max(H_{\rm ss}) - \min(H_{\rm ss})$ against $\mathcal{W}_r$ for different modulation amplitude ϱ. Arrow indicates results for increasing ϱ. (b) The cusp bifurcation exhibited by the two fold points $\mathcal{W}_{\rm f1}$ (upper branch) and $\mathcal{W}_{\rm f2}$ (lower branch) as ϱ is varied. Pink dashed line is the weakly-nonlinear prediction given by Eq. (5.16).

The prediction of the critical modulation amplitude $\varrho^*_{\rm wna}$ given by Eq. (5.16) from weakly-nonlinear analysis is also plotted in Fig. 5.6(b) for comparison. It can be seen that it agrees with the exact numerical solution reasonably well when $\mathcal{W}_r \approx 1$ (i.e., $\mathcal{W} \approx \mathcal{W}_c$). As $\mathcal{W}_r$ deviates from 1 (i.e., $\mathcal{W}$ deviates from $\mathcal{W}_c$), the agreement worsens as expected because the assumption $\mathcal{W} \approx \mathcal{W}_c$ no longer holds.

5.4.2.3 Comparison with analytical theory

Here we compare the analytical results derived in Section 5.2 to the exact numerical solutions. The structure height $\max(H_{\rm ss}) - \min(H_{\rm ss})$ against $\mathcal{W}_r$ for $D_0 = 2.5$ and $\varrho = 0.01$ obtained via PALC is shown as black solid in Fig. 5.7(a) for reference. The linear solution $2\Delta H_{\rm lin}$ from Eq. (5.9) is shown as yellow dash-dotted line and shows excellent

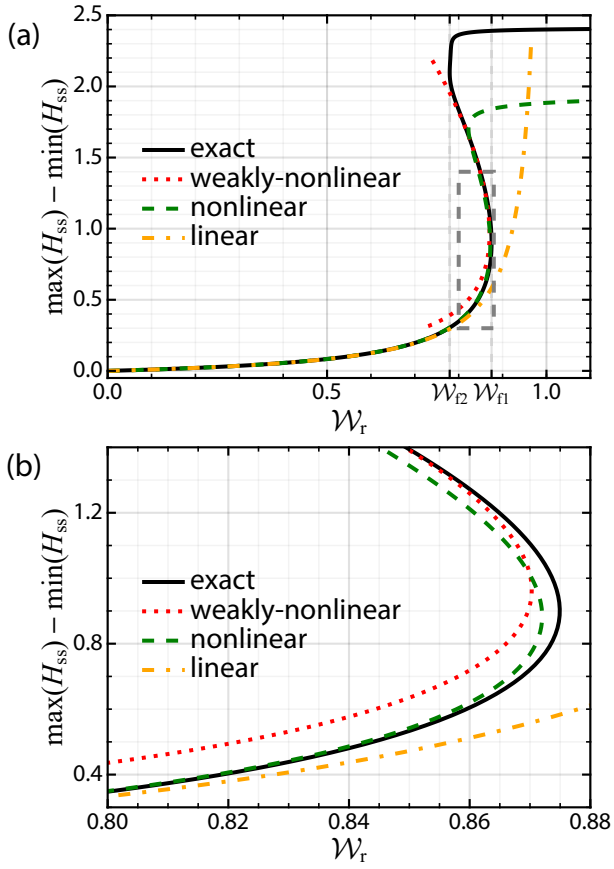

Figure 5.7: Comparison of the structure height $(\max(H_{ss}) - \min(H_{ss}))$ against $\mathcal{W}_r$ calculated by different methods. Parameters: $D_0 = 2.5$, $\varrho = 0.01$. (i) exact numerical solution (black solid line) by solving Eq. (5.17), (ii) linear approximation (orange dash-dotted line) by solving Eq. (5.9), (iii) weakly-nonlinear approximation (red dotted line) by solving Eq. (5.12), and (iv) nonlinear approximation (green dash line) by solving Eq. (5.24). The magnified view near the first fold point is shown in (b).

agreement with the exact numerical solution when ΔH_{lin} is small. As $\mathcal{W}_r \to 1$, ΔH_{lin} diverges since the linear theory does not predict the existence of fold point as $\mathcal{W} \to \mathcal{W}_{\text{f1}}$ and ΔH_{lin} can increase without bound.

The weakly-nonlinear solution derived from solving Eq. (5.12) is shown as red dotted line. It predicts the first fold point reasonably well for small ϱ as already discussed in Fig. (5.2.2). Surprisingly, it predicts the amplitude more accurately for the unstable middle branch than the bottom stable branch, though which solution branch shows better agreement seems to depend on the value of D_0, as well as the bifurcation parameter chosen for the multi-scale expansion (e.g., expanding K_p instead of $\mathcal{W}$).

We also consider a simplified non-linear estimate of the deformation amplitude which was first carried out in [57]. For a patterned mask given by $D(X) = D_0\,[1 + \varrho\cos(K_p X)]$,

we can approximate the liquid film shape as $H(X) \approx 1 - \Delta H \cos(K_p X)$. Equating the stationary state condition given by Eq. (5.17) at the liquid film maximum and minimum gives

$$-K_p^2 \Delta H + \Pi(H^+, D^-) = K_p^2 \Delta H + \Pi(H^-, D^+), \tag{5.24}$$

where $H^\pm = 1 \pm \Delta H$ and $D^\pm = D_0(1 \pm \varrho)$ are the maximum and minimum values of the liquid film and patterned mask.

Eq. (5.24) is solved using PALC, and the corresponding structure height $2\Delta H$ is shown in Fig. 5.7 as green dash line. It predicts the presence of both fold points with reasonably good accuracy for the first fold point at $\mathcal{W}_r = \mathcal{W}_{\mathrm{f1}}$, showing that a simple consideration of pressure balance is sufficient to elucidate the qualitative features of how the ΔH varies with $\mathcal{W}_r$. It fails to accurately predict the structure height for the upper stable branch, because the assumption of a sinusoidal shape limits the maximum deformation amplitude to 1 and the actual stationary state shapes differ considerably from the simple assumption of sinusoidal shape.

5.4.3 Multiple ridges in 1D system

In the previous section, we studied the stationary states and stability of the liquid film in a system with size $L_x = \Lambda_p$, neglecting any possible interactions involving multiple protrusions. In this section, we first study the instability of a 1D system with size $L_x = \Lambda_p$ against perturbations with different wave number K_x by solving Eq. (5.21) with $K_y = 0$. Phenomena involving multiple protrusions such as coalescence can be taken into account by allowing K_x to vary between 0 and $K_p/2$. We then perform time-dependent simulations of Eq. (5.1) in a large system with $L_x = 16\Lambda_p$ to study the spatiotemporal evolution of a liquid film supporting multiple protrusions.

5.4.3.1 Dispersion relations $\beta(K_x)$

By solving Eq. (5.21) and varying K_x using PALC, the dispersion relation $\beta(K_x)$ for increasing $\mathcal{W}_r$ at fixed $D_0 = 2.5$ and $\varrho = 0.05$ is shown in Fig. 5.8. Fig. 5.8(a) and (b) show dispersion relations of the two most unstable modes. The single protrusion case studied in Section 5.4.2 corresponds to setting $K_x = 0$, and it can immediately be seen that while $\beta(K_x = 0)$ is non-positive for all $\mathcal{W}_r$ for both modes, $\beta(K_x > 0)$ can become positive for certain values of $\mathcal{W}_r$ and K_x, showing that even if a single protrusion is stable against vertical growth or shrinkage by considering pressure balance, it can still go unstable due to interactions with neighboring protrusions. Due to symmetry, $\beta(K_x) = \beta(-K_x)$, so the other half of the dispersion diagram is not shown.

The first mode shown in Fig. 5.8(a) is similar to type II instability for flat mask at small $\mathcal{W}_r$ except $\beta(K_x = K_p/2)$ attains a local extremum due to the imposed periodicity.

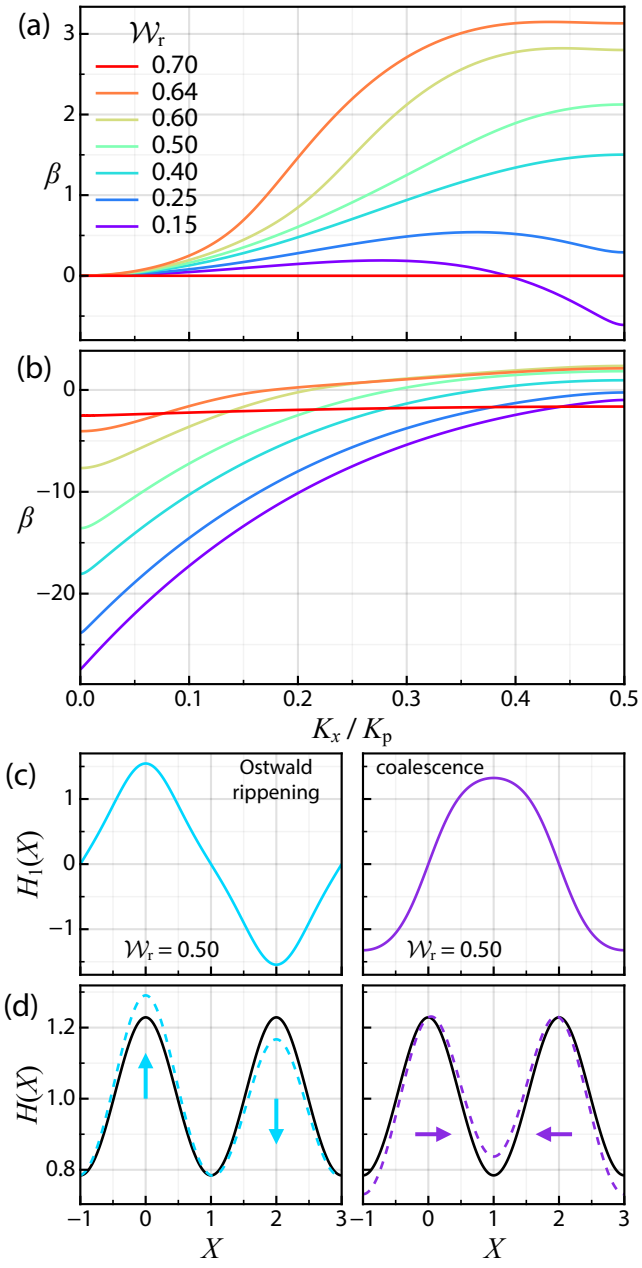

Figure 5.8: Floquet-Bloch LSA of a 1D system with size $L_x = \Lambda_p$ for $D_0 = 2.5$ and $\varrho = 0.05$. (a)-(b): The dispersion relation $\beta(K_x)$ for different $\mathcal{W}_r$ obtained by solving Eq. (5.21) for the two most unstable modes. (c): The eigenmode $H_1(X) = \text{Re}[\hat{H}_1(X)e^{iK_xX}]$ for $K_x = K_p/2$ and $\mathcal{W}_r = 0.5$ for the Ostwald ripening mode (left column in cyan) and the coalescence mode (right column in purple). (d): The stationary state $H_{\text{ss}}(X)$ (black solid line) superimposed with the eigenmodes $H_{\text{ss}}(X)+0.04H_1(X)$ (colored dashed lines) for the Ostwald ripening mode (left column in cyan) and the coalescence mode (right column in purple). Arrows indicate the movement of the two protrusions. For both (c) and (d), the spatial domain is extended to $L_x = 2\Lambda_p$ for visualizing the eigenmodes.

For $\mathcal{W}_r = 0.15$, β attains maximum at $K_x \approx 0.3K_p$, suggesting that the most unstable mode involves interactions involving ~ 3 protrusions. As $\mathcal{W}_r$ increases, $\max(\beta)$ also increases and the corresponding fastest growing wave number shifts toward $K_p/2$. This suggests the most unstable mode for sufficiently large $\mathcal{W}_r$ involves interaction with the nearest neighboring protrusion. When $\mathcal{W}_r$ is further increased to 0.7, $\beta(K_x) \leq 0$ for all K_x, which imply that a large enough $\mathcal{W}_r$ can stabilize the stationary state.

The second most unstable mode shown in Fig. 5.8(b) always has a negative growth rate at $K_x = 0$, and β increases with K_x until it attains maximum at $K_x = K_p/2$. Similar to the first mode, $\max(\beta)$ becomes larger as $\mathcal{W}_r$ increases, until a large enough $\mathcal{W}_r$ is achieved when $\beta(K_x) < 0$ for all K_x.

To understand the physical mechanism of the two modes, their eigenstates $H_1(X)$ at $\mathcal{W}_r = 0.5$ and $K_x = K_p/2$ are shown in Fig. 5.8(c). The stationary states superimposed with the eigenmodes, i.e., $H_{\text{ss}}(X) + 0.1H_1(X)$, are plotted in Fig. 5.8(d) to illustrate the movement of the protrusions. We can see that the first mode shown in the left column corresponds to one protrusion growing in size at the expense of the neighboring one, which is analogous to the phenomenon of Ostwald ripening [7]. The second mode shown in the right column corresponds to both protrusions approaching each other to coalescence or merge mid-way between the two [8]. We note that the dispersion relations $\beta(K_x)$ shown in Fig. 5.8(a) and (b) do not always strictly correspond to Ostwald ripening and coalescence modes, respectively. When $K_x = K_p/2$, the two modes are swapped at $\mathcal{W}_r = 0.6$ and 0.64 because the two dispersion curves cross at intermediate value of K_x. It is also difficult to draw a direct analogy to Ostwald ripening and coalescence involving two protrusions when $K_x < K_p/2$ because the corresponding length scale of the mode given by $2\pi/K_x$ involves more than two protrusions. Nevertheless, the Ostwald ripening and coalescence modes involving two protrusions (i.e., at $K_x = K_p/2$) provide an intuitive picture of the fundamental destabilization mechanism when more than one protrusion is present.

5.4.3.2 Stability phase diagram

Next, we study the conditions for achieving high fidelity patterns and present the results as a phase diagram by finding the values of $\mathcal{W}_r$ and ϱ where $\max(\beta) \leq 0$. The results shown in Fig. 5.9 and 5.11 consist of three different types of information:

[7] The original phenomenon of Ostwald ripening refers to a two-phase mixture where the second phase is dispersed in a matrix. The total energy of the system can be decreased by increasing the size scale (i.e., decreasing the total interfacial area) of the second phase [129]. Many pattern-forming systems [11, 45, 131] show qualitatively similar phenomenon where the size of a protrusion or mesa increases at the expense of neighboring one, and have borrowed the term 'Ostwald ripening' to describe such phenomena. The term 'mass competition' is also sometimes used in literature to describe this mode.

[8] Also sometimes called 'collision' mode in literature.

1. The background grayscale heatmap shows the minimum liquid film thickness $\min(H_{\text{ss}})$ and the minimum air gap thickness $\min(D - H_{\text{ss}})$. It tells us whether the ridges formed by the liquid film touches the mask as indicated by small $\min(D - H_{\text{ss}})$ or develops very thin precursor as indicated by small $\min(H_{\text{ss}})$.

2. The lines represent the contours where the local extremum at $\beta(K_x = K_p/2)$ reaches zero for the two most unstable modes illustrated in Fig. 5.8. They are obtained using the method outlined in Ref [54] and is briefly summarized as follow:

   We begin with an 'inverted' dispersion relation where instead of solving for $\beta(K_x)$ as in Fig. 5.8(a), we solve for $K_x(\beta)$ by treating β as the independent variable (i.e., the parameter to be varied in PALC) and the wave number K_x as the dependent variable when solving for the set of nonlinear equations consisting of Eq. (5.17) and (5.21). The maximum in the dispersion relation $\beta(K_x)$ shown in Fig. 5.8(a) and 5.13(a) then becomes a fold point when expressed as $K_x(\beta)$, and the corresponding independent variable represents the maximum growth rate $\beta = \max(\beta)$. A fold point continuation can then be performed at such fold point, varying β as the first parameter and $\mathcal{W}$ as the second parameter. When the results are expressed as $\beta(\mathcal{W})$, we can then find the value of $\mathcal{W}$ when β (i.e., $\max(\beta)$) approaches a small number $\beta = \beta_{\text{zero}}$ where $|\beta_{\text{zero}}| \ll 1$ (typically 10^{-5}). A second fold point continuation is performed by fixing $\beta = \beta_{\text{zero}}$, varying $\mathcal{W}$ as the first parameter and ϱ as the second parameter. The corresponding $\mathcal{W}$ and ϱ of the solution branch are then plotted in the phase diagram, and they represent solutions with $\max(\beta) = \beta_{\text{zero}} \approx 0$. The maximum growth rate is positive on one side of the contour, and negative on the other side.

   For the coalescence mode, $\max(\beta)$ always occurs at $K_x = K_p/2$, so tracking the local extremum at $\beta(K_x = K_p/2)$ is equivalent to tracking the maximum growth rate, and the purple line truly represents the stability threshold. For the Ostwald-ripening mode, we find that tracking the local extremum at $K_x = K_p/2$, which is not necessarily equal to the global maximum for small $\mathcal{W}_r$, seems to less likely lead to numerical convergence issue when performing PALC. As a result, the cyan line strictly represents the parameters for $\beta(K_x = K_p/2) = 0$, but for sufficiently large $\mathcal{W}_r$, it does approximates the stability threshold.

3. The symbols are the results of time-dependent simulation grouped into four categories depending on the stability and pattern fidelity of the non-uniform shapes formed by the liquid film:

   - Inaccessible: $\mathcal{E}_{\text{rms}}(\tau) \geq 0.01 \;\forall\; 0 \leq \tau \leq \tau_f$

     An initially flat (but randomly perturbed) liquid film never evolves into the predicted stationary state, i.e., the initial state of the liquid film does not fall

within the basin of attraction of the stationary state.

- Stable: $\mathcal{E}_{\text{rms}}(\tau_f) \leq 0.01$

  The liquid film does evolve into the predicted stationary state, and remain at such state up to τ_f. While this does not necessarily prove that the stationary state is asymptotically stable at very late time since the arbitrarily chosen τ_f may not be large enough, it does show that a high fidelity pattern can be obtained at a time relatively long compared to the initial time for forming patterns.

- Unstable: $\mathcal{E}_{\text{rms}}(\tau) \leq 0.01$ for some τ, but $\mathcal{E}_{\text{rms}}(\tau_f) \geq 0.01$.

  The liquid film does evolve into the predicted stationary state, but destabilize at some later time which results in large RMS deviation at time τ_f. This corresponds to a saddle point in the high-dimensional solution space where it is stable along certain directions (e.g., from initially flat film to non-uniform stationary state) but unstable along the others (e.g., from non-uniform stationary states with the same periodicity as the patterned mask to some other states with coalescenced protrusions).

Note that the above classification is only based on the liquid film shape at a *finite* time $\tau = \tau_f = 20 \times \tau_{\max}$ from time dependent simulations with a specific size of the spatial domain and initial condition given by Eq. (4.9).

Small D_0 ($D_0 = 2.5$) Fig. 5.9 shows the stability phase diagram for 1D sinusoidal modulation in a 1D spatial domain for $D_0 = 2.5$. We can roughly divide the phase diagram into two regions: the small deformation regime (dark background color) and the large deformation regime (light background color). The small deformation regime is characterized by large precursor film thickness between neighboring ridges (i.e., large $\min(H_{\text{ss}})$) and large air gap above the ridges (i.e., large $\min(D - H_{\text{ss}})$), while the large deformation regime is characterized by small air gap and small precursor film thickness (except at large ϱ where geometric constraint prevents the thinning of liquid film).

The purple solid line represents the stability contour for the coalescence mode computed by PALC where $\max(\beta) = 0$. Parameters inside the enclosed region have $\max(\beta) > 0$ and hence unstable, while those outside are stable. The cyan solid line represents the stability contour for the Ostwald ripening mode where $\beta(K_x = K_p/2) = 0$. The region below the bottom branch (i.e., small $\mathcal{W}_r$) is unstable as $\beta(K_x) > 0$ for some nonzero $0 < K_x < K_p$ (e.g., $\mathcal{W}_r = 0.15$ in Fig. 5.8(a)). This represents destabilization via interactions involving multiple protrusions. The region enclosed by the cyan line represents parameters where $\beta(K_x = K_p/2) > 0$ (e.g., $\mathcal{W}_r = 0.5$ in Fig. 5.8(a)), which corresponds to Ostwald ripening with two neighboring protrusions and is also unstable. The region above the top branch corresponds to the stable region where

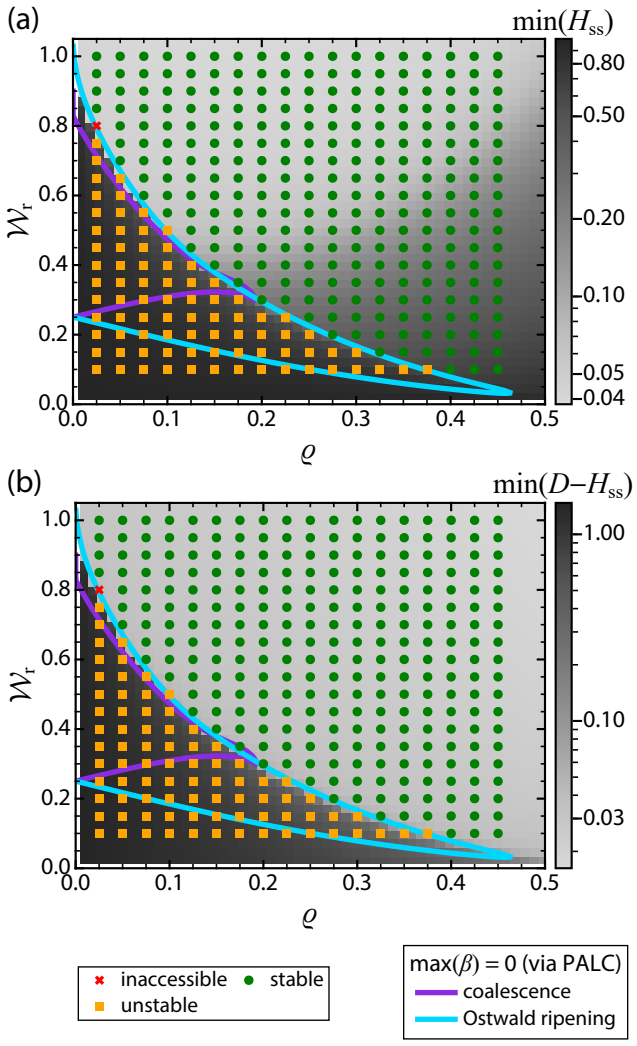

Figure 5.9: Stability phase diagram for 1D system with $D_0 = 2.5$. Cyan and purple lines denote Ostwald ripening and coalescence modes with $\beta(K_x = K_p/2) = 0$ computed by PALC. Background heat map colors represents (a) minimum liquid film thickness $\min(H_{\rm ss})$ and (b) minimum air gap thickness $\min(D - H_{\rm ss})$ in logarithmic scale. Symbols denote unstable (orange square) and stable (green circle) states evaluated at $\tau = \tau_f = 20\tau_{\rm max}$. The phases are classified based on $\min(\mathcal{E}_{\rm rms}(\tau))$ and $\mathcal{E}_{\rm rms}(\tau_f)$ (see main text for descriptions) averaged across 5 independent realizations for each parameter. Note that the state at $\varrho = 0.05$ and $\mathcal{W}_r = 0.8$ is classified as inaccessible within the time frame of the simulation because it takes a very long time for the liquid film to reach the stationary state which is located very close to the fold point at $\mathcal{W}_r = \mathcal{W}_{\rm fl}$.

$\beta(K_x) < 0 \ \forall \ K_x$ (e.g., $\mathcal{W}_r = 0.7$ in Fig. 5.8(a)). We can see that since the region enclosed by the purple line mostly resides within the region enclosed by the cyan line, the stability is mainly governed by the Ostwald ripening mode except at the very small region near $(\varrho, \mathcal{W}_r) = (0.15, 0.35)$ where the coalescence mode is unstable while Ostwald ripening mode is stable. The top branch of the cyan line also divides the small and large deformation regimes depicted by the grayscale heatmap. This shows that for the Ostwald ripening mode to be stable requires liquid film contact with the patterned mask.

To further study the nonlinear dynamics of the liquid film and corroborate the results of LSA, Eq. (5.1) is solved numerically with a randomly perturbed flat film as the initial condition in a large 1D domain with $L_x = 16\Lambda_p$. The symbols show the classification of the state of the liquid film based on $\mathcal{E}_{\text{rms}}(\tau)$ averaged across five independent realizations for each set of $(\varrho, \mathcal{W}_r)$. The 'stable' states only occur for the large deformation regime, while the 'unstable' states fall into the small deformation regime. Fig. 5.10 shows two particular examples with $\varrho = 0.1$ but different $\mathcal{W}_r$: (a) one below and (b) one above the cyan line. When $\mathcal{W}_r = 0.4$, the liquid film develops ridges with amplitude of roughly 0.3, and the ridges then destabilize via the Ostwald-ripening mode where some ridges grow in size while neighboring ones shrink. Also notice that the positions of the ridges, i.e., the X coordinate of the liquid film maximum, remain the same at all time. If two neighboring ridges destabilize via coalescence mode instead, then new ridges will be formed between the two original ridges. For $\mathcal{W}_r = 0.55$, the liquid film develops ridges with large deformation that touch the top patterned mask, and high fidelity pattern is maintained throughout the whole simulation.

Combining the results from both LSA and time-dependent simulations shows that for relatively small electrode separation ($D_0 = 2.5$), the necessary condition for obtaining high fidelity patterns is for the liquid film to develop large deformation and touch the patterned mask such that the liquid film can no longer grow any further. As noted previously, these states are more appropriately described as 'saturated states' due to the constraint on the allowable space to grow.

Large D_0 ($D_0 = 5.0$) The stability phase diagram for a system with larger electrode separation, i.e., $D_0 = 5.0$, is shown in Fig. 5.11. The region enclosed by the purple line is the unstable parameter range for the coalescence mode, and is qualitatively very similar to that for $D_0 = 2.5$. The cyan line is the contour where $\beta(K_x = K_p/2) = 10^{-2}$ for the Ostwald ripening mode. in the region enclosed by the cyan line, the maximum growth rate of the Ostwald ripening is $10^{-2} > \max(\beta) > 0$. Outside the top branch of the cyan line (i.e., for large $\mathcal{W}_r$), the maximum growth rate becomes negative. Fig. 5.12 shows the spatiotemporal evolution of the liquid film for $\varrho = 0.2$ but different $\mathcal{W}_r$. We can classify the phase diagram into roughly three regions:

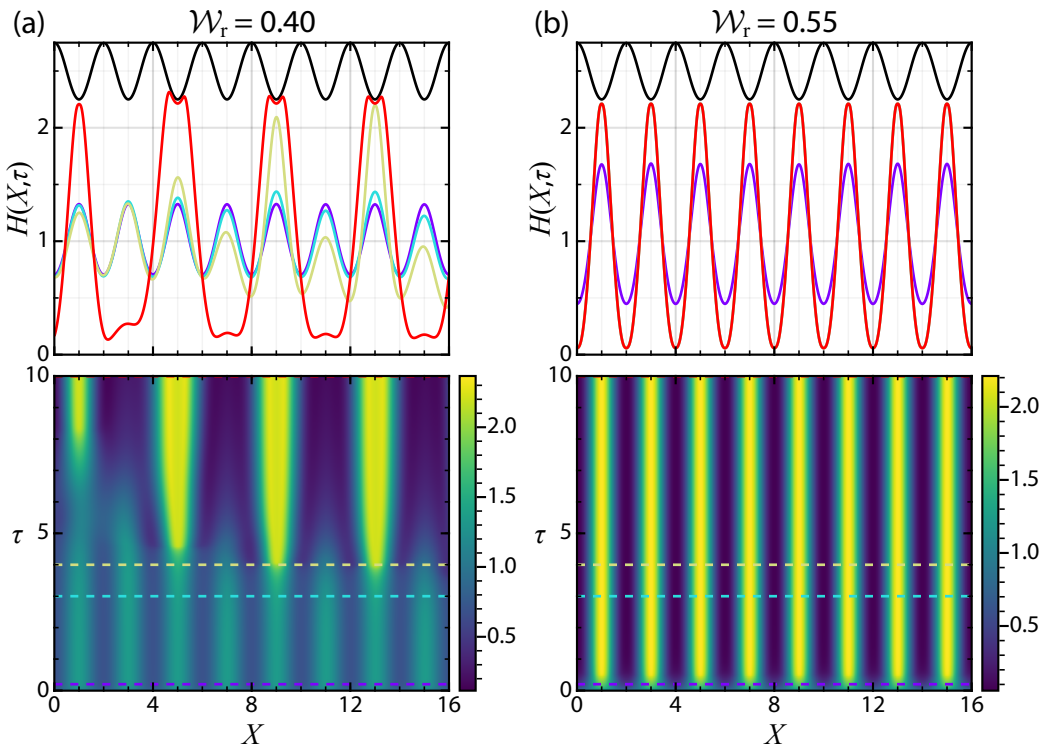

Figure 5.10: Selected snapshots of liquid film shape $H(X,\tau)$ at $\tau = 0.2, 3, 4, 10$ for (a) $\mathcal{W}_r = 0.4$ and (b) $\mathcal{W}_r = 0.55$. Parameters: $D_0 = 2.5$, $\varrho = 0.1$, $L_x = 16\Lambda_p = 32$. In the top figure of (a), (b) and (c), solid lines with different colors represent $H(X,\tau)$ at different time. The bottom figure of (a), (b) and (c) shows the 'bird-eye' view of the liquid film's spatiotemporal evolution. The colored horizontal dash lines indicate the time where the liquid film shape is shown in (a) and (b). Note that only half of spatial domain is shown.

1. The first regime corresponds to stationary states with small deformation with relatively thick precursor film (i.e., large $\min(H_{\rm ss})$ in Fig. 5.11(a)) and does not touch the patterned mask (i.e., large $\min(D - H_{\rm ss})$ in Fig. 5.11(b)). The orange square symbols in that region show that the liquid film shape at $H(X,\tau_f)$ is classified as unstable because of the large RMS deviation signifying significant departure from the stationary shapes. Fig. 5.12(a) shows an example with $\varrho = 0.2$ and $\mathcal{W}_r = 0.25$. The liquid film develops ridges with amplitude of roughly 0.7, but then destabilizes via the Ostwald-ripening mode at a later time and shows noticeable deviation from the stationary state at $\tau = 34$.

2. The second regime corresponds to stationary states with large deformation that do not touch the patterned mask. This is the region enclosed by the cyan line with small $\min(H_{\rm ss})$ and large $\min(D - H_{\rm ss})$. While the maximum growth rate for the Ostwald ripening mode is still positive (but smaller than 10^{-2}), time-dependent simulations show that liquid film shape $H(X,\tau_f)$ still closely resembles

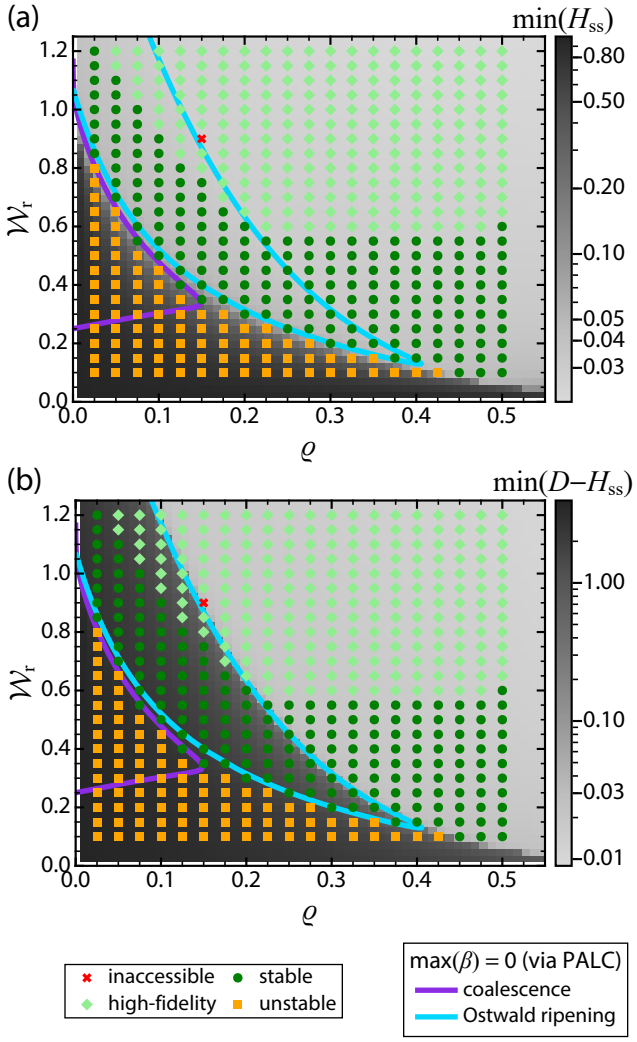

Figure 5.11: Stability phase diagram for 1D system with $D_0 = 5.0$. Purple line denotes coalescence mode with $\beta(K_x = K_p/2) = 0$, while cyan line denotes Ostwald ripening mode with $\beta(K_x = K_p/2) = 10^{-2}$. Background heat map colors represents (a) minimum liquid film thickness $\min(H_{ss})$ and (b) minimum air gap thickness $\min(D - H_{ss})$ in logarithmic scale. Symbols denote inaccessible (red cross), unstable (orange square), stable (green circle) and 'high fidelity' (light green circle) states evaluated at $\tau = \tau_f = 20\tau_{max}$. The phases are classified based on $\min[\mathcal{E}_{rms}(\tau)]$, $\mathcal{E}_{rms}(\tau_f)$ and $\mathcal{E}_{shifted}(\tau_f)$ (see main text for descriptions) averaged across 5 independent realizations for each parameter.

the stationary state shapes with $\mathcal{E}_{\rm rms}(\tau_f) < 0.01$. Fig. 5.12(b) shows an example with $\varrho = 0.2$ and $\mathcal{W}_r = 0.4$. The liquid film develops ridges with large deformation and a very thinned layer of precursor film between neighboring ridges. The patterns persist for a long time up to $\tau = 34$, which is significantly longer than the time scale of $\mathcal{O}(0.1)$ that it takes to develop the ridges in the first place. Thus, the stationary states in the regime can still be classified as at least 'quasi-stable' with the possibility of being solidified in experiments. If the numerical simulation is run for a longer time, the protrusions again destabilize via Ostwald ripening mode, though it occurs at a much longer time scale (e.g., $\tau \sim \mathcal{O}(10^3 - 10^4)$) compared to the time for forming the protrusions in the first place.

3. The third regime corresponds to stationary states with large deformation that does touch the patterned mask. This is region above the top branch of the cyan line with small $\min(H_{\rm ss})$ and small $\min(D - H_{\rm ss})$. Time dependent simulations show that an initially flat (but randomly perturbed) liquid film evolves toward the predicted stationary state where the dark green circle symbols denote $\mathcal{E}_{\rm rms}(\tau_f) < 0.01$.

   The light green circle symbols denote states where $\mathcal{E}_{\rm rms}(\tau_f) > 0.01$ but $\mathcal{E}_{\rm shifted}(\tau_f) < 0.01$. They are classified as 'high-fidelity' in the phase diagram as it takes a long time to reach the stationary states (hence the large $\mathcal{E}_{\rm rms}(\tau_f)$), but they still exhibit high degree of spatial uniformity as indicated by the small $\mathcal{E}_{\rm shifted}(\tau_f)$. Fig. 5.12(c) shows an example with $\varrho = 0.2$ and $\mathcal{W}_r = 0.8$, and (d) is a magnified view of (c). It is clear that up to $\tau = 34$, the ridges developed by the liquid film still exhibits high degree of spatial uniformity, but further inspection of the precursor film region in Fig. 5.12(d) shows that it takes a much longer time scale for the liquid film to reach the stationary state with a flattened profile. This explains the relatively large $\mathcal{E}_{\rm rms}(\tau_f)$ for some parameters in this regime despite the overall patterns still exhibiting high pattern fidelity. These are also the truly stable (saturated) states where the protrusions persist up to at least $\tau \sim \mathcal{O}(10^4)$ from time-dependent simulations with much larger τ_f. This is consistent with the fact that the Ostwald ripening mode is stable.

While the results from LSA and time-dependent simulations with much longer τ_f (not shown here) suggest contact with the patterned mask is still required for the Ostwald ripening mode to become truly stable ($\max(\beta) < 0$), when combined with the results of time-dependent simulations, the necessary condition for the liquid film to form quasi-stable patterns whose shape can be maintained up to a long time for relatively large electrode separation ($D_0 = 5.0$) is the thinning of the precursor film layer. This can be understood by the small mobility factor in the thinned region which inhibits fluid flow among neighboring protrusions necessary for destabilization. As previously mentioned, these stationary states may be more accurately described as 'mass-limited' states since

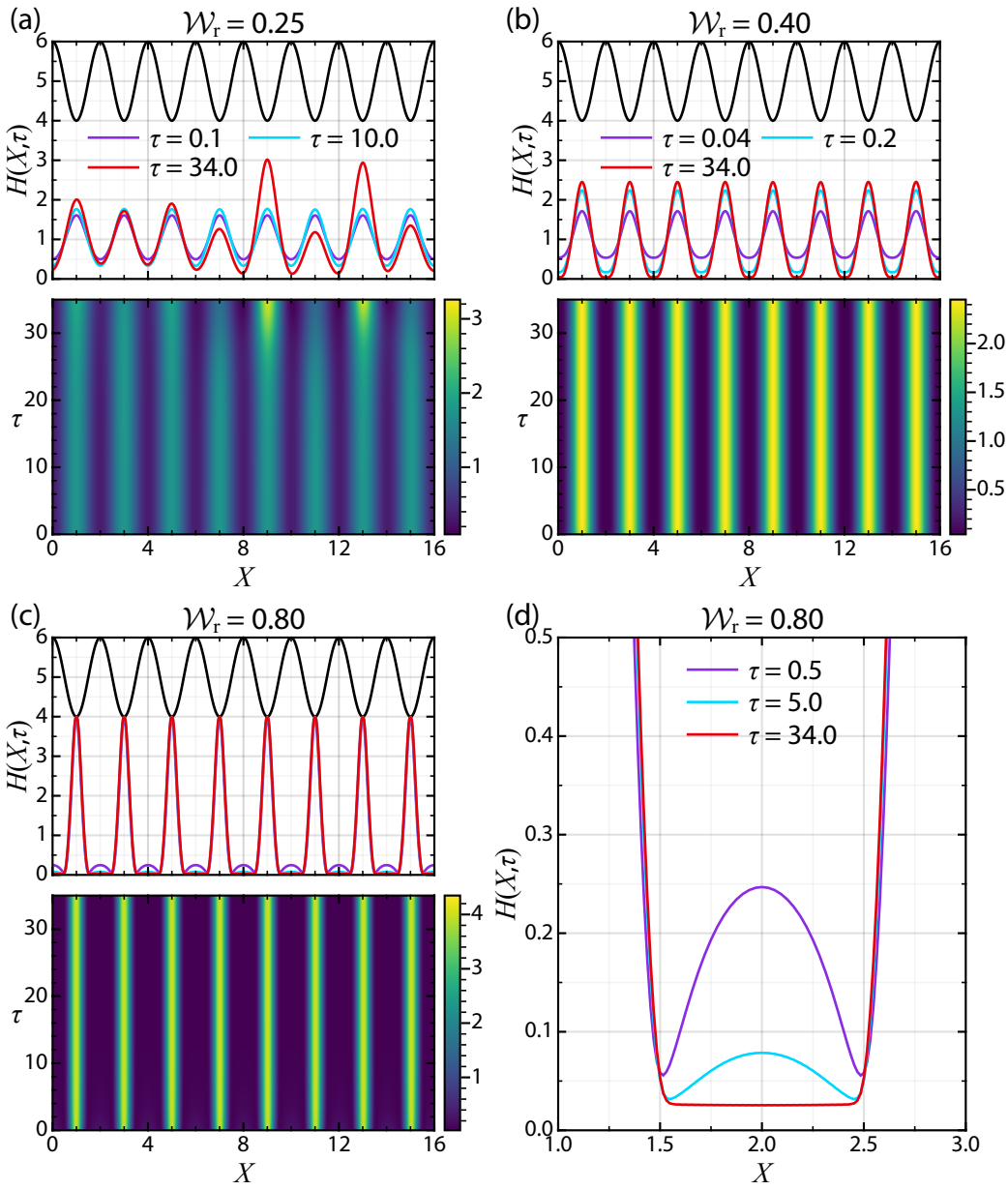

Figure 5.12: Selected snapshots of liquid film shape $H(X,\tau)$ obtained with large electrode separation. Parameters: $D_0 = 2.5$, $\varrho = 0.2$, $L_x = 16\Lambda_p = 32$. (a) $\mathcal{W}_r = 0.25$, (b) $\mathcal{W}_r = 0.4$ and (c) $\mathcal{W}_r = 0.8$. In the top figure of (a), (b) and (c), solid lines with different colors represent $H(X,\tau)$ at different time. The bottom figure of (a), (b) and (c) shows the 'bird-eye' view of the liquid film's spatiotemporal evolution. Note that only half of spatial domain is shown. (d) is a magnified view of (c) near the thinned precursor film region.

further growth of the ridges is limited by the supply of fluid near the thinned precursor layer.

5.4.4 Multiple ridges in 2D system

In this section, the stability of parallel stripes are studied in a full 2D system by allowing the liquid film to vary along the Y direction, $H = H(X, Y, \tau)$.

5.4.4.1 Dispersion relation $\beta(K_y)$

The dispersion relation $\beta(K_x)$ shown in Fig. 5.8 suggests that stability is usually determined at relatively large $\mathcal{W}_r$ where the maximum growth rate occurs at $K_x = K_p/2$. This corresponds to interactions involving only two ridges in a system with size $2\Lambda_p$. Building upon this observation, we study the stability of the stationary states against perturbations along the Y direction (with nonzero K_y) by analyzing a simplified system of two parallel ridges in a 2D system with size $L_x = 2\Lambda_p$ and $K_x = 0$. While a 2D periodic system with two ridges is inherently different from a much larger system with many ridges that is commonly studied experimentally, studying such a simplified system involving only two ridges still provides valuable insights into the stability of two neighboring ridges and forms the basis for more complicated phenomena, but at a much lower computational cost.

By solving Eq. (5.17) and (5.17) for $L_x = 2\Lambda_p$, we can obtain the four most unstable modes which are the symmetric/asymmetric varicose and zigzag modes. Their dispersion relations $\beta(K_y)$ for $D_0 = 2.5$, $\mathcal{W}_r = 0.5$ and $\varrho = 0.05$ are shown in Fig. 5.13(a), and a schematic showing the shapes of the eigenmodes are shown in Fig. 5.13(b).

The varicose mode corresponds to the breakup of the ridges into droplet-like structures, and neighboring ridges are in-phase (anti-phase) with each other in the symmetric (asymmetric) mode. Similar break-up phenomena have also been reported for liquid film dewetting dominated by van-der Waals' interactions [31, 54, 117], and comparison to the classic Rayleigh-Plateau instability for free-standing liquid jet [91] has also been drawn in those studies. The symmetric varicose mode has a dispersion relation qualitatively similar to the type-II instability for flat electrode, and it always has zero eigenvalue at $\beta(K_y = 0) = 0$. Such zero eigenmode does not exist in a strictly 1D system because mean$(H_1) \neq 0$ and so volume conservation is violated. In a 2D system, however, the eigenmode has the form $H_1(X, Y) \propto e^{iK_y Y}$, so integration along the Y direction allows volume conservation to be satisfied. For the asymmetric varicose mode, $\beta(K_y) > 0$ for small D_0, and at $K_y = 0$, it is equivalent to the Ostwald ripening mode discussed in Section 5.4.3 corresponding to the transfer of fluid from one ridge to the other. For large D_0 and sufficiently large $\mathcal{W}_r$, the thickness of the precursor film between two neighboring ridges becomes very small and the two ridges can be considered independent of

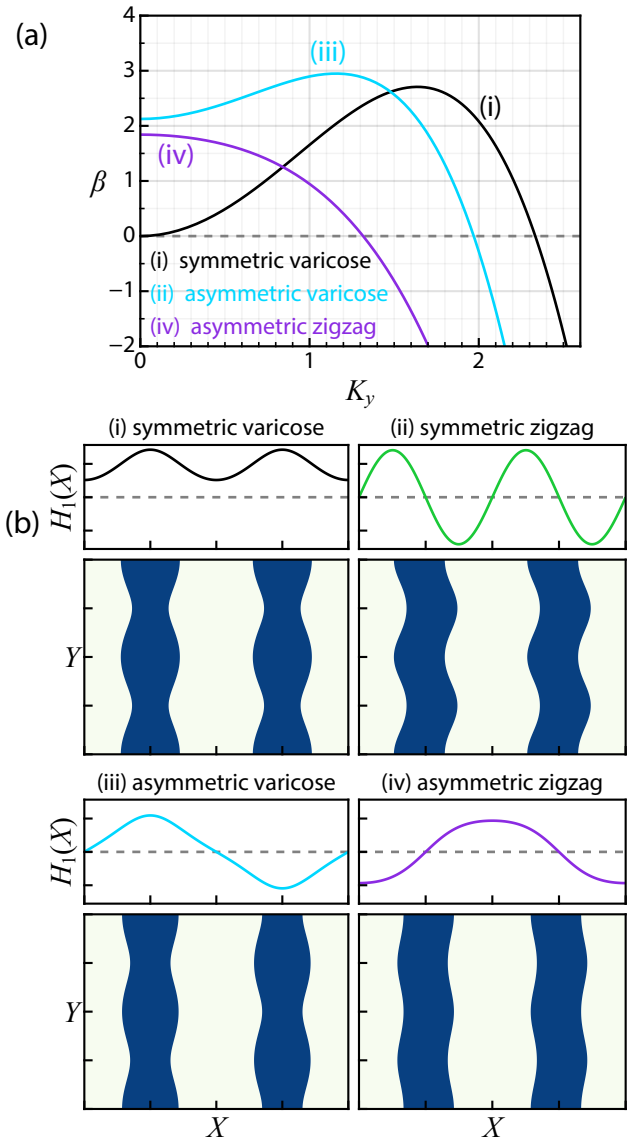

Figure 5.13: Dispersion relations and schematics of the four most unstable modes in a 2D system with two parallel stripes. Parameters: $D_0 = 2.5$, $\mathcal{W}_r = 0.5$, $\varrho = 0.05$, $L_x = 2\Lambda_p$. (a) The dispersion relation $\beta(K_y)$ obtained by solving Eq. (5.21) with $K_x = 0$. The symmetric zigzag mode is always stable and not shown. (b) Schematics showing the actions of the four most unstable modes. The top plot shows the eigenmodes $H_1(X)$, while the bottom plot shows how the two parallel ridges evolve under the four eigenmodes.

each other. In such case, $\beta(K_y = 0) \to 0$ for the asymmetric varicose mode, and the dispersion relations of both the symmetric and asymmetric varicose modes become the same.

For the zigzag modes, at $K_y = 0$, the symmetric (asymmetric) mode corresponds to the translation and coalescence modes discussed in 5.4.2. The symmetric zigzag mode which emerges from the translational invariance is always stable due to symmetry breaking when $\varrho > 0$. For the asymmetric zigzag mode, its growth rate appears to be always maximized at $K_y = 0$ and decreases with K_y.

5.4.4.2 Stability Phase Diagram

Here we present the stability phase diagram for the 2D system shown in Fig. 5.14 and 5.16 which are similar to their 1D counterparts shown in Fig. 5.9 and 5.11. The background heatmaps showing $\min(H_{\rm ss})$ and $\min(D - H_{\rm ss})$ remain unchanged since the stationary states $H_{\rm ss}(X)$ are the same. However, the symbols and lines now represent something slightly different:

1. The lines now represent the parameters where maximum growth rate for selected unstable modes shown in Fig. 5.13 become zero, i.e., $\max[\beta(K_y)] = 0$. Note that these modes correspond to two parallel ridges only.

   The stability contour for the asymmetric zigzag mode is the same as 1D coalescence mode, because the growth rate for 1D coalescence mode is always maximized at $K_x = K_p/2$ which corresponds to the asymmetric zigzag mode for *two* ridges with $K_x = 0$. Results with two parallel ridges further show that the growth rate is maximized at $K_y = 0$. Since it is equivalent to the coalescence mode in 1D system, it is not further explored here for parallel ridges in 2D system.

2. The symbols now represent the phase of the liquid film $H(X, Y, \tau_f)$ in 2D simulations with $(L_x, L_y) = (4\Lambda_p, 6\Lambda_p)$ and $\tau_f = 20\tau_{\rm max}$. The classification of the phases are the same as in the 1D case.

Comparison between the 2D results shown in Fig. 5.14 and 5.16 and the 1D results shown in Fig. 5.9 and 5.11 reveals the differences brought up by an extra dimension along the Y direction.

Small D_0 ($D_0 = 2.5$) The stability phase diagram for $D_0 = 2.5$ is shown in Fig. 5.14. The stability contour of the symmetric varicose mode (black solid line) encompasses all the other unstable modes and is the deciding factor for stability for two parallel ridges. Furthermore, inspection of $H_1(X)$ for the symmetric varicose mode from Fig. 5.13(b) clearly shows that the both ridges are subject to the same effects and so we can simply

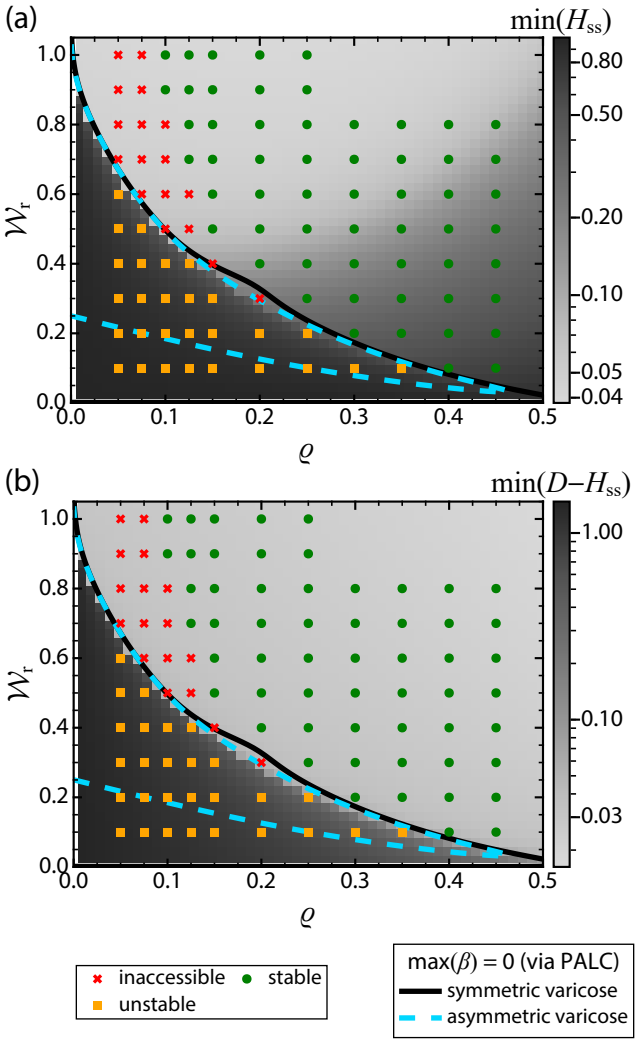

Figure 5.14: Stability phase diagram for 2D system with $D_0 = 2.5$. Black solid line and cyan dash line denote symmetric and asymmetric varicose mode for two parallel ridges with $\max(\beta) = 10^{-5}$ computed by PALC. Background heat map colors represents (a) minimum liquid film thickness $\min(H_{ss})$ and (b) minimum air gap thickness $\min(D - H_{ss})$ (same as in Fig. 5.9). Symbols denote (a) RMS deviation and (b) maximum deviation given by Eq. (5.23) for 2D time-dependent simulation with $(L_x, L_y) = (4\Lambda_p, 6\Lambda_p)$ and $\tau_f = 20\tau_{max}$. The value represents averaged quantity across 3 independent realizations for each parameter.

consider a single ridge while studying the symmetric varicose mode. This implies the stability of the system is not affected whether there exists one or two ridges. The black solid line also separates the small and large deformation regimes, which shows that having large deformation is a necessary condition for the symmetric varicose mode to be stable, i.e., $\max[\beta(K_y)] \leq 0$. Symbols representing 2D direct numerical simulation results also show that 'stable' stationary states (i.e., $\mathcal{E}_{\rm rms}(\tau_f) \leq 0.01$) only occurs in the large deformation regime. This shows that necessary condition for an initially flat liquid film to evolve toward the stationary state is by touching the patterned mask, and is the same for both 1D and 2D for $D_0 = 2.5$.

One notable difference compared to the 1D case is that for small ϱ and large $\mathcal{W}_r$ that lies in the large deformation regime, there is a cluster of states classified as 'inaccessible' where $\mathcal{E}_{\rm rms}(\tau)$ never reaches below 0.01 within the time frame of the simulation. This is because as the liquid film forms ridges that keep growing upward, they break up before establishing contact with the patterned mask. An example is shown in Fig. 5.15 for $\varrho = 0.1$ and $\mathcal{W}_r = 0.8$. Undulation along the top of the ridges can be seen at $\tau = 0.08$ which then destabilize into disjointed ridges. This phenomenon can be explained as follow: a larger $\mathcal{W}_r$ results in larger electrostatic stress, and balancing such destabilizing stress by capillarity becomes more difficult. On the other hand, a small ϱ results in larger electrode separation in the region where the liquid film forms protrusions, so it takes longer time for the liquid film to establish contact with the patterned mask, which in turn makes it more susceptible to destabilization due to electrostatic stress. Therefore, as liquid film is forming those parallel ridges, those ridges are more like to breakup into isolated ridges or column-like structures.

Large D_0 ($D_0 = 5.0$) The case for $D_0 = 5.0$ is shown in Fig. 5.16. There are two notable differences when compared to the 1D case shown in Fig. 5.11. The first is that for ridges with large deformation but not touching the patterned mask (i.e., the region enclosed by the cyan line in Fig. 5.11 with small $\min(H_{\rm ss})$ and large $\min(D - H_{\rm ss})$), 2D direct numerical simulations show that they are no longer 'stable'. This can be explained by the fact that fluid can now flow freely along the Y direction in 2D which was previously held constant in 1D, so fluid reorganization along the ridges to form column-like structures is possible in 2D. This is also consistent with the fact that varicose modes are unstable with large maximum growth rate at nonzero K_y, while in 1D the Ostwald ripening mode (corresponding to asymmetric varicose mode with $K_y = 0$) has a very small growth rate. Therefore, the necessary condition for forming high fidelity patterns, i.e., having $\mathcal{E}_{\rm rms}(\tau_f) \leq 0.01$, for $D_0 = 5.0$ appears to be forming saturated states which touch the mask.

The other difference is that many states are now classified as 'inaccessible' as $\mathcal{E}_{\rm rms}(\tau)$ never drops below the threshold of 0.01. Accessible stationary states are only obtained

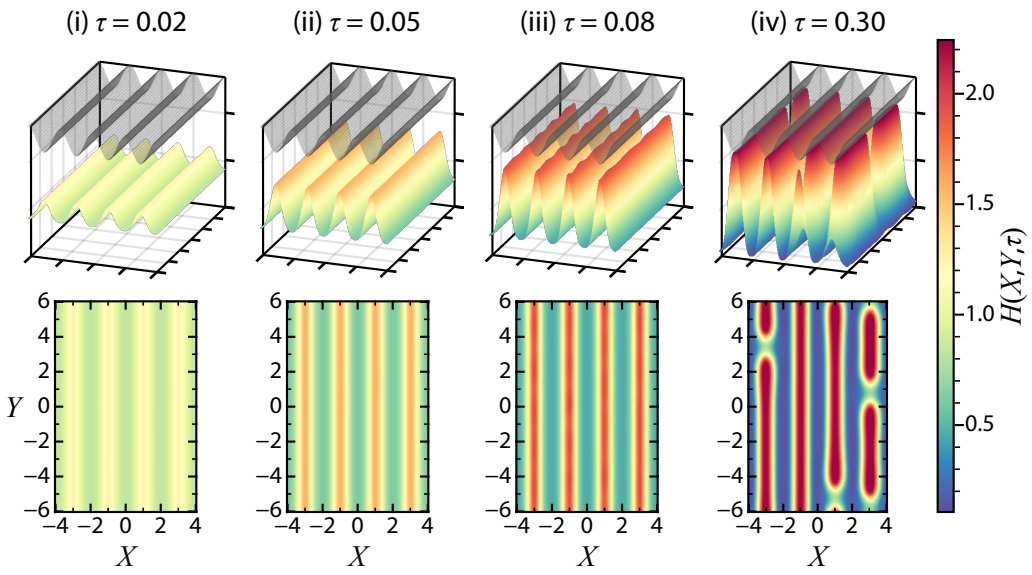

Figure 5.15: Selected snapshots of liquid film shape $H(X, Y, \tau)$ at $\tau = 0.02$, 0.05, 0.08, 0.3. Parameters: $D_0 = 2.5$, $\mathcal{W}_r = 0.8$, $\varrho = 0.1$, $(L_x, L_y) = (4\Lambda_p, 6\Lambda_p) = (8, 12)$.

in the bottom right region of the diagrams with large ϱ and small $\mathcal{W}_r$. Large ϱ leads to smaller electrode separation in the region where ridges form so the growth of ridges only need to cover a shorter distance, and small $\mathcal{W}_r$ has smaller electrostatic stress so the ridges are less susceptible to amplification of tiny perturbation by the destabilizing electrostatic stress.

5.4.4.3 Effects of different parameters and modulations on symmetric varicose mode

We next investigate how variations in different parameters and mask topographies affect the stability of a single ridge. We focus on the symmetric varicose mode since it is the deciding factor for stability in ridges.

Variation in D_0 Fig. 5.17 shows the stability contours for the symmetric varicose modes for different shapes of $D(X)$: sinusoidal modulation given by Eq. (5.3a) and rectangular modulation given by Eq. (5.3b). Regions above the contours (i.e., large $\mathcal{W}_r$) represent the stable parameter range, which requires the liquid film to establish contact with the patterned mask based on our previous discussion. For both types of spatial modulations, larger D_0 results in larger $\mathcal{W}_r$ for the same ϱ in order to ensure stability. This is because with a larger electrode separation, more fluid needs to be transported to the top of the ridges to reach the patterned mask, and this requires larger electrostatic stress, and hence larger $\mathcal{W}_r$.

When $D_0 \geq 3.0$, the stability contours for both sinusoidal and rectangular modulations

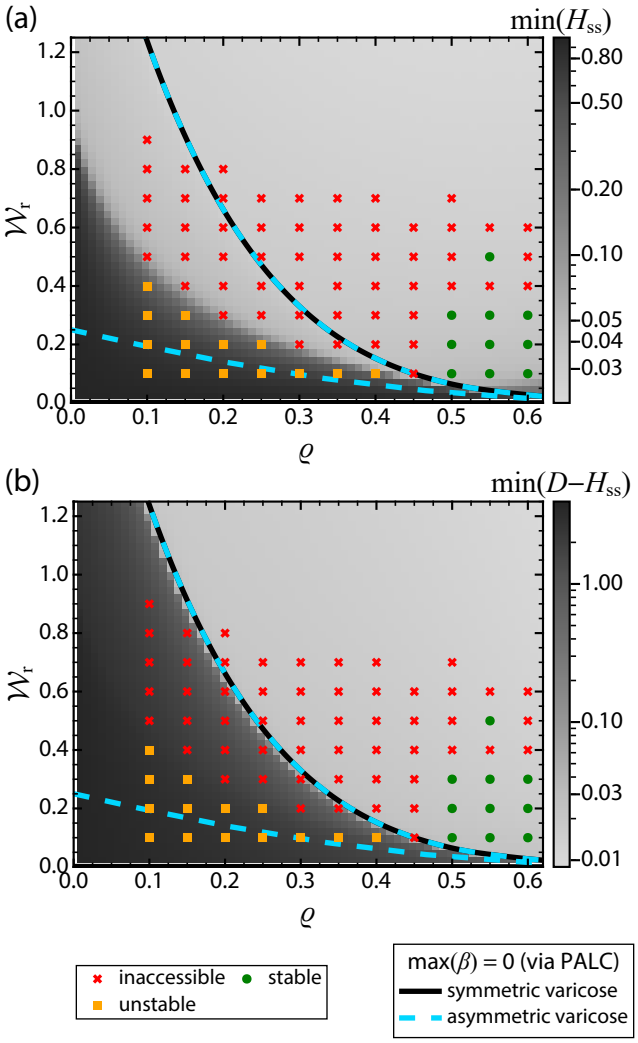

Figure 5.16: Stability phase diagram for 2D system with $D_0 = 5.0$. Black solid line and cyan dash line denote symmetric and asymmetric varicose mode for two parallel ridges with $\max(\beta) = 10^{-5}$ computed by PALC. Background heat map colors represents (a) minimum liquid film thickness $\min(H_{ss})$ and (b) minimum air gap thickness $\min(D - H_{ss})$ (same as in Fig. 5.9). Symbols denote (a) RMS deviation and (b) maximum deviation given by Eq. (5.23) for 2D time-dependent simulation with $(L_x, L_y) = (4\Lambda_p, 6\Lambda_p)$ and $\tau_f = 20\tau_{max}$. The value represents averaged quantity across 3 independent realizations for each parameter.

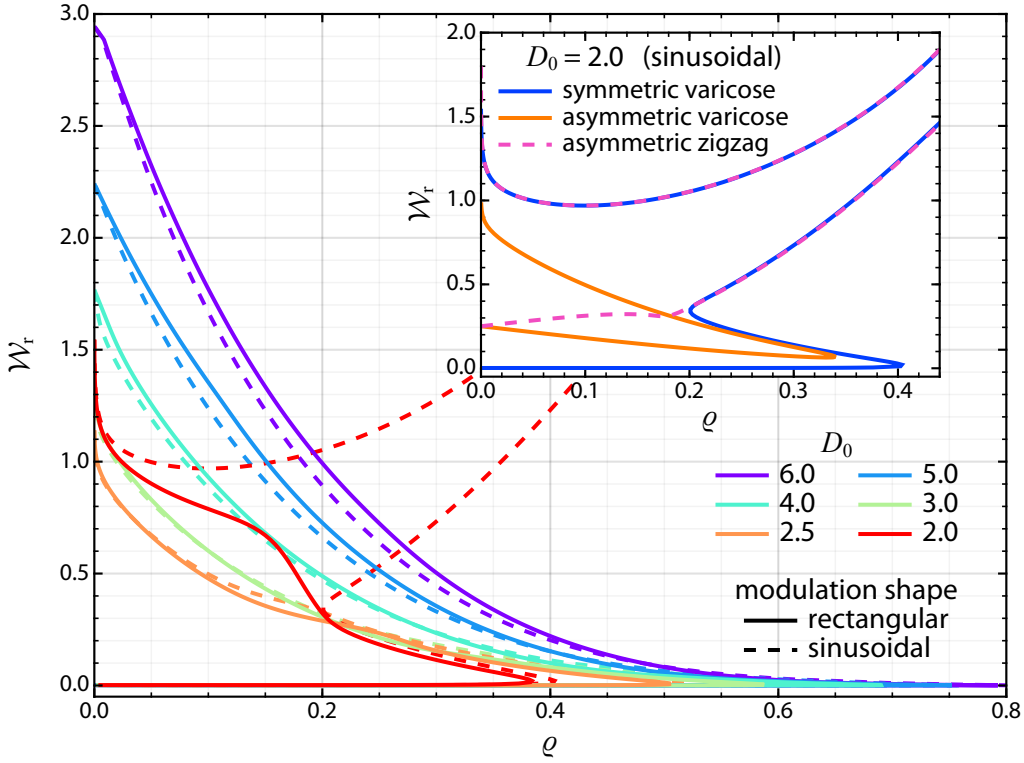

Figure 5.17: Influence of D_0 on the stability phase diagram for sinusoidal (Eq. (5.3a)) and rectangular (Eq. (5.3b)) modulation in mask topography ($\xi = D$). Solid (dashed) lines denote the stability contour for the symmetric varicose mode for sinusoidal (step-like) modulation, while different colors represent different values of D_0. Inset shows the stability contours for the symmetric varicose, asymmetric varicose and asymmetric zigzag modes for sinusoidal modulation with $D_0 = 2.0$.

are qualitatively similar. This is because as D_0 increases, the effects of the specific topography of the patterned mask on the resulting spatial profile of the electrostatic stress becomes less important. For $D_0 = 2.0$, however, there is a new unstable parameter range in the phase diagram which corresponds to large ϱ and $\mathcal{W}_r$. The inset further shows the stability contours for the asymmetric varicose and asymmetric zigzag modes for $D_0 = 2.0$, and it can be seen that the asymmetric zigzag mode is also unstable. The emergence of this new unstable parameter range can be explained by the large contact area of the liquid film with the patterned mask when ϱ and $\mathcal{W}_r$ are both large. Because of the sinusoidal topography of the mask, the liquid film exhibits two local maxima on near the patterned mask on either side, and it is easy for the fluid to flow from one protrusion to the other via the asymmetric zigzag (i.e., coalescence) mode as the mobility factor $M(H)$ remains high throughout the whole liquid film when D_0 is small.

Variation in mask topography (l_{rect}) In order to further investigate the effects of mask topography on the stability phase diagram, the parameter l_{rect} in Eq. (5.3b) which

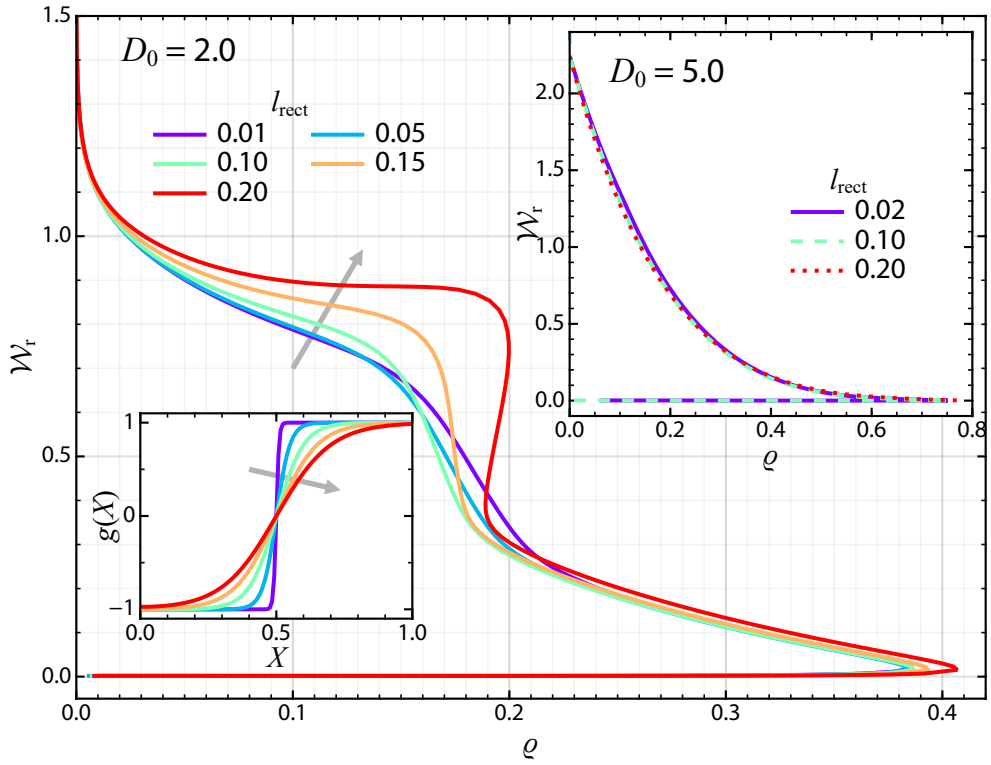

Figure 5.18: Influence of $l_{\rm rect}$ on the stability phase diagram for step-like (Eq. (5.3b)) modulation in mask topography ($\xi = D$). The main plot shows the stability contours for the symmetric varicose mode for $D_0 = 2.0$. Arrow indicates increasing values of $l_{\rm rect}$ which is represented by different colors. The left inset shows $g(X) = \text{rect}(X)$ for different $l_{\rm rect}$. The right inset shows the stability contours for the symmetric varicose mode for $D_0 = 5.0$.

controls the slope of the step-like modulation profile is varied. The stability contours for different $l_{\rm rect}$ are shown in Fig. 5.18. The left inset shows the modulation function $g(X)$ given by Eq. (5.3b) for different $l_{\rm rect}$, and it can be seen that larger $l_{\rm rect}$ gives a shape that better resemble a sinusoidal shape, while smaller $l_{\rm rect}$ gives a shape that approximates a step-like function. As $l_{\rm rect}$ increases, the corresponding stability contour also shows the emergence of the unstable parameter range shown in Fig. (5.17) for $D_0 = 2.0$. In contrast, the stability contours are quantitatively very similar for $D_0 = 5.0$ regardless of $l_{\rm rect}$. This further supports the claim that the mask topography can have profound influence on the stability for small D_0 in the parameter range where the liquid film shows large contact area with the patterned mask.

Variation in dimensionless Hamaker constant $\mathcal{A}$ Fig. 5.19 shows effect of varying the dimensionless Hamaker constant $\mathcal{A}$. For $D_0 = 2.0$, increasing $\mathcal{A}$ has a stabilizing effect which reduces the unstable parameter range as shown in Fig. 5.19(a). For larger D_0, the effect is again very minimal as shown in Fig. 5.19(b).

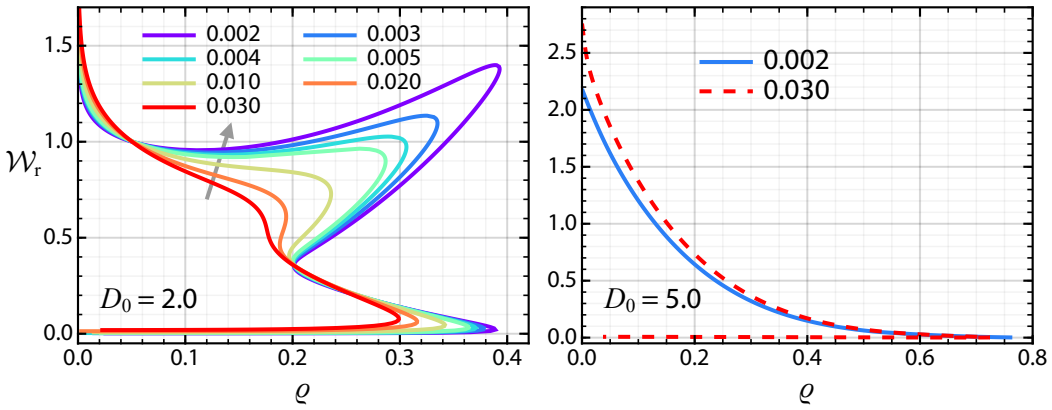

Figure 5.19: Influence of $\mathcal{A}$ on the stability phase diagram for sinusoidal modulation in mask topography for (a) $D_0 = 2.0$ and (b) $D_0 = 5.0$. Different colors represent different values of $\mathcal{A}$ labeled in the legend. Gray arrow in (a) indicates increasing $\mathcal{A}$.

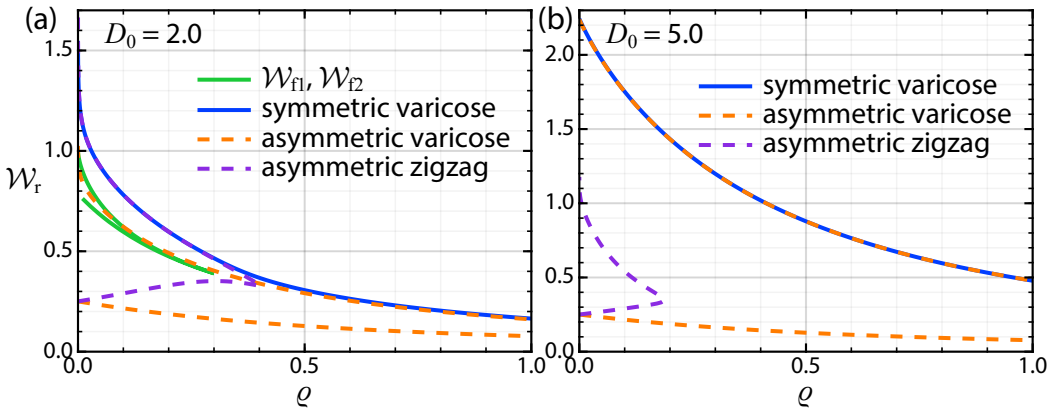

Figure 5.20: Stability phase diagrams for sinusoidal modulation in applied voltage ($\xi = \Psi_\Delta$) for (a) $D_0 = 2.0$ and (b) $D_0 = 5.0$. Lines with different colors and line styles correspond to different modes as indicated in the legend.

Modulation in applied voltage ($\xi = \Psi_\Delta$) Fig. 5.20 shows the stability phase diagram for sinusoidal modulation in the applied voltage, i.e., $\Psi_\Delta(X) = 1 + \varrho\cos(K_p X)$. Compared to modulation in $D(X)$, ϱ can extend to much larger value because it is no longer related to the geometric constraint as in the case for $\xi = D$. No turning points in the stability contours have been numerically found up to $\varrho = 1.0$, though the large spatial variation in the applied voltage resulted form such large ϱ may invalidate the LWA. The qualitative features of the stability contours of different modes are similar to modulation in $D(X)$ shown in previous figures.

5.4.5 2D array of protrusions with egg carton modulation

In this section, we present initial exploratory study on 2D spatial modulation in the mask topography using Eq. (5.3c) where the modulation function is given by an 'egg carton' shape as shown in Fig. 3.2(b). For parallel ridges studied in the previous section, the stability in a 1D system is very different from that in a 2D system as fluid flow along the Y direction can destabilize the ridges unless the ridges have established contact with the patterned mask. For egg carton pattern, however, it has an imposed periodicity along both X and Y directions, so intuitively we expect the fluid flow and stability to resemble more closely the results from Section 5.4.3 for ridges in a 1D system since the patterned mask is sinusoidally modulated in both X and Y directions.

$D_0 = 2.5$ Fig. 5.21 shows the stability phase diagram for 2D egg carton modulation in $D(\mathbf{X})$ with $D_0 = 2.5$. The heat map colors represent (a) the minimum liquid film thickness $\min(H_{\rm ss})$ and (b) the minimum air gap thickness $\min(D - H_{\rm ss})$. We can still classify the stationary states as having either small or large deformation which is evident from the two distinct background colors in Fig. 5.21(b). However, the minimum film thickness $\min(H_{\rm ss})$ is not necessarily small for the large deformation regime due to the small electrode separation and the topography of the mask shaped as an egg carton. The cyan solid line denotes the fold points at $\mathcal{W} = \mathcal{W}_{\rm f1}$ and $\mathcal{W}_{\rm f2}$ computed via PALC. The upper branch denotes the first fold point at $\mathcal{W} = \mathcal{W}_{\rm f1}$ and coincides with the abrupt change in color shown in Fig. 5.21(b) indicating transition from small to large deformation as expected.

The symbols represent the various phases based on comparing $H(X, Y, \tau_f)$ and the stationary states. Stationary states with small ϱ and large $\mathcal{W}_r$ are again classified as inaccessible as $\min[\mathcal{E}_{\rm rms}(\tau)] \geq 0.01$. Other stationary states, while accessible, are mostly unstable except those obtained with relatively large ϱ. While $\min(H_{\rm ss})$ given by Fig. 5.21 is relatively large which means fluid flow between neighboring protrusions is relatively unimpeded due to the large mobility factor, 'stable' states (i.e., $\mathcal{E}_{\rm rms}(\tau_f) \leq 0.01$) is still possible with strong electrostatic stress and small electrode separation at the position of the protrusions which ensure the protrusions are strongly pinned to the patterned mask.

$D_0 = 5.0$ The case for relatively large electrode separation of $D_0 = 5$ is shown in Fig. 5.22. The two distinct background colors of the heatmap of $\min(H_{\rm ss})$ and $\min(D - H_{\rm ss})$ shows that the stationary states can again be classified as having either small or large deformation. In the large deformation regime, the precursor film thickness is $\sim \mathcal{O}(0.01)$ when $\mathcal{W}_r \gtrsim 0.4$. Apart from isolated parameters near the fold points indicated by the cyan solid line, most states in the large deformation regime are classified as 'stable' while those in the small deformation regimes are 'unstable'.

The results suggest the sufficient condition for achieving high fidelity patterns is for the

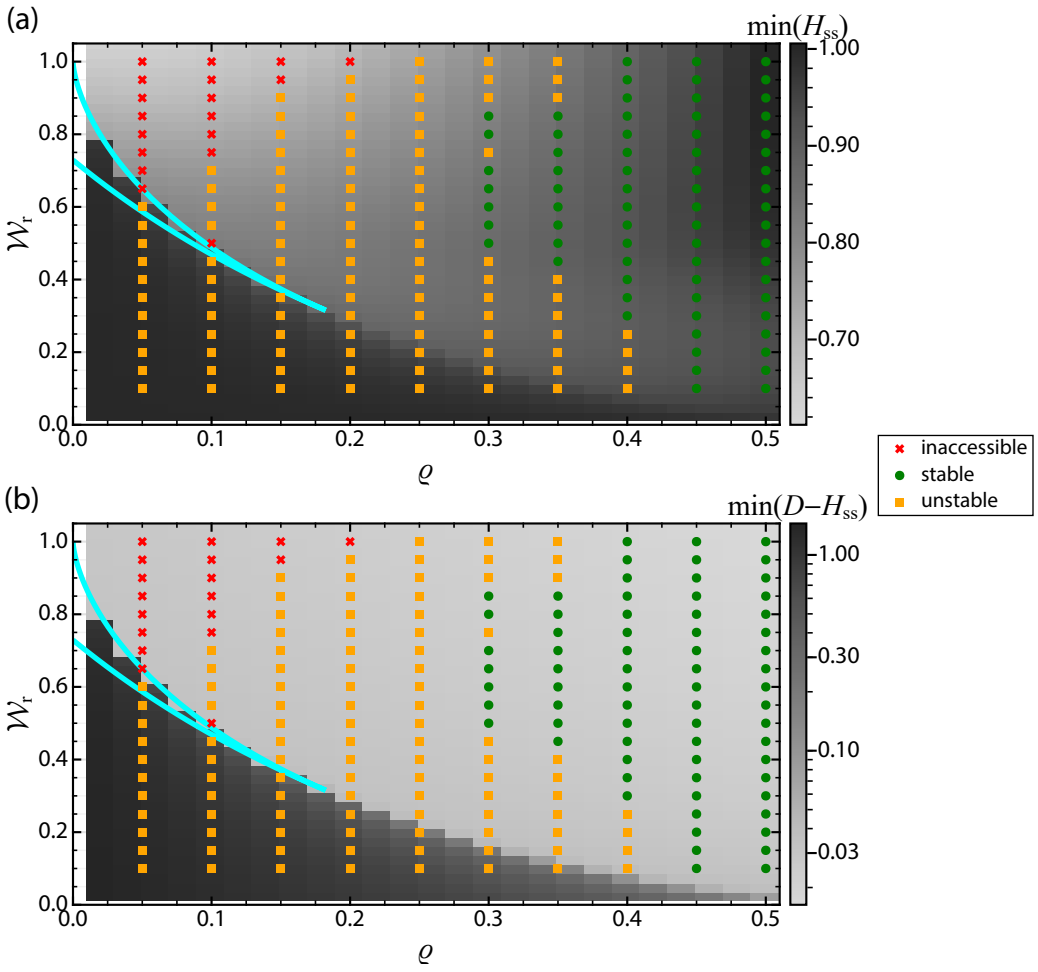

Figure 5.21: Stability phase diagram for egg carton modulation given by Eq. (5.3c) for patterned mask with $D_0 = 2.5$. The background heatmap color shows (a) the minimum liquid film thickness $\min(H_{\rm ss})$ and (b) the minimum air gap thickness $\min(D - H_{\rm ss})$. Symbols denote the RMS deviation and maximum deviation for time-dependent simulations evaluated with $L_x = L_x = 4\Lambda_p = 8$ at $\tau = 20\tau_{\max}$, each averaged across 5 independent realizations. Cyan solid line denotes the fold points $\mathcal{W}_{\rm f1}$ and $\mathcal{W}_{\rm f2}$ computed via PALC.

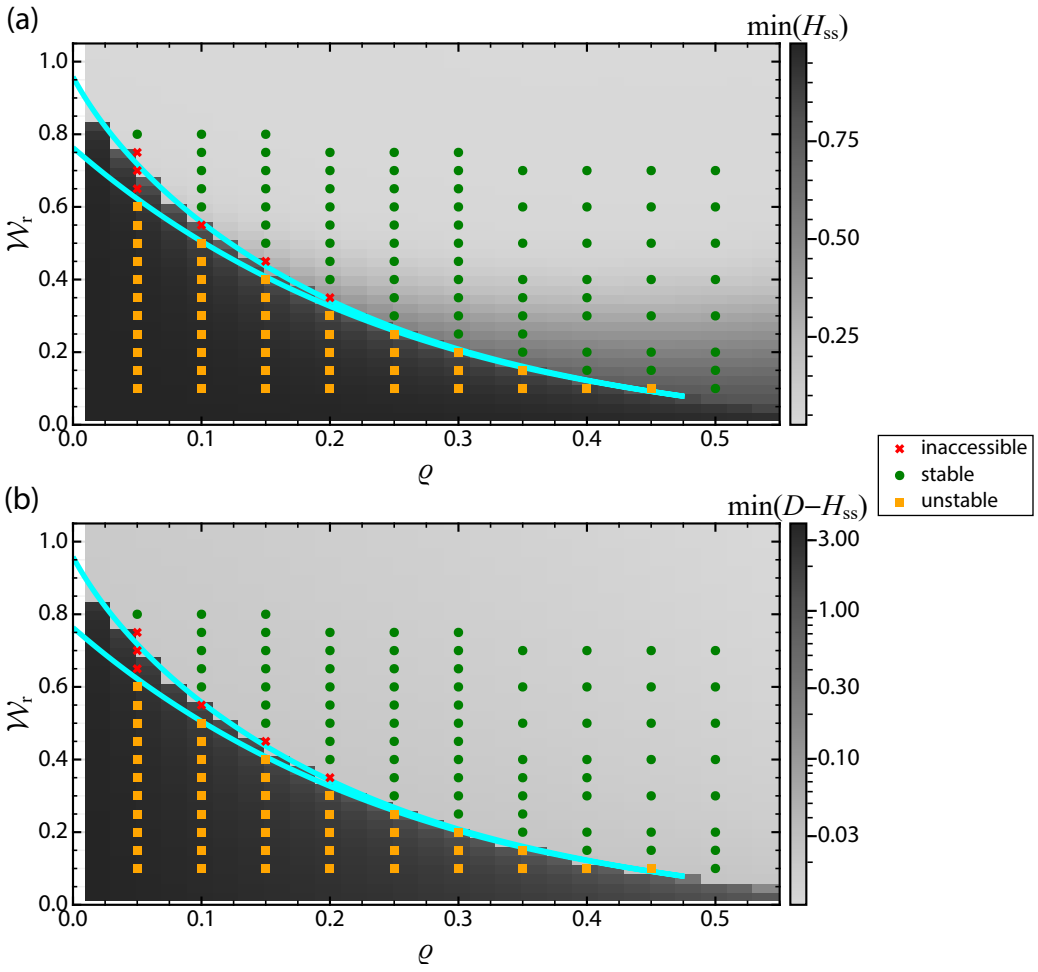

Figure 5.22: Stability phase diagram for egg carton modulation given by Eq. (5.3c) for patterned mask with $D_0 = 5.0$. The background heatmap color shows (a) the minimum liquid film thickness $\min(H_{ss})$ and (b) the minimum air gap thickness $\min(D-H_{ss})$. Symbols denote the RMS deviation and maximum deviation for time-dependent simulations evaluated with $L_x = L_x = 4\Lambda_p = 8$ at $\tau = 20\tau_{max}$, each averaged across 5 independent realizations. Cyan solid line denotes the fold points $\mathcal{W}_{f1}$ and $\mathcal{W}_{f2}$ computed via PALC.

liquid film to form protrusions with large deformations and small precursor film thickness, although more definitive conclusions cannot be drawn before exploring wider range of parameters as well as performing Floquet-Bloch LSA similar to those for parallel ridges.

5.5 Discussion

It appears a thin viscous film can only form a 'stable' (or at least 'quasi-stable') stationary state when fluid flow is suppressed by either fluid depletion at the precursor layer or geometric constraint imposed by the mask, i.e., at least one of the liquid-air interface is at close proximity with the electrode. A 'true' stable steady state where the free surface does not approach either the substrate or mask has not been found in this study, which is not a surprise given the nature of the runaway growth of protrusions when subject to electrostatic stress. One important limitation of this study is that as the air gap thickness decreases, the electric field strength also increases, and dielectric breakdown may occur [62] in which Eq. (5.1) becomes invalid. Therefore, the precise determination of stationary states and the associated stability when air gap thickness becomes small may require further treatment beyond the scope of this work in certain parameter range involving very small electrode separation and very large applied voltage.

One area of future study is to investigate quasi-steady states where the liquid film develops non-uniform patterns that while asymptotically unstable, can still be maintained for a long time before the patterns show substantial deviation away from the stationary states. Such quasi-steady states mainly correspond to those 'unstable' stables in the small deformation regime shown in Fig. 5.14 and 5.16, and are of practical interests since the non-uniform shapes can potentially be retained via solidification of the liquid film by cooling or photochemical reactions. Intuitively thinking, we expect these quasi-steady to occur when $\mathcal{W}_r$ is relatively small so that the destabilizing Maxwell stress is not too strong. This leads to a trade-off between stability of the patterns and the aspect ratio of the protrusions or ridges where large aspect ratio features are usually considered more desirable in a lithographic context (and also more challenging to obtain). However, executing this strategy experimentally requires a precise determination of the dimensional characteristic time scale $t_0 = l_0^4\mu/h_0^3\gamma$ which depends on the viscosity μ that is known to be highly temperature dependent.

In numerical studies into the spatiotemporal evolution of the liquid film, the quasi-steady time scale is also highly dependent on the magnitude of the unstable mode present in the system, which is usually seeded in the initial condition of the liquid film via a random function similar to Eq. (4.9). Comparison among different studies become very difficult since the initial power spectrum of the liquid film is seldom reported with sufficient details as that depends on the amplitude of the initial perturbation σ_{rand}, the grid size ΔX and the size of the spatial domain L_x. As an example, recent results on rapid EHD patterning via ultra-high voltage [86] show early sign of ridge break-up (see Fig. S4(b)

in Ref [86] for simulations with $\lambda_m/\lambda_p = 5$) despite its potential to achieve high-fidelity patterns. Such breakup phenomena often go un-noticed because the simulations were terminated prematurely. Therefore, more detailed studies on the dynamic evolution of the liquid film in forming quasi-steady states are needed in order to assess the feasibility of utilizing quasi-steady states in practice.

Finally, we comment on the conditions for obtaining high fidelity patterns which many previous studies have looked at. The most commonly mentioned rule of thumb is matching $\lambda_p \approx \lambda_m$, which according to Eq. (5.5) gives $\mathcal{W}_r = 2$, i.e., in the large deformation regime. For 1D spatial modulation, the ridges formed will likely breakup into column-like structures before the liquid film can establish contact with the patterned mask. In fact, having $\lambda_p < \lambda_c$ (i.e., $\mathcal{W}_r < 1$) seems to be more favorable to achieve quasi-steady states or accessible saturated states when ϱ and D_0 are also chosen appropriately. For 2D spatial modulation, however, the imposed periodicity along the Y direction might help to reinforce the pattern length scale via some resonant-like phenomena if λ_m and λ_p are matched appropriately. While more studies are still needed to arrive at a more definitive rule for obtaining high fidelity patterns, the results presented in all the phase diagrams in this chapter clearly shows that stable or quasi-stable patterns depend on the system geometry including electrode separation D_0, and modulation amplitude ϱ, as well as electric Weber number $\mathcal{W}$ (which is related to the ratio λ_p/λ_m), all of which affect the stability and basin of attraction of the stationary states and cannot be accurately described by a simple matching rule between λ_p and λ_m alone.

5.6 Conclusion

In this chapter, the shapes and stability of non-uniform stationary states formed by a single layer of viscous thin film subject to a heterogeneous electric field are studied. Time-dependent simulation of Eq. (5.1) is also carried out to study the dynamics of the liquid film and whether the liquid film conforms to the imposed pattern on the mask.

For a single ridge without interactions with neighboring ridges, pressure balance results in two fold bifurcations for small modulation amplitude ϱ. The presence of the first fold point at $\mathcal{W}_r = \mathcal{W}_{\mathrm{f1}}$ which has been previously reported in literature can be quantitatively explained by a weakly-nonlinear analysis described in Section 5.2.2 in the limit of $\mathcal{W} \to \mathcal{W}_c$.

When interactions with neighboring protrusions are allowed, it is found that stable stationary states in the case of single ridge can become unstable due to Ostwald ripening and coalescence modes in a 1D system supporting multiple ridges. The Ostwald ripening is the dominant destabilization mode because it has a larger growth rate and the unstable mode spans a larger region in the parameter space. In a 1D system, the Ostwald ripening mode can be suppressed by having thin precursor layers among protrusions,

leading to the formation of quasi-stable patterns which persist for a long time. the Ostwald ripening mode can only be truly stabilized by contact with the patterned mask. In a 2D system where Y direction is no longer invariant, contact with the patterned mask becomes a necessary condition for the liquid film to form stable stationary ridges, and the ridges can still break up into ridges before establishing contact with the patterned mask.

These results provide further physical insights into the stabilization mechanism in EHD patterning for forming stripes, as well as practical design rules in the form of stability phase diagram which we hope can stimulate further experimental work in this interesting area.

5.7 Derivations and Proofs for Chapter 5

This section presents the derivations to certain results in this Chapter 5 which can be skipped on a first reading. Note that lowercase letters are often used (in this section only) for brevity.

5.7.1 General solution to the linearized thin film equation

In this section, we derive the general solution to the following equation

$$\frac{\partial u}{\partial t} = -M\left[\frac{\partial^4 u}{\partial x^4} + k_c^2 \frac{\partial^2 u}{\partial x^2}\right] + f(x), \tag{5.25}$$

where M and k_c are constants representing the mobility factor and critical wave number in the thin film equation.

The boundary conditions are

$$u(x=0,t) = u(x=L,t), \qquad f(x=0) = f(x=L), \tag{5.26}$$

and the initial condition for $u(x,t)$ is

$$u(x,t=0) = \sum_{n=1}^{\infty} \left[a_n \cos\left(2\pi n x/L\right) + b_n \sin\left(2\pi n x/L\right)\right], \tag{5.27}$$

Define $k_{\min} = 2\pi/L$, $k_n = nk_{\min}$, the patterning periodicity λ_p, $k_p = 2\pi/\lambda_p$, and assume $k_p = Nk_{\min}$, or alternatively $L = N\lambda_p$, for integer values of N.

Since $u(x,t)$ and $f(x)$ are periodic functions, they can be expressed in terms of Fourier series:

$$u(x,t) = \sum_{n=1}^{\infty} \left[u_{c,n}(t)\cos(k_n x) + u_{s,n}(t)\sin(k_x x) \right], \tag{5.28a}$$

$$f(x) = \sum_{m} \left[f_{c,m}\cos(mk_p x) + f_{s,m}\sin(mk_p x) \right]. \tag{5.28b}$$

The coefficients $f_{\alpha,n}$ $(i = s, c)$ are assumed to be known since it is the external forcing we impose on the system. Substituting Eq. (5.28) into Eq. (5.25) gives

$$\sum_{n=1}^{\infty} \Bigg\{ \left[\frac{\mathrm{d}u_{c,n}}{\mathrm{d}t} + M(h_0)\left(-k_c^2 k_n^2 + k_n^4\right) u_{c,n} - f_{c,m}\delta_{mN,n} \right] \cos(k_n x) + \left[\frac{\mathrm{d}u_{s,n}}{\mathrm{d}t} + M(h_0)\left(-k_c^2 k_n^2 + k_n^4\right) u_{s,n} - f_{s,m}\delta_{mN,n} \right] \sin(k_n x) \Bigg\} = 0, \tag{5.29}$$

where $\delta_{mN,n}$ is the Kronecker delta to handle the difference in fundamental frequency in $u(x,t)$ and $f(x)$. Applying the orthonormality condition for the Fourier coefficients and using the dispersion relation defined by Eq. (3.7), Eq. (5.29) can be rewritten as

$$\frac{\mathrm{d}u_{\alpha,n}}{\mathrm{d}t} = \beta(k_n) u_{\alpha,n} + f_{\alpha,m}\delta_{mN,n}, \tag{5.30}$$

where $\beta(k_n) = M(1)k_c^2(k_c^2 - k_n^2)$ is the growth rate of the mode with $k = k_n = nk_{\min}$. Using the method of integrating factor, we can solve for $u_{\alpha,n}$:

$$\begin{aligned} u_{\alpha,n}(t) &= u_{\alpha,n}(t=0)e^{\beta(k_n)t} + e^{\beta(k_n)t}\int_0^t f_{\alpha,m}\delta_{mN,n}e^{-\beta(k_n)s}\mathrm{d}s \\ &= u_{\alpha,n}(t=0)e^{\beta(k_n)t} - \frac{f_{\alpha,m}\delta_{mN,n}}{\beta(k_n)}\left[1 - e^{\beta(k_n)t}\right]. \end{aligned} \tag{5.31}$$

In this thesis, we consider spatial forcing $f(x)$ expressed in the following form

$$f(x) = \sum_{m} f_m \cos(mk_p x). \tag{5.32}$$

The general solution of $u(x,t)$ for $f(x)$ given by Eq. (5.32) can then be expressed as

$$\begin{aligned} u(x,t) = &\sum_{n} \left[a_n \cos(k_n x) + b_n \sin(k_n x) \right] e^{\beta(k_n)t} \\ &- \sum_{m} \frac{f_m}{\beta(mk_p)}\left[1 - e^{\beta(mk_p)t}\right]\cos(mk_p x). \end{aligned} \tag{5.33}$$

For EHD patterning where the linearized thin film equation is given by Eq. (5.6), the general solution given by Eq. (5.8) can be obtained using the following substitutions in Eq. (5.33):

$$u(x,t) \to H_1(X,\tau), \quad M \to M(1), \quad k_c \to K_c, \quad k_p \to K_p,$$
$$f_1 \to M(1)K_p^2\xi_0 \frac{\partial \Pi(1,\xi_0)}{\partial \xi}.$$

we substitute $u(x,t) \to H_1(X,\tau)$, $M \to M(1)$, $f_1 \to M(1)K_p^2\xi_0 \partial\Pi/\partial\xi$ into Eq. (5.33):

$$H_1(X,\tau) = \xi_0 \frac{\partial \Pi}{\partial \xi} \frac{1}{K_p^2 - K_c^2} \left[1 - e^{\beta(K_p)\tau}\right] \cos(K_p X) \tag{5.34}$$

5.7.2 Derivation of amplitude equation via multi-scale expansion

While the method of multiscale expansion is a well-known technique, and it has been applied to study different hydrodynamic problems governed by the thin film equations in literature, we find that the specific scalings were often stated without much elaboration or justification, and to the best of our knowledge those studies often did not incorporate spatial modulation except Ref [57]. In this section, we present the complete derivation leading up to the amplitude equation given by Eq. (5.35) for completeness and to justify the scalings used in literature. The derivation largely follows that presented in Ref [88].

We consider the following thin film equation

$$\frac{\partial h}{\partial t} = f(h,\xi;R) = -\nabla \cdot \left\{ M(h) \nabla \left[\nabla^2 h + \Pi(h,\xi;R) \right] \right\}, \tag{5.35}$$

where lowercase letters are used for brevity, ξ is a label to denote the quantity being spatially modulated, and R is the control parameter which represents the electric Weber number $\mathcal{W}$ in the main text, though in principle it can represent any other parameters in the equation such as the relative permittivity ε_r or the patterning wave number k_p as in Ref [15, 57].

Let R_c denote the parameter value at bifurcation, i.e., $f(h,\xi;R_c) = 0$. To investigate the behavior of the system near the bifurcation $R = R_c$, we can perform a multi-scale expansion near R_c with the following expansions:

$$R = R_c + \delta R_1 + \delta^2 R_2 + \cdots, \tag{5.36a}$$
$$h = h_0 + \delta h_1(x,t) + \delta^2 h_2(x,t) + \cdots. \tag{5.36b}$$

A hierarchy of time scales $t_k = \delta^k t$ are introduced such that the time derivative becomes

$$\frac{\partial}{\partial t} = \frac{\partial}{\partial t_0} + \delta \frac{\partial}{\partial t_1} + \delta^2 \frac{\partial}{\partial t_2} + \cdots . \tag{5.37}$$

We also introduce the following notations for simplifying the expressions:

$$\begin{aligned} \Pi_h &= \frac{\partial \Pi}{\partial h} = k_p^2, & \Pi_{hh} &= \frac{\partial^2 \Pi}{\partial h^2}, & \Pi_{hhh} &= \frac{\partial^3 \Pi}{\partial h^3}, \\ \Pi_\xi &= \frac{\partial \Pi}{\partial \xi}, & \Pi_{hR} &= \frac{\partial^2 \Pi}{\partial h \partial R} \end{aligned} \tag{5.38}$$

Note that all the above expressions are evaluated at $h = h_0$, $\xi = \xi_0$ and $R = R_c$, and are simply constants.

5.7.2.1 Without spatial modulation: $\xi(x) = \xi_0$

We first consider the case without spatial modulation, i.e., $\xi = \xi_0$ is spatially constant. Substituting the expansions given in Eq. (5.36) and (5.37) to Eq. (5.35), to $\mathcal{O}(\delta)$ we recover $f(h_0, \xi_0; R_c) = 0$, which is simply the bifurcation condition.

To $\mathcal{O}(\delta)$, we obtain

$$\frac{\partial h_1}{\partial t_0} = -M(h_0) \left(\frac{\partial^4 h_1}{\partial x^4} + k_p^2 \frac{\partial^2 h_1}{\partial x^2} \right) = \mathcal{L}(h_1), \tag{5.39}$$

where $\mathcal{L}$ is the linear operator representing the RHS of Eq. (5.39). Suppose $h_1 \sim e^{ik_p x}$. The solution to Eq. (5.39) when $|R - R_c|$ is large, i.e., when k_p is far from k_c, is

$$h_1(t_0) \sim h_1(t_0 = 0) e^{\beta(k_p) t_0}. \tag{5.40}$$

The summation term in Ref [15, Eq. (29)] basically generalizes Eq. (5.40) to a Fourier sum under periodic boundary condition. This is also the $\mathcal{O}(\delta e^{-4\pi^2 t})$ term in Ref [33, Eq. (36)].

Since we are interested in studying the bifurcation near the critical point $R = R_c$, we look for solutions satisfying $\mathcal{L}h_1 = 0$ (i.e., on the bifurcation or 'center' manifold where the eigenvalue vanishes) whose dynamics needs to be determined by a nonlinear amplitude equation to be obtained in higher order expansion of δ [88, see text between Eq. (7) and (8)]. The solution of h_1 becomes

$$h_1 = a_1(t_1, t_2, \dots) \cos\left[k_p x + \theta_1(t_1, t_2, \dots)\right]. \tag{5.41}$$

To $\mathcal{O}(\delta^2)$, we have

$$\frac{\partial h_1}{\partial t_1}+\frac{\partial h_2}{\partial t_0}=-M(h_0)\left(\frac{\partial^4 h_2}{\partial x^4}+k_p^2\frac{\partial^2 h_2}{\partial x^2}\right)-M(h_0)\Pi_{hR}R_1\frac{\partial^2 h_1}{\partial x^2}$$
$$-M(h_0)\Pi_{hh}\left[\left(\frac{\partial h_1}{\partial x}\right)^2+h_1\frac{\partial^2 h_1}{\partial x^2}\right]-M'(h_0)\left[\Pi_h\left(\frac{\partial h_1}{\partial x}\right)^2\right.$$
$$\left.+\frac{\partial h_1}{\partial x}\frac{\partial^3 h_1}{\partial x^3}+h_1\left(k_p^2\frac{\partial^2 h_1}{\partial x^2}+\frac{\partial^4 h_1}{\partial x^4}\right)\right]. \tag{5.42}$$

We require h_2 to remain stationary on the fast time scale t_0, otherwise it may outgrow h_1 at long times [88, see text before Eq.(10)]. This leads to $\partial h_2/\partial t_0 = 0$. Substituting the general solution of h_1 given by Eq. (5.41) into Eq. (5.42), we obtain

$$\frac{\partial h_1}{\partial t_1}=\mathcal{L}h_2+M(h_0)k_p^2\Pi_{hR}R_1a_1\cos(k_px+\theta_1)$$
$$+M(h_0)k_p^2\Pi_{hh}a_1^2\cos[2(k_px+\theta_1)] \tag{5.43}$$

We need to impose a set of solvability conditions in order to solve for h_2. It can be shown using Fredholm alternative that parts of the inhomogeneous term which projects on the principle harmonic of the mode, i.e., $\cos(k_px)$ and $\sin(k_px)$, contribute to the solvability condition. Operationally, we need to set the coefficients of all $\sin(k_px)$ and $\cos(k_px)$ terms in Eq. (5.43) to zero, which are resulted from the $\partial h_1/\partial t_1$ and Π_{hR} terms:

$$\frac{\partial a_1}{\partial t_1}=M(h_0)k_p^2\Pi_{hR}R_1a_1, \tag{5.44a}$$
$$\frac{\partial \theta_1}{\partial t_1}=0. \tag{5.44b}$$

The solutions to Eq. (5.44) are

$$a_1(t_1)=a_1(0)\exp[M(h_0)k_p^2\Pi_{hR}R_1t_1], \tag{5.45a}$$
$$\theta(t_1)=\text{const.} \tag{5.45b}$$

Recall that $t_1=\delta t_0$, $R=R_c+\delta R_1+\mathcal{O}(\delta^2)$, and $\Pi_{hR}=\partial^2\Pi/\partial h\partial R$ evaluated at $R=R_c$, the exponent in Eq. (5.45a) can be re-expressed as

$$
\begin{aligned}
M(h_0)k_p^2\Pi_{hR}R_1t_1 &= M(h_0)k_p^2\frac{\partial}{\partial R}\left[\frac{\partial\Pi(h_0,\xi_0;R_c)}{\partial h}\right]\left[R-R_c+\mathcal{O}(\delta^2)\right]t_0 \\
&= M(h_0)k_p^2\left[\frac{\partial\Pi(h_0,\xi_0;R)}{\partial h}-\frac{\partial\Pi(h_0,\xi_0;R_c)}{\partial h}+\mathcal{O}(\delta^2)\right]t_0+\mathcal{O}(\delta^2) \\
&= M(h_0)k_p^2(k_c^2-k_p^2)t_0+\mathcal{O}(\delta^2) \\
&= \beta(k_p)t_0+\mathcal{O}(\delta^2). \qquad (5.46)
\end{aligned}
$$

To leading order, we simply recover the dispersion relation from the amplitude equation for a_1, and so we gain nothing new about the nonlinear behavior at the bifurcation manifold. This shows that we need to continue the expansion to higher order, i.e., to $\mathcal{O}(\delta^3)$, in order to obtain the desired (nonlinear) amplitude equation for a_1. As explained in [88, see Section 2.2.3], in order to continue the expansion, we restrict the parametric deviation in such a way that the dependence on t_1 be suppressed. Therefore, we set $R_1 = 0$ from now on.

Setting $R_1 = 0$ and dropping the t_1 dependence, there is no secular terms in the equation, and we can solve for h_2:

$$
h_2(x,t_2) = a_2(t_2)\cos\left[k_px+\theta_2(t_2)\right]+\frac{\Pi_{hh}}{12k_p^2}a_1(t_2)^2\cos[2(k_px+\theta_2(t_2))]. \qquad (5.47)
$$

To $\mathcal{O}(\delta^3)$, after substituting the expressions of $h_1(x,t_2)$ and $h_2(x,t_2)$, we obtain

$$
\begin{aligned}
\frac{\partial h_1}{\partial t_2} = \mathcal{L}h_3 &+ \frac{M(h_0)}{12}a_1^3\cos(k_px+\theta_1)\Big\{\left[-4+9\cos(2k_px+2\theta_1)\right]\Pi_{hh}^2 \\
&+ 3k_p^2\left[-1+3\cos(2k_px+2\theta_1)\right]\Pi_{hhh}\Big\} \\
&+ k_p^2a_1M(h_0)\left[2a_2\cos(2k_px+\theta_1+\theta_2)\Pi_{hh}+R_2\cos(k_px+\theta_1)\Pi_{hR}\right]. \qquad (5.48)
\end{aligned}
$$

The solvability conditions are

$$
\frac{\partial\theta_1}{\partial t_2} = 0, \qquad (5.49a)
$$

$$
\frac{\partial a_1}{\partial t_2} = M(h_0)k_p^2\left[\frac{1}{24}\left(\frac{\Pi_{hh}^2}{k_p^2}+3\Pi_{hhh}\right)a_1^3+\Pi_{hR}R_2a_1\right]. \qquad (5.49b)
$$

Eq. (5.49) is the required nonlinear amplitude equation for $a_1(t_2)$. There are a few important results from this: (1) $t_2 = \delta^2t_0$ is the slow time appropriate for the problem, and (2) $R = R_c+\delta^2R_2$ is the expansion appropriate for the bifurcation parameter. This justifies the scaling used in previous studies including Ref [15, 33, 57, 93].

5.7.2.2 With spatial modulation: $\xi(x) = \xi_0[1 + \varrho\cos(k_p x)]$

Next, we consider the case of having spatial modulation to the system. Let $\xi = \xi_0\,[1 + \varrho\cos(k_p x)]$ be the spatially modulated variable in the system. Since the amplitude equation comes from the $\mathcal{O}(\delta^3)$ term, we can intuitively set $\varrho = \delta^3$ in anticipation of having the effect of spatial modulation at $\mathcal{O}(\delta^3)$. This scaling can also be deduced from Eq. (5.8) once we accept the $t = \delta^2 t_2$ and $R = R_c + \delta^2 R_2$ (e.g., $\mathcal{W} = \mathcal{W}_c + \delta^2\mathcal{W}_2$) scalings:

$$\Delta h_{\text{lin}} \sim \frac{\varrho}{|\mathcal{W} - \mathcal{W}_c|} = \frac{\varrho}{\delta^2\mathcal{W}_2} \sim \delta h_1. \tag{5.50}$$

In order for the amplitude Δh_{lin} derived under the linear analysis to match the leading order term in the multiscale expansion δh_1 as $\mathcal{W} \to \mathcal{W}_c$, we need $\varrho/\delta^2 \sim \delta$, which requires $\varrho = \delta^3$.

The methodology for deriving the amplitude equation is the same as that without spatial modulation except now the pressure $\Pi = \Pi(h, \xi; R)$ also depends on a spatially varying $\xi(x)$. This results in the following extra term while doing expansion around $\Pi(h_0, \xi_0; R_c)$:

$$\Pi = \cdots + \delta^3 \frac{\partial\Pi(h_0, \xi_0; R_c)}{\partial\xi}\xi_0\cos(k_p x) + \ldots, \tag{5.51}$$

and when substituted into the governing equation, we get the following extra term in the $\mathcal{O}(\delta^3)$ expansion:

$$M(h_0)k_p^2\xi_0\Pi_\xi\cos(k_p x) \tag{5.52}$$

Eq. (5.48) then becomes

$$\begin{aligned}\frac{\partial h_1}{\partial t_2} = \mathcal{L}h_3 + \frac{M(h_0)}{12}a_1^3\cos(k_p x + \theta_1)\Big\{&[-4 + 9\cos(2k_p x + 2\theta_1)]\,\Pi_{hh}^2 \\ &+ 3k_p^2\,[-1 + 3\cos(2k_p x + 2\theta_1)]\,\Pi_{hhh}\Big\} + M(h_0)k_p^2\xi_0\Pi_\xi\cos(k_p x) \\ &+ k_p^2 a_1 M(h_0)\Big[2a_2\cos(2k_p x + \theta_1 + \theta_2)\Pi_{hh} + R_2\cos(k_p x + \theta_1)\Pi_{hR}\Big],\end{aligned} \tag{5.53}$$

where the highlighted term is due to spatial modulation. The solvability conditions become

$$\frac{\partial \theta_1}{\partial t_2} = 0, \tag{5.54}$$

$$\frac{\partial a_1}{\partial t_2} = M(h_0) k_p^2 \left[\frac{1}{24} \left(\frac{\Pi_{hh}^2}{k_p^2} + 3\Pi_{hhh} \right) a_1^3 + \Pi_{hR} R_2 a_1 + \xi_0 \Pi_\xi \right]. \tag{5.55}$$

Note that since $\frac{\partial \theta_1}{\partial t_2} = 0$, we can simply set $\theta_1 = \text{const.} = 0$ without loss of generality. The solvability condition then becomes the coefficient of the $\cos(k_p x)$ term. The amplitude equation can be re-written as

$$\frac{\partial a_1}{\partial t_2} = f_{\text{wnl}}(a_1; R_2) = c_3 a_1^3 + c_1 R_2 a_1 + c_0, \tag{5.56}$$

where the coefficients are given by Eq. (5.13).

Chapter 6

HIGH FIDELITY PATTERNS UNDER THERMOCAPILLARY STRESS

6.1 Introduction

We begin this chapter by providing a brief overview of the literature on TC patterning, especially on the use of external spatial modulation in improving pattern fidelity. We then state the equation and form of spatial modulation to be studied mathematically, and give a brief outline of the chapter.

6.1.1 Literature review

Over two decades ago, Schäffer and co-workers [100–102] reported observation of localized arrays of micro protrusions in an initially flat molten polymeric nanofilm exposed to a large temperature gradient. They proposed that these formations develop in response to a long wavelength instability due to gradients in acoustic phonon radiation pressure within the film. However, their experimental measurements and results turned out to be difficult to interpret. For example, the actual experimental setup consisted of a tilted plate geometry while the theoretical prediction requires the plates to be parallel. In addition, the measurements of the patterns' length scales were taken at the final time once peak heights had contacted the opposing cold substrate where fluid reorganization and solidification upon contact with the cold substrate likely further altered the patterns due to physical effects not incorporated into the model, while the predictions of the linear stability model are strictly predicated on early time growth to ensure only small amplitude deformation of an initial flat film.

Some years later, a different mechanism was proposed based on a long wavelength thermocapillary instability [28, 29]. Experiments [36, 37, 74] designed to better accord with key assumptions of that model were also conducted. Detailed measurements of the array pitch and peak growth rates at early times were found to be in good agreement with predictions of a LSA describing the competition between destabilizing thermocapillary forces and the stabilizing capillary forces. More recent theoretical work examining late time dynamics in the nonlinear regime has also demonstrated how fluid protrusions driven by significant thermocapillary stresses will sharpen in time due to a self-similar runaway process [146] which leads to cusp-like shapes.

Having established the physical origin of the destabilizing mechanism, recent studies turn to how the liquid film evolves when heated non-uniformly. For example, Nazaripoor et al. [79] studied the dynamics of liquid film in forming ridges with topographically patterned mask and substrate. They also investigated the use of both thermocapillary and electric effects in patterning liquid film [80–82] and found that the inclusion of

thermocapillary effects leads to patterns with smaller feature size but more susceptible to lateral motions compared to the base case of EHD patterning alone. However, simulations were only conducted for very few parameters, so it is difficult to generalize the findings to a broader parameter range similar to the literature in EHD patterning. On the other hand, Yang et al. [138] also studied the 1D stationary states of the liquid film under topographically patterned mask and discovered fold bifurcations in the stationary state shape against variation in the Marangoni number $\mathcal{M}$ [1]. However, they incorrectly applied the expression of the Lyapunov free energy for uniform heating to the case of non-uniform heating (see discussion in Section 2.3.1.3) when studying the stability of the liquid film, and interactions with neighboring protrusions were also neglected. Direct numerical simulations of the full Navier-Stokes equation without invoking LWA have also been performed [78, 111, 140, 141]. However, these studies only focused on the 1D periodic patterns with identical shapes for all protrusions, and phenomena such as coalescence and Ostwald ripening involving multiple protrusions were not investigated likely due to the high computational cost associated with running the simulations in a large spatial domain while taking into account the large disparity in time scales associated with different stages of the pattern formation process.

Apart from TC patterning with a setup which consists of two parallel plates held at different temperatures, we also mention the experimental study by Eshel et al. [34] which utilized thermocapillary effect to pattern silicone oil using UV lamp to make microlenses. For applications other than microfabrication, Frumkin and coworkers [41–43] studied the transport of droplets in a similar setup to ours (Fig. 1.1(b)) using spatially modulated temperature of the substrate in the form of thermal traveling waves.

In view of the limited studies in literature dealing with non-uniform heating in TC patterning, we follow a similar approach as in Chapter 5 to study the stationary states and dynamics of the liquid film subject to periodic spatial modulation in the temperature profile. We specifically focus on the role of thermocapillary stress and compare the differences between TC and EHD patterning.

6.1.2 Problem statement

The governing equation for TC patterning is re-stated below for convenience:

$$\begin{aligned}\frac{\partial H}{\partial \tau} &= \nabla_{\parallel}\cdot\left\{M_{\perp}(H)\nabla_{\parallel}P - M_{\parallel}(H)\nabla_{\parallel}\Gamma(H,\xi)\right\}\\ &= -\nabla_{\parallel}\cdot\left\{M_{\perp}(H)\nabla_{\parallel}\left[\nabla_{\parallel}^2 H + \Pi_{\mathrm{vdw}}(H,\xi)\right] + M_{\parallel}(H)\nabla_{\parallel}\Gamma(H,\xi)\right\},\end{aligned} \tag{6.1}$$

where $M_{\perp}(H) = H^3/3$ and $M_{\parallel}(H) = H^2/2$ are the mobility factors associated with the flux due to normal stress and shear stress, $P = -\nabla_{\parallel}^2 H - \Pi_{\mathrm{vdw}}$ is the total pressure,

[1] Similar bifurcation phenomena have been thoroughly discussed in chapter 5.4.2 for EHD patterning.

Π_{vdw} is the disjoining pressure due to van der Waals' effects, and asterisk $(*)$ for the dimensionless in-plane gradient operator has been dropped for brevity. While the governing equations for both TC and EHD patterning (see Eq. (5.1)) possess an external pressure term Π inside P, in TC patterning fluid flow is mainly driven by the Marangoni term $\nabla_{\parallel}\Gamma$ which is absent in EHD patterning. The overall effects of Π are much weaker compared to the Marangoni term and is only significant when the liquid film is at the immediate vicinity of the mask or substrate.

Similar to chapter 5, the symbol ξ represents the control or process variable being spatially modulated. For TC patterning, it can be either topographically patterning the top electrode ($\xi = D(\mathbf{X})$), spatially modulating the temperature of the cold mask ($\xi = \Theta_{\mathrm{cold}}(\mathbf{X})$) or the hot substrate cold mask ($\xi = \Theta_{\mathrm{hot}}(\mathbf{X})$), which are depicted in Fig. 6.1. Specifically, we consider the following form of spatial modulation:

$$\xi = D: \qquad D(\mathbf{X}) = D_0\left[1 + \varrho g(\mathbf{X})\right], \tag{6.2a}$$

$$\xi = \Theta_{\mathrm{hot}}: \quad \Theta_{\mathrm{hot}}(\mathbf{X}) = 1 + \varrho g(\mathbf{X}), \tag{6.2b}$$

$$\xi = \Theta_{\mathrm{cold}}: \quad \Theta_{\mathrm{cold}}(\mathbf{X}) = \varrho g(\mathbf{X}). \tag{6.2c}$$

We only study 1D spatial modulation given by Eq. (5.3a) or (5.3b) in this chapter. 2D spatial modulation (e.g. egg carton shape described by Eq. (5.3c)(c)) is not considered due to limitation in time.

6.1.3 Outline

In Section 6.2, we summarize the main analytical results for TC patterning for the same analysis done in chapter 5.2. In Section 6.3, we summarize the main equations for stationary states in TC patterning and the numerical methods for computing the solutions. In Section 6.4, we discuss in detail the simulation results of the thin film equation for selected parameters to illustrate the spatiotemporal evolution of the liquid film in developing small versus large deformations. In Section 6.5, we study the stability of the non-uniform stationary states via LSA of two parallel ridges and time-dependent simulations and present the results in the form of stability phase diagram similar to those shown in chapter 5.4 for EHD patterning. Finally, we complete this chapter with a discussion in Section 6.6 and a conclusion in Section 6.7.

6.2 Analytical Results

Similar to Section 5.2, we first perform analytical analysis of Eq. (6.1) under the limits of small modulation strength $\varrho \ll 1$ and near the onset of instability when $\mathcal{M} \to \mathcal{M}_c$. The methodology is similar to that carried out in Section 5.2, so we only focus on highlighting the differences between TC and EHD patterning.

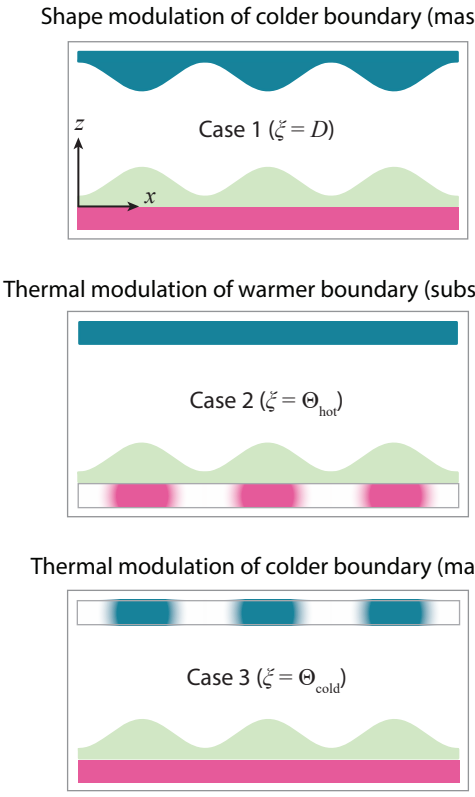

Figure 6.1: Schematic diagram showing the three types of spatially periodic thermal modulation examined in this work. Darker stripes signify cooler regions of modulated boundaries. Published as Fig. 2 in Ref [15].

In this chapter, the Marangoni number $\mathcal{M}$ is often represented as the ratio $\mathcal{M}/\mathcal{M}_c$:

$$\mathcal{M}_c = \frac{2K_p^2}{3}\frac{(D_0+\kappa-1)^2}{\kappa D_0}, \qquad \mathcal{M}_r \equiv \frac{\mathcal{M}}{\mathcal{M}_c} = \frac{\mathcal{M}\kappa D_0}{(D_0+\kappa-1)^2}, \tag{6.3}$$

where $\mathcal{M}_c$ (first introduced in Section 3.1.4) is only a function of D_0 when K_p and κ are held fixed. The parameters are also often reported using ratios of wavelength or wave number in literature, and they are related to $\mathcal{M}_r$ via

$$\mathcal{M}_r = \frac{\mathcal{M}}{\mathcal{M}_c} = \left(\frac{K_c}{K_p}\right)^2 = \frac{1}{2}\left(\frac{K_m}{K_p}\right)^2 = 2\left(\frac{\lambda_p}{\lambda_m}\right)^2, \tag{6.4}$$

where λ_p is the dimensional patterning wavelength, and λ_m is fastest-growing wavelength under LWA given by Eq. (3.13).

6.2.1 Linear theory under small modulation strength $\varrho \ll 1$

When the 1D spatial modulation is given in the form $\xi(\mathbf{X}) = \xi_0\left[1+\varrho\cos(K_p X)\right]$ where $\varrho \ll 1$ is small, we can expand the liquid film thickness as $H(\mathbf{X},\tau) = 1 + \varrho H_1(X) +$

$\mathcal{O}(\varrho^2)$. Since we only look for solutions where $|\varrho H_1|$ is small, the liquid film shape is far from either the mask or substrate so the effects of Π_{vdw} are negligible in the linear analysis. Setting $\Pi_{\text{vdw}} = 0$, Eq. (6.1) can be linearized to give

$$\frac{\partial H_1}{\partial \tau} = -M_\perp(1)\left[K_c^2\frac{\partial^2 H_1}{\partial X^2} + \frac{\partial^4 H_1}{\partial X^4}\right] + M_\parallel(1)K_p^2\xi_0\frac{\partial \Gamma(1,\xi_0)}{\partial \xi}\cos(K_p X), \tag{6.5}$$

which has the same form as Eq. (5.6) for EHD patterning except the expression of the forcing term is different: it now originates from thermocapillary stress and involves $\partial\Gamma/\partial\xi$ whose expression for different types of spatial modulations is given in Appendix B Table B.2. Following the same method described in Section 5.7.1 to solve Eq. (6.5), or simply using the substitution $\partial\Pi/\partial\xi \to [M_\parallel(1)/M_\perp(1)]\partial\Gamma/\partial\xi$, we can obtain the following general solution for $H_1(X,\tau)$ in TC patterning:

$$\begin{aligned} H_1(X,\tau) = &\sum_n \left[a_n\cos(K_n X) + b_n\sin(K_n X)\right] e^{\beta(K_n)\tau} \\ &+ \frac{M_\parallel(1)\xi_0}{M_\perp(1)(K_p^2 - K_c^2)}\frac{\partial\Gamma(1,\xi_0)}{\partial\xi}\cos(K_p X)\left[1 - e^{\beta(K_p)\tau}\right]. \end{aligned} \tag{6.6}$$

If $K_p > K_c$ and $\beta(K_n) < 0 \;\forall\; K_n = 2\pi n/L_x$, the liquid film develops sinusoidal corrugation with the amplitude

$$\begin{aligned} \Delta H_{\text{lin}} \equiv \max[H(\tau\to\infty) - 1] &= \frac{\varrho M_\parallel(1)\xi_0}{M_\perp(1)(K_p^2 - K_c^2)}\left|\frac{\partial\Gamma(1,\xi_0)}{\partial\xi}\right| \\ &= \begin{cases} \dfrac{\varrho K_c^2}{K_p^2 - K_c^2} & \text{if } \xi = D \\ \dfrac{\varrho}{K_p^2 - K_c^2}\dfrac{\mathcal{M}\kappa}{D_0 + \kappa - 1} & \text{if } \xi = \Theta_{\text{hot}} \\ \dfrac{\varrho}{K_p^2 - K_c^2}\dfrac{\mathcal{M}(D_0 - 1)}{D_0 + \kappa - 1} & \text{if } \xi = \Theta_{\text{cold}} \end{cases} \end{aligned} \tag{6.7}$$

and the characteristic time for developing the patterns is $\tau_p = 1/|\beta(K_p)|$ which is the same as Eq. (5.10) for EHD patterning.

6.2.2 Multi-scale expansion near $\mathcal{M} \approx \mathcal{M}_c$

As $K_p \to K_c$, or similarly as $\mathcal{M} \to \mathcal{M}_c$, the solution given by Eq. (6.7) diverges, and the linear theory carried out in Section 6.2.1 no longer holds as the deformation amplitude is no longer small. We can carry out a multi-scale expansion near $\mathcal{M} = \mathcal{M}_c$ using similar scalings as in Section 5.2.2 except the bifurcation parameter is now $\mathcal{M} = \mathcal{M}_c + \delta^2\mathcal{M}_2$.

Expand the liquid film as $H(X,\tau) = 1 + \delta H_1(X,\tau) + \delta^2 H_2(X,\tau) + \cdots$, introduce a slow time as $\tau_2 = \delta^2\tau$, and expand the spatially modulated process variable as $\xi = \xi_0\left[1 + \delta^3\cos(K_p X)\right]$, we have the same leading order solution as in Eq. (5.11)

$$H_1(X,\tau) = a_1(\tau_2)\cos(K_p X), \tag{6.8}$$

where the amplitude $a_1(\tau_2)$ satisfies an amplitude equation with the same form as in Eq. (5.12):

$$\frac{\mathrm{d}a_1}{\mathrm{d}\tau_2} = f_{\mathrm{wnl}}(a_1;\mathcal{M}_2) = c_3 a_1^3 + c_1\mathcal{M}_2 a_1 + c_0, \tag{6.9}$$

but with different coefficients which are now given by [2]

$$c_3 = K_p^4\frac{2D_0^2 + 45(D_0/3+\kappa-1)^2}{72\left[D_0+\kappa-1\right]^2}, \tag{6.10a}$$

$$c_1 = K_p^2 M_{\parallel}(1)\frac{\partial^2\Gamma}{\partial H\partial\mathcal{M}} = -K_p^2 M_{\parallel}(1)\frac{D_0-1}{D_0+\kappa-1}, \tag{6.10b}$$

$$c_0 = K_p^2 M_{\parallel}(1)\xi_0\frac{\partial\Gamma}{\partial\xi}. \tag{6.10c}$$

There exists a critical modulation amplitude ϱ^* given by:

$$\varrho^*_{\mathrm{wna}} = \left|\frac{\mathcal{M}_c - \mathcal{M}}{\mathcal{M}_2^*}\right|^{3/2}. \tag{6.11}$$

For fixed $\mathcal{M}$, the liquid film develops stable sinusoidal corrugation for $\varrho < \varrho^*$. When $\varrho > \varrho^*$, the capillary stress can no longer balance the thermocapillary stress, and so the liquid film exhibits large deformation with a shape that differs from the sinusoidal corrugation substantially.

6.3 Numerical Methods for Studying Stability

Unlike EHD patterning under the perfect dielectric model where the stationary equation can be reduced to Eq. (5.17) which simply states that the fluidic pressure is a constant, in TC patterning the stationary pressure $P_{\mathrm{ss}}(\mathbf{X})$ is no longer a constant due to the addition of shear stress, and the full stationary equations given by Eq. (3.19) needs to be solved which are repeated below for convenience:

[2] In Ref [15], the expansion parameter is the wave number where $K_p = (1+\delta^2 K_2)K_c$. The coefficient c_1 in the resulting amplitude equation are different, but c_3 and c_0 are the same (see Eq. (35)-(36) in Ref [15]).

$$\nabla_\parallel \cdot \left[M_\perp(H_{\rm ss}) \nabla_\parallel P_{\rm ss} - M_\parallel(H_{\rm ss}) \nabla_\parallel \Gamma \right] = 0, \tag{6.12a}$$

$$P_{\rm ss} + \nabla_\parallel^2 H_{\rm ss} + \Pi(H_{\rm ss}) = 0, \tag{6.12b}$$

Unlike EHD patterning where the stationary states do not depend on the mobility factors, here in TC patterning the stationary states depend on both mobility factors $M_\perp(H)$ and $M_\parallel(H)$ since shear stress is present and there is flow within the liquid film. For a 1D spatial domain with N_x grid points, Eq. (6.12) constitutes $2N_x$ equations in $2N_x$ unknowns. In order to enforce volume conservation, one of the equations for Eq. (6.12)(a) is replaced by the equation $\mathrm{mean}[H_{\rm ss}(X)] = 1$. To study the stability of the ridges against perturbation along the Y direction, we can perform LSA by solving the following generalized eigenvalue problem

$$\beta \begin{pmatrix} 1 & 0 \\ 0 & 0 \end{pmatrix} \begin{pmatrix} \hat{H}_1 \\ \hat{P}_1 \end{pmatrix} = \begin{pmatrix} f_{1H} & f_{1P} \\ f_{2H} & f_{2P} \end{pmatrix} \begin{pmatrix} \hat{H}_1 \\ \hat{P}_1 \end{pmatrix}, \tag{6.13a}$$

$$\begin{aligned} f_{1H}\hat{H}_1 = & \left[M'_\perp(H_{\rm ss}) \frac{\partial P_{\rm ss}}{\partial X} - M'_\parallel(H_{\rm ss}) \frac{\partial \Gamma(H_{\rm ss})}{\partial X} - M_\parallel(H_{\rm ss}) \frac{\partial \Gamma'(H_{\rm ss})}{\partial X} \right] \hat{H}_1 \\ & + \left\{ M'_\perp(H_{\rm ss}) \frac{\partial P_{\rm ss}}{\partial X} - M'_\parallel(H_{\rm ss}) \frac{\partial \Gamma(H_{\rm ss})}{\partial X} - M_\parallel(H_{\rm ss}) \frac{\partial \Gamma(H_{\rm ss})}{\partial X} \right. \\ & \left. - \frac{\partial}{\partial X} \left[M_\parallel(H_{\rm ss}) \Gamma'(H_{\rm ss}) \right] \right\} \frac{\partial \hat{H}_1}{\partial X} \\ & - M_\parallel(H_{\rm ss}) \Gamma'(H_{\rm ss}) \frac{\partial^2 \hat{H}_1}{\partial X^2}, \end{aligned} \tag{6.13b}$$

$$f_{1P}\hat{P}_1 = \frac{\partial}{\partial X} \left[M_\perp(H_{\rm ss}) \frac{\partial \hat{P}_1}{\partial X} \right] - K_y^2 M_\perp(H_{\rm ss}) \hat{P}_1, \tag{6.13c}$$

$$f_{2H}\hat{H}_1 = \left[\frac{\partial^2}{\partial X^2} - K_y^2 \right] \hat{H}_1, \tag{6.13d}$$

$$f_{2P}\hat{P}_1 = \mathbf{I}\hat{P}_1. \tag{6.13e}$$

where the coefficients of the Jacobian are Eq. (3.26) with $K_x = 0$. Eq. (6.13) can also be obtained from Eq. (3.26) by setting $K_x = 0$. As there are two additional unknowns β and K_y in Eq. (6.13), one of them needs to be held fixed (or varied as an independent variable in PALC) with the other becoming one of the dependent variable to be solved. An extra equation is obtained from $\int |H_1|^2 \mathrm{d}\mathbf{X} = 1$ in order constrain the norm of the eigenmodes.

Eq. (6.12) and (6.13) are solved numerically using Newton's method coupled with PALC implemented in the Julia package `BifurcationKit.jl` [126] as described in Chapter 4.

Linear elements with element size $\Delta X = \Lambda_p/128$ are used for spatial discretization. The time-dependent thin film equation given by Eq. (6.1) using with grid size $\Delta X = \Lambda_p/128$ in 1D and $\Delta X = \Lambda_p/32$ in 2D. The size of the spatial domain varies for different simulations which will be specified.

6.4 Numerical Results for 1D Ridges with $D_0 = 5$

In this section, we present and describe in detail the simulation results for modulated system with $D_0 = 5.0$ from Ref [15]. Eq. (6.1) is solved numerically with $D_0 = 5.0$, $\kappa = 0.25$, $\mathcal{A} = 0$, $\Lambda_p = 1$ ($K_p = 2\pi$) [3] and $L_x = 64\Lambda_p$. The initial condition is

$$H(X_n, \tau = 0) = 1 + 10^{-3} \times \text{randn}(X_n), \tag{6.14}$$

where randn(X_n) returns a random number drawn from a standard normal distribution and X_n are the coordinates of the discretized grid points. For each set of parameters, the simulation is repeated 50 times, each initialized with a different random initial condition.

Identification of those normal modes that dominate fluid response during growth allowed determination of various physical mechanisms responsible for structure formation during different stages of the patterning process. To that end, spectral analysis was based on the norm $\mathbb{N}(K/K_p, \tau)$ of the DFT of the interface displacement according to

$$\mathbb{N}(K/K_p, \tau)\Big| = \left| \sum_{n=0}^{N-1} \left[H(X_n, \tau) - 1\right] e^{-2\pi i (n/N)(K/K_p)} \right|. \tag{6.15}$$

The wave number with the fastest growth rate computed by Floquet-Bloch analysis given by Eq. (6.13) is denoted by $Q_{\max}$, i.e., $\beta(Q_{\max}) = \max(\beta)$.

First studied by Yang et al. [138], the deformation amplitude of the non-uniform stationary states under spatial modulation increases with $\mathcal{M}_r$ and exhibits bifurcations similar to that shown in Fig. 5.4 for EHD patterning where the liquid film either displays small or large deformation depending on whether $\mathcal{M}_r$ is below or above the fold point $\mathcal{M}_{\text{f1}}$ (analogous to $\mathcal{W}_{\text{f1}}$ for EHD patterning). We will show how the liquid film evolves for both small and large amplitude deformation under spatial modulation in the mask topography and substrate temperature.

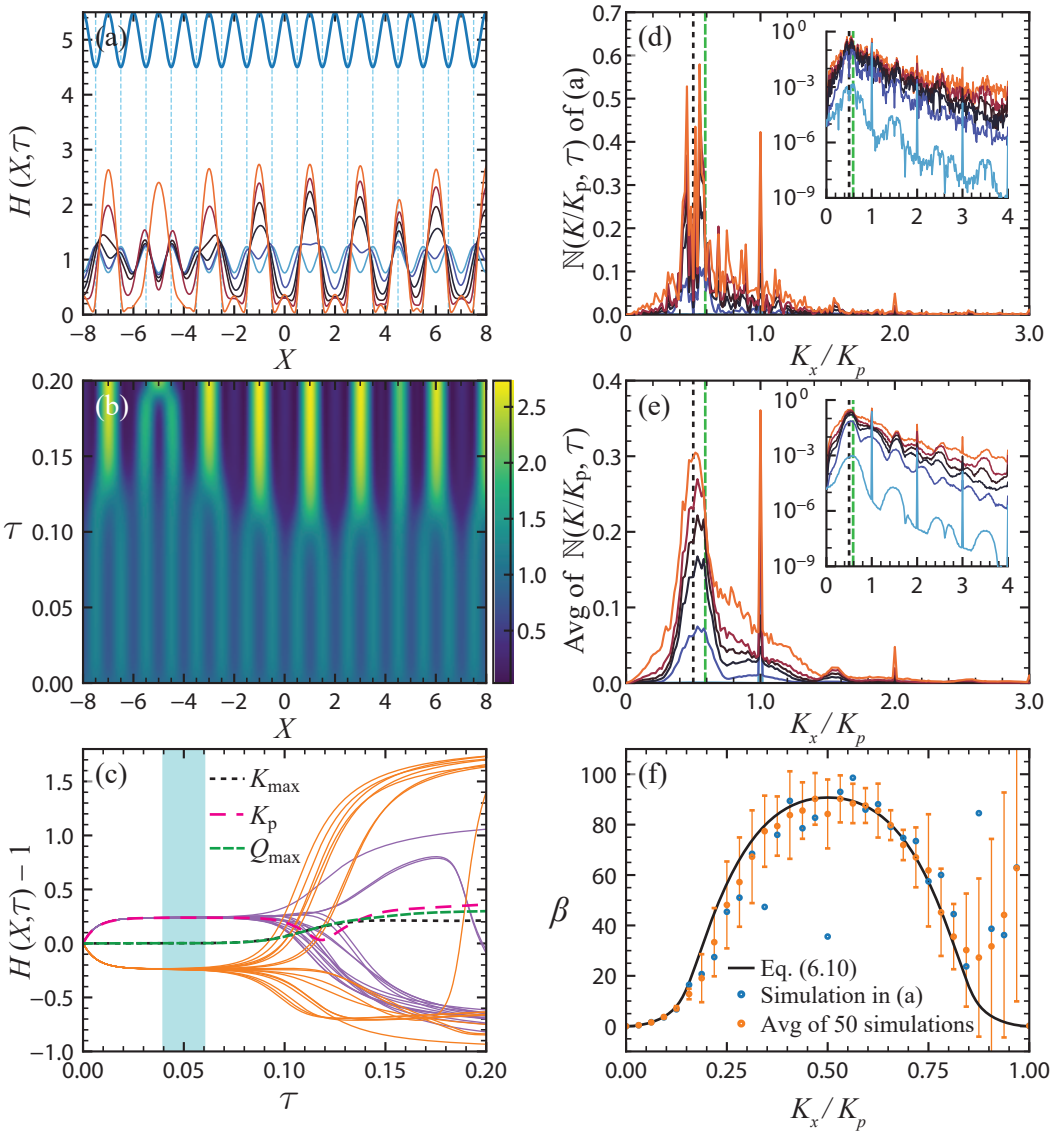

Figure 6.2: Evolution dynamics of liquid film with topographically patterned mask. Parameters: $K_p/K_c = 1.2$ ($\mathcal{M}_r = 0.6944$), $\varrho = 0.1$, $D_0 = 5.0$. (a) Evolution of $H(X,\tau)$ at $\tau = 0.05, 0.1, 0.115, 0.125, 0.14, 0.2$ (partial domain shown). (b) Plan view of structure formation in (a). Lighter colors signify thicker regions of film. (c) Time traces of $H(X,\tau)$ at selected locations: dark curves (purple) signify values at $X_{\rm i} = -7.5, -6.5, \ldots + 6.5, +7.5$; light curves (orange) signify values at $X_{\rm i} = -8.0, -7.0, -6.0, \ldots + 6.0, +7.0, +8.0$. (d) DFT values from Eq. (6.15) for the run in (a) – inset shows same results on a log-linear scale. Vertical dashed lines signify values $Q_{\max}/K_p = 0.5$ (dashed green) and $K_m/K_p = 0.58926$ (dashed black). (e) Average DFT values based on 50 independent runs initialized by Eq. (6.14) – inset shows same results on a log-linear scale. Curves K_m, K_p and $Q_{\max}$ in (c) represent average DFT values extracted from (e). (f) Modal growth rates $\beta(K_x/K_p)$ from Eq. (6.13) for a noise-free periodic state and from DFT results initialized by Eq. (6.14) for $0.04 \le \tau \le 0.06$ (shaded region in (c)). Published as Fig. 6 in Ref [15].

6.4.1 Topographically patterned mask

6.4.1.1 Small amplitude deformation

We begin with the case where the liquid film develops ridges with relatively small deformation which does not touch the mask or substrate.

Shown in Fig. 6.2 are results for $\varrho = 0.10$. Figure 6.2(a) depicts the evolution of multiple protrusions advancing toward the colder sinusoidal boundary. The vertical dashed lines (blue) represent those points of the initial liquid film which are relatively cooler than adjacent regions due to their proximity to the overhangs of the cold boundary. After initial growth, several of the liquid protrusions undergo binary coalescence producing taller structures whose tips on average no longer align with the dashed lines since the coalesced shapes can no longer sustain the pitch enforced by the external modulation. Were the growth process solely controlled by thermocapillary forces without mitigation from capillary forces, then these tips would advance in alignment with the vertical lines. The fact this does not occur reflects the inherent competition between thermocapillary and capillary forces, which varies in time. Figure 6.2(b) shows a plan view of the evolving film thickness in (a). While for $\tau < 0.10$ the array appears to be spatially periodic, uniformity is lost for $\tau > 0.10$ whereupon numerous pairs of protrusions coalesce into single taller protrusions with corresponding faster growth than nearby formations. Such coalescence events lead to final state array configurations which are highly non-uniform and characterized by a larger average pitch than externally prescribed.

Fig. 6.2(c) depicts time traces of the run in (a). After initiation of film deformation, the system settles into a quasi-steady periodic state dominated by the K_p mode which persists for some time. The curves labeled K_m and $Q_{\max}$ (fastest growing mode from coalescence events) indicate corresponding results extracted from (e). This quasi-steady configuration represents the resonant-like state approximated by Eq. (6.6) (as $\tau \to \infty$). The formation of such a uniform, small amplitude periodic state suggests that modulated thermocapillary patterning of thin films offers a high fidelity replication technique (provided the pattern can be solidified *in-situ* during this stationary period). The results in Fig. 6.2(c) indicate that this state eventually becomes unstable to coalescence events in response to interactions induced by a noisy initial condition and interference of the K_p and $Q_{\max}$ modes. Once the majority of peaks have coalesced into pairs, further growth is considerably restrained by the large viscous stresses which develop in the interstitial regions due to progressively more rapid thinning.

Shown in Fig. 6.2(d) are the DFT values obtained from Eq. (6.15) for the run in (a).

[3] The results presented in this section (Fig. 6.2-6.5) came from Ref [15] whose choice of characteristic length scale $l_0 = \lambda_p$ differs slightly from the rest of the thesis by a factor of two. This leads to $\Lambda_p = 1$ and $K_p = 2\pi$ instead of $\Lambda_p = 2$ and $K_p = \pi$ as in the rest of the thesis. The results can be rescaled to match the scalings employed in the rest of this thesis by $H(X,\tau) \to H(2X, 16\tau)$ and $\mathcal{M} \to 4\mathcal{M}$. Note that $\mathcal{M}_r$ remains the same when $\mathcal{M}$ is scaled accordingly.

The average DFT results in Fig. 6.2(e) more clearly highlight the broadband response with the development of significant peaks at $Q_{\max}$, K_p and its higher harmonics. These results, coupled with the modal curves shown in (c), indicate that while the spectral coefficient for K_p remains strong over time, there develops a comparable contribution from $Q_{\max}$ as well. Film coarsening from coalescence, however, ultimately generates a final state marked by considerable non-uniformity in peak height and pitch.

Shown in Fig. 6.2(f) is a comparison of modal growth rates extracted from the DFT analysis for $0.04 \leq \tau \leq 0.06$ along with the predictions for $\beta(K_x)$ given by Eq. (6.13) for a noise-free steady periodic base state. In this run, the symmetry about $K_x/K_p = 0.50$ reflects the periodicity of the underlying Bloch wave in Eq. (3.22) which must satisfy $\hat{H}_1(X) = \hat{H}_1(X + \Lambda_p)$. The results confirm unstable growth for $0 < K_x/K_p < 1$, affirming the observed transition in (c) from a quasi-steady periodic state to a non-uniform final state. The deviations between the eigenvalues $\beta(K_x)$ and the DFT results underscore the influence of noisy initial conditions. These deviations, which increase significantly as K_x approaches K_p, evidence faster growth rates than estimated from a noise-free initial condition.

6.4.1.2 Large amplitude deformation

The behavior just described contrasts significantly with that for $\varrho = 0.25 > \varrho^*_{\text{wna}}$. As evident in Fig. 6.3(a), here the profiles manifest rather perfect registration with the external pitch with strong uniformity in peak amplitude and shape for all times. The liquid tips advance in synchrony and align with the vertical dashed lines denoting the coldest points of the initial liquid film. The plan view in (b) highlights strong uniformity in growth with no evidence of coalescence despite the noisy initial condition. The corresponding time traces in Fig. 6.3(c) neatly collapse onto two curves – the upper one showing peak heights and the lower one the valleys between peaks. The curve marked K_p exactly follows the evolution of peak heights. The film patterning process rapidly approaches its asymptotic periodic configuration without formation of any intermediate, small amplitude periodic state nor subsequent coalesced state. Instead, the DFD results in Figs. 6.3(d) and (e) confirm growth dominated by K_p that is practically uninfluenced by noise, the effects of which only become visible in the inset image. This example shows that for $\varrho > \varrho^*$ and $\mathcal{M}_r < 1$, external modulation is very effective in synchronizing rapid growth despite the presence of small amplitude noise in the initial condition.

The results in Fig. 6.3(f) contrast modal growth values from Eq. (3.7) for $\beta(K)$ based on a noise-free initial condition with results extracted from the DFT analysis for $0 \leq \tau \leq 0.005$ based on a noisy initial condition. The discrepancies in values increase with increasing K_x and becomes significantly larger as $K_x \to K_p$. Capillary forces are therefore not as effective in suppressing thermocapillary growth in thin films subject to a

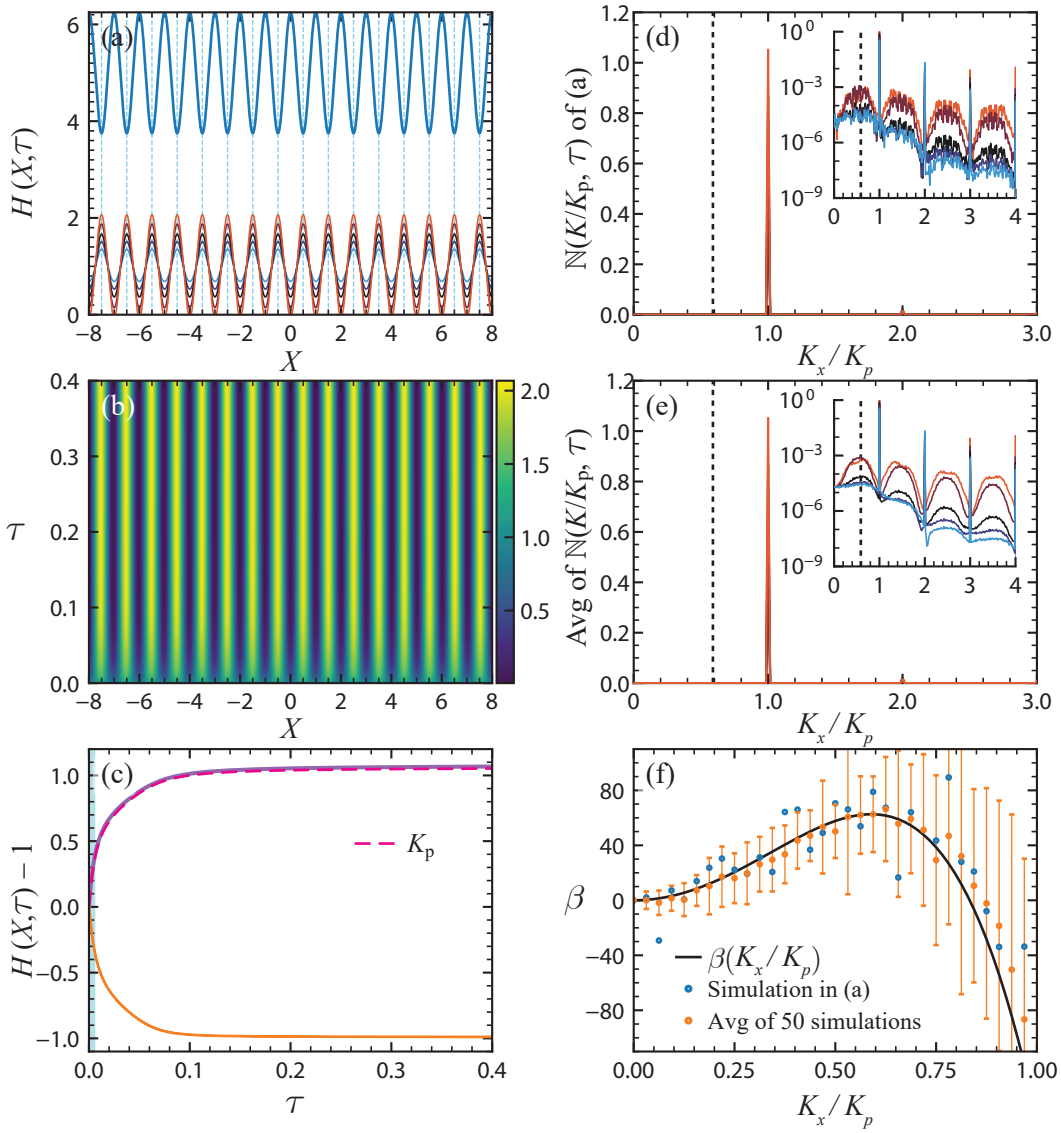

Figure 6.3: Evolution dynamics of liquid film with topographically patterned mask. Parameters: $K_p/K_c = 1.2$ ($\mathcal{M}_r = 0.6944$), $\varrho = 0.25 > \varrho^*$, $D_0 = 5.0$. (a) Evolution of $H(X,\tau)$ at $\tau = 0.005, 0.01, 0.02, 0.05, 0.4$ (partial domain shown). (b) Plan view of structure formation in (a). Lighter colors signify thicker regions of film. (c) Time traces of $H(X,\tau)$ at selected locations: dark curves (purple) signify values at $X_\mathrm{i} = -7.5, -6.5, \ldots + 6.5, +7.5$; light curves (orange) signify values at $X_\mathrm{i} = -8.0, -7.0, -6.0, \ldots + 6.0, +7.0, +8.0$. (d) DFT values obtained from Eq. (6.15) for the run in (a) – inset shows same results on a log-linear scale. Vertical dashed line (black): K_m given by Eq. (3.8). (e) Average DFT values based on 50 independent runs initialized by Eq. (6.14) – inset shows same results on a log-linear scale. Curve K_p in (c) represents average DFT values extracted from (e). (f) Modal growth rates $\beta(K_x/K_p)$ from linear theory given by Eq. (3.7) and numerically computed growth rate from DFT results initialized by Eq. (6.14) for $0 \le \tau \le 0.005$ (shaded region in (c)). Published as Fig. 7 in Ref [15].

small degree of noise. Once again, the influence of noise and resonant excitation effects near K_p appears to increase instability growth rates.

6.4.2 Spatially modulated substrate temperature

As shown in Fig. 6.1, external modulation can also be enforced with flat and parallel boundaries, one of which is subject to spatially periodic thermal modulation. We discuss next a couple of examples for spatially modulated substrate temperature given by $\Theta_{\rm hot}(X) = 1 + \varrho\cos(K_p X)$. As before, we seek guidelines on imprinting films with a finer pitch than accessible to unmodulated systems and here examine systems with $K_p/K_c = 3.0$ and $\varrho = 0.1$ and 0.4.

6.4.2.1 Small amplitude deformation

Shown in Fig. 6.4 are results of simulations conducted with $K_p/K_c = 3.0$ ($\mathcal{M}_r = 0.111$) and $\varrho = 0.10$. The colored horizontal strip shown at the bottom of the image in (a) depicts the periodic thermal modulation of the warmer substrate – the darkest segments (red) and corresponding vertical dashed lines signify the hottest points of the substrate. At early times, the liquid film, now in direct contact with the modulated boundary, undergoes rapid thinning in the vicinity of the hottest points due to the thermocapillary effect, which draws fluid away from the warmer and toward the cooler regions. As time progresses the majority of protrusions undergo coalescence to form fewer and taller peaks. The final configuration resembles a highly irregular array with significant non-uniformity in peak height, shape and pitch. The plan view in (b) and time traces in (c) illustrate more clearly the immediate formation of a quasi-steady periodic state dominated by the mode K_p which persists for a prolonged period in time. The evolution time scales in this example are about an order of magnitude larger than those in Figs. 6.2 and 6.3 since here $\mathcal{M}_r$ is about a factor 6.25 smaller. The time traces and DFT results in Fig. 6.4(c) confirm that the intermediate time periodic state and spectral coefficient of the K_p mode track closely together in time. Eventually, the growth of the unstable mode $Q_{\rm max}$ overcomes influence from the K_p mode which undergoes continual decay. This behavior is also evident from the full DFT data in (d), which shows the dominance of K_p at early and intermediate times and that of $Q_{\rm max}$ at late times. The small contribution from K_m at very early times quickly decays away. The average DFT profiles in (e) highlight this exchange in modal response even more clearly.

The results in Fig. 6.4(f) show the modal growth rates $\beta(Q/K_p)$ from Eq. (6.13) for a noise-free periodic state along with DFT results for $0.20 \le \tau \le 0.40$ initialized by the noisy condition in Eq. (6.14). The growth rates are everywhere positive over the entire range $0 < K_x/K_p < 1.0$ indicating that the quasi-steady periodic state is unstable to coalescence events. Surprisingly, despite the presence of white noise, the agreement between the DFT based results and Eq. (6.13) is remarkably good and likely due to

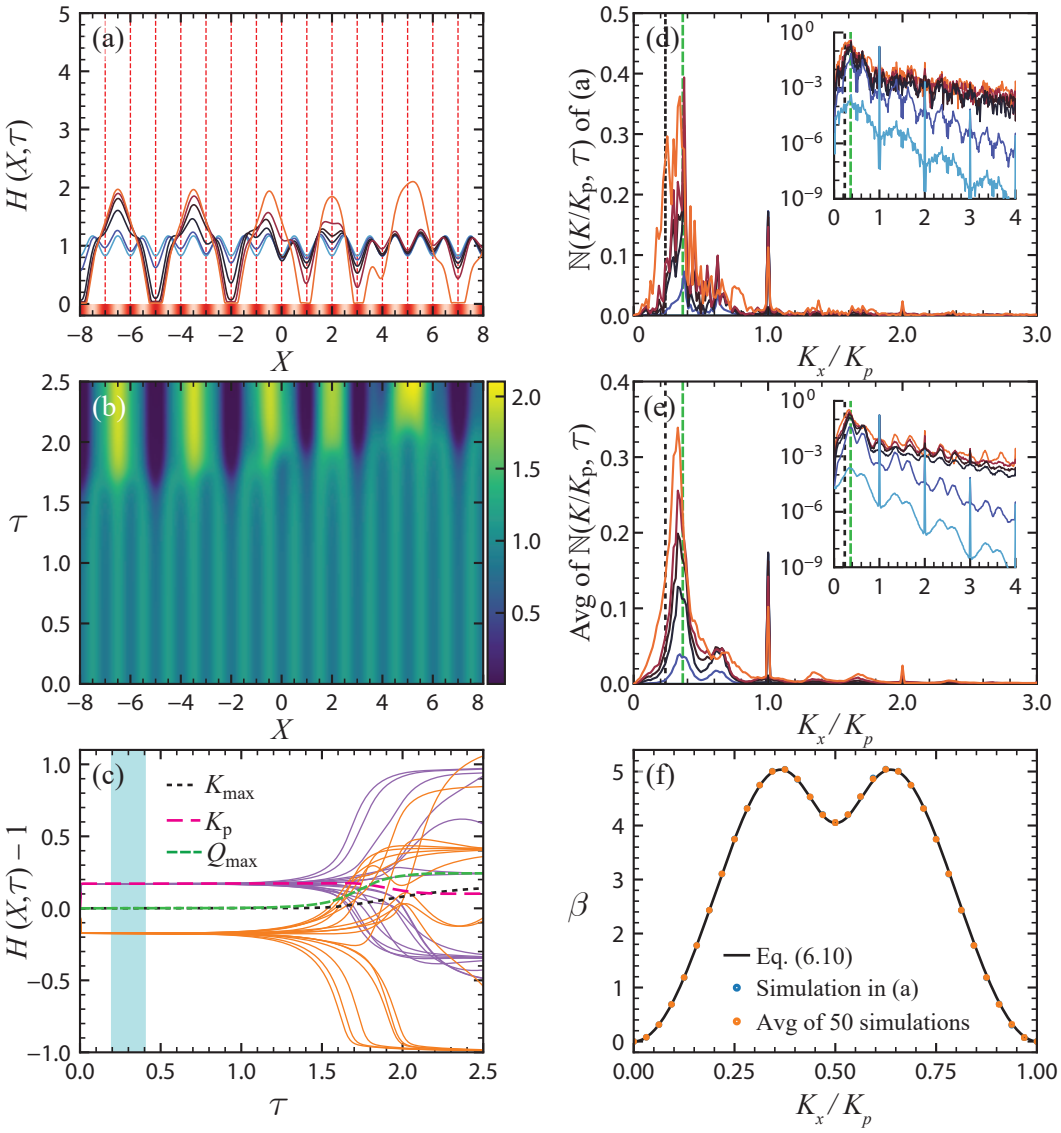

Figure 6.4: Evolution dynamics of liquid film with modulated substrate temperature. Parameters: $K_p/K_c = 3.0$ ($\mathcal{M}_r = 0.111$), $\varrho = 0.1$, $D_0 = 5.0$. (a) Evolution of $H(X,\tau)$ at $\tau = 0.5, 1.5, 1.7, 1.8, 1.9, 2.5$ (partial domain shown). (b) Plan view of structure formation in (a). Lighter colors signify thicker regions of film. (c) Time traces of $H(X,\tau)$ at selected locations: dark curves (purple) signify values at $X_i = -7.5, -6.5, \ldots + 6.5, +7.5$; light curves (orange) signify values at $X_i = -8.0, -7.0, -6.0, \ldots + 6.0, +7.0, +8.0$. (d) DFT values from Eq. (6.15) for the run in (a) – inset shows same results on a log-linear scale. Vertical dashed lines signify $K_m/K_p = 0.23570$ (black) and $Q_{\max}/K_p = 0.365$ (green). (e) Average DFT values based on 50 independent runs initialized by Eq. (6.14) – inset shows same results on a log-linear scale. Curves K_m, K_p and $Q_{\max}$ in (c) represent average DFT values extracted from (e). (f) Modal growth rates $\beta(K_x/K_p)$ from Eq. (6.13) for a noise-free periodic state and from DFT results initialized by Eq. (6.14) for $0.20 \leq \tau \leq 0.40$ (shaded region in (c)). Error bars from multiple simulations are not visible since they are smaller than the marker diameter. Published as Fig. 10 in Ref [15].

two reasons. The first is that the liquid film is in direct contact with the thermally modulated boundary, which affords more direct external control. In addition, the ratio K_p/K_c is fairly large so as to suppress any effects from underlying resonant excitations which occur for smaller values of that ratio.

6.4.2.2 Large amplitude deformation

The behavior shown in Fig. 6.5 for $\varrho = 0.40$ contrasts sharply with that in Fig. 6.4 for smaller modulation amplitude. Despite that the Marangoni number $\mathcal{M} = 42.257$ is much smaller than in all the other examples shown in Figs. 6.2 – 6.3, the fluid undergoes rapid formation of highly uniform arrays with larger amplitude that are in excellent registry with the externally prescribed pitch. The plan view in (b) highlights the persistence of the array regularity, which as evident in Fig. 6.5(c), is controlled by the external modulation wave number K_p. The results in Figs. 6.5 (d) and (e) indicate dominance of the K_p mode with hardly any influence from its higher harmonics and no indication of the mode K_m. This example confirms that external thermal modulation enforced by direct contact of the film with the modulated boundary allows superior control over the pitch and shape of the final periodic state.

The results in Fig. 6.5(f) contrast the modal growth rates for $\beta(K_x/K_p)$ from Eq. (3.7) for a noise-free initial condition with results from DFT analysis for $0 \leq \tau\ 0.005$ based on a noisy initial condition. The values $\beta(K_x/K_p)$ are positive over the range $0 < K_x/K_p < 0.328125$, with a maximum near the point $(K_x/K_p = 0.234375, \beta = 1.6032396)$. The symmetry about $K_x/K_p = 0.50$ is simply related to the periodicity of the underlying Bloch wave. The mean value of the DFT results is in excellent agreement with the theoretical prediction predicated on a noise-free initial condition. These results indicate that the large value of $K_p/K_c = 3.0$ prevents any resonant excitation effects from setting in and allows capillary forces to dampen growth rates at larger wave numbers, just as occurs in the idealized analysis with noise-free initial conditions.

6.5 Stability Results for Ridges

After illustrating the spatiotemporal dynamics of the liquid film for a few selected parameters with $D_0 = 5.0$ in the previous section, here we turn to study the stationary states and the associated stability for a much wider range of parameters by presenting the results in the form of phase diagram similar to those shown in Section 5.4.

The parameters for all the simulations presented in this section are fixed at $\kappa = 0.25$, $\mathcal{A} = 10^{-3}$, $\Lambda_p = 2$ $(K_p = \pi)$ and $\tau_f = 20\tau_{\max}$ unless otherwise specified.

We attempt to address the problem of high fidelity pattern formation again using two approaches: LSA of two parallel ridges and the time-dependent simulations of Eq. (6.1) in a large spatial domain which supports the development of multiple ridges. For LSA,

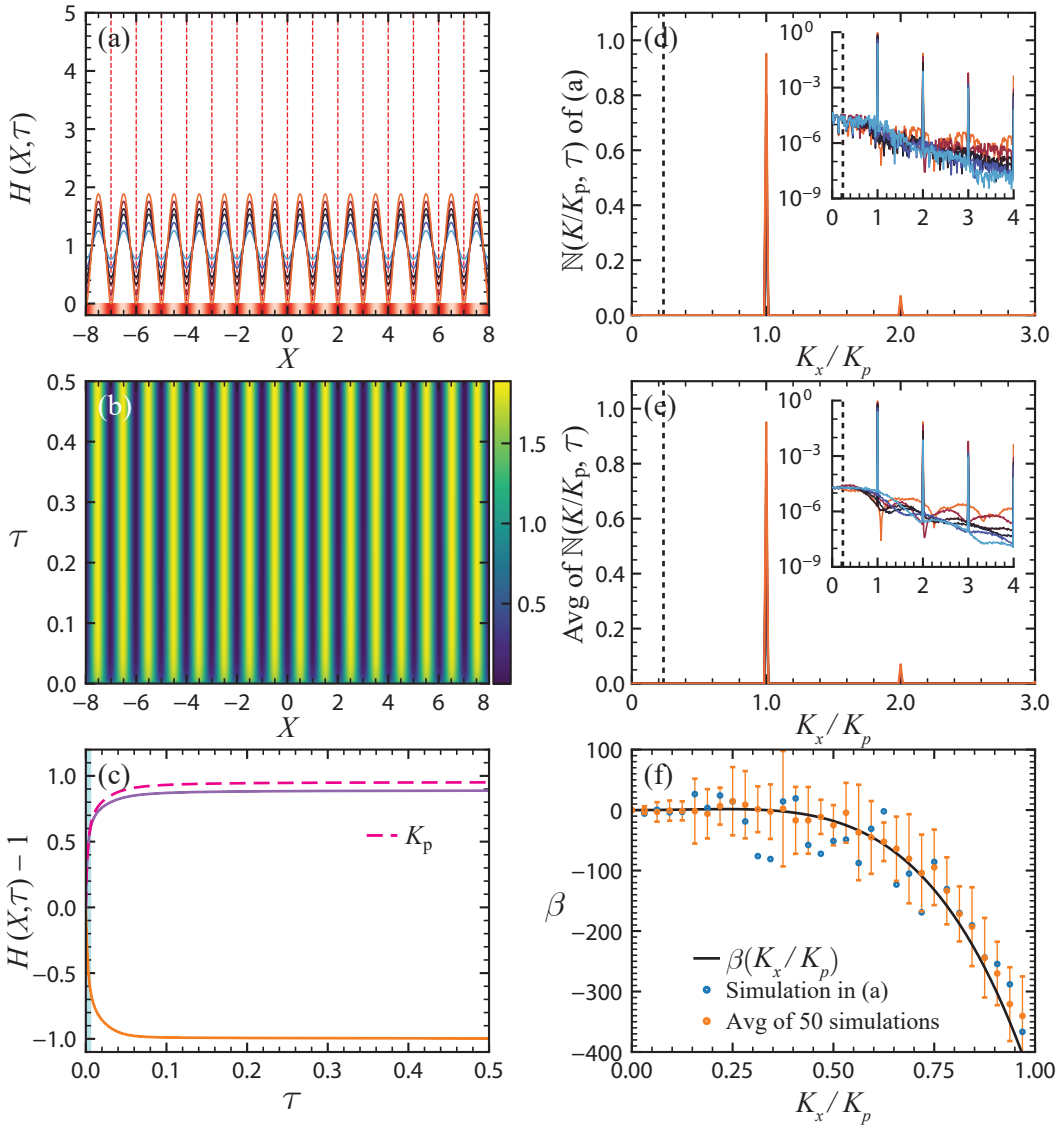

Figure 6.5: Evolution dynamics of liquid film with modulated substrate temperature. Parameters: $K_p/K_c = 3.0$ ($\mathcal{M}_r = 0.111$), $\varrho = 0.4$, $D_0 = 5.0$. (a) Evolution of $H(X,\tau)$ at $\tau = 0.001, 0.002, 0.004, 0.007, 0.02, 0.5$ (partial domain shown). (b) Plan view of structure formation in (a). Lighter colors signify thicker regions of film. (c) Time traces of $H(X,\tau)$ at selected locations: dark curves (purple) signify values at $X_\mathrm{i} = -7.5, -6.5, \ldots + 6.5, +7.5$; light curves (orange) signify values at $X_\mathrm{i} = -8.0, -7.0, -6.0, \ldots + 6.0, +7.0, +8.0$. (d) DFT values from Eq. (6.15) for the run in (a) – inset shows same results on a log-linear scale. Vertical dashed line: $K_m/K_p = 0.23570$ (black). (e) Average DFT values based on 50 independent runs initialized by Eq. (6.14) – inset shows same results on a log-linear scale. Curve K_p in (c) represents average DFT values extracted from (e). (f) Modal growth rates $\beta(K/K_p)$ from Eq. (3.7) for a noise-free initial condition and from DFT results initialized by Eq. (6.14) for $0 \le \tau \le 0.005$ (shaded region in (c)). Published as Fig. 11 in Ref [15].

we proceed directly to the analysis of two parallel ridges by probing the response of the four most unstable modes (symmetric/asymmetric varicose/zigzag modes as shown in Fig. 5.13(b)) to perturbation with wave number K_y. We skip the the Floquet-Bloch analysis with nonzero K_x having already studied a similar system for EHD patterning in Chapter 5 and discovered that stability in 1D is usually decided at $K_x = K_p/2$ which involves the interactions between two ridges. For the time-dependent simulations, we again study 1D and 2D system separately to understand the differences between the two spatial dimensions – one of which (X) is periodic and the other (Y) is not.

6.5.1 Sinusoidal modulation in mask topography

We start with studying 1D sinusoidal modulation in the mask topography given by $D(X) = D_0\,[1 + \varrho\cos(K_p X)]$. Similar to Section 5.4.3.2 (see page 85 for details), the results presented mainly involve (1) minimum precursor and air gap thickness as the background heatmap, (2) stability contours obtained with PALC which represent parameters where $\max[\beta(K_y)] = 0$ for the four most unstable modes in a system with two parallel ridges, and (3) phase of the liquid film based on $\mathcal{E}_{\rm rms}(\tau_f)$, $\min[\mathcal{E}_{\rm rms}(\tau)]$ and $\mathcal{E}_{\rm shifted}(\tau_f)$ from time-dependent simulations.

6.5.1.1 1D system

We first investigate whether high fidelity patterns can be formed in a 1D system for two different electrode separations: $D_0 = 3$ and $D_0 = 5$.

Fig. 6.6 shows the results for $D_0 = 3$. The background gray scale heat map (in logarithmic scale for better visualization) shows the minimum film and air gap thickness of the stationary states. The sharp transition in color originating from $\mathcal{M}_r \approx 1.0$ shows the bifurcation in the deformation amplitude. In the large deformation amplitude case (i.e., large $\mathcal{M}_r$ with light background color), $\min(H_{\rm ss})$ is small, which implies the precursor film thickness between neighboring ridges is very thin. However, the air gap $\min(D - H_{\rm ss})$ is not necessarily small especially for small ϱ where the minimum air gap thickness is $\mathcal{O}(10^{-1})$. As ϱ increases, the separation between the mask and substrate decreases in the region where ridges are formed, and the top of the ridges become closer to the patterned mask.

The symbols show that all parameters in the small deformation regime are 'unstable' when inspected at $\tau = 20\tau_{\rm max}$. Even in the large deformation regime, the majority of the stationary states under investigated are still unstable or even inaccessible, except those with small ϱ and large $\mathcal{W}_r$ which do not touch the patterned mask. This shows that for the specific case of sinusoidally modulated mask topography with $D_0 = 3.0$, contact with the patterned mask does *not* lead to high fidelity patterns as in the case for EHD patterning.

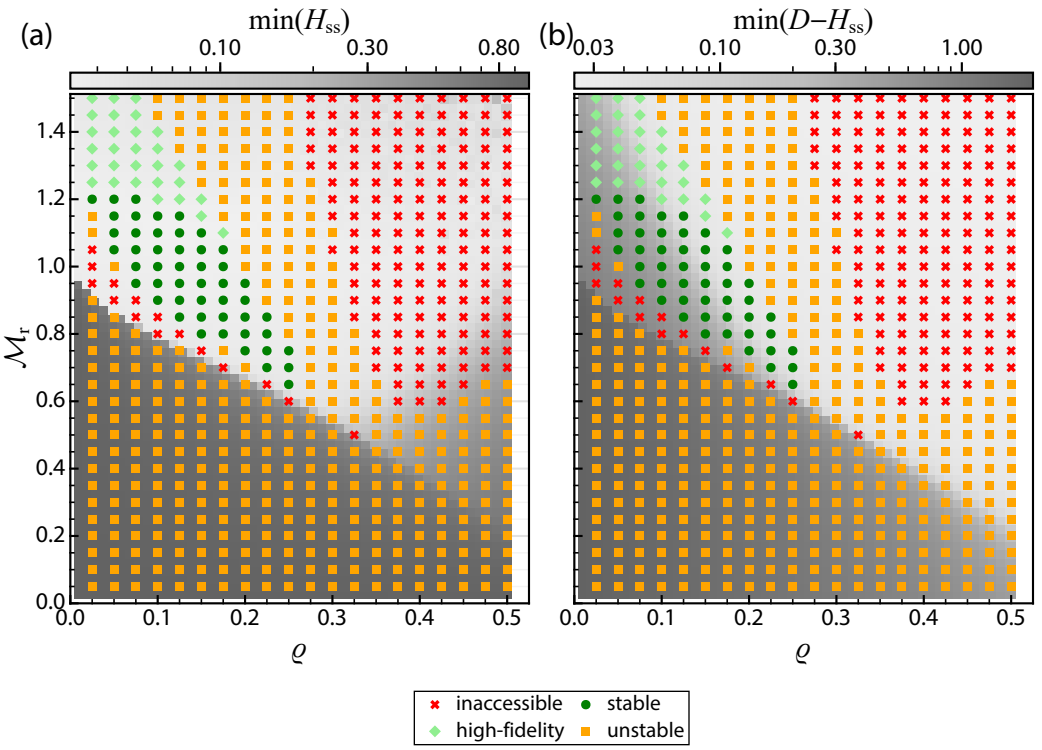

Figure 6.6: Stability phase diagram based on time-dependent simulations for sinusoidal modulation in $D(X)$ with $D_0 = 3.0$. Background grayscale heat map represents (a) minimum film thickness $\min(H_{\rm ss})$ and (b) minimum air gap thickness $\min(D - H_{\rm ss})$ in logarithmic scale. Symbols represent the phase of the stationary states according to the criteria in section 5.4.3.2 on page 85, where $\mathcal{E}_{\rm rms}(\tau)$ and $\mathcal{E}_{\rm shifted}(\tau)$ are averaged across 10 independent realizations evaluated at $\tau = 20\tau_{\rm max}$ for 1D time dependent simulations with $L_x = 16\Lambda_p$.

Fig. 6.7 shows the results for $D_0 = 5.0$. From the background gray scale colors, in the large deformation regime (i.e., large $\mathcal{M}_r$ with light background color) the stationary state has very thin precursor film thickness $\min(H_{\rm ss})$, but does not establish contact with the patterned mask except for $\varrho \gtrsim 0.35$. More stationary states over a broader parameter range in the large deformation regime are classified as 'stable' (i.e., $\mathcal{E}_{\rm rms}(\tau_f) < 0.01$) or 'high fidelity' ($\mathcal{E}_{\rm shifted}(\tau_f) < 0.01$), and they all have relatively large air gap thickness. This again suggests the conditions for forming high fidelity patterns to be having large deformations with small precursor film thickness without touching the top.

6.5.1.2 2D system

Next, we turn to 2D system and study the stability by first considering the LSA of two parallel ridges, then the time-dependent simulations in a large 2D spatial domain.

The stability contours for the (a)symmetric varicose modes and zigzag modes com-

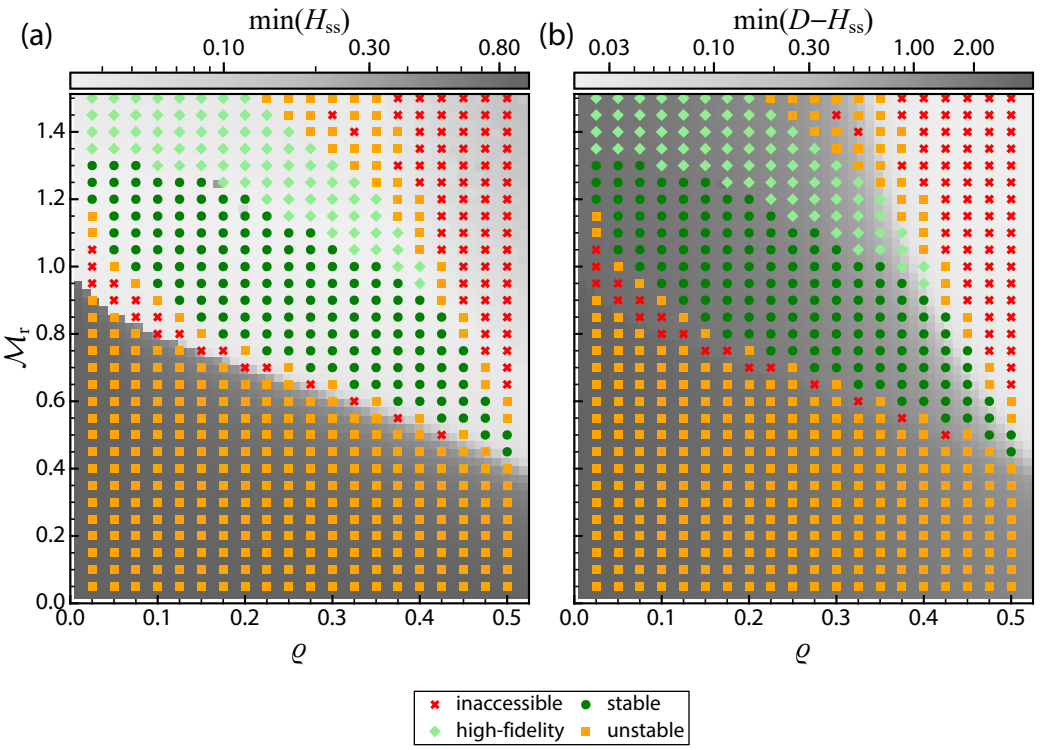

Figure 6.7: Stability phase diagram based on time-dependent simulations for sinusoidal modulation in $D(X)$ with $D_0 = 5.0$. Background grayscale heat map represents (a) minimum film thickness $\min(H_{\rm ss})$ and (b) minimum air gap thickness $\min(D - H_{\rm ss})$ in logarithmic scale. Symbols represent the phase of the stationary states according to the criteria in Section 5.4.3.2 on page 85, where $\mathcal{E}_{\rm rms}(\tau)$ and $\mathcal{E}_{\rm shifted}(\tau)$ are averaged across 10 independent realizations evaluated at $\tau = 20\tau_{\rm max}$ for 1D time dependent simulations with $L_x = 16\Lambda_p$.

puted using PALC are shown in Fig. 6.8(a) and (b), respectively, for $D_0 = 3.0$. The shaded region bounded by the colored line represents the unstable parameter range where $\max[\beta(K_y)] > 0$. For comparison with EHD patterning, the stability contours for the (a)symmetric varicose modes can be found in Fig. 5.14 and 5.16, while the asymmetric zigzag mode can be found in Fig. 5.9 and 5.11 (as the 1D coalescence mode). A couple similarities and differences can be observed and they are summarized below:

- The symmetric varicose mode (black/gray in Fig. 6.8(a)) is unstable under the investigated range of ϱ and $\mathcal{M}_r$ except a narrow stable range between $0.1 < \varrho < 0.32$ and $\mathcal{M}_r > 0.6$. This is qualitatively different from that in EHD patterning where the symmetric varicose mode is stable for large ϱ and $\mathcal{W}_r$ (i.e., upper right half of Fig. 5.14 and 5.16).
- The asymmetric varicose mode (blue in Fig. 6.8(a)) is qualitatively similar to that in EHD patterning where it has a bounded unstable parameter region. It is stable

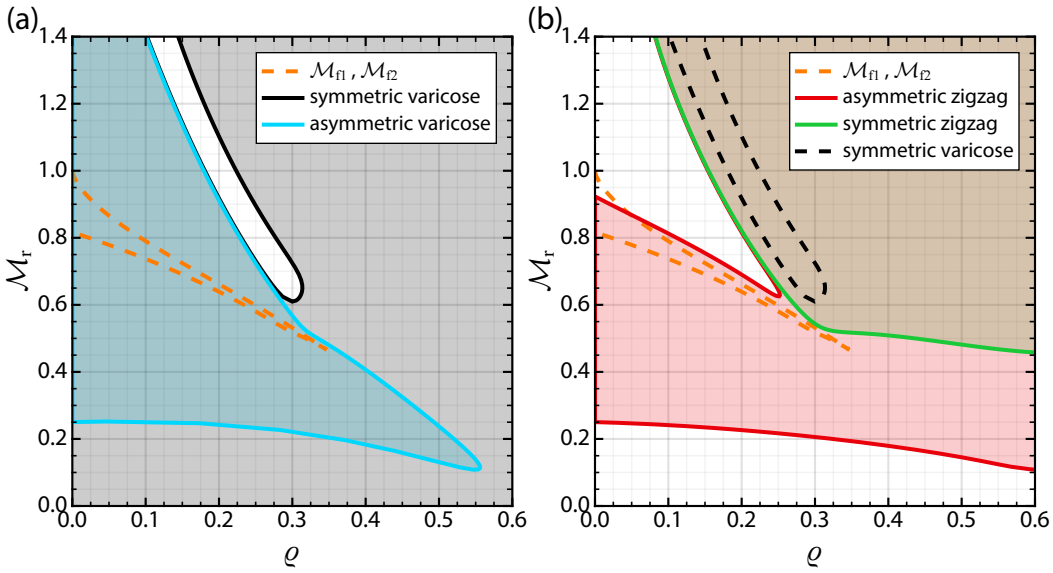

Figure 6.8: Stability phase diagram for four major modes in TC patterning for sinusoidal modulation in $D(X)$ with $D_0 = 3.0$. (a) Symmetric (black/gray) and asymmetric (blue) varicose modes. (b) Symmetric (red) and asymmetric (green) zigzag modes. Solid lines represent contours with $|\max(\beta)| \leq 10^{-3}$. Shaded region represents unstable parameter range for the corresponding mode. Dashed orange line represents the fold points $\mathcal{M}_{f1}$ and $\mathcal{M}_{f2}$.

for large ϱ and $\mathcal{M}_r$, and also for the small $\mathcal{M}_r$ below the bottom branch of the stability contour where the thermocapillary stress is relatively weak.

- Symmetric zigzag mode (green in Fig. 6.8(b)) is unstable for sufficiently large $\mathcal{M}_r$ and ϱ, i.e., the upper right region of the diagram, which is drastically different from the case in EHD patterning where the symmetric zigzag mode is always stable regardless of ϱ and $\mathcal{W}_r$ within the range of parameters investigated. The dispersion relation $\beta(K_y)$ (not shown) is always maximized at $K_y = 0$ which corresponds to the translation mode in a 1D system.

- The asymmetric zigzag mode (red in Fig. 6.8(b)) is also unstable for a large range of parameters except for large $\mathcal{M}_r$ and small ϱ in the top left region of the diagram, as well as the bottom region with small $\mathcal{M}_r$. The dispersion relation $\beta(K_y)$ (not shown) is always maximized at $K_y = 0$ which corresponds to the coalescence of two neighboring ridges at halfway point.

The results from Fig. 6.8 explain why all the stable states in Fig. 6.6 are clustered in top left corner: the asymmetric zigzag mode, which is equivalent to the 1D coalescence mode, is only stable in that small region with large $\mathcal{M}_r$ and small ϱ. Note

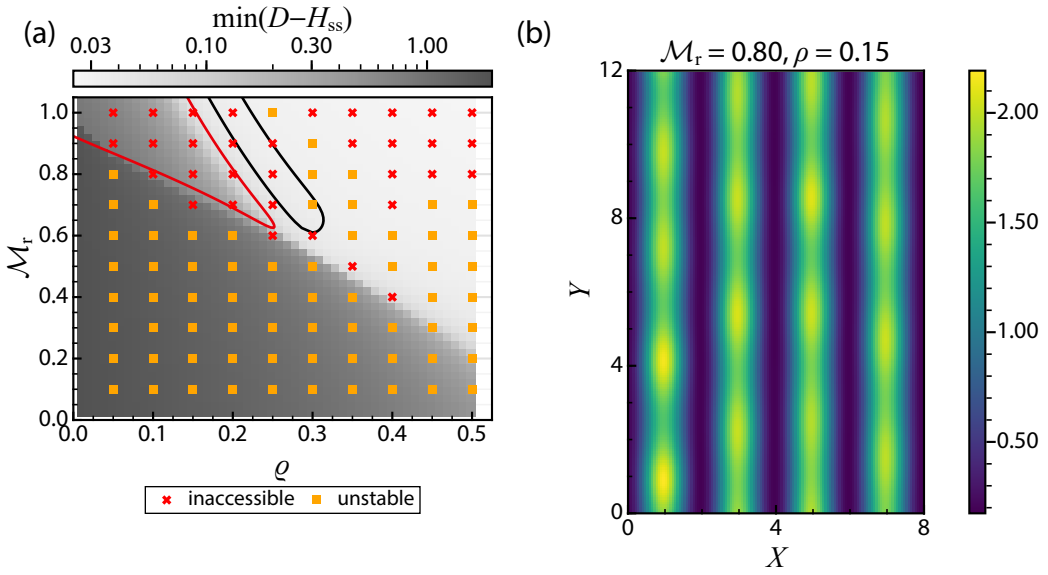

Figure 6.9: Time-dependent simulation results of Eq. (6.1). Parameters: $D_0 = 3.0$, $(L_x, L_y) = (4\Lambda_p, 6\Lambda_p)$, $\tau_f = 20\tau_{\max}$. (a) Symbols represent the phase of the stationary states according to the criteria in Section 5.4.3.2 on page 85, where $\mathcal{E}_{\rm rms}(\tau)$ and $\mathcal{E}_{\rm shifted}(\tau)$ are averaged across 3 independent realizations. Background color represents the minimum film thickness $\min(H_{\rm ss})$. The red and black solid lines are the stability contours for the asymmetric zigzag and symmetric varicose modes from Fig. 6.8 respectively.(b) One particular realization of the liquid film shape $H(X, Y)$ for $\varrho = 0.15$ and $\mathcal{M}_r = 0.8$ evaluated at the time where the $\mathcal{E}_{\rm rms}(\tau)$ is the smallest.

that the symmetric varicose mode does not exist in a 1D system as it violates volume conservation.

The stable parameter range for the symmetric varicose mode is also plotted in Fig. 6.8(b) as black dash line. It is clear that the stable parameter range of the symmetric varicose mode and the zigzag modes do not overlap, hence two parallel ridges under sinusoidally modulated mask is unstable for *all* ϱ and $\mathcal{M}_r$ investigated in a 2D system where the liquid film can vary along the Y direction. This is in contrast to the EHD patterning where for all the parameters investigated, there is always certain parameter range leading to stable stationary states.

Next, we turn to 2D time-dependent simulations of Eq. (6.1) with $(L_x, L_y) = (4\Lambda_p, 6\Lambda_p)$, and the results are shown in Fig. 6.9(a). Consistent with the results in Fig. 6.8 that no stable stationary state is achievable for two parallel ridges, no high fidelity patterns can be sustained up to $\tau = 20\tau_{\max}$ as the ridges destabilize for all the parameters investigated. Fig. 6.9(b) shows an example of the liquid film at the time where $\mathcal{E}_{\rm rms}(\tau)$ is minimized for $\varrho = 0.15$ and $\mathcal{M}_r = 0.8$. Careful inspection of the figure shows that width and height of the ridges are not uniform but instead show early sign of destabilization via the varicose mode. This gives an example of the inaccessible states where the ridges

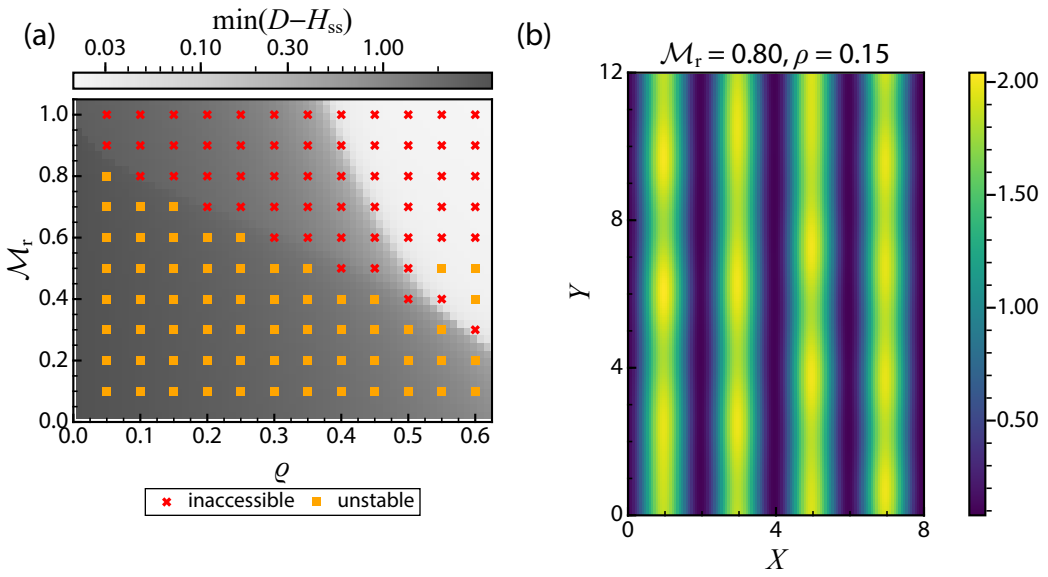

Figure 6.10: Time-dependent simulation results of Eq. (6.1). Parameters: $D_0 = 5.0$, $(L_x, L_y) = (4\Lambda_p, 6\Lambda_p)$, $\tau_f = 20\tau_{\max}$. (a) Markers represent the minimum achievable RMS deviation averaged across 3 independent realizations. Background color represents the minimum film thickness $\min(H_{\rm ss})$. (b) One particular realization of the liquid film shape $H(X, Y)$ for $\varrho = 0.15$ and $\mathcal{M}_r = 0.8$ evaluated at the time where the instantaneous RMS deviation is the smallest. (c) The quasi-steady time scale $\tau_{\rm qs}$ as a function of $\mathcal{M}_r$ and ϱ averaged across 3 independent realizations. (d) The ratio $\tau_p = 1/|\beta(K_p)|$ using the same results as (c).

destabilize before the film reaches the predicted stationary state for small ϱ and large $\mathcal{M}_r$.

Fig. 6.10 shows the results for 2D time dependent simulations for $D_0 = 5$. The results are qualitatively similar to those shown in 6.9 for $D_0 = 3$, suggesting that the general trends observed hold for different electrode separations.

6.5.2 Rectangular modulation in mask topography

Next, we study the rectangular modulation in $D(X)$ given by Eq. (5.3b) with $w_{\rm rect} = 0.5$ and $l_{\rm rect} = 0.02$. Its shape is shown in the inset of Fig. 5.18. Compared to a sinusoidally patterned mask, the rectangular modulation results in a flat surface in the region closest to the tip of the ridges.

6.5.2.1 Stability for two parallel ridges

Fig. 6.11 shows the stability contours and the corresponding unstable parameters for the four fundamental modes of two parallel stripes with $D_0 = 3.0$. Comparison with Fig. 6.8 for sinusoidal modulation reveals a few similarities and differences. First, symmetric and asymmetric varicose modes as well as the asymmetric zigzag modes have topologically

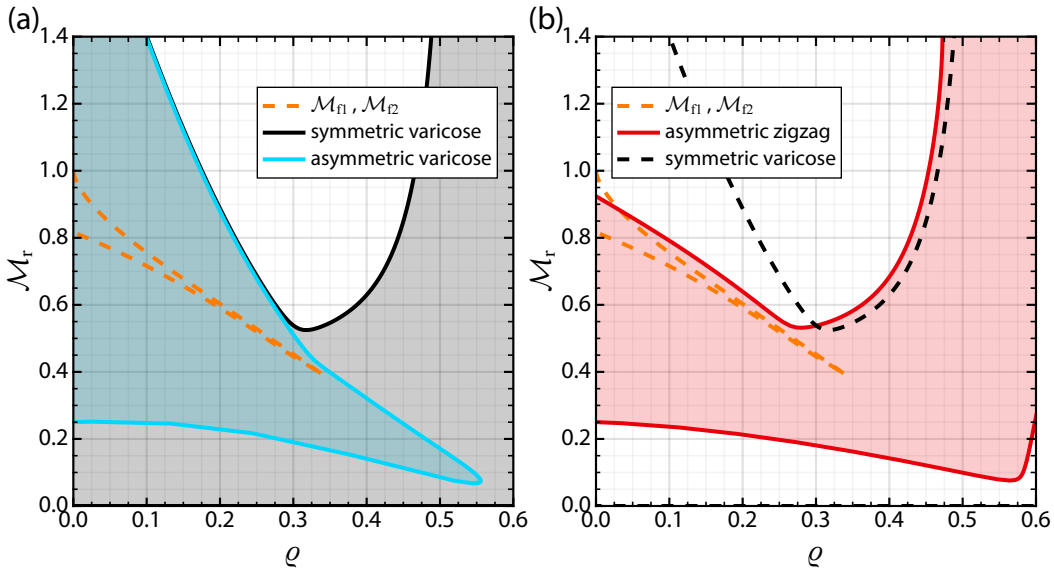

Figure 6.11: Stability phase diagram for four major modes in TC patterning for rectangular modulation (Eq. (5.3b) with $l_{\text{rect}} = 0.02$) in $D(X)$ with $D_0 = 3.0$. (a) Symmetric (black/gray) and asymmetric (blue) varicose modes. (b) Symmetric (red) and asymmetric (green) zigzag modes. Solid lines represent contours with $|\max(\beta)| \leq 10^{-3}$. Shaded region represents unstable parameter range for the corresponding mode. Dashed orange line represents the fold points $\mathcal{M}_{f1}$ and $\mathcal{M}_{f2}$.

similar stable and unstable regions in the parameter space, but the symmetric varicose and asymmetric zigzag modes both exhibit much larger stable regions than that for sinusoidal modulation, resulting in region of the parameter space (center top region) where both modes are stable. Second, the symmetric zigzag mode which is not shown in Fig. 6.11 is now stable for all parameters investigated. This is in stark contrast to the case of sinusoidal modulation where the symmetric zigzag mode is unstable for large $\mathcal{M}_r$ and ϱ.

6.5.2.2 Time dependent simulations in 1D

Fig. 6.12 shows the stability phase diagram where the symbols denote the phase of the stationary states evaluated at the final time τ_f. 'Stable' stationary states occur in the stable region for the coalescence mode (i.e., above the red solid line), and whether it touches the patterned mask no longer affects the stability as long as the precursor film thickness remains thin.

The results for rectangular modulation in mask topography for $D_0 = 3.0$ suggests that the sufficient condition for obtaining high fidelity patterns in 1D are simply having thin precursor film thickness regardless of contact with the patterned mask.

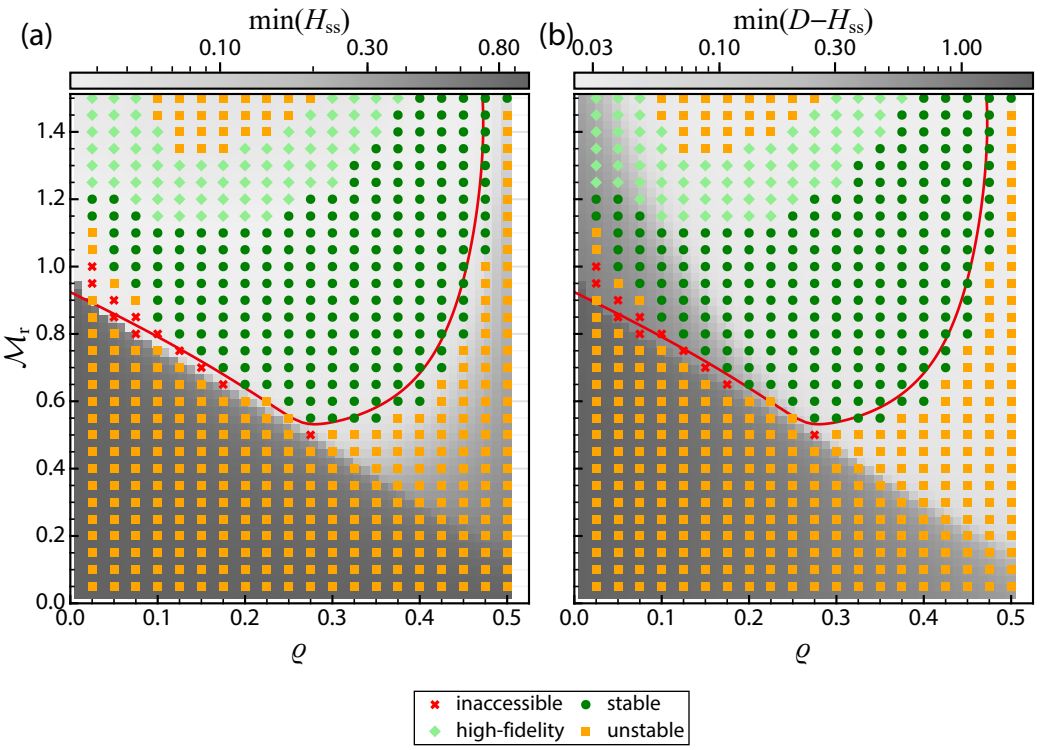

Figure 6.12: Stability phase diagram based on time-dependent simulations for rectangular modulation (Eq. (5.3b) with $l_{\rm rect} = 0.02$) in $D(X)$ with $D_0 = 3.0$. Background grayscale heat map represents (a) minimum film thickness $\min(H_{\rm ss})$ and (b) minimum air gap thickness $\min(D - H_{\rm ss})$ in logarithmic scale. Symbols represent the phase of the stationary states according to the criteria in Section 5.4.3.2 on page 85, where $\mathcal{E}_{\rm rms}(\tau)$ and $\mathcal{E}_{\rm shifted}(\tau)$ are averaged across 10 independent realizations evaluated at $\tau = 20\tau_{\rm max}$ for 1D time dependent simulations with $L_x = 16\Lambda_p$. Solid red line represents the stability contour for the asymmetric zigzag mode (equivalent to 1D coalescence mode).

6.6 Discussion

Marangoni effect due to thermocapillarity results in a shear stress which drives fluid to flow even at stationary state. In contrast to EHD patterning (under perfect dielectric model) where the electrostatic stress pulls the free surface of the liquid film in the normal direction, here the thermocapillary stress pulls the free surface in the lateral direction. When the protrusions or the ridges contact the patterned mask, they are no longer 'pinned' upward to the mask as in EHD patterning but instead have a tendency to flow laterally. This intuitive picture is consistent with the stability results for two parallel ridges shown in Fig. 6.8 and 6.11 where the zigzag modes become unstable over a larger parameter range. The ridges also destabilize mainly via coalescence of neighboring ridges, which is different from EHD patterning where the ridges destabilize via Ostwald-ripening. This is apparent from inspecting Fig. 6.2 and 6.4 where the neighboring ridges merge and form larger ridges in between the original position of the smaller ridges,

while in EHD patterning we see the growth of ridges at the same position drawing fluid from neighboring ridges. The results are also consistent with previous numerical studies on EHD-TC combined patterning [80, 82] which reported the lateral movement of protrusions due to the addition of thermocapillary effect.

The precise shape of the topographically patterned mask also deserves more attention in future studies as it appears to have a major role in determining the stability of the ridges when they contact the patterned mask. This can be seen by comparing the results of sinusoidal and rectangular modulation in mask topography shown in Fig. 6.8 and 6.11 where difference in the mask topography significantly alters the stability of the zigzag modes. Another instance of this is in EHD patterning for relatively small electrode separation of $D_0 = 2.0$ shown in Fig. 5.17. In that case, when sinusoidally modulated mask is used, the asymmetric zigzag mode becomes unstable for certain parameters where a large portion of the stationary state is in contact with the patterned mask. The stability of such stationary states with small D_0 may depend sensitively on the direction of the force acting on the free surface, and hence the precise shape of the mask topography.

Finally, for ridges with small deformation amplitude, while they are linearly unstable, results from time-dependent simulations shown in Fig. 6.2-6.5 clearly show that time scale for destabilization can be relatively long compared to the initial time scale for forming patterns. Similar to EHD patterning, such quasi-steady states deserve more thorough study in future works as they may provide a window of opportunity for external intervention to solidify the film and retain high fidelity patterns in practice.

6.7 Conclusion

In TC patterning where the liquid film is deformed by thermocapillary stress, linear and weakly-nonlinear theory arrive at the same governing equation as in EHD patterning. This gives qualitatively similar results on the deformation amplitude of a single ridge where there exists small and large deformation regimes as the modulation amplitude ϱ and the dimensionless number for the destabilizing effect $\mathcal{M}_r$ are varied.

In a 1D system, contact with the patterned mask no longer guarantees stable stationary states because the zigzag modes can become unstable for certain topography of the patterned mask, while thinning of the precursor layer between neighboring ridges appears to be sufficient for forming stable mass-limited patterns when the zigzag modes remain stable. In 2D, premature breakup of ridges results in inaccessible states similar to those in EHD patterning. However, time-dependent simulation results suggest quasi-steady states may still be achievable for a wide range of parameters.

Chapter 7

OPTIMAL CONTROL OF ELECTROHYDRODYNAMIC PATTERNING

7.1 Background and Motivation

Despite the huge potential applications of thin liquid film patterning including the EHD and TC patterning discussed in Chapters 5 and 6, more widespread development and adoption of the technology are limited because of the inherent difficulty in precisely controlling the shape of the liquid film for device fabrication. Most previous studies in literature as well as Chapters 5 and 6 of this thesis focus on what we call the 'direct' or 'forward' problems which focus on how changes to the material properties or experimental conditions affect the resulting spatiotemporal evolution of the liquid film. However, this approach falls short in addressing the needs for lithographic purposes, where we are often interested in finding the optimal strategies, such as designing the electrode shape or the applying suitable voltage signal, for controlling the spatiotemporal evolution of the liquid film toward a predetermined shape dictated by the intended functionality of the device. It is difficult, if not impossible, to determine the optimal spatiotemporal profiles of these control variables for shaping the liquid film by trial and error or by generalizing the results from studying the direct problems due to the highly nonlinear nature of the resulting dynamics of the liquid film. This motivates us to apply optimal control techniques in studying the optimal strategy of shaping liquid film toward arbitrary shapes.

Here we first review recent literature on the control of free surface flow in thin liquid film, focusing on systems governed by nonlinear parabolic-type PDEs similar to the ones studied in this thesis. We focus on studies trying to control the shape of the free surface $H(\mathbf{X}, \tau)$ to match a specific target shape, such as a uniform flat film, non-uniform film and traveling wave solutions. The control of more general hydrodynamic system can be found in Gunzburger [51], while the inverse problem in free surface flow was reviewed in Sellier [106].

The most straight forward approach to the control of the liquid film shape is to solve the inverse problem of the unknown control variable from the stationary equation using the target shape as the given free surface shape, i.e., finding the control variables (such as mask topography) which solve $\partial H_{\text{target}}/\partial\tau = 0$ where H_{target} is the target shape we want the liquid film to evolve into. For example, Sellier and Panda [107] studied the required substrate topography in order for a gravity-driven thin liquid film to match an intended shape, while Eshel et al. [34] studied the required substrate temperature profile in a variant of thermocapillary patterning for shaping the liquid film to fabricate different

optical elements like diffraction gratings with very small aspect ratio. This approach, however, assumes the target shape is a stationary state and neglects the dynamics of the liquid film, which can become highly nonlinear when the target shape has large deformation.

The second type of study focuses on the use of feedback in stabilizing the liquid film toward specific shapes not necessarily spatially uniform, and the control signal usually scales with deviation of the liquid film or other quantities such as surface temperature away from their target values. This includes the study by Or et al. [84] on the suppression of long wave Bénard-Marangoni instability by controlling the substrate temperature, and more recently those by Samoilova and Nepomnyashchy [95–98] on the control of oscillatory instability in Marangoni convection. The suppression of evaporatively driven instabilities by spatially non-uniform radiative heating was studied in Grigoriev [49]. The suppression of contact line instability in a thermally driven liquid film was studied theoretically in Grigoriev [48] and experimentally in Garnier et al. [44]. Finally, for a liquid film falling down an inclined plane under gravity, the feedback control using fluid injection and removal at the substrate was also studied in Cimpeanu et al. [19], Holroyd et al. [53], and Thompson et al. [118] where the effect of inertia was included (i.e., nonzero Reynolds number).

We are often interested in the *optimal* control problem, where the optimal control strategy is determined through minimizing an appropriately chosen metric involving the intended outcome, i.e., how close we can bring the liquid film shape to the intended target shape, and the cost of control. The optimal control problem of a thin liquid film subject to only capillarity was studied in Klein and Prohl [60] where the control was treated as an external mass-conserving flux. Boujo and Sellier [10] studied the optimal substrate kinematics in order to flatten a gravity driven liquid film, taking into account solidification which was modeled using a temperature-dependent viscosity, but neglecting capillarity. Lunz [68] studied the optimal substrate temperature gradient to suppress any free surface deformation for a liquid film flowing down an inclined substrate heated from below by considering only the stationary problem. Wray et al. [130] studied the optimal applied voltage for controlling a liquid film toward arbitrary shape, taking into account inertia. Biswal et al. [7] studied the optimal boundary flux for a liquid film flowing down a cylindrical fiber. In the context of fluid-based microfabrication, Stanley et al. [113] studied the optimal control of a patterning technique based on solutal-Marangoni effect where the surface tension depends on the concentration of photosensitive solutes. The optimized photomask, which in turn controls the initial concentration of the solutes, was determined using the genetic algorithm such that the contour of the protrusion developed by the liquid film, as opposed to the whole free surface, matched the intended shape. We also mention the study by Shankar et al. [109] on the optimal transport of an active sessile droplet which can be modeled using a thin-film-like equation. A comparison of

the above mentioned studies involving the control of liquid film shape is summarized in Table 7.1.

It is also worth noting that many systems of thin liquid film, such as gravity-driven liquid film flowing down an included plane, can be reduced under weakly-nonlinear analysis to the well-known Kuramoto-Sivashinsky (KS) equation whose feedback control was first studied in Armaou and Christofides [2] and Christofides [18]. More recent studies could be found in Gomes et al. [47] and Tomlin et al. [119] and references therein.

Despite the extensive literature related to the control of thin liquid film, to the best of our knowledge, the inverse problem or the optimal control of either EHD or TC patterning studied in this thesis has not been investigated. While there are several similar studies in literature on optimal control, there are limitations which restrict their applicability to EHD or TC patterning: Eshel et al. [34] and Lunz [68] only studied the stationary problem where the target shape is either flat or has features with very shallow corrugation, while Wray et al. [130] considered only a perfectly conducting liquid in the regime where gravity and inertia are important, both of which can be safely neglected for EHD or TC patterning. In Boujo and Sellier [10], capillarity was neglected, while in Klein and Prohl [60], an appropriate destabilization term from normal or shear stress was absent. In Biswal et al. [7], the control was implemented as boundary flux which is not suitable for EHD or TC patterning, and the form of the governing equation does not allow spatially modulated boundaries. Given the importance of accurate shape control to fully utilize the potential of EHD and TC patterning and the lack of literature in addressing this issue, here we provide an in-depth study of the relevant optimal control problem.

In Ref [145], the open-loop terminal control of EHD patterning was formulated as a PDE-constrained optimization problem under the long-wavelength approximation [22, 85], and the optimal mask topography for evolving the liquid film to a prescribed heart-shaped structure was computed using the adjoint method. Only the liquid film shape at the final or 'terminal' time was considered, because the solidification of the liquid film often occurs at a much faster time scale than the evolution of the liquid film, and its shape at the terminal time can be quenched experimentally by simply removing the heat source to the polymer film or photochemical treatment.

In this paper, we build upon the preliminary study in Ref [145] to consider both spatial and temporal controls using either the patterned electrode or voltage profile as the control variable. A comprehensive parametric study was conducted to analyze how different applied voltage, processing time, target shapes, regularization as well as roughening of the optimized mask topography affect the final achievable liquid film shape. The motivation of this study is twofold: (1) to provide a computational framework for computing the optimal control variable (e.g., the topography of the patterned mask or

the spatiotemporal profile of the imposed voltage or temperature difference) in order to shape the liquid film into a given target shape, which is an example of the more general fourth-order parabolic-type nonlinear PDE, and (2) to conduct a comprehensive study on how changes in different variables and parameters affect the *optimal* control of liquid thin film patterning, which in turn provide further insights into the limitations of liquid thin film patterning and conditions for obtaining high fidelity patterns.

The outline of the remainder of this article is organized as follow. We first state the problem mathematically in Section 7.2, and then formulate the optimal control framework in Section 7.3 applicable to both EHD and TC patterning, as well as both terminal and regulation control. In Section 7.4, we present the numerical results for optimization, specializing to the case of terminal control in EHD patterning. Finally, in Section 7.5 we summarize the results and discuss a few limitations and possible extensions.

	Physical effects												
Studies	Capillarity	Gravity	Inertia	Evaporation	Thermocapillarity	Solutal-Marangoni	Electrostatics	Solidification	Active Stress	Stationary States ?	Feedback Control ?	Optimal Control ?	Control Strategy / Variable
Sellier and Panda [107]	✓	✓								✓			Substrate topography
Eshel et al. [34]	✓	✓			✓					✓			Substrate temperature
Or et al. [84]	✓	✓			✓						✓		Substrate temperature
Samoilova and Nepomnyashch [95–98]	✓	✓			✓						✓		Substrate heat flux
Grigoriev [49]	✓	✓		✓	✓						✓		Substrate temperature
Grigoriev [48]	✓				✓						✓		Substrate temperature
Thompson et al. [118] Cimpeanu et al. [19] Holroyd et al. [53]	✓	✓	✓								✓		fluid injection & removal at substrate
Klein and Prohl [60]	✓											✓	external mass-conserving flux
Boujo and Sellier [10]		✓						✓				✓	substrate rotation kinematics
Lunz [68]	✓	✓			✓					✓		✓	substrate temperature gradient
Shankar et al. [109]	✓							✓				✓	elongated active units
Wray et al. [130]	✓	✓	✓				✓					✓	applied voltage
Biswal et al. [7]	✓	✓										✓	boundary flux
Stanley et al. [113]	✓					✓						✓	initial solute concentration

Table 7.1: Summary of different studies on the control of thin liquid film.

7.2 Problem Statement

7.2.1 Governing equation

We first recall the governing equation for EDH or TC patterning, which has the following general form

$$\frac{\partial H}{\partial \tau} = \nabla_{\parallel} \cdot \left\{ -M_{\perp}(H) \nabla_{\parallel} \left[\nabla_{\parallel}^2 H + \Pi(H,\xi) \right] + M_{\parallel}(H) \nabla_{\parallel} \Gamma(H,\xi) \right\}, \tag{7.1}$$

$$\Pi(H,\xi) = \mathcal{A} \left[\frac{1}{H^3} - \frac{1}{(D-H)^3} \right] + \frac{\mathcal{W} \varepsilon_r (\varepsilon_r - 1) \Psi_{\Delta}^2}{2\left[H + \varepsilon_r (D-H)\right]^2},$$

$$\Gamma(H,\xi) = -\frac{\mathcal{M}\left[\kappa H \Theta_{\text{cold}} + (D-H)\Theta_{\text{hot}}\right]}{D - (1-\kappa)H},$$

where $M_{\perp}(H) = H^3/3$ and $M_{\parallel}(H) = H^2/2$ are the mobility factors associated with normal and shear stress, $\Pi(H,\xi)$ includes van-der-Waals interaction and electrostatic pressure, and $\Gamma(H,\xi)$ is the dimensionless surface tension which varies with temperature at the free surface at $Z = H$. The control variable $\xi(\mathbf{X},\tau)$ represents any general control strategies.

7.2.2 Examples of physical implementation of control

The following are examples of physical implementations of the control $\xi(\mathbf{X},\tau)$ most relevant to EHD and TC patterning:

1. Topographically patterning the mask (or substrate): $\xi = D(\mathbf{X})$
2. Changing the applied voltage (spatially or/and temporally): $\xi = \Psi_{\Delta}(\mathbf{X},\tau)$
3. Changing the temperature at the mask electrodes or substrates: $\xi = \Theta_{\text{hot}}(\mathbf{X},\tau)$ or $\Theta_{\text{cold}}(\mathbf{X},\tau)$
4. Chemically patterning the substrate, i.e., changing the wettability: $\xi = \mathcal{A}(\mathbf{X},\tau)$

The optimal control formalism presented in Section 7.3 does not depend on the specific details of how the control is implemented, and alternative strategies not listed above can also be used, provided that the control variable enters the governing Eq. (7.1) through the pressure Π or/and the surface tension Γ term *only*. Control ξ appearing as an external source term or the mobility factors, for instance, cannot be directly handled using the present formalism by simple substitutions into the derived mathematical expressions, though it can be easily generalized to cover those other cases.

7.2.3 Cost function

The present objective is to control the liquid film shape $H(\mathbf{X},\tau)$ towards some given target states, either at the final time τ_f towards $H_{\text{term}}(\mathbf{X})$, or across a time interval $0 \leq \tau \leq \tau_f$ towards $H_{\text{reg}}(\mathbf{X},\tau)$. We would also like to minimize the mean-squared deviation $\mathcal{E}_{\text{ms}}$ by applying some control $\xi(\mathbf{X},\tau)$ at minimal cost — usually in terms of the energy cost, or the gradients of the control which can represent the engineering difficulties. Therefore, we define the objective functional as

$$\begin{aligned}\mathcal{J}(H,\xi) = &\frac{\Upsilon_{\text{term}}}{2|\Omega|}\int_{\Omega}\left[H(\mathbf{X},\tau_f) - H_{\text{term}}(\mathbf{X})\right]^2 \mathrm{d}\mathbf{X} \\ &+ \frac{\Upsilon_{\text{reg}}}{2|\Omega|}\int_0^{\tau_f}\int_{\Omega}\varsigma(\tau)\left[H(\mathbf{X},\tau) - H_{\text{reg}}(\mathbf{X},\tau)\right]^2 \mathrm{d}\mathbf{X}\ \mathrm{d}\tau + \mathcal{R}(\xi),\end{aligned} \tag{7.2}$$

where $\mathcal{J}$ is a functional of the liquid film shape $H(\mathbf{X},\tau)$ and the control variable $\xi(\mathbf{X},\tau)$, and consists of the following terms:

1. Mean-squared deviation of H away from $H_{\text{term}}(\mathbf{X})$ at $\tau = \tau_f$ (**term**inal control).
2. Mean-squared deviation of H away from $H_{\text{reg}}(\mathbf{X})$ weighted by $\varsigma(\tau)$ across the whole duration(**reg**ulation control).
3. Regularization $\mathcal{R}(\xi)$ measuring the 'cost' of control $\xi(\mathbf{X},\tau)$.

The constants $\Upsilon_{\text{term}}, \Upsilon_{\text{term}} \geq 0$ control the relative importance between terminal and regulation control. The specific case for terminal control, which will be discussed in detail in Section 7.4, can be obtained by setting $\Upsilon_{\text{term}} = 1$ and $\Upsilon_{\text{reg}} = 0$. The function $\varsigma(\tau)$ in the regulation control provides additional flexibility, for example, we can set $\varsigma(\tau)$ as a weighting function which slowly increases from 0 to 1 which allows less emphasis on the initial transient phase and H_{reg} to have greater importance at late time.

7.2.4 Fourier representation of control variable

In order to simplify the calculation, the control variable is assumed to be separable, i.e., $\xi(\mathbf{X},\tau) = \xi_X(X)\xi_Y(Y)\xi_\tau(\tau)$, where $\xi_X(X)$, $\xi_Y(Y)$ and $\xi_\tau(\tau)$ can each be expressed as a Fourier series:

$$\xi_X(X) = \sum_{m=0}^{n_x}\left[a_m \cos\left(\frac{2\pi m X}{L_x}\right) + b_m \sin\left(\frac{2\pi m X}{L_x}\right)\right], \tag{7.3a}$$

and similarly for $\xi_Y(Y)$ and $\xi_\tau(\tau)$. The control variable $\xi(\mathbf{X},\tau)$ can then be expressed as follow

$$\xi(X,Y,\tau) = \sum_{m=0}^{n_x}\sum_{n=-n_y}^{n_y}\sum_{r=-n_t}^{n_t}\left\{a_{mnr}\cos\left[2\pi\left(m\frac{X}{L_x}+n\frac{Y}{L_y}+r\frac{\tau}{\tau_f}\right)\right]\right.$$
$$\left. + b_{mnr}\sin\left[2\pi\left(m\frac{X}{L_x}+n\frac{Y}{L_y}+r\frac{\tau}{\tau_f}\right)\right]\right\}, \tag{7.4}$$

where $L_x = 2$ and $L_y = 2$ is the size of the (dimensionless) domain along X and Y direction[1]. Therefore, the control variable becomes a set of Fourier coefficients $\mathbf{c} = \{a_{mnr}, b_{mnr}\}$. The use of Fourier series for the spatial part of $\xi(\mathbf{X},\tau)$ follows naturally the use of periodic boundary condition imposed on the spatial domain. The evolution of the liquid film and hence the control variable need not be time periodic, but requiring $\xi(\tau = 0) = \xi(\tau = \tau_f)$ simplifies the expressions for the gradient $\mathrm{d}\mathcal{J}/\mathrm{d}\xi$ due to cancellation of the boundary term resulted from integration by part in τ. In addition, we find from numerical experiments that having time-periodic control helps achieve convergence during optimization, and prevents large variation of ξ, i.e., large $\partial\xi/\partial\tau$, near $\tau = 0$ and $\tau = \tau_f$. Therefore, time-periodic control is assumed in this study.

7.2.5 Regularization

The following form of the regularization $\mathcal{R}(\xi)$ is used:

$$\mathcal{R}(\xi) = \mathcal{R}_1(\xi) + \mathcal{R}_2(\xi),$$
$$\mathcal{R}_1(\xi) = \frac{1}{2|\Omega|\tau_f}\int_0^{\tau_f}\int_\Omega\left[\Upsilon_1\left(\nabla_\parallel\xi\right)^2 + \Upsilon_t\left(\frac{\partial\xi}{\partial\tau}\right)^2\right]\mathrm{d}\mathbf{X}\,\mathrm{d}\tau, \tag{7.5a}$$
$$\mathcal{R}_2(\xi) = \frac{\Upsilon_2}{2\left[\mathrm{mean}(\xi) - \xi_{\mathrm{ref}}\right]^2}. \tag{7.5b}$$

The non-negative constants Υ_1, Υ_t and Υ_2 control the relative importance of each regularization term relative to the deviation term in the cost functional $\mathcal{J}$.

The $\mathcal{R}_1$ term penalizes control with large spatial and/or temporal gradient, which represents, for example, engineering difficulties in fabricating patterned mask with very steep sidewalls, or in realizing rapidly changing voltage signal. Penalizing the $\nabla_\parallel\xi$ also helps ensure the validity of LWA which neglects the second derivative of the external fields (e.g. voltage or temperature) along the horizontal direction.

The $\mathcal{R}_2$ term prevents the control from approaching the reference level ξ_{ref}. This is useful, for example, when the control represents the patterned mask, i.e., $\xi = D(\mathbf{X})$,

[1] In this chapter, we set $l_0 = \lambda_p/2$ as the characteristic horizontal length scale so that the dimensionless patterning wavelength is $\Lambda_p = 2$. With a spatial domain which supports one unit of the periodic structure, we have $L_x = L_y = 2$.

and we want to prevent the mask from being too close to the liquid free surface. As shown in Section 7.4.2.5, the combination of both $\mathcal{R}_1$ and $\mathcal{R}_2$ terms allows a wide variety of patterned mask to be realized, some of which are less susceptible to fabrication imperfect.

When the control variable is represented by Eq. (7.4), the regularization terms become

$$\mathcal{R}_1(\mathbf{c}) = \pi^2 \sum_{m=0}^{n_x} \sum_{n=-n_y}^{n_y} \sum_{r=-n_t}^{n_t} \left(\frac{\Upsilon_1}{L_x^2} m^2 + \frac{\Upsilon_1}{L_y^2} n^2 + \frac{\Upsilon_t}{\tau_f^2} r^2 \right) \left(a_{mnr}^2 + b_{mnr}^2 \right), \tag{7.6a}$$

$$\mathcal{R}_2(\mathbf{c}) = \frac{\Upsilon_2}{2\left(a_{\mathbf{0}} - \xi_{\mathrm{ref}}\right)^2}. \tag{7.6b}$$

7.2.6 PDE constraint

We would like to find the control variable $\xi(\mathbf{X}, \tau)$ which minimizes the objective functional $\mathcal{J}$ subject to the PDE constraint given by Eq. (7.1):

$$\min_{\xi(\mathbf{X},\tau)} \mathcal{J} \qquad \text{subject to Eq. (7.1).} \tag{7.7}$$

Many common optimization algorithms require the gradient of $\mathcal{J}$ with respect to ξ, i.e., $\mathrm{d}\mathcal{J}/\mathrm{d}\xi$, for computing the descent direction. While the gradient can be computed using finite difference, it is not numerically tractable since $\xi(\mathbf{X}, \tau)$ is a function and its degree of freedom is of the same order as the number of grid points or/and time steps used for discretizing Eq. (7.1). Gradient-free methods, such the genetic algorithm or other evolutionary-type algorithms used in Shankar et al. [109] and Stanley et al. [113], may also not be practical due to the high computational cost of evaluating of $\mathcal{J}$ many times to explore the parameter space. In this chapter, we use the *formal Lagrange method* [120], or more commonly known as the method of Lagrange multiplier, for solving the optimization problem given in Eq. (7.7). The method leads to an efficient computation of the gradient by solving only two PDEs — the original governing PDE and the so-called adjoint equation, regardless of the degree of freedom in $\xi(\mathbf{X}, \tau)$.

7.3 Optimal Control Formalism

7.3.1 Optimality conditions

We note that the formal Lagrange method [120, see Sections 2.10 and 5.10] presented in this section allows us to *derive* the correct form of the gradient, but it is not mathematically rigorous as there are no general theorems addressing various technicalities, such as the existence of solutions and the differentiability of $\mathcal{J}$, when the PDE constraint has the specific form of Eq. (7.1). We are not aware of any recent studies on addressing these technicalities except Klein and Prohl [60] who proved some results on the existence of optimal control for the thin film equation with only the fourth-order capillarity term.

We do not aim to address these technicalities in this chapter. Instead, we simply derive the gradient assuming such an optimal control exists, and provide numerical evidence in Section 7.4 to show that the liquid film can indeed be controlled toward the target states under fairly general conditions.

The PDE constraint in Eq. (7.1) can be incorporated to the objective functional $\mathcal{J}$, resulting in the following Lagrangian $\mathcal{L}$

$$\mathcal{L}(H, \Lambda, \xi) = \mathcal{J}(H, \xi) - \int_0^{\tau_f} \int_\Omega \Lambda \left[\frac{\partial H}{\partial \tau} - f(H, \xi) \right] \mathrm{d}\mathbf{X}\, \mathrm{d}t, \tag{7.8}$$

where $\Lambda(\mathbf{X}, \tau)$ is the Lagrange multiplier, also known as the 'adjoint variable', enforcing the PDE constraint, and $f(H, \xi)$ is the right hand side of Eq. (7.1). The constrained optimization stated in Eq. (7.7) now becomes an unconstrained minimization of Eq. (7.8).

The derivative of a general functional $F(h)$ is denoted as [120, Chapter 2.6]

$$\delta F(H; \chi) = \frac{\partial F(H)}{\partial H} \chi = \lim_{\delta \to 0} \frac{F(H + \delta\chi) - F(H)}{\delta}, \tag{7.9}$$

where $\delta F(H; \chi)$ is known as the directional derivative of F at H along the direction χ. If the limit exists for all χ, then $\partial F / \partial H$ is known as the Gâteaux derivative of F at H. It can be proved [94, see Theorems 1–2] that if the Gâteaux derivative exists at H and is continuous at H, then the Fréchet derivative exists and is identical to the Gâteaux derivative.

Let $(\bar{H}, \bar{\Lambda}, \bar{\xi})$ denote the optimal values of (H, Λ, ξ). First order necessary condition requires the derivatives of $\mathcal{L}$ with respect to the state variable H, the adjoint variable Λ and the control variable ξ vanish at the optimal points:

$$\delta\mathcal{L}(\bar{H}, \bar{\Lambda}, \bar{\xi}; \Lambda - \bar{\Lambda}) = 0, \tag{7.10a}$$

$$\delta\mathcal{L}(\bar{H}, \bar{\Lambda}, \bar{\xi}; H - \bar{H}) = 0, \tag{7.10b}$$

$$\delta\mathcal{L}(\bar{H}, \bar{\Lambda}, \bar{\xi}; \xi - \bar{\xi}) \geq 0. \tag{7.10c}$$

Eq. (7.10a) results in the governing PDE given by Eq. (7.1), also known as the *forward* equation. Eq. (7.10b) results in the so-called *adjoint* equation which we will derive in Section 7.3.2. Eq. (7.10c) is a variational inequality which must be satisfied by the optimal control $\bar{\xi}$. To formally obtain the gradient of the objective functional, we first define the *reduced objective functional* as $\overline{\mathcal{J}}(\xi) = \mathcal{J}(H(\xi), \xi)$ where $H = H(\xi)$ is the solution to Eq. (7.1) for a given control ξ. The gradient of $\overline{\mathcal{J}}$ with respect to the control ξ is given by [120, Section 2.10 Remarks (ii)]

$$\frac{\mathrm{d}\overline{\mathcal{J}}(\xi)}{\mathrm{d}\xi} = \frac{\partial \mathcal{L}(H, \Lambda, \xi)}{\partial \xi}, \tag{7.11}$$

where $H = H(\xi)$ and $\Lambda = \Lambda(\xi)$. Eq. (7.11) can also be obtained heuristically by considering the total derivative of $\mathcal{L}$ [10]:

$$\frac{\mathrm{d}\mathcal{L}}{\mathrm{d}\xi} = \frac{\partial \mathcal{L}}{\partial \xi} + \frac{\partial \mathcal{L}}{\partial H}\frac{\partial h}{\partial \xi} + \frac{\partial \mathcal{L}}{\partial \Lambda}\frac{\partial \Lambda}{\partial \xi}. \tag{7.12}$$

When the first two optimality conditions given by Eq. (7.10a) and (7.10b) are satisfied, $\partial\mathcal{L}/\partial H = \partial\mathcal{L}/\partial\Lambda = 0$. Furthermore, when the governing PDE given in Eq. (7.1) is satisfied, then $\mathcal{L} = \mathcal{J}$ by construction. Therefore, $\mathrm{d}\mathcal{J}/\mathrm{d}\xi = \mathrm{d}\mathcal{L}/\mathrm{d}\xi = \partial\mathcal{L}/\partial\xi$.

7.3.2 Derivation of adjoint equation

In this section, we derive the adjoint equation, which is given by Eq. (7.26) at the end of this section.

Using the substitution $H = \bar{H} + \delta\chi$, where $\chi(\mathbf{X}, \tau)$ is an arbitrary function and $\delta \ll 1$, Eq. (7.10b) can be evaluated by expanding $\mathcal{L}$ around $\bar{H}$:

$$\mathcal{L}(\bar{H} + \delta\chi, \bar{\Lambda}, \bar{\xi}) = \mathcal{J}(\bar{H} + \delta\chi, \bar{\xi}) - \int_0^{\tau_f}\int_\Omega \bar{\Lambda}\left[\frac{\partial(\bar{H} + \delta\chi)}{\partial\tau} - f(\bar{H} + \delta\chi, \bar{\xi})\right]\mathrm{d}\mathbf{X}\ \mathrm{d}\tau. \tag{7.13}$$

We expand each term in Eq. (7.13) around the optimal solutions $(\bar{H}, \bar{\Lambda}, \bar{\xi})$ one-by-one. Starting with $\mathcal{J}$, we have

$$\left[(\bar{H} + \delta\chi)|_{\tau=\tau_f} - H_{\mathrm{term}}\right]^2 = \left(\bar{H}|_{\tau=\tau_f} - H_{\mathrm{term}}\right)^2 + 2\delta\left(\bar{H}|_{\tau=\tau_f} - H_{\mathrm{term}}\right)\chi|_{\tau=\tau_f} + \mathcal{O}(\delta^2) \tag{7.14a}$$

$$\left[(\bar{H} + \delta\chi) - H_{\mathrm{reg}}\right]^2 = \left(\bar{H} - H_{\mathrm{reg}}\right)^2 + 2\delta\left(\bar{H} - H_{\mathrm{reg}}\right)\chi + \mathcal{O}(\delta^2) \tag{7.14b}$$

Expanding $\mathcal{J}(\bar{H} + \delta\chi, \bar{\xi})$, and using Eq. (7.14):

$$
\begin{aligned}
&\mathcal{J}(\bar{H}+\delta\chi,\bar{\xi}) \\
&= \frac{\Upsilon_{\text{term}}}{2|\Omega|}\int_\Omega \left[(\bar{H}+\delta\chi)|_{\tau=\tau_f} - H_{\text{term}}\right]^2 \mathrm{d}\mathbf{X} \\
&\quad + \frac{\Upsilon_{\text{reg}}}{2|\Omega|}\int_0^{\tau_f}\int_\Omega \varsigma\left[\bar{H}+\delta\chi - H_{\text{reg}}\right]^2 \mathrm{d}\mathbf{X}\ \mathrm{d}\tau + \mathcal{R}(\bar{\xi}) \\
&= \mathcal{J}(\bar{H},\bar{\xi}) + \delta\Bigg\{\frac{\Upsilon_{\text{term}}}{|\Omega|}\int_\Omega \left(\bar{H}|_{\tau=\tau_f} - H_{\text{term}}\right)\chi|_{\tau=\tau_f}\ \mathrm{d}\mathbf{X} \\
&\qquad\qquad + \frac{\Upsilon_{\text{reg}}}{|\Omega|}\int_0^{\tau_f}\int_\Omega \varsigma(\bar{H}-H_{\text{reg}})\chi\ \mathrm{d}\mathbf{X}\ \mathrm{d}\tau\Bigg\} + \mathcal{O}(\delta^2).
\end{aligned} \tag{7.15}
$$

Next, for the term enforcing the PDE constraint, we can expand the nonlinear function as $f(\bar{H}+\delta\chi,\bar{\xi}) = f(\bar{H},\bar{\xi}) + \delta f_h(\bar{H},\bar{\xi})\chi + \mathcal{O}(\delta^2)$ where f_h is the Jacobian given below:

$$
\begin{aligned}
f_h(\bar{H},\bar{\xi})\chi = -\nabla_\parallel\cdot\Bigg\{&M_\perp(\bar{H})\nabla_\parallel\left[\nabla_\parallel^2\chi + \frac{\partial\Pi(\bar{H},\bar{\xi})}{\partial H}\chi\right] \\
&+ \frac{\partial M_\perp(\bar{H})}{\partial H}\nabla_\parallel\left[\nabla_\parallel^2\bar{H} + \Pi(\bar{H},\bar{\xi})\right]\chi \\
&+ M_\parallel(\bar{H})\nabla_\parallel\left[\frac{\partial\Gamma(\bar{H},\bar{\xi})}{\partial H}\chi\right] + \frac{\partial M_\parallel(\bar{H})}{\partial H}\nabla_\parallel\Gamma(\bar{H},\bar{\xi})\chi\Bigg\}.
\end{aligned} \tag{7.16}
$$

The PDE constraint term becomes

$$
\begin{aligned}
&\int_0^{\tau_f}\int_\Omega \bar{\Lambda}\left\{\frac{\partial\bar{H}}{\partial\tau} + \delta\frac{\partial\chi}{\partial\tau} - \left[f(\bar{H},\bar{\xi}) + \delta f_h(\bar{H},\bar{\xi})\chi + \mathcal{O}(\delta^2)\right]\right\}\mathrm{d}\mathbf{X}\ \mathrm{d}\tau \\
&= \int_0^{\tau_f}\int_\Omega \bar{\Lambda}\left[\frac{\partial\bar{H}}{\partial\tau} - f(\bar{H},\bar{\xi})\right]\mathrm{d}\mathbf{X}\ \mathrm{d}\tau + \delta\int_0^{\tau_f}\int_\Omega \bar{\Lambda}\left[\frac{\partial\chi}{\partial\tau} - f_h(\bar{H},\bar{\xi})\chi\right]\mathrm{d}\mathbf{X}\ \mathrm{d}\tau + \mathcal{O}(\delta^2)
\end{aligned} \tag{7.17}
$$

We then apply integration by part in the time integral for the term involving $\partial\bar{\chi}/\partial\tau$:

$$
\begin{aligned}
\int_0^{\tau_f}\int_\Omega\left(\bar{\Lambda}\frac{\partial\chi}{\partial\tau}\right)\mathrm{d}\mathbf{X}\ \mathrm{d}\tau &= \int_\Omega\left\{\left[\bar{\Lambda}\chi\right]_{\tau=0}^{\tau=\tau_f} - \int_0^{\tau_f}\chi\frac{\partial\bar{\Lambda}}{\partial\tau}\mathrm{d}\tau\right\}\mathrm{d}\mathbf{X} \\
&= \int_\Omega\left(\bar{\Lambda}|_{\tau=\tau_f}\ \chi|_{\tau=\tau_f} - \int_0^{\tau_f}\chi\frac{\partial\bar{\Lambda}}{\partial\tau}\mathrm{d}\tau\right)\mathrm{d}\mathbf{X},
\end{aligned} \tag{7.18}
$$

where we use the fact that $\chi|_{\tau=0} = 0$ since the initial condition $H(\mathbf{X},0) = \bar{H}(\mathbf{X},0) + \delta\chi(\mathbf{X},0)$ should remain unchanged. The full expression of the term involving the Jacobian f_h is

$$\int_\Omega \bar{\Lambda}\left[f_h(\bar{H},\bar{\xi})\chi\right]\mathrm{d}\mathbf{X} = -\int_\Omega \bar{\Lambda}\nabla_\parallel\cdot\Big\{M_\perp(\bar{H})\nabla_\parallel^3\chi + M_\perp(\bar{H})\nabla_\parallel\left[\frac{\partial\Pi(\bar{H},\bar{\xi})}{\partial H}\chi\right] + \frac{\partial M_\perp(\bar{H})}{\partial H}\nabla_\parallel\left[\nabla_\parallel^2\bar{H}+\Pi(\bar{H},\bar{\xi})\right]\chi + M_\parallel(\bar{H})\nabla_\parallel\left[\frac{\partial\Gamma(\bar{H},\bar{\xi})}{\partial H}\chi\right] + \frac{\partial M_\parallel(\bar{H})}{\partial H}\nabla_\parallel\Gamma(\bar{H},\bar{\xi})\chi\Big\}\mathrm{d}\mathbf{X}. \quad (7.19)$$

In order to proceed, we need to separate the arbitrary function $\chi(\mathbf{X},\tau)$ from the linear operator f_h in Eq. (7.19), which can be done using integration by parts. For the term on the first line of the right hand side of Eq. (7.19), we have

$$\begin{aligned}\int_\Omega \bar{\Lambda}\nabla_\parallel\cdot\left[M_\perp(\bar{H})\nabla_\parallel^3\chi\right]\mathrm{d}\mathbf{X} &= -\int_\Omega \nabla_\parallel\bar{\Lambda}\cdot\left[M_\perp(\bar{H})\nabla_\parallel^3\chi\right]\mathrm{d}\mathbf{X}\\ &= \int_\Omega \nabla_\parallel\cdot\left[M_\perp(\bar{H})\nabla_\parallel\bar{\Lambda}\right]\nabla_\parallel^2\chi\ \mathrm{d}\mathbf{X}\\ &= -\int_\Omega \nabla_\parallel\left\{\nabla_\parallel\cdot\left[M_\perp(\bar{H})\nabla_\parallel\bar{\Lambda}\right]\right\}\cdot\nabla_\parallel\chi\ \mathrm{d}\mathbf{X}\\ &= \int_\Omega \nabla_\parallel^2\left\{\nabla_\parallel\cdot\left[M_\perp(\bar{H})\nabla_\parallel\bar{\Lambda}\right]\right\}\chi\ \mathrm{d}\mathbf{X}. \end{aligned} \quad (7.20)$$

For the second line of the right hand side of Eq. (7.19), we have:

$$\begin{aligned}&\int_\Omega \bar{\Lambda}\nabla_\parallel\cdot\left\{M_\perp(\bar{H})\nabla_\parallel\left[\frac{\partial\Pi(\bar{H},\bar{\xi})}{\partial H}\chi\right] + \frac{\partial M_\perp(\bar{H})}{\partial H}\nabla_\parallel\left[\nabla_\parallel^2\bar{H}+\Pi(\bar{H},\bar{\xi})\right]\chi\right\}\mathrm{d}\mathbf{X}\\ &= -\int_\Omega \nabla_\parallel\bar{\Lambda}\cdot\left\{M_\perp(\bar{H})\nabla_\parallel\left[\frac{\partial\Pi(\bar{H},\bar{\xi})}{\partial H}\chi\right] + \frac{\partial M_\perp(\bar{H})}{\partial H}\nabla_\parallel\left[\nabla_\parallel^2\bar{H}+\Pi(\bar{H},\bar{\xi})\right]\chi\right\}\mathrm{d}\mathbf{X}\\ &= \int_\Omega \left\{\nabla_\parallel\cdot\left[M_\perp(\bar{H})\nabla_\parallel\bar{\Lambda}\right]\frac{\partial\Pi(\bar{H},\bar{\xi})}{\partial H} - \frac{\partial M_\perp(\bar{H})}{\partial H}\nabla_\parallel\bar{\Lambda}\cdot\nabla_\parallel\left[\nabla_\parallel^2\bar{H}+\Pi(\bar{H},\bar{\xi})\right]\right\}\chi\ \mathrm{d}\mathbf{X}\end{aligned} \quad (7.21)$$

The third line of the right hand side of Eq. (7.19) is similar to the second line:

$$\begin{aligned}&\int_\Omega \bar{\Lambda}\nabla_\parallel\cdot\left\{M_\parallel(\bar{H})\nabla_\parallel\left[\frac{\partial\Gamma(\bar{H},\bar{\xi})}{\partial H}\chi\right] + \frac{\partial M_\parallel(\bar{H})}{\partial H}\nabla_\parallel\Gamma(\bar{H},\bar{\xi})\chi\right\}\mathrm{d}\mathbf{X}\\ &= \int_\Omega \left\{\nabla_\parallel\cdot\left[M_\parallel(\bar{H})\nabla_\parallel\bar{\Lambda}\right]\frac{\partial\Gamma(\bar{H},\bar{\xi})}{\partial H} - \frac{\partial M_\parallel(\bar{H})}{\partial H}\nabla_\parallel\bar{\Lambda}\cdot\nabla_\parallel\Gamma(\bar{H},\bar{\xi})\right\}\chi\ \mathrm{d}\mathbf{X}\end{aligned} \quad (7.22)$$

Note that all boundary terms arising from integration by parts vanish due to the use of periodic boundary conditions. The same also holds when Neumann boundary conditions

(i.e., requiring $\nabla_\parallel \bar{\Lambda} = 0$ on the boundary) are applied instead. Combining Eq. (7.20), (7.21) and (7.22), Eq. (7.19) becomes

$$
\begin{aligned}
&\int_\Omega \bar{\Lambda}\left[f_h(\bar{H},\bar{\xi})\chi\right]\mathrm{d}\mathbf{X} = \int_\Omega \chi\left[f_h^\dagger(\bar{H},\bar{\xi})\bar{\Lambda}\right]\mathrm{d}\mathbf{X} \\
&= -\int_\Omega \chi\Bigg\{\left[\nabla_\parallel^2 + \frac{\partial\Pi(\bar{H},\bar{\xi})}{\partial H}\right]\nabla_\parallel\cdot\left[M_\perp(\bar{H})\nabla_\parallel\bar{\Lambda}\right] - \frac{\partial M_\perp(\bar{H})}{\partial H}\nabla_\parallel\bar{\Lambda}\cdot\nabla_\parallel\left[\nabla_\parallel^2\bar{H} + \Pi(\bar{H},\bar{\xi})\right] \\
&\quad + \nabla_\parallel\cdot\left[M_\parallel(\bar{H})\nabla_\parallel\bar{\Lambda}\right]\frac{\partial\Gamma(\bar{H},\bar{\xi})}{\partial H} - \frac{\partial M_\parallel(\bar{H})}{\partial H}\nabla_\parallel\bar{\Lambda}\cdot\nabla_\parallel\Gamma(\bar{H},\bar{\xi})\Bigg\}\mathrm{d}\mathbf{X},
\end{aligned}
\tag{7.23}
$$

where the terms inside the curly parenthesis is equal to $f_h^\dagger(\bar{H},\bar{\xi})\bar{\Lambda}$, and χ is now separated. Using Eq. (7.15), (7.17), (7.18) and (7.23), Eq. (7.13) becomes

$$
\begin{aligned}
&\mathcal{L}(\bar{H}+\delta\chi,\bar{\Lambda},\bar{\xi}) - \mathcal{L}(\bar{H},\bar{\Lambda},\bar{\xi}) \\
&= \delta\Bigg\{\frac{\Upsilon_{\mathrm{term}}}{|\Omega|}\int_\Omega\left(\bar{H}|_{\tau=\tau_f} - H_{\mathrm{term}}\right)\chi|_{\tau=\tau_f}\,\mathrm{d}\mathbf{X} + \frac{\Upsilon_{\mathrm{reg}}}{|\Omega|}\int_0^{\tau_f}\int_\Omega \varsigma(\bar{H}-H_{\mathrm{reg}})\chi\,\mathrm{d}\mathbf{X}\,\mathrm{d}\tau \\
&\quad - \int_\Omega\left(\bar{\Lambda}|_{\tau=\tau_f}\,\chi|_{\tau=\tau_f} - \int_0^{\tau_f}\chi\frac{\partial\bar{\Lambda}}{\partial\tau}\mathrm{d}\tau\right)\mathrm{d}\mathbf{X} + \int_0^{\tau_f}\int_\Omega\left[f_h^\dagger(\bar{H},\bar{\xi})\bar{\Lambda}\right]\chi\,\mathrm{d}\mathbf{X}\,\mathrm{d}\tau\Bigg\} + \mathcal{O}(\delta^2) \\
&= \delta\Bigg\{\int_\Omega\left[\frac{\Upsilon_{\mathrm{term}}}{|\Omega|}\left(\bar{H}|_{\tau=\tau_f} - H_{\mathrm{term}}\right) - \bar{\Lambda}|_{\tau=\tau_f}\right]\chi|_{\tau=\tau_f}\,\mathrm{d}\mathbf{X} \\
&\quad + \int_0^{\tau_f}\int_\Omega\left[\frac{\partial\bar{\Lambda}}{\partial\tau} + f_h^\dagger(\bar{H},\bar{\xi})\bar{\Lambda} + \frac{\Upsilon_{\mathrm{reg}}}{|\Omega|}\varsigma(\bar{H}-H_{\mathrm{reg}})\right]\chi\,\mathrm{d}\mathbf{X}\,\mathrm{d}\tau\Bigg\} + \mathcal{O}(\delta^2).
\end{aligned}
\tag{7.24}
$$

Since $\chi(\mathbf{X},\tau)$ is arbitrary, the first variation of $\mathcal{L}$ with respect to H vanishes only when terms inside the two square parentheses in Eq. (7.24) each vanish. This results in the following equations

$$
\frac{\partial\bar{\Lambda}(\mathbf{X},\tau)}{\partial\tau} + f_h^\dagger(\bar{H},\bar{\xi})\bar{\Lambda}(\mathbf{X},\tau) + \frac{\Upsilon_{\mathrm{reg}}}{|\Omega|}\left[\bar{H}(\mathbf{X},\tau) - H_{\mathrm{reg}}(\mathbf{X},\tau)\right]\varsigma(\tau) = 0, \tag{7.25a}
$$

$$
\bar{\Lambda}(\mathbf{X},\tau=\tau_f) = \frac{\Upsilon_{\mathrm{term}}}{|\Omega|}\left[\bar{H}(\mathbf{X},\tau=\tau_f) - H_{\mathrm{term}}(\mathbf{X})\right], \tag{7.25b}
$$

where the so-called adjoint equation (which is solved *backward* in time) and the corresponding terminal condition come from the terms highlighted in blue and red, respectively, in Eq. (7.24). We can see that terminal control results in the terminal condition for the adjoint variable, while regulation control results in an additional source term in the adjoint equation.

Introducing $\tau' = \tau_f - \tau$ and substituting the full expression of $f_h^\dagger$ given in Eq. (7.23), Eq. (7.25) becomes

$$\begin{aligned}\frac{\partial \bar{\Lambda}(\mathbf{X},\tau')}{\partial \tau'} = &-\left[\nabla_\parallel^2 + \frac{\partial \Pi(\bar{H},\bar{\xi})}{\partial H}\right]\nabla_\parallel \cdot \left[M_\perp(\bar{H})\nabla_\parallel \bar{\Lambda}\right] \\ &+ \frac{\partial M_\perp(\bar{H})}{\partial H}\nabla_\parallel \bar{\Lambda}\cdot\nabla_\parallel\left[\nabla_\parallel^2 \bar{H} + \Pi(\bar{H},\bar{\xi})\right] \\ &- \nabla_\parallel \cdot \left[M_\parallel(\bar{H})\nabla_\parallel \bar{\Lambda}\right]\frac{\partial \Gamma(\bar{H},\bar{\xi})}{\partial H} + \frac{\partial M_\parallel(\bar{H})}{\partial H}\nabla_\parallel \bar{\Lambda}\cdot\nabla_\parallel \Gamma(\bar{H},\bar{\xi}) \\ &- \frac{\Upsilon_{\mathrm{reg}}}{|\Omega|}\left[\bar{H}(\mathbf{X},\tau_f-\tau') - H_{\mathrm{reg}}(\mathbf{X},\tau_f-\tau')\right]\varsigma(\tau_f-\tau'), \qquad (7.26a)\end{aligned}$$

$$\bar{\Lambda}(\mathbf{X},\tau'=0) = \frac{\Upsilon_{\mathrm{term}}}{|\Omega|}\left[\bar{H}(\mathbf{X},\tau_f-\tau') - H_{\mathrm{term}}(\mathbf{X})\right], \qquad (7.26b)$$

which is now solved *forward* in time τ'. Eq. (7.26) is the actual PDE solved numerically when computing the gradient.

7.3.3 Gradient

The expression of the gradient $\mathrm{d}\mathcal{J}/\mathrm{d}\xi$ depends on how the control variable ξ is represented.

The derivation of the gradient $\mathrm{d}\mathcal{J}/\mathrm{d}\xi$ is similar to that of the adjoint equation in Section 7.3.2. Using the substitution $\mathbf{c} = \bar{\mathbf{c}} + \delta\tilde{\boldsymbol{c}}$, where $\bar{\mathbf{c}}$ is the vector of the optimal Fourier coefficients, and $\tilde{\boldsymbol{c}}$ is the perturbation vector, we can expand $\mathcal{L}$ as follow:

$$\mathcal{L}(\bar{H},\bar{\Lambda},\bar{\mathbf{c}}+\delta\tilde{\boldsymbol{c}}) = \mathcal{J}(\bar{H},\bar{\mathbf{c}}+\delta\tilde{\boldsymbol{c}}) - \int_0^{\tau_f}\int_\Omega \bar{\Lambda}\left[\frac{\partial \bar{H}}{\partial \tau} - f(\bar{H},\bar{\mathbf{c}}+\delta\tilde{\boldsymbol{c}})\right]\mathrm{d}\mathbf{X}\,\mathrm{d}\tau. \qquad (7.27)$$

The expansion of f is

$$\begin{aligned} f(\bar{H},\bar{\mathbf{c}}+\delta\tilde{\boldsymbol{c}}) &= \nabla_\parallel\cdot\left\{-M_\perp(H)\nabla_\parallel\left[\nabla_\parallel^2 H + \Pi(\bar{H},\bar{\mathbf{c}}+\delta\tilde{\boldsymbol{c}})\right] + M_\parallel(\bar{H})\nabla_\parallel\Gamma(\bar{H},\bar{\mathbf{c}}+\delta\tilde{\boldsymbol{c}})\right\} \\ &= f(\bar{H},\bar{\mathbf{c}}) + \delta\nabla_\parallel\cdot\left\{-M_\perp(\bar{H})\nabla_\parallel\left[\frac{\partial\Pi(\bar{H},\bar{\xi})}{\partial\xi}\frac{\partial\xi}{\partial\mathbf{c}}\tilde{\boldsymbol{c}}\right]\right. \\ &\quad \left. + M_\parallel(\bar{H})\nabla_\parallel\left[\frac{\partial\Gamma(\bar{H},\bar{\xi})}{\partial\xi}\frac{\partial\xi}{\partial\mathbf{c}}\tilde{\boldsymbol{c}}\right]\right\} + \mathcal{O}(\delta^2), \qquad (7.28)\end{aligned}$$

where chain rule is used to differentiate Π and Γ with respect to $\xi = \xi(\mathbf{c})$. Performing integration by parts twice, we have

$$\begin{aligned}
&\int_\Omega \bar{\Lambda}\nabla_\parallel \cdot \left\{ -M_\perp(\bar{H})\nabla_\parallel \left[\frac{\partial \Pi(\bar{H},\bar{\xi})}{\partial \xi} \frac{\partial \xi}{\partial \mathbf{c}} \tilde{\boldsymbol{c}} \right] + M_\parallel(\bar{H})\nabla_\parallel \left[\frac{\partial \Gamma(\bar{H},\bar{\xi})}{\partial \xi} \frac{\partial \xi}{\partial \mathbf{c}} \tilde{\boldsymbol{c}} \right] \right\} \mathrm{d}\mathbf{X} \\
&= \int_\Omega \left\{ -\nabla_\parallel \cdot \left[M_\perp(\bar{H})\nabla_\parallel \bar{\Lambda} \right] \frac{\partial \Pi(\bar{H},\bar{\xi})}{\partial \xi} + \nabla_\parallel \cdot \left[M_\parallel(\bar{H})\nabla_\parallel \bar{\Lambda} \right] \frac{\partial \Gamma(\bar{H},\bar{\xi})}{\partial \xi} \right\} \frac{\partial \xi}{\partial \mathbf{c}} \tilde{\boldsymbol{c}} \, \mathrm{d}\mathbf{X} \\
&= \int_\Omega f_\xi^\dagger(\bar{H},\bar{\xi}) \frac{\partial \xi}{\partial \mathbf{c}} d\mathbf{X} \; \tilde{\boldsymbol{c}},
\end{aligned} \tag{7.29}$$

where the terms inside the curly parenthesis on the second line (highlighted in blue) equals $f_\xi^\dagger(\bar{H},\bar{\xi})$. For the cost functional $\mathcal{J}$, since its only dependence on ξ (i.e., $\mathbf{c}$) comes via $\mathcal{R}(\xi)$, its expansion around $\bar{\mathbf{c}}$ is

$$\mathcal{J}(\bar{H},\tilde{\boldsymbol{c}}) = \mathcal{J}(\bar{H},\bar{\mathbf{c}}) + \delta \frac{\partial \mathcal{R}(\bar{\mathbf{c}})}{\partial \mathbf{c}} \tilde{\boldsymbol{c}} + \mathcal{O}(\delta^2). \tag{7.30}$$

Substituting Eq. (7.28), (7.29) and (7.30) into Eq. (7.27), we obtain the gradient:

$$\frac{\mathrm{d}\mathcal{J}}{\mathrm{d}\mathbf{c}} = \frac{\partial \mathcal{L}}{\partial \mathbf{c}} = \frac{\partial \mathcal{R}}{\partial \mathbf{c}} + \int_0^{\tau_f} \int_\Omega f_\xi^\dagger(\bar{H},\bar{\xi}) \frac{\partial \xi}{\partial \mathbf{c}} \, \mathrm{d}\mathbf{X} \, \mathrm{d}\tau. \tag{7.31}$$

The derivative $\partial\mathcal{R}/\partial\mathbf{c}$ in Eq. (7.31) is obtained by differentiating Eq. (7.6) with respect to the specified Fourier coefficients:

$$\frac{\partial \mathcal{R}_0}{\partial a_{mnr}} = \frac{\Gamma_0}{2} \times \begin{cases} 2(a_{000} - \xi_0) & \text{if } m = m = r = 0, \\ a_{mnr} & \text{otherwise,} \end{cases}, \tag{7.32a}$$

$$\frac{\partial \mathcal{R}_0}{\partial b_{mnr}} = \frac{\Gamma_0}{2} b_{mnr}. \tag{7.32b}$$

$$\frac{\partial \mathcal{R}_1}{\partial a_{mnr}} = 2\pi^2 \left(\frac{\Upsilon_1}{L_x^2} m^2 + \frac{\Upsilon_1}{L_y^2} n^2 + \frac{\Upsilon_t}{\tau_f^2} r^2 \right) a_{mnr}, \tag{7.33a}$$

$$\frac{\partial \mathcal{R}_1}{\partial a_{mnr}} = 2\pi^2 \left(\frac{\Gamma_{1x}}{L_x^2} m^2 + \frac{\Gamma_{1x}}{L_y^2} n^2 + \frac{\Gamma_{1t}}{\tau_f^2} r^2 \right) b_{mnr}. \tag{7.33b}$$

$$\frac{\partial \mathcal{R}_2}{\partial \mathbf{c}} = \begin{cases} -\dfrac{\Upsilon_2}{[a_{000} - \xi_{\mathrm{ref}}]^3} & \mathbf{c} = a_{000}, \\ 0 & \text{otherwise} \end{cases} \tag{7.34}$$

The derivative $\partial\xi/\partial\mathbf{c}$ is obtained by differentiating Eq. (7.4) with respect to the specified Fourier coefficient, e.g., $\partial\xi/\partial a_{mnr} = \cos\left[2\pi(mx/L_x + ny/L_y + r\tau/\tau_f)\right]$.

7.3.4 Solution procedure

The cost functional $\mathcal{J}$ can be minimized iteratively using gradient-based optimization methods where the gradient $\mathrm{d}\mathcal{J}/\mathrm{d}\xi$ is obtained by computing Eq. (7.31). The numerical algorithm is summarized in Algorithm 1.

Algorithm 1: Adjoint-based optimization of control variable ξ

Input: Initial guess (iteration $k = 0$) for control variable ξ_k as a set of Fourier coefficients
Output: Optimal control variable ξ_{opt}
Parameter: absolute tolerance abstol $= 10^{-6}$, relative tolerance reltol $= 10^{-4}$
`/* For convergence check or termination */`
while true **do**
  Given ξ_k, solve Eq. (7.1) to obtain $H_k(\mathbf{X}, \tau)$;
  Given ξ_k and H_k, solve Eq. (7.2) to obtain cost function $\mathcal{J}_k = \mathcal{J}(H_k, \xi_k)$;
  Given ξ_k and H_k, solve Eq. (7.26) to obtain $\Lambda_k(\mathbf{X}, \tau)$;
  Given ξ_k, H_k and Λ_k, solve Eq. (7.31) to obtain gradient $(\mathrm{d}\mathcal{J}/\mathrm{d}/\xi)_k$;
  if $\mathcal{J}_k \leq$ abstol or $|\mathcal{J}_k - \mathcal{J}_{k-1}|/\mathcal{J}_k \leq$ reltol **then**
    $\xi_{\text{opt}} = \xi_k$;
    return ξ_{opt} ;
  else
    Obtain ξ_{k+1} with a gradient-based method using $(\mathrm{d}\mathcal{J}/\mathrm{d}\xi)_k$;
    Repeat computation of H_{k+1}, $\mathcal{J}_{k+1}$ and Λ_{k+1} until convergence

Note that at each iteration, only two PDEs need to be solved, namely the forward and adjoint equations.

7.4 Numerical Results for Terminal Control

In this section, we present the numerical results for the terminal control problem for EHD patterning. Regulation control as well as optimal control for TC patterning are not studied due to time constraint, but is an interesting topic for future work.

7.4.1 Details of numerical simulations

7.4.1.1 Numerical Methods

Solving $\partial H/\partial\tau$ and $\partial\Lambda/\partial\tau$ Both the forward and adjoint equations given by Eq. (7.1) and (7.26), respectively, are solved numerically using the solvers and settings described in section 4.2. Specifically, 'setting A' is used where the system size is $-1 \leq X \leq +1$ for 1D system, and $-1 \leq X, Y \leq +1$ for 2D system. The initial condition for the forward problem is a perfectly flat film, i.e., $H(\mathbf{X}, \tau = 0) = 1$, while the initial condition for the adjoint problem is given by Eq. (7.26b). The grid size used for numerical simulation is $\Delta X/L_x = 1/128$ for 1D system, and $\Delta X/L_x = \Delta Y/L_y = 1/64$ for 2D system. With this grid size, the numerical error from spatial discretization is estimated to be $\mathcal{O}(10^{-5})$ by comparing the solution $H(\mathbf{X}, \tau_f)$ obtained with $\Delta X/L_x = 1/128$ and

$\Delta X/L_x = 1/256$ (i.e., half the grid size).

For the actual minimization of the cost functional $\mathcal{J}$, the limited-memory Broyden-Fletcher-Goldfarb-Shanno (L-BFGS) algorithm implemented in the Julia package `Optim.jl` [77] is used. L-BFGS algorithm is a quasi-Newton method where the Hessian is approximated by the gradient information. Note that L-BFGS algorithm only returns a *local* minimum instead of the global minimum. Details can be found in classic optimization textbooks such as [83].

At each iteration, typically 2 to 4 evaluations of $\mathcal{J}$ and $\mathrm{d}\mathcal{J}/\mathrm{d}\xi$ are required in order to compute the line-search direction and step size. Convergence is typically achieved within 200 iterations, and the convergence criteria is as follow:

1. $\mathcal{J} \leq \texttt{abstol} = 10^{-6}$: The cost functional is sufficiently minimized where $\mathcal{E}_{\mathrm{rms}} \sim \mathcal{O}(10^{-3})$ is achieved. Note that without regularization, this corresponds to a liquid film deviation of $\mathcal{O}(10^{-3})$ away from the target shape $H_{\mathrm{term}}(\mathbf{X})$, which is order of magnitude smaller than the estimated numerical error of $\mathcal{O}(10^{-5})$. Setting an even smaller absolute tolerance for convergence does not give meaningful improvement since the deviation will become comparable to the numerical error. Such 'optimal' solution is also unlikely to be realized in practice due to the presence of noise and other uncertainties in a real system.

2. $|\mathcal{J}_k - \mathcal{J}_{k-1}|/\mathcal{J}_k \leq \texttt{reltol} = 10^{-4}$: The relative change in the cost functional between successive iteration k and $k-1$ is sufficiently small. The solution has likely reached a local minimum, and further iterations are unlikely to yield significant improvement.

Initial guess for $\xi(\mathbf{X}, \tau)$ In the absence of any rigorous mathematical proof, the cost functional $\mathcal{J}$ given by Eq. (7.2) is not expected to be convex due to the highly nonlinear nature of the PDE constraint. As a result, the high-dimensional solution space may possess many local minima. The choice of initial guess becomes very important as it can affect whether a sufficiently 'good' solution (see Section 7.4.1.3) can be obtained.

All the results presented in the subsequent section uses a *constant* function as the initial guess ($\xi_{k=0}$ in Algorithm 1), i.e., $\xi_{k=0} = D_0$ when optimizing the mask topography or $\xi_{k=0} = 1$ when optimizing the profile of the applied voltage, because it is the simplest possible choice without requiring any prior knowledge of the possible form of the control, and alternative initial guess does not appear to offer better optimization results. When optimizing the mask topography, sinusoidal shapes with different amplitudes and phase have been tested as the initial guess, and the optimizer always converge to the same final solution. A featureless electrode with different mean separation has also been tested as the initial guess, and it is found that the mean separation of the final optimal mask

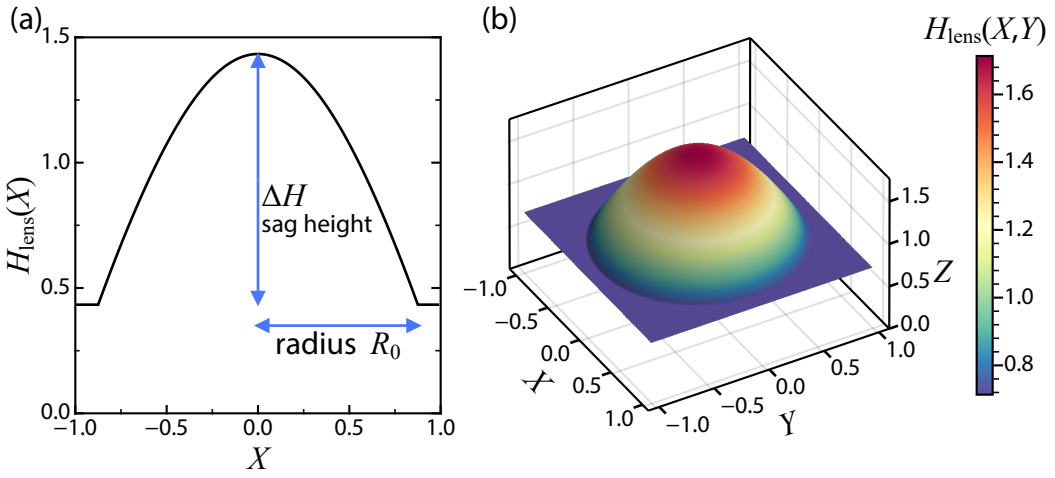

Figure 7.1: Schematic of the hyperbolic lens as the target shape $H_{\rm term}$ in (a) 1D and (b) 2D. The lens radius and sag height are labeled as R_0 and ΔH.

correlates with that of the initial guess. Nevertheless, the values of the minimized cost function $\mathcal{J}$ are very similar regardless of the initial guess and the corresponding solution of the optimal mask. This shows that despite the presence of multiple local minima in the solution space, they all have roughly the same values.

When optimizing the electrode topography, the initial guess D_0 can neither be too large nor too small, otherwise the initial guess might not fall within the basin of attraction in the solution space which results in convergence failure at the first few iterations. In order to ensure a reasonable starting value for the electrode separation, D_0 is chosen via the relation $\mathcal{W} = \mathcal{W}_c$ where the Maxwell stress should neither be too small nor too large. This choice is found to be very robust to a wide range of $\mathcal{W}$ and τ_f based on results from numerical experiments. Increasing the regularization parameters Υ_1, Υ_t or Υ_2 is also found to make the computed optimal control variable much less dependent on the initial guess, likely because regularization makes the optimization problem less ill-posed.

7.4.1.2 Target shape

For proof-of-concept demonstration, we consider an aspheric lens shown in Fig. 7.1 as the target terminal shape. The center is shaped as a hyperbola for the region $|\mathbf{X}| \leq R_0$, and is flat in the periphery. The central hyperbolic lens has radius R_0 and sag height ΔH, and is described by the following analytical expression:

$$H_{\rm lens}(\mathbf{X}) = \begin{cases} z_0 - a\sqrt{1+|\mathbf{X}|^2}, & \text{if } |\mathbf{X}| \leq R_0, \\ H_{\rm min}, & \text{if } |\mathbf{X}| > R_0, \end{cases} \tag{7.35}$$

where the constant a is determined by the condition $\Delta H \equiv H_{\text{lens}}(|\mathbf{X}| = 0) - H_{\text{lens}}(|\mathbf{X}| = R_0)$:

$$a = \frac{\Delta H}{\sqrt{1 + R_0^2} - 1}, \tag{7.36}$$

the constant z_0 is determined by volume conservation $\text{mean}[H_{\text{term}}(\mathbf{X})] = 1$ and differs in a 1D domain (i.e., a line) and 2D domain (i.e., a square):

$$\text{1D:} \qquad z_0 = 1 + \frac{a}{2}\sinh^{-1}(R_0) - \frac{a(R_0 - 2)}{2}\sqrt{1 + R_0^2}, \tag{7.37a}$$

$$\text{2D:} \qquad z_0 = 1 + \frac{1}{12}\left[\sqrt{1 + R_0^2}\left(12 - \pi R_0^2\right) + 2\pi\left(\sqrt{1 + R_0^2} - 1\right)\right], \tag{7.37b}$$

and the constant H_{min} can be determined once a and z_0 are known:

$$H_{\text{min}} \equiv H_{\text{lens}}(|\mathbf{X}| = R_0) = z_0 - a\sqrt{1 + R_0^2}. \tag{7.38}$$

Note that the thickness of the base H_{min} differ in 1D and 2D for the same lens radius R_0 and sag height ΔH. The symbol H_{lens} and H_{term} will be used interchangeably, but it should be stressed that the target terminal shape does not need to be a lens but can be any arbitrary shape. The specific lens given by Eq. (7.35) is chosen because it can be shown using Fermat's principle of least action that an object placed at infinity can be focused without spherical aberration by a hyperbolic lens shown in Fig. 7.1. Therefore, this presents an interesting example with potential applications in optics, and the presence of both flat and curved segments also makes it a challenging target shape for the control problem as it will be shown in the results section.

7.4.1.3 Metrics for quantifying deviations

In order to quantify the optimization results, we define the **dev**iation between the liquid film and the target shape H_{dev}

$$H_{\text{dev}}(\mathbf{X}) = H(\mathbf{X}, \tau_f) - H_{\text{term}}(\mathbf{X}), \tag{7.39}$$

as well as the (root-)mean-squared deviation

$$\mathcal{E}_{\text{ms}} = \frac{1}{|\Omega|}\int_{\Omega}\left[H_{\text{dev}}(\mathbf{X})\right]^2 \mathrm{d}\mathbf{X}, \quad \mathcal{E}_{\text{rms}} = \sqrt{\mathcal{E}_{\text{ms}}}, \tag{7.40a}$$

$$\mathcal{E}_{\text{max}} = \max\left|H_{\text{dev}}(\mathbf{X})\right|. \tag{7.40b}$$

We also use the subscript 'opt' (which stands for **opt**imal) to denote the final converged optimal control variable, e.g., ξ_{opt}, D_{opt} and Ψ_{opt}.

7.4.1.4 Parameters

Unless otherwise specified, the parameters are fixed at $\varepsilon_r = 2.5$, $\mathcal{A} = 10^{-3}$, $\mathcal{W} = 2000$, $\tau_f = 0.01$, $R_0 = 0.875$, $\Delta H = 1.0$, and $\Upsilon_1 = \Upsilon_2 = \Upsilon_t = 0$. For optimization in mask topography, i.e., $\xi = D(\mathbf{X})$, $n_x = 16$ (and $n_t = 0$) Fourier terms are used to represent the control variable given by Eq. (7.4). For optimization in the time-dependent voltage, i.e., $\xi = \Psi_\Delta(\tau)$, $n_t = 1$ and $n_x = 0$ Fourier terms are used. Different parameters are varied in different sections with the remaining parameters kept at the base values given here.

7.4.2 Optimization in mask topography: $\xi = D(\mathbf{X})$

7.4.2.1 Detailed analysis of base parameters

We first analyze the optimization results for the base case ($R_0 = 0.0875$, $\Delta H = 1.0$, $\mathcal{W} = 2000$, $\tau_f = 0.01$, $\Upsilon_1 = \Upsilon_2 = 0$ and $n_x = 16$) in detail, before investigating the effects of varying different parameters in latter sections.

Qualitative features of optimal mask The optimal mask shape $D_{\text{opt}}(X)$ computed for $\mathcal{W} = 2000$, $\tau_f = 0.01$, $\Upsilon_1 = \Upsilon_2 = 0$ and $n_x = 16$ (for a 1D target lens with $R_0 = 0.875$ and $\Delta H = 1.0$) is shown in Fig. 7.2(a) in orange line (right axis). A smaller electrode separation, i.e., smaller $D(X)$, results in larger electric field (under constant voltage), and hence larger magnitude of Maxwell stress acting on the liquid surface. Since the direction of Maxwell stress points upward (when the upper gas layer has a smaller relative permittivity than the liquid film), a smaller local electrode separation is needed in region where the liquid film is expected to attain larger local thickness. This explains the smaller electrode separation near the middle region of $|X| \lesssim R_0$ where the protrusion of the lens is formed. The rapid change in electrode separation near the edge, notably the rise at $|X| = R_0$ and fall at $|X| = 1$, is needed in order to maintain a flat surface in $R_0 \leq |X| \leq 1$. As shown in Section 7.4.2.2, these features become less pronounced when the sharp junction at $|X| = R_0$ is rounded.

Optimal shaping strategy At early time ($\tau = 0.05\tau_f$), the liquid film forms two protrusions near $|X| \approx 0.8$, while the center region remains relatively flat. The protruded region continues growing upward and inward while drawing liquid from the region near $|X| = 1$, eventually forming the final aspheric lens shape via the merging of two local maxima. The lateral flow is driven by the large pressure gradient ∇P caused by the large gradient in Maxwell stress as a result of the electrode topography.

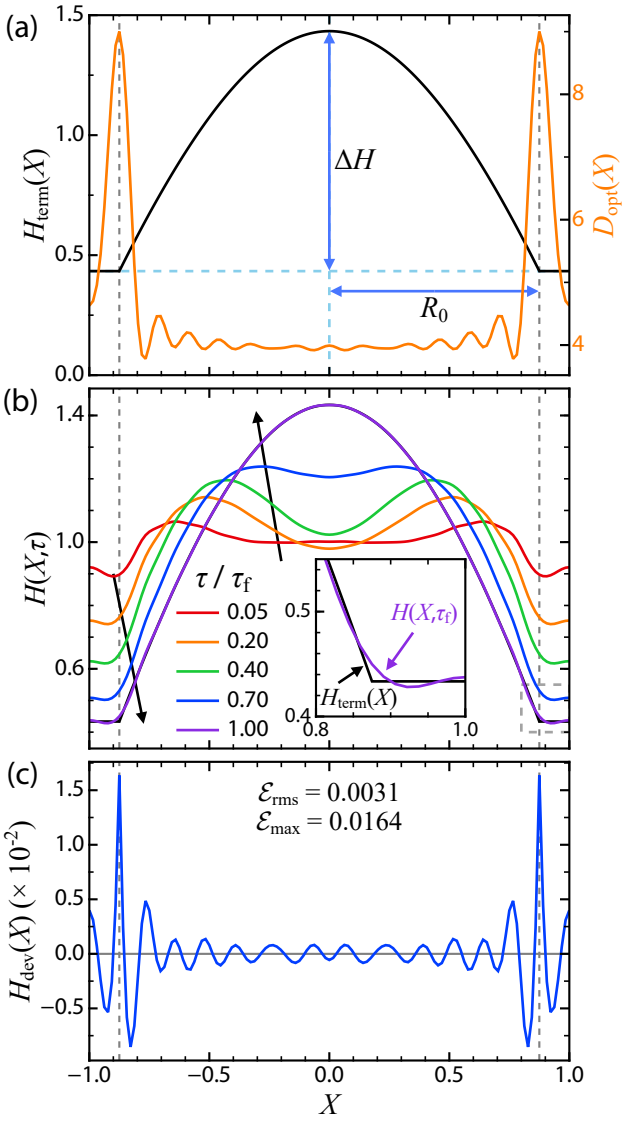

Figure 7.2: Optimization of mask topography for 1D lens with $R_0 = 0.875$ and $\Delta H = 1.0$. Parameters: $\mathcal{W} = 2000$, $\tau_f = 0.01$, $\Upsilon_1 = \Upsilon_2 = \Upsilon_t = 0$, $n_x = 16$. (a) The target lens shape $H_{\rm term}(X)$ (left axis) and the corresponding optimal mask topography $D_{\rm opt}(X)$ (right axis). (b) Liquid film shape $H(X,\tau)$ at different time τ. Arrow indicates direction of increasing time. Inset shows the magnified view near $X = R_0$. (c) Final deviation $H_{\rm dev}(X) \equiv H(X,\tau_f) - H_{\rm term}(X)$. Vertical dashed lines in all subplots indicate $|X| = R_0$.

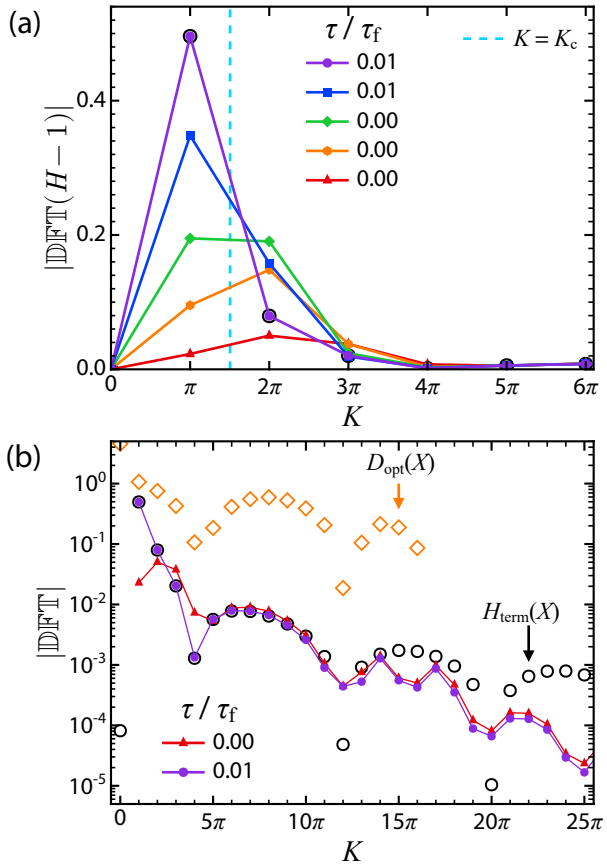

Figure 7.3: The normalized discrete Fourier transform (DFT) of the liquid film. (a) The DFT of the liquid film $|\mathbb{DFT}\{H-1\}|$ at selected time corresponding to those shown in Fig. 7.2(b). (b) The DFT of the liquid film $H(X,\tau)-1$, the optimal mask $D_{\text{opt}}(X)$ and the target shape $H_{\text{term}}(X)$ in logarithmic scale. Note that the DFT given by Eq. A.23 is multiplied by the factor $2/N_x$ where $N_x = 128$ is the number of grid points so that the final quantities represent the Fourier coefficients of the underlying periodic function.

It is interesting to see that the optimal strategy of obtaining the aspheric lens is via forming two smaller bumps away from the center, and then merging the two by inward flow, instead of pulling from the center at the beginning which might be what intuition suggests.

Qualitative features of final deviation The final deviation $H_{\text{dev}}(X) = H(X,\tau_f) - H_{\text{term}}(X)$ is shown in Fig. 7.2(c). The oscillations present in $|X| \le R_0$ for $H_{\text{dev}}(X)$ are the result of the spatial oscillations of the Maxwell stress imposed by the optimal mask which show similar oscillation patterns. The largest deviation occurs at $|X| = R_0$ where the liquid film fails to conform to the sudden change in curvature in the given target lens shape. Parametric studies on varying R_0 and ΔH (see Section 7.4.2.3) and varying $\mathcal{W}$ and τ_f (see Section 7.4.2.4) confirms the occurrence of the largest deviation

at $|X| = R_0$ to be rather general irrespective of parameters.

Spatiotemporal evolution in Fourier space In order to study how different spectral components evolve in time, Fig. 7.3 shows (the magnitude of) the DFT of the liquid film $H(X, \tau)$, the target shape $H_{\text{term}}(X)$ and the optimal mask $D_{\text{opt}}(X)$ where the DFT is defined in Appendix A.5.

Fig. 7.3(a) shows the DFT of the liquid film at different times corresponding to those in Fig. 7.2(b). At early times ($\tau = 0.05\tau_f$), the peak at $K = 2\pi$ corresponds to the formation of two smaller protrusions shown in Fig. 7.2(b), while at late time the peak at $K = \pi$ corresponds to one large protrusion representing the hyperbolic lens at the center. Fig. 7.3(b) shows the DFT of the liquid film shape at $\tau = 0.05\tau_f$ and $\tau = \tau_f$, the optimal mask and target lens shape in logarithmic scale. Good agreement between the spectral profile for $5\pi \lesssim K \lesssim 10\pi$ has already been established at $\tau = 0.05\tau_f$, while matching the smaller K components is accomplished between the intermediate and late time through the coalescence of smaller protrusions. There is noticeable discrepancy in matching the large K components ($K \gtrsim 15\pi$), which cannot be improved even if more Fourier terms (i.e., increasing n_x) are incorporated into the representation of $D_{\text{opt}}(X)$ in Eq. (7.4). This corresponds to features smaller than 0.13 in real space, which matches the length of the flat segment between $0.875 \leq X \leq 1$. The spectral profile of the optimal mask (orange unfilled diamonds) show some qualitative resemblance to that of the target lens, but more quantitative relation between the two is not currently known.

The early time growth of the $K = 2\pi$ mode may also suggest the optimal shaping of the liquid film is achieved mainly via the nonlinear growth rather than the intrinsic electrostatic instability. For reference, the cut-off wave number K_c given by Eq. (3.5) estimated for parallel electrodes ($D(X) = \text{const.} \approx \min[D_{\text{opt}}(X)]$) is indicated by the vertical dashed line in Fig. 7.3. The modes which are predicted to be linearly stable by LSA for flat electrodes (e.g., $K = 2\pi, 3\pi$, etc.) actually grow faster than the unstable mode with $K = \pi$ at early time. While the stability of a mode in a system with featureless electrode does not necessarily imply stability in a system with patterned electrode, the fact that the mode we suspect to be most unstable only grows significantly at later time suggests the intrinsic instability plays a rather minor role in the optimal shaping of liquid film.

7.4.2.2 Effects of varying target lens: Smoothing sharp junction

In this section, we study the effects of varying the shape of the target hyperbolic lens. The target lens studied in the previous section has a sharp junction at $|X| = R_0$. To study the effects of having a smoothed junction on the optimization results, a Gaussian kernel $\mathcal{K}$ is applied to the target shape H_{term} via the operation

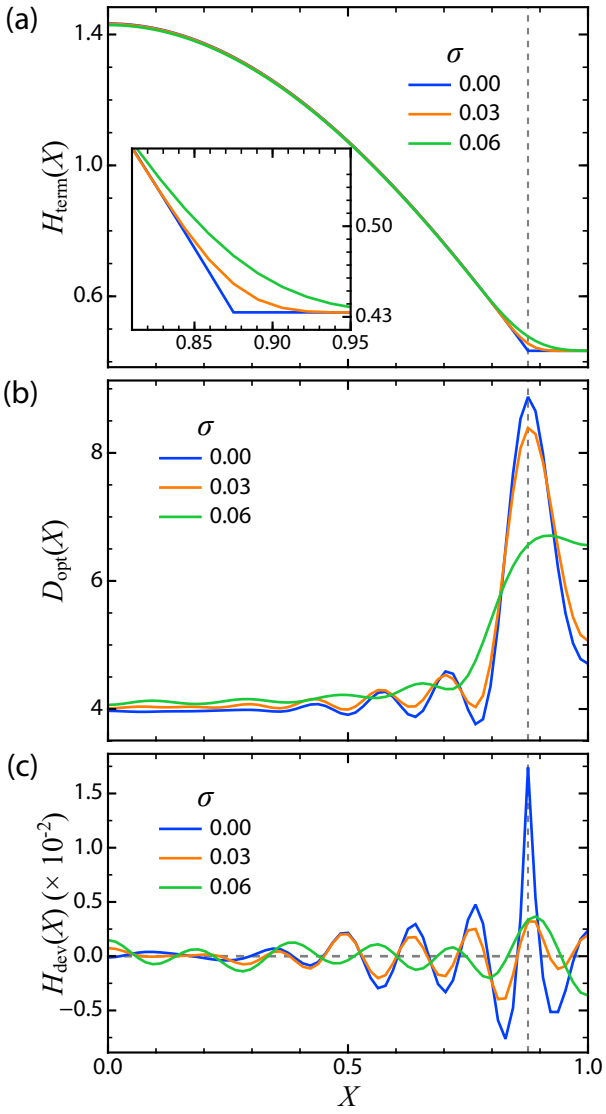

Figure 7.4: Influence of rounding the abrupt transition at $|X| = R_0$ of the target shape (i.e., varying smoothing factor σ) on the optimization results. Parameters: $\mathcal{W} = 2000$, $\tau_f = 0.01$, $\Upsilon_1 = \Upsilon_2 = \Upsilon_t = 0$, $n_x = 16$. (a) The target shape $H_{\mathrm{term}}(X)$ obtained with different amount of smoothing (represented by σ) applied. Inset shows the magnified view near the $|X| = R_0$. (b) The optimal mask shape $D_{\mathrm{opt}}(X)$ obtained for the corresponding target shapes shown in (a). (c) The final deviation $H_{\mathrm{dev}}(X)$ for the corresponding target shapes shown in (a). Vertical dashed lines indicate $|X| = R_0$.

$$\widetilde{H}_{\text{term}}[i] = \sum_j H_{\text{term}}[i+j]\mathcal{K}[j], \tag{7.41}$$

where the notation $H_{\text{term}}[i] = H_{\text{term}}(X_i)$ denotes the value at the grid point $X = X_i$ after spatial discretization. The Gaussian kernel is parameterized by the smoothing width σ, and Fig. 7.4(a) shows the target lens after the application of the Gaussian kernel with different σ. Larger σ results in a smoother transition at $|X| = R_0$, and $\sigma = 0$ corresponds to no smoothing. Note that the region in $|X| \leq R_0$ no longer has the exact shape of a hyperbola for nonzero σ.

The corresponding optimal mask $D_{\text{opt}}(X)$ for the three specific target lenses are shown in Fig. 7.4(b). It can be seen that the amplitudes of the oscillations in the central region $|X| \lesssim R_0$ are reduced as σ increases. The rapid change in electrode topography in $|X| \gtrsim R_0$ is also less pronounced, and the overall electrode topography has a smoother profile. The final deviation $H_{\text{dev}}(X)$ as shown in Fig. 7.4(c) shows similar magnitude for the three cases in the central region, but the large deviation at $|X| = R_0$ for the unsmoothed case of $\sigma = 0$ is greatly reduced. Further inspection of the Fourier transform of the rounded target lens (not shown here) shows that the magnitude of the large K components corresponding to small feature size are greatly reduced, making it easier to match the spectral profiles of the liquid film shape to that of the target shape. This is consistent with the intuitive expectation that if no sharp features are present in the desired target shapes, the corresponding optimal mask adopts a much smoother profiles.

7.4.2.3 Variation in lens radius R_0 and sag height ΔH

We next investigate the influence of varying the lens radius R_0 and sag height ΔH of the 1D target lens on the optimization of the mask topography $D(X)$ while keeping other parameters the same at $\mathcal{W} = 2000$, $\tau_f = 0.01$, $\Upsilon_1 = \Upsilon_t = \Upsilon_2 = 0$ and $n_x = 16$.

The RMS deviation $\mathcal{E}_{\text{rms}}$ achieved after optimization as a function of R_0 and ΔH is shown in Fig. 7.5(a). $\mathcal{E}_{\text{rms}}$ is generally smaller when the aspect ratio $\Delta H/R_0$ is smaller (bottom right purple region of the plot) and vice versa. This provides a quantitative verification of the intuition that it is generally easier to shape the liquid film to form protrusions or features with smaller aspect ratio. The maximum deviation $\mathcal{E}_{\text{max}}$ is shown in Fig. 7.5(b), which shows a very similar qualitative trend to that of $\mathcal{E}_{\text{rms}}$ except the numerical values are usually 4 to 6 times larger. The X coordinate where the final deviation magnitude is at maximum, i.e., $X_{\mathcal{E}}$ where $|H_{\text{dev}}(X = X_{\mathcal{E}})| = \mathcal{E}_{\text{max}}$, is shown in Fig. 7.5(c). There is a clear trend that $X_{\mathcal{E}} = R_0$ regardless of the values of R_0 and ΔH. This shows that the large deviation at $|X| = R_0$ seen in Fig. 7.2(c) is fairly general even when the geometry of the target shape changes.

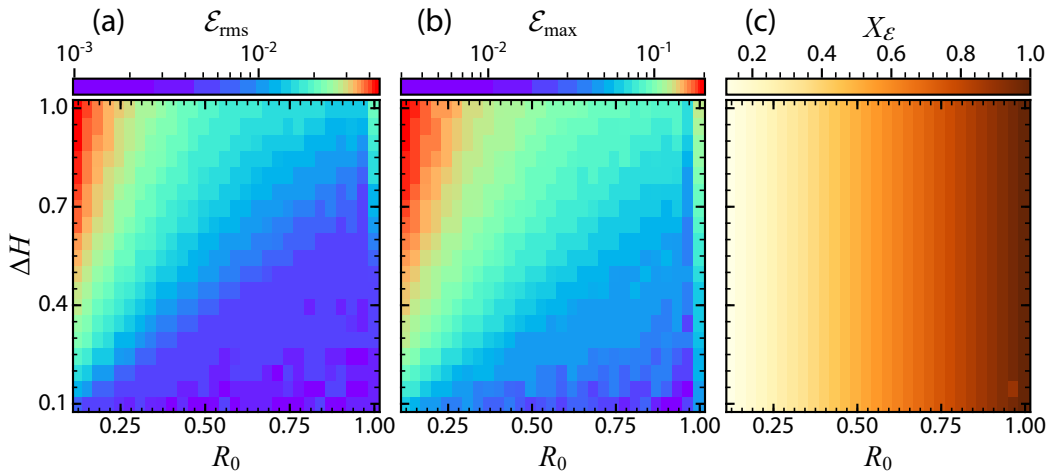

Figure 7.5: Influence of changing the sag height ΔH and the lens radius R_0 of the 1D target lens on the optimization results. Parameters: $\mathcal{W} = 2000$, $\tau_f = 0.01$, $\Upsilon_1 = \Upsilon_2 = \Upsilon_t = 0$, $n_x = 16$. (a) The RMS deviation $\mathcal{E}_{\rm rms}$. (b) The maximum deviation $\mathcal{E}_{\rm max}$. (c) The X-coordinate $X_{\mathcal{E}}$ where the $H_{\rm dev}(X)$ is maximized.

The observations seen in Fig. 7.5 also appears when different $\mathcal{W}$ ($2000 \leq \mathcal{W} \leq 10000$) and τ_f ($0.005 \leq \tau_f \leq 0.02$) are used, as well as for both spatial and spatiotemporal voltage control, i.e., $\xi = \Psi_\Delta(X)$ or $\xi = \Psi_\Delta(X, \tau)$. This shows that the general trend seen in Fig. 7.5 is quite general over a wide range of parameters and also holds for different types of control.

7.4.2.4 Variation in $\mathcal{W}$ and τ_f

We next investigate the effects of varying $\mathcal{W}$ and τ_f on the optimization of the mask topography $D(X)$ while keeping other parameters the same at $R_0 = 0.875$, $\Delta H = 1.0$, $\Upsilon_1 = \Upsilon_t = \Upsilon_2 = 0$ and $n_x = 16$.

The RMS deviation $\mathcal{E}_{\rm rms}$ achieved as a function of $\mathcal{W}$ and τ_f is shown in Fig. 7.6(a). The colored (gray-scale) region shows the range of $\mathcal{W}$ and τ_f where $\mathcal{E}_{\rm rms} \leq 0.01$ ($\mathcal{E}_{\rm rms} \geq 0.01$). Relatively small RMS deviation of $\mathcal{E}_{\rm rms} \leq 0.005$ is achievable for $\mathcal{W} \gtrsim 10^3$, and the acceptable range of $\mathcal{W}$ ($\propto V_0^2$ where V_0 is the dimensional applied voltage) spans more than an order of magnitude. Fig. 7.6(b) shows the mean electrode separation of the corresponding optimal mask mean$[D_{\rm opt}(X)]$, which generally increases with $\mathcal{W}$. This implies if the applied voltage is fixed at a larger value, the optimization automatically selects a mask profile with larger average separation to balance out the increase in applied voltage to keep the electric field strength and thus the Maxwell stress within a preferred range.

For each given $\mathcal{W}$, small $\mathcal{E}_{\rm rms}$ is achieved when τ_f is neither too large nor too small, e.g., when $\mathcal{W} = 2000$, $0.005 \lesssim \tau_f \lesssim 0.1$ for $\mathcal{E}_{\rm rms} \leq 0.004$. When τ_f is smaller, there is less

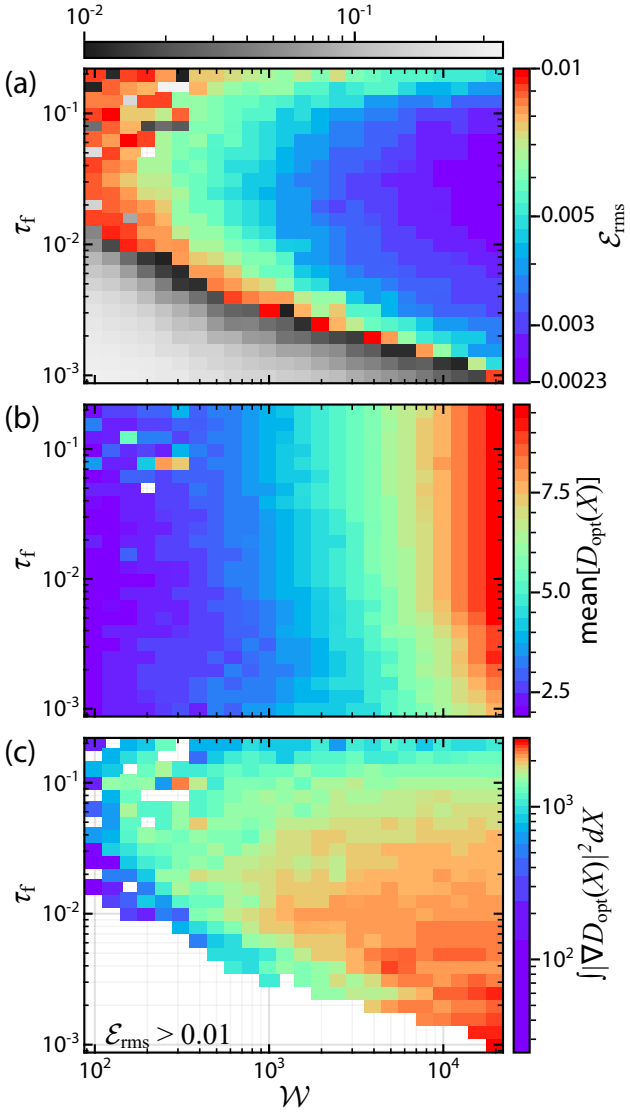

Figure 7.6: Influence of changing $\mathcal{W}$ and τ_f on the optimization of $D_{\rm opt}(X)$ for 1D lens with $R_0 = 0.875$ and $\Delta H = 1.0$. Parameters: $\Upsilon_1 = \Upsilon_2 = \Upsilon_t = 0$, $n_x = 16$. (a) The RMS deviation $\mathcal{E}_{\rm rms}$. Two different color maps are used to more clearly show the variation in $\mathcal{E}_{\rm rms}$, and $\mathcal{E}_{\rm rms} = 0.01$ is the cutoff value separating the two color maps. (b) Mean electrode separation of the optimal mask. (c) $\int_\Omega |D_{\rm opt}(X)|^2 dX$. The bottom left empty region corresponds to $\mathcal{E}_{\rm rms} > 0.01$ in (a) and is not shown.

time to shape the liquid film into the required final shape, and so the required gradient in the mask topography $\nabla D_{\text{opt}}(X)$, and thus the Maxwell stress, needs to be larger for more 'aggressive' shaping of the liquid film. This can be seen in Fig. 7.6(c) which shows $\int |\nabla D_{\text{opt}}(X)|^2 \mathrm{d}X$ as a measure of the spatial gradient present in the optimal mask, which is generally larger for smaller τ_f. When τ_f is too small, there is insufficient time to shape the liquid film despite the large gradient in Maxwell stress externally imposed on the liquid film by the electrode configuration. On the other hand, when τ_f is very large, large gradient in Maxwell stress from the patterned electrode is no longer needed, and the mask topography approaches a flat electrode. The time scale associated with the growth of liquid film cannot greatly exceed the time scale for natural instability under flat electrodes given by $1/\beta(K_m)$. Using the values of mean$[D_{\text{opt}}(X)]$ and $\mathcal{W}$ shown in Fig. 7.6 as an estimate for D_0 and $\mathcal{W}$ in Eq. (3.7) gives $1/\beta(K_m) \approx \mathcal{O}(0.1)$ as the approximate instability time scale, which is an order of magnitude larger than the optimal τ_f which is $\mathcal{O}(0.01)$.

The gray scale region in Fig. 7.6(a) corresponds to relatively large $\mathcal{E}_{\text{rms}}$, due to insufficient time (i.e., small τ_f) for liquid shaping or/and insufficient Maxwell stress (i.e., small $\mathcal{W}$) to appropriately deform the liquid film. This presents an example where the electrode topography computed by the optimization algorithm does not necessarily lead to good agreement between the liquid film and the target shape due to limitations in the underlying physics.

7.4.2.5 Variation in regularization parameters

Variation in Υ_1 We first study the effects of varying Υ_1, keeping $\Upsilon_2 = 0$. Fig. 7.7(a) shows the values of cost function $\mathcal{J}$, regularization term $\mathcal{R}_1$, RMS deviation $\mathcal{E}_{\text{rms}}$ and maximum deviation $\mathcal{E}_{\text{max}}$ achieved after optimization as a function of Υ_1, all of which generally increase with Υ_1. Fig. 7.7(b) shows the maximum, minimum and mean value of the optimal mask $D_{\text{opt}}(X)$, as well as $\int |D_{\text{opt}}(X)|^2 \mathrm{d}X$, the quantity being penalized in the $\mathcal{R}_1$ regularization term, and four quantities generally decrease with Υ_1. Fig. 7.7(c) shows the actual profile of the optimal mask $D_{\text{opt}}(X)$ for selected values of Υ_1. The optimal mask $D_{\text{opt}}(X)$ has qualitatively similar shape regardless of Υ_1: a relatively flat middle region with smaller local electrode separation, and rapid change in topography near $|X| = R_0$. However, as Υ_1 is increased, the overall profile is 'squeezed' vertically and becomes smoother, with fewer oscillations in the middle section and a more gentle change in local electrode separation near $|X| = R_0$.

The trends observed in Fig. 7.7 can be explained as follow: as Υ_1 increases, the quantity $\int |D_{\text{opt}}(X)|^2 \mathrm{d}X$ tends to become smaller in order to prevent the $\mathcal{R}_1$ from being too large. This reduces the large spatial variation present in $D_{\text{opt}}(X)$ and results in the smoother profiles seen in Fig. 7.7(c). In order to compensate for the loss in Maxwell

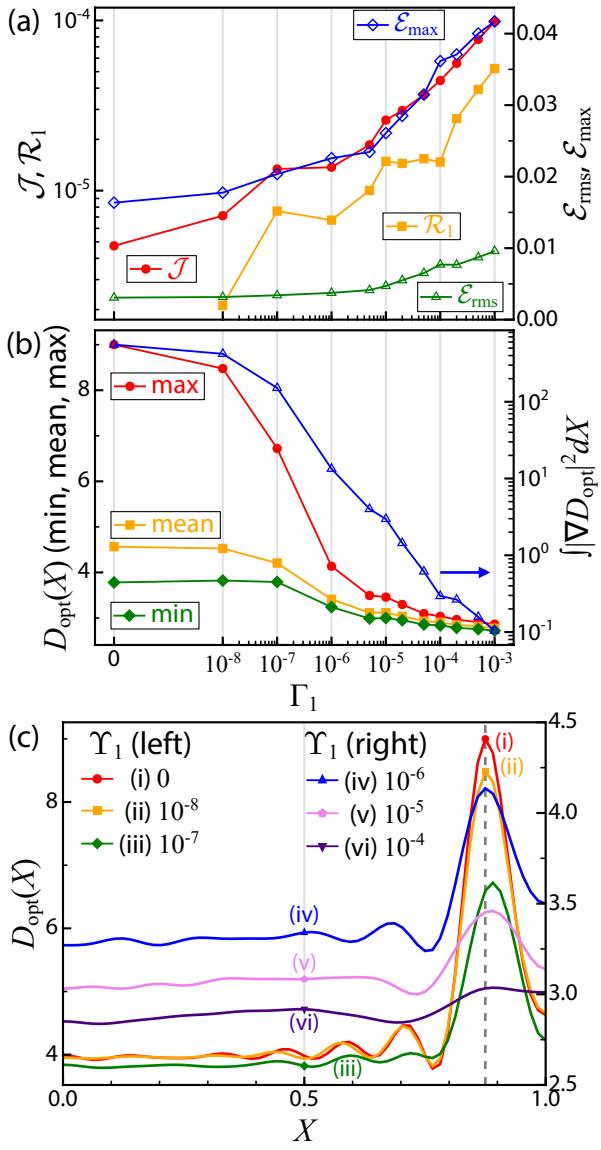

Figure 7.7: Influence of changing Υ_1 on the optimization of $D_{\rm opt}(X)$ for 1D lens with $R_0 = 0.875$ and $\Delta H = 1.0$. Parameters: $\mathcal{W} = 2000$, $\tau_f = 0.01$, $\Upsilon_2 = \Upsilon_t = 0$, $n_x = 16$. (a) Left axis: the cost function $\mathcal{J}$ and regularization term $\mathcal{R}_1$; right axis: the RMS and maximum deviation, as a function of Υ_1. (b) Left axis: the maximum, mean and minimum of the optimal mask $D_{\rm opt}(X)$; right axis: $\int |\nabla D_{\rm opt}(X)|^2 dX$. (c) The optimal mask topography $D_{\rm opt}(X)$ for (left axis) $\Upsilon_1 = 0, 10^{-8}, 10^{-7}$ and (right axis) $10^{-6}, 10^{-5}, 10^{-4}$.

stress gradient due to a smoother mask topography, the optimal shape and the position of the mask is closer to the liquid film so that the average Maxwell stress strength is larger, which explains the overall trend shown in Fig. 7.7(b). Besides, the smoother optimal mask profile resulted from larger Υ_1 also leads to less effective liquid film shaping due to the smaller Maxwell stress gradient exerted on the liquid film surface, leading to larger $\mathcal{E}_{\mathrm{rms}}$, $\mathcal{E}_{\mathrm{max}}$ and $\mathcal{J}$ as shown in Fig. 7.7(a).

Variation in Υ_2 Next, we study the effects of varying Υ_2, keeping $\Upsilon_1 = 10^{-5}$. A nonzero Υ_1 is needed to prevent the optimal mask from having unacceptably large maximum as Υ_2 is increased.

Fig. 7.8(a) shows the value of cost function $\mathcal{J}$, regularization terms $\mathcal{R}_1$ and $\mathcal{R}_2$, as well as the RMS deviation $\mathcal{E}_{\mathrm{rms}}$ and maximum deviation $\mathcal{E}_{\mathrm{max}}$ as Υ_2 is increased. The overall trend is similar to that shown in Fig. 7.7(a) when Υ_1 is varied instead. Fig. 7.8(b) shows the maximum, mean and minimum value of the optimal mask $D_{\mathrm{opt}}(X)$ against Υ_2, while Fig. 7.8(c) shows the optimal mask $D_{\mathrm{opt}}(X)$ for selected Υ_2. As Υ_2 is increased, the mean value of the optimal mask increases as expected, since the $\mathcal{R}_2$ regularization penalizes mask topography which is close to the reference point $\xi_{\mathrm{ref}} = \max[H_{\mathrm{term}}(X)]$. The minimum and maximum value of $D_{\mathrm{opt}}(X)$ also increase accordingly. As the mask becomes further away from the liquid film, its spatial profile acquires a slightly larger gradient to restore the overall Maxwell stress gradient for shaping the liquid film, leading to the small increase in $\mathcal{R}_1$ as shown in Fig. 7.8(a).

7.4.3 Optimization results for roughened mask topography

All the previous results assume the control variable ξ, which is the mask topography $D(X)$, can be engineered precisely. That is seldom achieved in practice, especially for the optimal mask shown in Fig. 7.2(a) which possess many sophisticated features at very small length scale. In this section, the effects of imperfect fabrication of the optimal mask on the final deviation $H_{\mathrm{dev}}(X)$ are discussed. Two methods to mitigate such effects are also explored: in Section 7.4.3.2 using the regularization to adjust the optimal mask shape, and in Section 7.4.5 using temporal control.

7.4.3.1 Illustration of roughened mask

A roughened mask is obtained by adding a random perturbation term to the computed optimal mask $D_{\mathrm{opt}}(X)$:

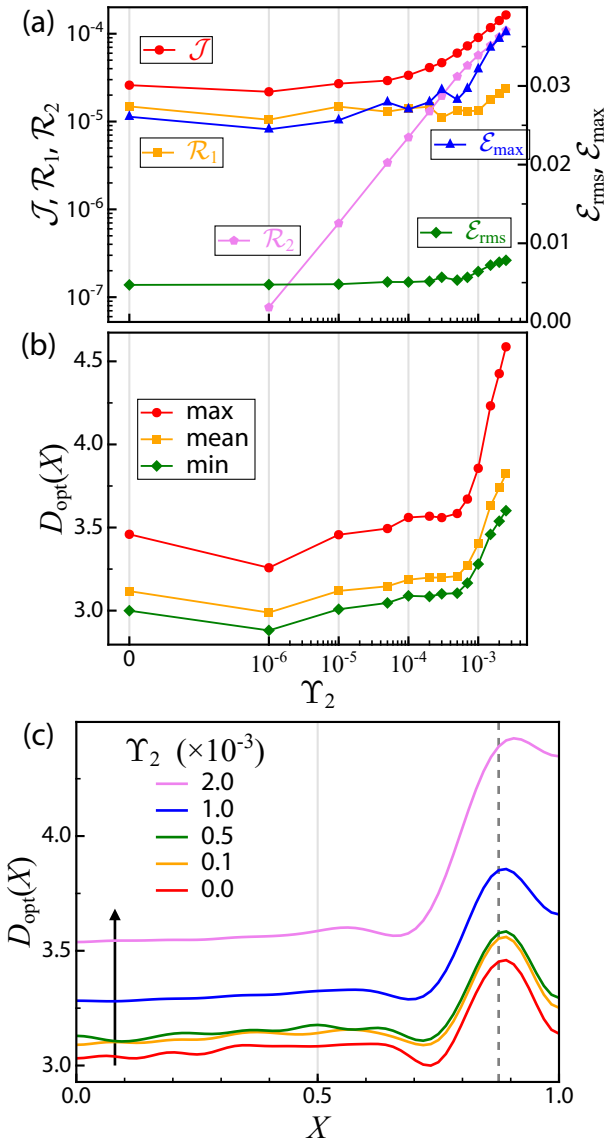

Figure 7.8: Influence of changing Υ_2 on the optimization of $D_{\rm opt}(X)$ for 1D lens with $R_0 = 0.875$ and $\Delta H = 1.0$. Parameters: $\mathcal{W} = 2000$, $\tau_f = 0.01$, $\Upsilon_1 = 10^{-5}$, $\Upsilon_t = 0$, $n_x = 16$. (a) Left axis: the cost function $\mathcal{J}$ and regularization term $\mathcal{R}_1$ and $\mathcal{R}_2$; right axis: the RMS and maximum deviation, as a function of Υ_1. (b) The maximum, mean and minimum of the optimal mask $D_{\rm opt}(X)$. (c) The optimal mask topography $D_{\rm opt}(X)$ for selected Υ_2. Arrow indicates direction of increasing Υ_2.

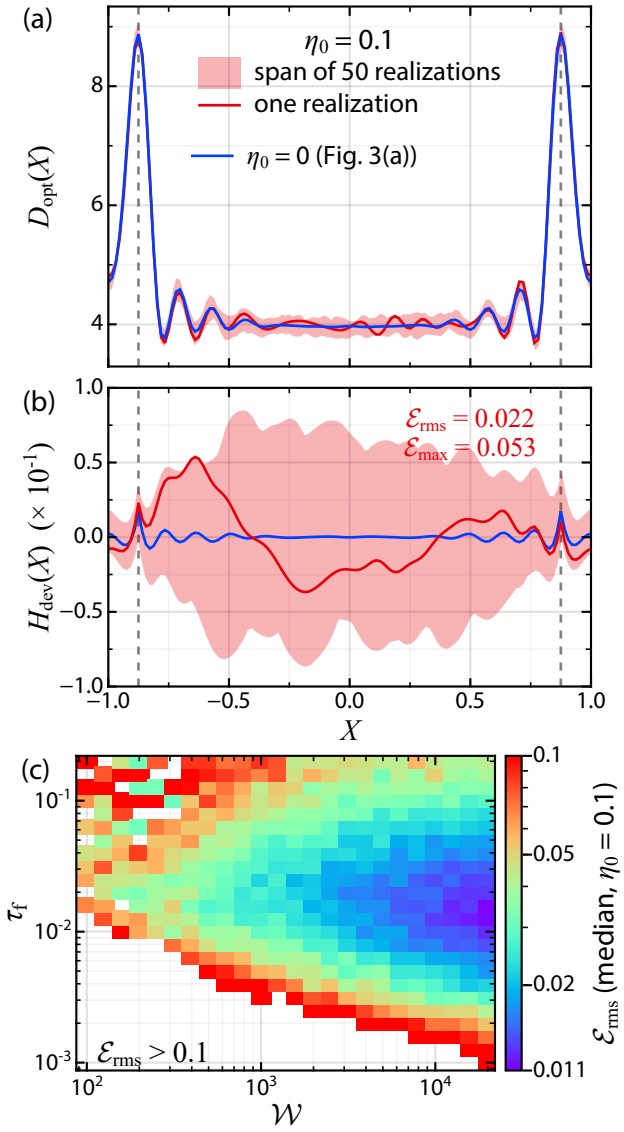

Figure 7.9: Influence of roughened mask topography on the final liquid film shape. Parameters: $R_0 = 0.875$, $\Delta H = 1.0$, $\Upsilon_1 = \Upsilon_2 = \Upsilon_t = 0$, $n_x = 16$. For (a) and (b), $\mathcal{W} = 2000$ and $\tau_f = 0.01$. (a) The optimal mask $D_{\rm opt}(X)$ shown in Fig. 7.2(a) (blue line), one particular realization of the roughened mask with $D(X) = D_{\rm opt}(X) + \eta(X)$ (red line) and the span of the roughened masks in 50 independent realizations (pink shade). (b) The final deviation $H_{\rm dev}(X)$ corresponding to the use of the given electrodes shown in (a). (c) The median of the RMS deviation $\mathcal{E}_{\rm rms}$ resulted from the use of roughened masks from 50 independent realizations as a function of $\mathcal{W}$ and τ_f. The bottom left region corresponds to $\mathcal{E}_{\rm rms} > 0.1$ and is not shown.

$$D(X) = D_{\text{opt}}(X) + \frac{\eta_0 \tilde{D}}{\sqrt{N}} \sum_{n=1}^{N} [a_n \cos(n\pi X) + b_n \sin(n\pi X)], \tag{7.42}$$
$$\tilde{D} = \sqrt{\frac{1}{|\Omega|} \int_{\Omega} \{D_{\text{opt}}(X) - \text{mean}[D_{\text{opt}}(X)]\}^2 \, dX},$$

where η_0 is the perturbation amplitude, a_n and b_n are random numbers drawn from a uniform distribution between -1 and $+1$, $N = 20$ is number of perturbation terms used, and $\tilde{D}$ is a measure of the spread in height of the optimal mask so that the added perturbation scales with the vertical span of the optimal mask.

The liquid film shape $H(X, \tau)$ is solved with the roughened mask $D(X) = D_{\text{opt}}(X) + \eta(X)$ in 50 independent realizations where each realization is seeded with a different random seed for generating with coefficients $\{a_n, b_n\}$, resulting in a different perturbation $\eta(X)$ and thus different mask topography $D(X)$. The resulting $\mathcal{E}_{\text{rms}}$ can then be computed with $H(X, \tau_f)$ for each roughened mask, and the median $\mathcal{E}_{\text{rms}}$ indicates the characteristic RMS deviation we can expect in a more realistic setting where the exact topography of optimal mask cannot be fabricated precisely.

Examples of roughened masks are shown in Fig. 7.9(a). The red solid line denotes one particular realization of the roughened mask with $\eta_0 = 0.1$, while the pink shaded region shows the span of all 50 independent realizations of roughened masks. For ease of comparison, the ideal smooth mask (the same mask topography shown in Fig. 7.2(a)) is shown in blue solid line.

The final deviation $H_{\text{dev}}(X)$ resulted from the use of roughened masks are shown in Fig. 7.9(b). Red solid line and pink shaded region correspond to $H_{\text{dev}}(X)$ achieved using the roughened masks shown in Fig. (7.9)(a), respectively. The region where largest deviation occurs changes from $|X| = R_0$ in the ideal smooth mask case to a relatively uniform region in the middle where $|X| \leq R_0$. This is because the Maxwell stress is the largest in the middle for pulling the liquid film upward, and tiny perturbation to the optimal Maxwell stress profile can significantly change the spatiotemporal evolution of the liquid film. For comparison, $H_{\text{dev}}(X)$ for an ideal smooth mask is shown in blue solid line in Fig. 7.9(b).

Fig. 7.9(c) shows the median of the RMS deviation using roughened masks as a function of $\mathcal{W}$ and τ_f (each parameter repeated with 50 independent realizations), with the remaining parameters the same as those in Fig. 7.6. Comparison between Fig. 7.6(a) and Fig. 7.9(c) shows that with the introduction of surface roughening with magnitude $\eta_0 = 0.1$ to the optimal mask, the resulting $\mathcal{E}_{\text{rms}}$ increase by close to an order of magnitude across different values of $\mathcal{W}$ and τ_f. The smallest possible $\mathcal{E}_{\text{rms}}$ is achieved with large $\mathcal{W}$, probably because of the larger separation between mask and substrate

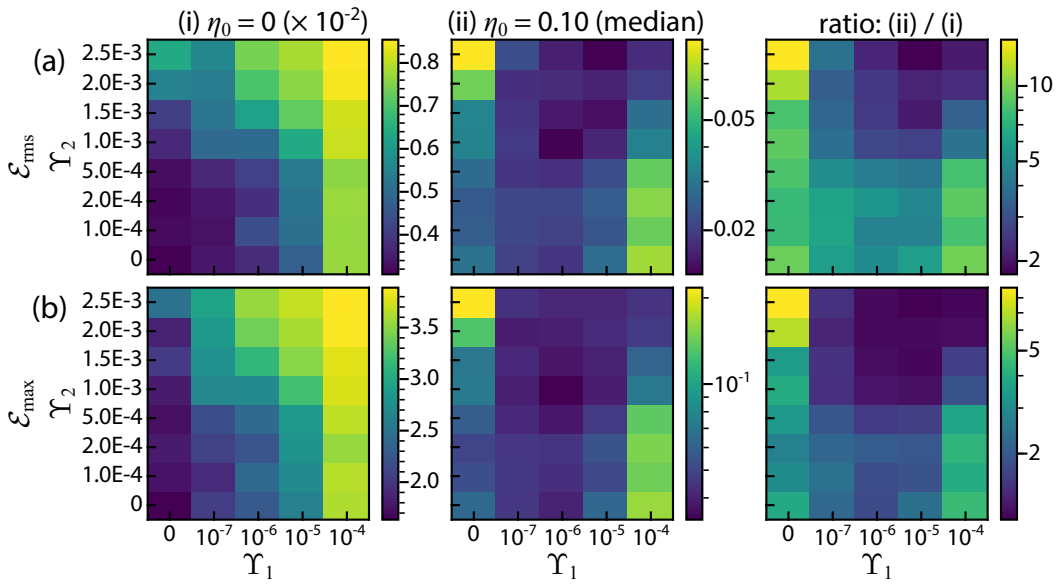

Figure 7.10: Influence of variation in Υ_1 and Υ_2 with ideal and roughened mask topography on the final deviation. (Parameters: $R_0 = 0.875$, $\Delta H = 1.0$, $\mathcal{W} = 2000$, $\tau_f = 0.01$) (a) The first row shows the RMS deviation, while (b) the second row shows the maximum deviation. The column (i) shows the results for ideal smooth mask ($\eta_0 = 0$), the second column (ii) shows the median of 50 independent realizations for roughened mask with $\eta_0 = 0.1$. The third column (iii) shows the ratio between the second and first column, where larger values indicate greater effect of the introduction of surface roughening to the optimal mask.

(see Fig. 7.6(b)) so the perturbation to the Maxwell stress is smoothed out over longer distances.

7.4.3.2 Mitigation of fabrication imperfection via regularization

A mask topography which is less susceptible to fabrication imperfection can be obtained by adjusting the regularization parameters. Fig. 7.10 shows the optimization results for the same set of parameters ($R_0 = 0.875$, $\Delta H = 1.0$, $\mathcal{W} = 2000$, $\tau_f = 0.01$) but with different Υ_1 and Υ_2. The first column shows $\mathcal{E}_{\rm rms}$ and $\mathcal{E}_{\rm max}$ for the ideal smooth mask with $\eta_0 = 0$. Consistent with the results presented in Section 7.4.2.5, smaller Υ_1 and Υ_2 (lower left corner) result in smaller deviation due to less constraint placed on $D_{\rm opt}(X)$. The second column shows the median of $\mathcal{E}_{\rm rms}$ and $\mathcal{E}_{\rm max}$ from 50 independent realizations where the roughened mask given by Eq. (7.42) with $\eta_0 = 0.1$ is used. While the absolute values of both $\mathcal{E}_{\rm rms}$ and $\mathcal{E}_{\rm max}$ increase across all choices of (Υ_1, Υ_2) due to the presence of imperfections on the roughened mask, smaller deviations are now achieved with larger Υ_1 and Υ_2 (upper right corner). The third column of Fig. 7.10 shows the ratio of deviations between the case of roughened mask and ideal smooth mask, and smaller values suggest the presence of surface roughening due to fabrication

imperfection has less impact on the final liquid film shape. It is clear that with larger values of Υ_1 and Υ_2, the effect of mask topography roughening due to fabrication imperfection is less pronounced.

Fig. 7.11 compares the effects of fabrication imperfection for the mask obtained without regularization (left column) and with regularization (right column). The one without regularization ($\Upsilon_1 = \Upsilon_2 = 0$) is the same as that shown in Fig. 7.9(a)-(b), while the one with regularization ($\Upsilon_1 = 10^{-5}$, $\Upsilon_2 = 2.5 \times 10^{-3}$) corresponds to a mask topography more robust to fabrication imperfection based on the general trend observed in Fig. 7.10. The optimal mask shown in Fig. 7.11(d) has a smoother profile, and the absence of sharp features located at $|X| = 1$ due to the $\mathcal{R}_1$ term penalizing large $\nabla_{\|} D_{\text{opt}}$. The resulting final liquid film shape $H(X, \tau_f)$ shown in Fig. 7.11(e) and the final deviation $H_{\text{dev}}(X)$ shown in Fig. 7.11(f) also display smaller deviation relative to the base case shown in 7.11(c). The numerical values in the second row correspond to the RMS deviation $\mathcal{E}_{\text{rms}}$ and maximum deviation $\mathcal{E}_{\text{max}}$, while the numerical values in the third row correspond to the lower quartile, median and upper quartile of $\mathcal{E}_{\text{rms}}$ and $\mathcal{E}_{\text{max}}$ computed from all 50 independent realizations. Comparison of these numerical values of $\mathcal{E}_{\text{rms}}$ and $\mathcal{E}_{\text{max}}$ clearly show that the performance of the optimal mask computed with appropriate choice of Υ_1 and Υ_2 deteriorate by a smaller extent when the fabrication is not perfect and surface roughening is present. The general rule for choosing the best regularization parameters is not currently known and likely depends on other parameters like $\mathcal{W}$ and τ_f as well as the given target shape $H_{\text{term}}(\mathbf{X})$.

7.4.4 Optimization of mask topography for 2D lens

All previous results shown in Sections 7.4 and 7.4.3 are based on a target shape in a 1D domain, i.e., $H_{\text{term}}(\mathbf{X}) = H_{\text{lens}}(X)$. In this section, we study the optimization of mask topography for a hyperbolic lens with $R_0 = 0.875$ and $\Delta H = 1.0$ in a 2D square domain. Note that the thickness of the flat region in $|\mathbf{X}| \geq R_0$ is slightly different than the 1D lens studied in Section 7.4.2.1 because of the change in spatial domain.

Fig. 7.12(a) shows the liquid film shape at selected time under the use of the optimal mask. The liquid film evolves very similarly to the 1D case: it first develops a rim shaped like a volcano in the periphery, which then slowly grows inward and upward to merge into a single bigger protrusion at the center.

Fig. 7.12(b) and (c) show 3D and 2D projection of the final deviation $H_{\text{dev}}(\mathbf{X})$, and Fig. 7.12(d) shows the 1D cut along $Y = 0$ and $Y = X$. The largest deviation again occurs at $|\mathbf{X}| = R_0$, and the deviation in the central region of $|\mathbf{X}| \leq R_0$ is generally smaller than that in $|\mathbf{X}| > R_0$. Compared to the 1D case shown in Fig. 7.2(c), both $\mathcal{E}_{\text{rms}}$ and $\mathcal{E}_{\text{max}}$ are slightly larger, and the deviation magnitude in the region $|\mathbf{X}| = R_0$ also appear slightly larger. Given that there are two principal curvatures in a 2D lens,

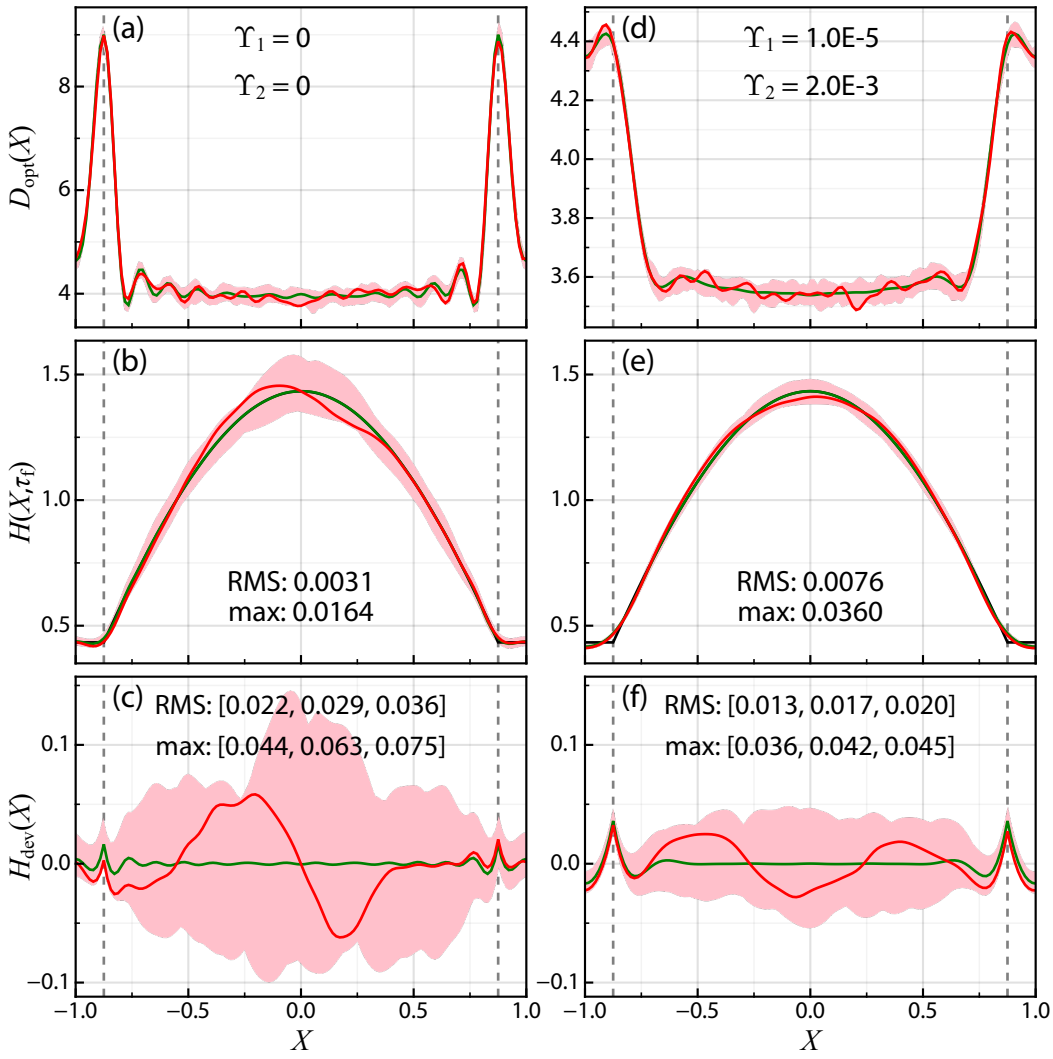

Figure 7.11: Comparison of the effects of mask roughening due to fabrication imperfection with two sets of (Υ_1,Υ_2). Parameters: $R_0 = 0.875$, $\Delta H = 1.0$, $\mathcal{W} = 2000$, $\tau_f = 0.01$. Left column (a)–(c) refers to $\Upsilon_1 = \Upsilon_2 = 0$, while the right column (d)–(f) refers to $\Upsilon_1 = 10^{-5}$ and $\Upsilon_2 = 2 \times 10^{-3}$. The first row ((a),(d)) shows the optimal mask with and without surface roughening described by Eq. (7.42). The second row ((b),(e)) shows the final liquid film shape $H(X, \tau_f)$, and the third row ((c),(f)) shows the final deviation. The green solid line in all subplots corresponds to the case with ideal smooth mask ($\eta_0 = 0$), the red solid line corresponds to one particular realization of the roughened mask case with $\eta_0 = 0.1$, and the pink shaded region corresponds to the span of all 50 independent realizations. The numerical values in (b) and (e) correspond to the RMS deviation $\mathcal{E}_{\rm rms}$ and maximum deviation $\mathcal{E}_{\rm max}$ for the ideal mask ($\eta_0 = 0$). The numerical values in (c) and (f) correspond to the lower quartile, median and upper quartile of $\mathcal{E}_{\rm rms}$ and $\mathcal{E}_{\rm max}$ computed from all 50 independent realizations of roughened masks.

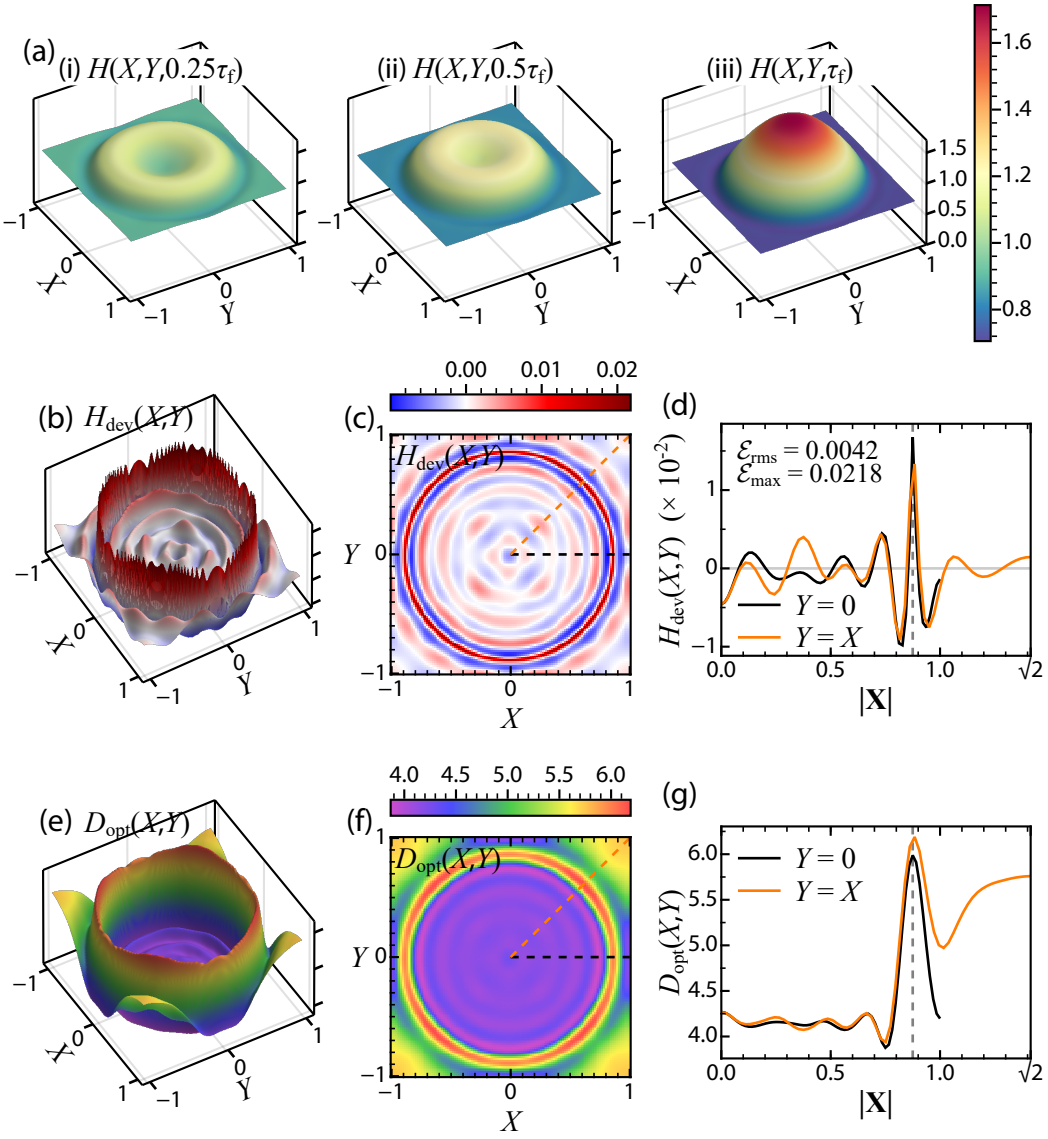

Figure 7.12: Optimization of mask topography for 2D lens with $R_0 = 0.875$ and $\Delta H = 1.0$. Parameters: $\mathcal{W} = 2000$, $\tau_f = 0.01$, $\Upsilon_1 = \Upsilon_2 = \Upsilon_t = 0$, $n_x = 16$. (a) The liquid film shape at (i) $\tau = \tau_f/4$, (ii) $\tau = \tau_f/2$ and (iii) $\tau = \tau_f$. (b)–(c): The 3D and 2D projection of the final deviation $H_{\rm dev}(\mathbf{X})$. (d) The 1D cross-section (indicated by dashed lines in (c)) of the final deviation along $Y = 0$ (black) and $Y = X$ (orange). (e)–(f): The 3D and 2D projection of the optimal mask $D_{\rm opt}(\mathbf{X})$ after optimization. (g) The 1D cross-section (indicated by dashed lines in (c)) of the optimal mask along $Y = 0$ (black) and $Y = X$ (orange).

larger electrostatic stress is needed to deform the liquid film into a 2D lens than a 1D lens (which is simply a 1D 'ridge' in the $X-Y$ plane), and larger deviation may be resulted.

Fig. 7.12(e) and (f) show the 3D and 2D projection of the optimal mask $D_{\rm opt}(\mathbf{X})$, and Fig. 7.12(g) shows the 1D cut along $Y=0$ and $Y=X$. Similar to the 1D case, the local electrode separation is smaller near the center, but changes rapidly near $|\mathbf{X}|=R_0$. The main qualitative difference lies at the boundary of the square domain where the electrode separation at the four corners $(X,Y)=(\pm1,\pm1)$ is larger than that at $(X,Y)=(0,\pm1)$ and $(X,Y)=(\pm1,0)$. While this specific shape might present additional challenges to mask fabrication, it is needed in order to maintain a flat horizontal surface in the liquid film where the inter-lens separation along the $Y=0$ and $Y=X$ directions are different by a factor of $\sqrt{2}$ when the lenses are arranged in a rectilinear manner. If the lenses are arranged in a hexagonal array where the inter-lens separation is the same, we expect the optimal mask topography to appear closer to an axisymmetric shape with less variation in height along the boundary of each unit cell.

7.4.5 Optimization in applied voltage with patterned mask

We now turn to the optimization of the applied voltage, i.e., $\xi=\Psi_\Delta$, for shaping the liquid film toward a 1D target shape. Preliminary results of the more general case of spatiotemporal control $\xi=\Psi_\Delta(X,\tau)$ shows no qualitative differences to the general trends observed in Fig. 7.5 and 7.6, so we do not discuss those results any further. Instead, we focus on the use of time-dependent voltage $\Psi_\Delta(\tau)$ as a method to mitigate the effects of roughened mask discussed in Section 7.4.3, and to provide additional flexibility in shaping liquid film toward *different* target shapes with the same experimental setup. Note that a spatially varying electrode $D=D(X)$ is still needed even though it is no longer the control variable to be optimized, otherwise $\partial H/\partial\tau=0$ at $\tau=0$ because $\nabla_\parallel\Pi=0$.

7.4.5.1 Mitigation of fabrication imperfection in roughened mask

For each of the roughened electrode $D(X)=D_{\rm opt}(X)+\eta(X)$ represented in Fig. 7.9(a) for $R_0=0.875$, $\Delta H=1.0$, $\mathcal{W}=2000$ and $\tau_f=0.01$, the optimal control problem is solved again where $\xi=\Psi(\tau)$ becomes the new control variable and $D(X)$ is a fixed variable in the external pressure Π. Fig. 7.13(a) shows the optimal temporal profile of the applied voltage $\Psi_{\rm opt}(\tau)$ with $n_t=1$ and $\Upsilon_t=10^{-8}$ when the roughened electrode shown in Fig. 7.9(a) in solid red line is used. The effects of varying Υ_t is similar to that of the spatial analog Υ_1: increasing Υ_t leads to smoother $\Psi_{\rm opt}(\tau)$ with more gentle gradient in time. $\Upsilon_t=10^{-8}$ is chosen to prevent excessively large variation in $\Psi_{\rm opt}(\tau)$ that is encountered when $\Upsilon_t=0$ (not shown). $n_t\approx1$ is found to be sufficient for convergence when $\Upsilon_t=10^{-8}$.

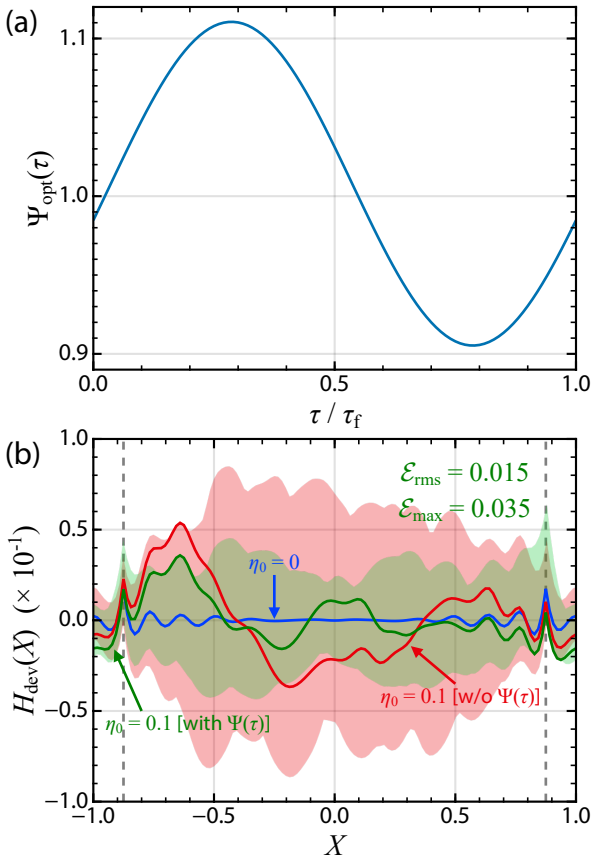

Figure 7.13: Illustration of temporal control in reducing the negative effects of surface roughening in the mask topography due to fabrication imperfection. Parameters: $R_0 = 0.875$, $\Delta H = 1.0$, $\mathcal{W} = 2000$, $\tau_f = 0.01$, $\Upsilon_t = 10^{-8}$, $n_t = 1$. (a) The optimal voltage $\Psi_{\rm opt}(\tau)$ used to correct the particular roughened mask shown in red line in Fig. 7.9(b). (b) The liquid film shape at $\tau/\tau_f = 0.2$, 0.4, 0.6, 0.8 and 1.0 without (red) and with (green) temporal control for one particular realization of roughened mask. (c) Comparison of the final deviation $H_{\rm dev}(X)$ for different cases: blue line shows the case for perfectly smooth mask ($\eta_0 = 0$); red (green) line shows the case with roughened mask given by $D(X) = D_{\rm opt}(X) + \eta(X)$ without (with) temporal control; red (green) shade shows the span of 50 independent realizations without (with) temporal control.

The final deviations $H_{\mathrm{dev}}(X)$ achieved with and without voltage temporal control are shown in Fig. 7.13(b). The blue solid line (perfect electrode), red solid line (one instance of roughened electrode) and pink shades (spans of all roughened electrodes) are reproduced from Fig. 7.9(b) for ease of comparison. The newly added green solid line denotes $H_{\mathrm{dev}}(X)$ obtained for the same roughened electrode shown in solid red line (Fig. 7.9(a)), but with the optimal voltage profile shown in Fig. 7.13(a) as extra control. The pale green shades denote the span of $H_{\mathrm{dev}}(X)$ for all 50 independent realizations, each under additional optimal voltage control. An overall decrease in $H_{\mathrm{dev}}(X)$ can be observed when comparing the red and green solid line, as well as the pink and pale green shaded regions.

Having a time-dependent voltage $\Psi(\tau)$ scales the whole spatial profile of the Maxwell stress by a time-dependent scaling factor. It is interesting to see how continuously changing this overall scaling factor can provide additional control of the liquid film towards the desired target shape. This strategy of using $\Psi(\tau)$ has been tested for $0.01 \leq \tau_f \leq 0.05$ and $2000 \leq \mathcal{W} \leq 10^4$, and both the spread and median of $\mathcal{E}_{\mathrm{rms}}$ are reduced under temporal voltage control for all the parameters investigated, showing the use of voltage temporal control as a viable strategy to improve the optimal control of EHD patterning.

7.4.5.2 Realizing different lens sag height with time-dependent voltage

The other use of time-varying voltage is to obtain different liquid shapes using the same patterned mask. Since the applied voltage can be controlled digitally, this allows different target shapes to be realized using the same experimental setup as the patterned mask whose spatial profile is assumed to be fixed once fabricated does not need to be switched.

Fig. 7.14 shows the results of using the same patterned mask shown in Fig. 7.11(d) (blue solid line) to obtain hyperbolic lens with the same lens radius $R_0 = 0.875$ but *different* sag height ΔH. The optimal voltage profile $\Psi_{\mathrm{opt}}(\tau)$ is shown in the top row, the liquid film shape at selected times are shown in the middle row, and the final deviation $H_{\mathrm{dev}}(X)$ is shown in the bottom row. The left, middle and right column corresponds to $\Delta H = 0.5$, 0.75 and 1.0, respectively. Larger ΔH requires larger deformation of the liquid film, so the corresponding optimal voltage also shows a larger average value in order to provide the necessary Maxwell stress to shape the liquid film. While the final deviation remains small for all three cases, it should be emphasized that since they share the same lens radius, the required spatial profile of the control variable is expected to be similar except for the overall scaling factor, which can easily be achieved by changing the temporal profile of the applied voltage. Applying the same strategy to other target shapes with different lens radius might be more challenging with less impressive results

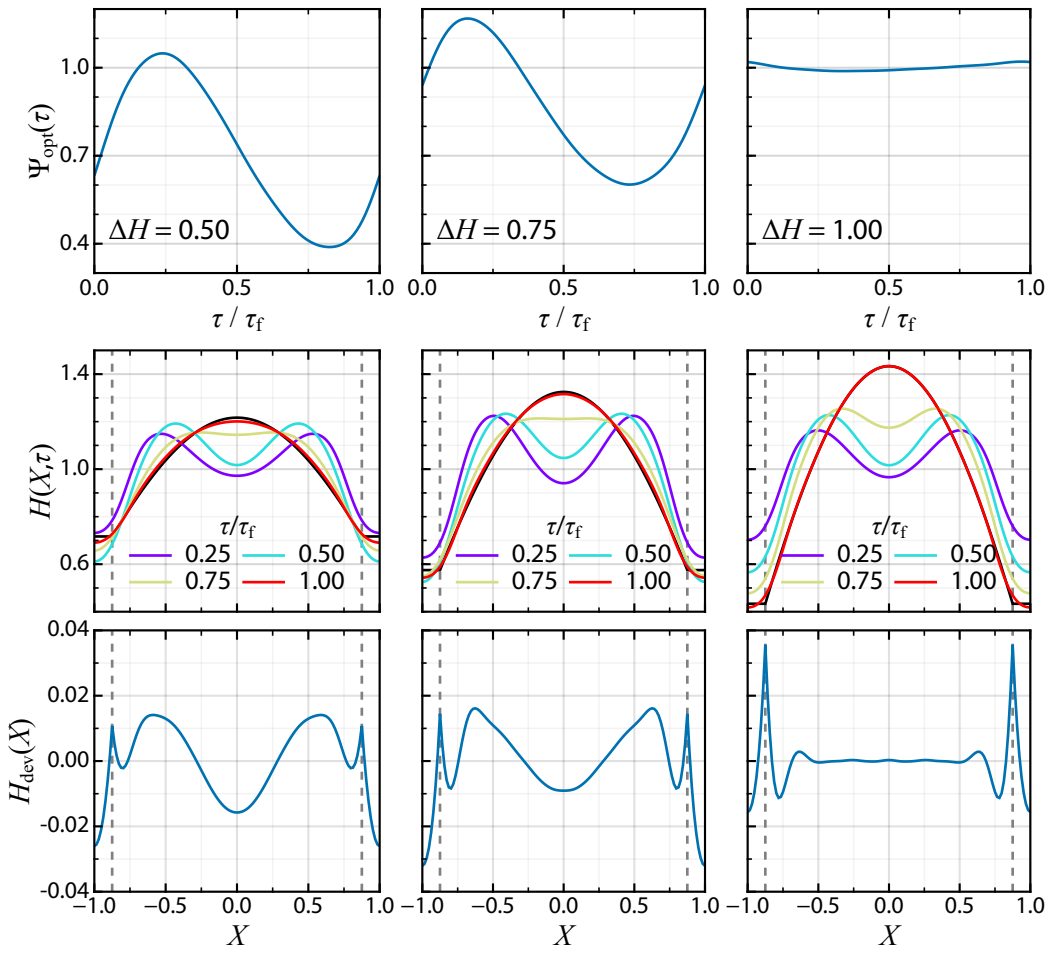

Figure 7.14: Demonstration of using temporal voltage control in conjunction with the patterned mask shown in Fig. 7.11(d) to obtain aspheric lens with different sag height ΔH. Parameters: $R_0 = 0.875$, $\mathcal{W} = 2000$, $\tau_f = 0.01$, $\Upsilon_t = 10^{-8}$, $n_t = 1$. The top row shows the optimal voltage profile $\Psi_{\text{opt}}(\tau)$. The middle row shows the liquid film shape at $\tau = \tau_f/4$, $\tau_f/2$, $3\tau_f/4$, τ_f. The bottom row shows the final deviation $H_{\text{dev}}(X)$. The left, middle and right column corresponds to $\Delta H = 0.5$, 0.75 and 1.0 respectively.

(i.e., larger $\mathcal{E}_{\text{rms}}$ and $\mathcal{E}_{\text{max}}$).

7.5 Discussion

In this chapter, the optimal control of EHD patterning is studied where the cost functional $\mathcal{J}$ given by Eq. (7.2) is minimized under the constraint of the governing PDE given by Eq. (7.1) derived under LWA, using the adjoint-based formalism presented in sSection 7.3.2 to derive the required gradient. The optimal mask topography $D_{\text{opt}}(\mathbf{X})$ or the applied voltage $\Psi_{\Delta}(\tau)$ is determined such that the liquid film evolves toward the prescribed target shape within a specified time interval τ_f. Satisfactory results exemplified by the small deviation between the liquid film shape and given target shape ($\mathcal{E}_{\text{rms}} \lesssim 0.01$) are achievable over a wide range of parameters as shown in Fig. 7.5 and 7.6, showing the success of the proposed optimal control framework. The algorithm fails to return a feasible optimal control (i.e., unacceptably large $\mathcal{E}_{\text{rms}}$) only when the actual process involved is challenging to realize due to limitations in the underlying physics, for example when the given processing time τ_f or the strength of electrostatic pressure $\mathcal{W}$ is too small (see bottom left of region in Fig. 7.6(a)), or when the aspect ratio of target lens is very large (see top left of Fig. 7.5) which requires very large surface forces to deform the liquid film.

Furthermore, by investigating the optimal control problem, we can arrive at a few general observations or principles, including:

1. Larger deviation (i.e., larger $\mathcal{E}_{\text{rms}}$), and hence more challenging liquid thin film patterning, for target shapes having features with large aspect ratio (Section 7.4.2.3) or abrupt change in curvature (Section 7.4.2.2).

2. The occurrence of maximum deviation at the region with largest change in curvature, i.e., $\mathcal{E}_{\text{max}} = |H_{\text{dev}}(|X| = R_0)|$

3. The optimal shaping strategy appears to be the initial development of smaller features followed by their coalescence into the final desired protrusion for the given target shape of a hyperbolic lens in both 1D (Section 7.4.2.1) and 2D (Section 7.4.4).

While these principles may not be too surprising, and may be inferred from many previous studies on the forward problem, it is difficult to arrive at those principles in a definitive way when the optimal control variable and the resulting spatiotemporal evolution of the liquid film are not known, something which can only be determined by studying the optimal control as is performed in this study.

While the lack of feedback might pose additional challenges for controlling a highly nonlinear system, the results shown in Section 7.4.3 show that in the particular case

of imperfect fabrication of patterned electrode, it is possible to systematically mitigate the undesirable effects of imperfect realization of the control variable by designing an optimal mask with regularization (Section 7.4.2.5), or using time-dependent applied voltage (Section 7.4.5). Studying the regulation control problem where the deviation from target shape distributed over the whole duration is taken into consideration, and the inclusion of feedback will be worthwhile directions for future study.

It is also worth mentioning that the effects of imperfect fabrication of the mask topography explored in Section 7.4.3 might be overestimated, as the $\partial^2 V/\partial x^2$ term is the Laplace equation governing the electric potential V is neglected under LWA. Reinstating such term will smooth out the electric potential along the horizontal direction, and hence the perturbation to the gradient of Maxwell stress. On the other hand, this also implies the liquid shaping capability of the original Maxwell stress profile is also overestimated, and so the sophisticated features seen in certain optimal masks, like the one in Fig. 7.2(a), are likely less effective in inducing large Maxwell stress in reality. It would be interesting to see how incorporating higher order correction to the Maxwell stress Π [130] changes the spatial profile of the control variables.

Finally, it should be pointed out that the cost function $\mathcal{J}$ in Eq. (7.2) and the regularization in Eq. (7.5) are intended for proof-of-concept demonstration. It might be preferable to incorporate other measures of deviation which are more suited for the intended functionality or purposes of the target shape. For instance, we may introduce deviation in the curvature $\nabla^2 H$ instead of the local deviation $H_{\text{dev}}(\mathbf{X})$ in Eq. (7.2) when we want to fabricate optimal elements like lenses. The current optimal control formalism can also be generalized to handle different form of the control (where the control variable does not directly enter through the pressure Π), different boundary conditions (e.g., pinned liquid film), or even additional physical effects. One example is in preventing dielectric breakdown [62] by constraining the maximum electric field strength through the regularization term.

Chapter 8

MAIN FINDINGS AND CONCLUDING PERSPECTIVES

This work studies analytically and numerically the use of spatially modulated external fields to pattern thin liquid films. While spatial modulation results in non-uniform stationary states which render many analytical analysis difficult to carry out, certain linear and weakly-nonlinear techniques can still be applied to gain physical insights about the stress balance and bifurcation in deformation amplitudes. To study the stability and dynamics of the liquid film outside the linear and weakly-nonlinear regime, two main approaches are used: linear stability analysis via solving a generalized eigenvalue problem, and direct numerical simulations of the thin film equation. The majority of Chapters 5 and 6 focus on the shapes and stability of ridges, and a few findings and remarks are summarized below:

1. For both EHD and TC patterning, the shapes of the ridges fall into either small or large deformation regimes which can be explained by a weakly-nonlinear analysis taking into account the balance of capillarity and the stress due to external fields.
2. In a 1D system, quasi-stable stationary states are achieved by mass limitation (through the thinning of precursor film), and truly stable stationary states can be achieved by saturation (through contact with the patterned mask).
3. In a 2D system, breakup of ridges is possible due to fluid flow along the Y direction which can only be suppressed by saturation.
4. The topography of the patterned mask can have profound influence on the stability of ridges by altering the stability of the zigzag modes.
5. Certain stationary states predicted to be stable from LSA are not accessible from a flat film.

In Chapter 7, optimal control techniques are also used to study the inverse problem of thin film patterning to arrive at the optimal mask topography or voltage profile that can optimally steer the liquid film toward a desired shape. The proposed optimal control framework successfully returns appropriate mask topography or voltage profile which allows the given target shape to be realized through shaping the liquid film over a wide range of system parameters. The minimum achievable deviation also allows us to understand the regime where liquid thin film patterning is less effective.

One key recurring theme throughout this thesis is the competition and trade-off of different physical effects. For example, it is found that stable patterns are achieved by inhibiting fluid flow through the thinning of precursor film or geometric confinement by the system (i.e., top plate). Large external field strengths are usually required to sufficiently deform the liquid film into forming protrusions with thin precursor layer or touching the mask. However, such large field strengths can also lead to premature breakup of ridges before they reach the stationary states which are predicted to touch the top and are stable. Thermocapillarity also provides additional shear stress to deform the liquid film so that smaller feature size are achievable, but the fluid is also more likely to destabilize along the lateral direction via zigzag modes. Contact between the liquid film and the mask suppresses further growth of the protrusions or ridges, but may also results in additional unstable zigzag modes especially when the mask topography are curved. Finally, in the context of optimal control, small scale features in the control variables lead to smaller deviation between the final liquid film shape and the target shape, but also make the control more susceptible to imperfect realization. The results presented in this work provides not only qualitative but also quantitative understanding of these trade-offs, which can be used to better guide the design of thin film patterning systems.

Finally, while this thesis focuses on the patterning of non-conducting thin liquid film with electrostatic or thermocapillary effects for lithographic applications, the results obtained may also be applicable to other systems subject to vastly different physical effects. As an example, in EHD patterning when both the liquid and gas layers are highly electrically conducting, the system may be reducible to the form of Eq. (2.46) where both normal and shear stresses due to electrostatics [59] are present. While the functional form of the dimensionless surface tension gradient is different from the one due to thermocapillary stress, both possess similar functional form for the numerator and denominator, so the qualitative findings presented in this work might somewhat generalize to those systems. Chapter 2.1.3 also discusses different straightforward extensions of the current thin film model to include more complex physical effects. The generalizability of the results obtained in this thesis to other systems is a topic for future research.

Appendix A

MATHEMATICS PRELIMINARY

A.1 Tensor Calculus

In this section, the conventions of taking the gradient or divergence of a vector or tensor are given, which follow those adopted in standard textbooks such as [63] and [26]. The 'del' operator ∇ is represented in Cartesian coordinates as

$$\nabla = \hat{\mathbf{e}}_1 \frac{\partial}{\partial x_1} + \hat{\mathbf{e}}_2 \frac{\partial}{\partial x_2} + \hat{\mathbf{e}}_3 \frac{\partial}{\partial x_3} = \sum_i \hat{\mathbf{e}}_i \frac{\partial}{\partial x_i}, \tag{A.1}$$

where $\hat{\mathbf{e}}_1 = \hat{\mathbf{e}}_x = \hat{\mathbf{x}}$, $\hat{\mathbf{e}}_2 = \hat{\mathbf{e}}_y = \hat{\mathbf{y}}$ and $\hat{\mathbf{e}}_3 = \hat{\mathbf{e}}_z = \hat{\mathbf{z}}$ are the unit vectors in the $x_1 = x$, $x_2 = y$ and $x_3 = z$ directions, respectively.

A vector $\mathbf{v}$ can be represented in Cartesian coordinates as

$$\mathbf{v} = v_1 \hat{\mathbf{e}}_1 + v_2 \hat{\mathbf{e}}_2 + v_3 \hat{\mathbf{e}}_3 = \sum_i^3 v_i \hat{\mathbf{e}}_i, \tag{A.2}$$

and a tensor $\mathbf{T}$ can be represented in Cartesian coordinates as

$$\mathbf{T} = \sum_i \sum_j T_{ij} \hat{\mathbf{e}}_i \hat{\mathbf{e}}_j = \begin{pmatrix} T_{11} & T_{12} & T_{13} \\ T_{21} & T_{22} & T_{23} \\ T_{31} & T_{32} & T_{33} \end{pmatrix}. \tag{A.3}$$

The gradient of a scalar ϕ is simply

$$\nabla \phi = \frac{\partial \phi}{\partial x_1} \hat{\mathbf{e}}_1 + \frac{\partial \phi}{\partial x_2} \hat{\mathbf{e}}_2 + \frac{\partial \phi}{\partial x_3} \hat{\mathbf{e}}_3 = \sum_i \frac{\partial \phi}{\partial x_i}, \tag{A.4}$$

while the gradient of a vector $\mathbf{v}$ is a tensor given by

$$\nabla \mathbf{v} = \sum_i \sum_j \frac{\partial v_j}{\partial x_i} \hat{\mathbf{e}}_i \hat{\mathbf{e}}_j = \begin{pmatrix} \frac{\partial v_1}{\partial x_1} & \frac{\partial v_2}{\partial x_1} & \frac{\partial v_3}{\partial x_1} \\ \frac{\partial v_1}{\partial x_2} & \frac{\partial v_2}{\partial x_2} & \frac{\partial v_3}{\partial x_2} \\ \frac{\partial v_1}{\partial x_3} & \frac{\partial v_2}{\partial x_3} & \frac{\partial v_3}{\partial x_3} \end{pmatrix}. \tag{A.5}$$

The divergence of a vector $\mathbf{v}$ is a scalar given by

$$\nabla \cdot \mathbf{v} = \frac{\partial v_1}{\partial x_1} + \frac{\partial v_2}{\partial x_2} + \frac{\partial v_3}{\partial x_3} = \sum_i \frac{\partial v_i}{\partial x_i}, \tag{A.6}$$

while the divergence of a tensor $\mathbf{T}$ is a vector given by

$$\nabla \cdot \mathbf{T} = \sum_i \sum_j \frac{\partial T_{ij}}{\partial x_i} \hat{\mathbf{e}}_j. \tag{A.7}$$

In Einstein notation, the above relations can be written compactly as

$$\nabla \phi = \partial_i \phi, \qquad \nabla \mathbf{v} = \partial_i v_j, \qquad \nabla \cdot \mathbf{v} = \partial_i v_i, \qquad \nabla \cdot \mathbf{T} = \partial_i T_{ij}. \tag{A.8}$$

Note that the alternative convention of $\nabla \mathbf{v} = \partial_j v_i$ and $\nabla \cdot \mathbf{T} = \partial_j T_{ij}$ are used in some other sources, including the software Mathematica (version 12.2).

A.2 Stress Tensor

$\mathbf{T}_{ij}$ represents the stress in the x_j-coordinate direction on a plane perpendicular to the x_i coordinate. For example, T_{yx} is the force per unit area in the $\hat{\mathbf{x}}$ direction on a plane perpendicular to the $\hat{\mathbf{y}}$ axis. The stress vector $\mathbf{t}$ is defined as the force per unit area on the surface, and is given by

$$\mathbf{t}(\hat{\mathbf{n}}) = \hat{\mathbf{n}} \cdot \sum_i \sum_j T_{ij} \hat{\mathbf{e}}_i \hat{\mathbf{e}}_j = \hat{\mathbf{n}} \cdot \mathbf{T} \qquad (t_j = n_i T_{ij}). \tag{A.9}$$

The above convention is adopted in [63], [26] and [6]. Note that in some other sources such as [4] and [35, Chapter 31-6], T_{ij} is defined the other way round, i.e., the i-component of the force exerted across a plane perpendicular to the $\hat{\mathbf{e}}_j$ axis, and the stress vector is defined as $t_i = T_{ij} n_j$.

A.3 Useful Mathematical Relations

A.3.1 Unit normal and tangent

The unit normal vector at a surface defined as $z = h(x, y)$ is given by

$$\hat{\mathbf{n}} = \frac{-\partial_x h \ \hat{\mathbf{x}} - \partial_y h \ \hat{\mathbf{y}} + \hat{\mathbf{z}}}{\sqrt{1 + (\partial_x h)^2 + (\partial_y h)^2}} = \frac{-\nabla_\parallel h + \hat{\mathbf{z}}}{\sqrt{1 + |\nabla_\parallel h|^2}}. \tag{A.10}$$

In 3D, there are infinitely many pairs of unit tangent vectors $\hat{\mathbf{t}}_i$ for $i = x, y$ satisfying $\hat{\mathbf{t}}_i \cdot \hat{\mathbf{n}} = 0$ and $\hat{\mathbf{t}}_i \cdot \hat{\mathbf{t}}_j = \delta_{ij}$. The following is one particular choice

$$\hat{\mathbf{t}}_x = \frac{\hat{\mathbf{x}} + \partial_x h \ \hat{\mathbf{z}}}{\sqrt{1 + (\partial_x h)^2}}, \qquad \hat{\mathbf{t}}_y = \frac{-(\partial_x h)(\partial_y h)\hat{\mathbf{x}} + [1 + (\partial_x h)^2]\hat{\mathbf{y}} + \partial_y h \ \hat{\mathbf{z}}}{\sqrt{1 + (\partial_x h)^2}\sqrt{1 + (\partial_x h)^2 + (\partial_y h)^2}}, \tag{A.11}$$

which are obtained by letting $\hat{\mathbf{t}}_x = (a, 0, c)$ and $\hat{\mathbf{t}}_y = (d, e, f)$ and solving the five unknowns with five equations $\hat{\mathbf{t}}_x \cdot \hat{\mathbf{n}} = 0$, $\hat{\mathbf{t}}_y \cdot \hat{\mathbf{n}} = 0$, $\hat{\mathbf{t}}_x \cdot \hat{\mathbf{t}}_y = 0$, $|\hat{\mathbf{t}}_x| = 1$ and $|\hat{\mathbf{t}}_y| = 1$. The relation $\hat{\mathbf{t}}_x \cdot \hat{\mathbf{y}} = 0$ is imposed so that the expressions in 3D are consistent with those in 2D when $\partial h/\partial y = 0$.

With the choice of $\hat{\mathbf{t}}_i$ given by Eq. (A.11), $\hat{\mathbf{t}}_i \cdot \nabla_s$ is given by

$$\hat{\mathbf{t}}_x \cdot \nabla_s = \frac{1}{\sqrt{1+h_x^2}} \frac{\partial}{\partial x}, \tag{A.12a}$$

$$\hat{\mathbf{t}}_y \cdot \nabla_s = \frac{1}{\sqrt{(1+h_x^2)(1+h_y^2+h_x^2)}} \left[-h_x h_y \frac{\partial}{\partial x} + (1+h_x^2) \frac{\partial}{\partial y} \right]. \tag{A.12b}$$

In 2D, only $\hat{\mathbf{t}}_x \cdot \nabla_s$ survives and $\hat{\mathbf{t}}_y \cdot \nabla_s = 0$.

A.3.2 Surface gradient ∇_s

The surface gradient $\nabla_s = (\mathbf{I} - \hat{\mathbf{n}}\hat{\mathbf{n}}) \cdot \nabla$ acting along a surface defined as $z = h(x, y)$ is given by [26, see Eq. (A.8-18)]

$$\nabla_s = \frac{1}{|\nabla_\parallel h|^2} \left\{ \left[\left(1+h_y^2\right) \hat{\mathbf{x}} - h_x h_y \hat{\mathbf{y}} + h_x \hat{\mathbf{z}} \right] \frac{\partial}{\partial x} + \left[-h_x h_y \hat{\mathbf{x}} + \left(1+h_x^2\right) \hat{\mathbf{y}} + h_y \hat{\mathbf{z}} \right] \frac{\partial}{\partial y} \right\}, \tag{A.13}$$

where $h_x = \partial h/\partial x$, $h_y = \partial h/\partial y$, and $|\nabla_\parallel h|^2 = 1 + h_x^2 + h_y^2$. For a 2D system where $h = h(x)$, $\partial h/\partial y = 0$, and Eq. (A.13) becomes

$$\nabla_s = \frac{\hat{\mathbf{x}} + (\partial_x h)\hat{\mathbf{z}}}{1 + (\partial_x h)^2} \frac{\partial}{\partial x}. \tag{A.14}$$

A.3.3 Curvature

The mean curvature $\mathscr{H}$ is defined as [26, see Eq. (A.8-22)]

$$\mathscr{H} = -\frac{1}{2} \nabla_s \cdot \hat{\mathbf{n}}. \tag{A.15}$$

It can be shown (using Mathematica) that $\nabla_s \cdot \hat{\mathbf{n}} = \nabla \cdot \hat{\mathbf{n}}$ in both 2D and 3D. For a surface defined by $z = h(x, y)$, $\mathscr{H}$ is given by [26, Eq. (A.8-23)]

$$2\mathscr{H} = -\nabla_s \cdot \hat{\mathbf{n}} = -\frac{-h_{yy}(1+h_x^2) + 2h_x h_y h_{xy} - h_{xx}(1+h_y^2)}{\left(1+h_x^2+h_y^2\right)^{3/2}} \tag{A.16}$$

In 2D where $z = h(x)$, Eq. (A.16) is simplified to [26, Eq. (A.8-24)]

$$2\mathscr{H} = -\nabla_s \cdot \hat{\mathbf{n}} = \frac{h_{xx}}{(1+h_x^2)^{3/2}}. \tag{A.17}$$

As an example, the curvature of a cylinder of radius R with the surface defined as $z = \sqrt{R^2 - x^2}$ and a sphere with $z = \sqrt{R^2 - x^2 - y^2}$ are given by

$$\mathscr{H} = -\frac{1}{2R} \quad \text{(cylinder)}, \qquad \mathscr{H} = -\frac{1}{R} \quad \text{(sphere)}. \tag{A.18}$$

Curvature defined using Eq. (A.15) follows the sign convention where $\mathscr{H} < 0$ when $\hat{\mathbf{e}}_z$ points away from the local center of curvature, and $\mathscr{H} > 0$ when $\hat{\mathbf{e}}_z$ points toward the local center of curvature. For a general closed surface, $\mathscr{H} < 0$ when the outward unit normal $\hat{\mathbf{n}}$ points away from the local center of curvature and vice versa.

A.4 Solution to 1D Laplace Equation

In this section, the general solution to the 1D Laplace equation for a system with two subdomains is given. Lowercase letters and symbols are used for brevity, and the scalar field $\phi_i(\mathbf{x}, z)$ can represent either the electric potential (in EHD patterning) or temperature (in TC patterning):

$$\frac{\partial^2 \phi_i}{\partial z^2} = 0, \qquad i = 1, 2, \tag{A.19}$$

with the following boundary conditions

$$\phi_1(z = d) = u_a, \tag{A.20a}$$
$$\phi_2(z = 0) = u_b, \tag{A.20b}$$
$$\phi_1(z = h) = \phi_2(z = h), \tag{A.20c}$$
$$c_1 \frac{\partial \phi_1(z = h)}{\partial z} = c_2 \frac{\partial \phi_2(z = h)}{\partial z}, \tag{A.20d}$$

where c_i are scalars representing either the relative electric permittivity ε_i or the thermal conductivity $\hat{k}_i$. Using the following trial solutions which already satisfy the first two boundary conditions

$$\phi_1(z) = u_a + \alpha_1(z - d), \quad \phi_2(z) = u_b + \alpha_2 z, \tag{A.21}$$

we can solve for α_i by imposing the last two boundary conditions. The solution is given by

$$\alpha_1 = \frac{c_2(\phi_a - \phi_b)}{c_1 h + c_2(d-h)}, \quad \alpha_2 = \frac{c_1(\phi_a - \phi_b)}{c_1 h + c_2(d-h)}. \tag{A.22}$$

Note that strictly speaking ϕ_i only depends on z, though in this thesis we let $h = h(\mathbf{x})$ and the boundary conditions $d = d(\mathbf{x})$, $u_a = u_a(\mathbf{x})$ and $u_b = u_b(\mathbf{x})$ to be all general functions of $\mathbf{x}$. As a result, the coefficients $\alpha_i = \alpha_i(\mathbf{x})$ as well as the scalar fields $\phi_i = \phi(\mathbf{x}, z)$ also depend on $\mathbf{x}$ through $h(\mathbf{x})$ and the boundary conditions at $z = 0$ and $z = d$.

A.5 Discrete Fourier Transform (DFT)

For a vector $H = \{H[1], H[2], \ldots, H[N]\}$ of length N (which may represent for example the liquid film shape after spatial discretization), its DFT is defined as

$$\mathbb{DFT}\{H\}[k] = \sum_{j=1}^{N} H[j] e^{-2\pi i (j-1)(k-1)}. \tag{A.23}$$

Eq. (A.23) assumes the vector starts at index 1, and follows convention used in many scientific software including Python `scipy.fft`, MATLAB `fft` and Julia `FFTW.jl`.

Appendix B

SUMMARY OF DERIVATIVES AND INTEGRALS OF Π AND Γ

In this appendix, we summarize the mathematical expressions involving the external pressure Π and surface tension Γ, including their derivatives and integrals with respect to different variables.

Specifically, we consider Π and Γ given by the following forms:

$$\Pi_{\mathrm{EM}} = \frac{\mathcal{W}\varepsilon_r(\varepsilon_r-1)\Psi_\Delta^2}{2\left[H+\varepsilon_r(D-H)\right]^2},$$
$$\Pi_{\mathrm{vdw}} = \mathcal{A}\left[\frac{1}{H^3}-\frac{1}{(D-H)^3}\right],$$
$$\Gamma_{\mathrm{TC}} = -\frac{\mathcal{M}\left[\kappa H\Theta_{\mathrm{cold}}+(D-H)\Theta_{\mathrm{hot}}\right]}{D+(\kappa-1)H}$$

The derivatives of the above variables with respect to film thickness H are shown in Table B.1; their derivatives with respect to the different process variables (which can be spatially modulated) are shown in Table B.2; their integrals with respect to H which give the energy densities are given in Table B.3.

Table B.1: Derivatives with respect to film thickness H. The symbol of Ξ represents either Π_{EM}, Π_{vdw}, or Γ_{TC}. The shorthand notation for temperature difference is $\Delta\Theta \equiv \Theta_{\mathrm{hot}}-\Theta_{\mathrm{cold}}$.

	$\Xi=\Pi_{\mathrm{EM}}$	$\Xi=\Pi_{\mathrm{vdw}}$	$\Xi=\Gamma_{\mathrm{TC}}$
$\frac{\partial\Xi}{\partial H}$	$\frac{\mathcal{W}\varepsilon_r(\varepsilon_r-1)^2\Psi_\Delta^2}{\left[H+\varepsilon_r(D-H)\right]^3}$	$-3\mathcal{A}\left[\frac{1}{H^4}-\frac{1}{(D-H)^4}\right]$	$\frac{\mathcal{M}\kappa D\Delta\Theta}{\left[D+(\kappa-1)H\right]^2}$
$\frac{\partial^2\Xi}{\partial H^2}$	$\frac{3\mathcal{W}\varepsilon_r(\varepsilon_r-1)^3\Psi_\Delta^2}{\left[H+\varepsilon_r(D-H)\right]^4}$	$12\mathcal{A}\left[\frac{1}{H^5}-\frac{1}{(D-H)^5}\right]$	$\frac{2\mathcal{M}\kappa D(\kappa-1)\Delta\Theta}{\left[D+(\kappa-1)H\right]^3}$
$\frac{\partial^3\Xi}{\partial H^3}$	$\frac{12\mathcal{W}\varepsilon_r(\varepsilon_r-1)^4\Psi_\Delta^2}{\left[H+\varepsilon_r(D-H)\right]^5}$	$-60\mathcal{A}\left[\frac{1}{H^6}-\frac{1}{(D-H)^6}\right]$	$\frac{6\mathcal{M}\kappa D(\kappa-1)^2\Delta\Theta}{\left[D+(\kappa-1)H\right]^4}$

Table B.2: Derivatives with respect to process variable ξ, i.e., $\partial\Xi/\partial\xi$, where Ξ stands for either Π_{EM}, Π_{vdw} or Γ_{TC}, and ξ stands for either D, Ψ_{Δ}, Θ_{hot} or Θ_{cold}. The shorthand notation for temperature difference is $\Delta\Theta \equiv \Theta_{\mathrm{hot}} - \Theta_{\mathrm{cold}}$. These expressions are used in Chapters 5, 6 and 7 for certain results related to spatial modulation and optimal control.

ξ	$\Xi = \Pi_{\mathrm{EM}}$	$\Xi = \Pi_{\mathrm{vdw}}$	$\Xi = \Gamma_{\mathrm{TC}}$
$D: \dfrac{\partial\Xi}{\partial D}$	$\dfrac{-\mathcal{W}\varepsilon_r^2(\varepsilon_r-1)\Psi_{\Delta}^2}{\left[H+\varepsilon_r(D-H)\right]^3}$	$\dfrac{3\mathcal{A}}{(D-H)^4}$	$\dfrac{-\mathcal{M}\kappa H\Delta\Theta}{\left[D+(\kappa-1)H\right]^2}$
$\Psi_{\Delta}: \dfrac{\partial\Xi}{\partial\Psi_{\Delta}}$	$\dfrac{\mathcal{W}\varepsilon_r(\varepsilon_r-1)\Psi_{\Delta}}{\left[H+\varepsilon_r(D-H)\right]^2}$	-	-
$\Theta_{\mathrm{cold}}: \dfrac{\partial\Xi}{\partial\Theta_{\mathrm{cold}}}$	-	-	$\dfrac{-\mathcal{M}\kappa H}{D+(\kappa-1)H}$
$\Theta_{\mathrm{hot}}: \dfrac{\partial\Xi}{\partial\Theta_{\mathrm{hot}}}$	-	-	$\dfrac{-\mathcal{M}(D-H)}{D+(\kappa-1)H}$

Table B.3: The energy density $\Phi(H)$ associated with the respective physical effects given by Π_{EM}, Π_{vdw} and Γ_{TC} in the energy functional given by Eq. (2.52). Note that the expression for Φ_{TC} is only applicable for constant separation between mask and substrate, i.e., $D = D_0 = \text{const.}$

Φ_{EM}	$-\dfrac{\mathcal{W}}{2}\dfrac{\varepsilon_r\Psi_{\Delta}^2}{H+\varepsilon_r(D-H)}$
Φ_{vdw}	$\dfrac{\mathcal{A}}{2}\left[\dfrac{1}{H^2}+\dfrac{1}{(D-H)^2}\right]$
Φ_{TC}	$-\dfrac{3\mathcal{M}\kappa}{2D_0}H\log\left[\dfrac{H}{1+(\kappa-1)H/D_0}\right]$

BIBLIOGRAPHY

[1] Gulraiz Ahmed, O Arjmandi Tash, J Cook, Anna Trybala, and Victor Starov. "Biological applications of kinetics of wetting and spreading". In: *Advances in Colloid and Interface Science* 249 (2017), pp. 17–36. DOI: 10.1016/j.cis.2017.08.004 (cit. on p. 1).

[2] Antonios Armaou and Panagiotis D Christofides. "Feedback control of the Kuramoto–Sivashinsky equation". In: *Physica D: Nonlinear Phenomena* 137.1-2 (2000), pp. 49–61. DOI: 10.1016/s0167-2789(99)00175-x (cit. on p. 144).

[3] Arnab Atta, David G Crawford, Charles R Koch, and Subir Bhattacharjee. "Influence of electrostatic and chemical heterogeneity on the electric-field-induced destabilization of thin liquid films". In: *Langmuir* 27.20 (2011), pp. 12472–12485. DOI: 10.1021/la202759j (cit. on p. 62).

[4] G. K. Batchelor. *An Introduction to Fluid Dynamics*. Cambridge University Press, 2000. DOI: 10.1017/cbo9780511800955 (cit. on p. 189).

[5] Jeff Bezanson, Alan Edelman, Stefan Karpinski, and Viral B. Shah. "Julia: A Fresh Approach to Numerical Computing". In: *SIAM Review* 59.1 (Jan. 2017), pp. 65–98. ISSN: 1095-7200. DOI: 10.1137/141000671 (cit. on p. 53).

[6] R. Byron Bird, Warren E. Stewart, and Edwin N. Lightfoot. *Transport Phenomena*. Second Edition. John Wiley & Sons, Inc., 2002 (cit. on p. 189).

[7] Shiba Biswal, Hangjie Ji, Karthik Elamvazhuthi, and Andrea L Bertozzi. "Optimal boundary control of a model thin-film fiber coating model". In: *Physica D: Nonlinear Phenomena* (2023), p. 133942. DOI: 10.1016/j.physd.2023.133942 (cit. on pp. 143, 144, 146).

[8] Felix Bloch. "Über die Quantenmechanik der Elektronen in Kristallgittern". In: *Zeitschrift für Physik* 52.7–8 (July 1929), pp. 555–600. ISSN: 1434-601X. DOI: 10.1007/bf01339455 (cit. on p. 48).

[9] Daniel Bonn, Jens Eggers, Joseph Indekeu, Jacques Meunier, and Etienne Rolley. "Wetting and spreading". In: *Reviews of Modern Physics* 81 (2 May 2009), pp. 739–805. DOI: 10.1103/RevModPhys.81.739 (cit. on pp. 1, 38, 39).

[10] E Boujo and Mathieu Sellier. "Pancake making and surface coating: Optimal control of a gravity-driven liquid film". In: *Physical Review Fluids* 4.6 (2019), p. 064802. DOI: 10.1103/physrevfluids.4.064802 (cit. on pp. 1, 143, 144, 146, 152).

[11] Fridtjof Brauns, Henrik Weyer, Jacob Halatek, Junghoon Yoon, and Erwin Frey. "Wavelength Selection by Interrupted Coarsening in Reaction-Diffusion Systems". In: *Physical Review Letters* 126 (10 Mar. 2021), p. 104101. DOI: 10.1103/PhysRevLett.126.104101 (cit. on p. 85).

[12] Pierre-Thomas Brun. "Fluid-Mediated Fabrication of Complex Assemblies". In: *JACS Au* 2.11 (2022), pp. 2417–2425. DOI: 10.1021/jacsau.2c00427 (cit. on p. 4).

[13] Lutz Brusch, Heiko Kühne, Uwe Thiele, and Markus Bär. "Dewetting of thin films on heterogeneous substrates: Pinning versus coarsening". In: *Physical Review E* 66.1 (2002), p. 011602. DOI: 10.1103/physreve.66.011602 (cit. on p. 72).

[14] Yunus A. Cengel and John M. Cimbala. *Fluid Mechanics Fundamentals and Applications. Fundamentals and applications*. 3. ed. New York, NY: McGraw-Hill, 2014. 1000 pp. ISBN: 9780077595463 (cit. on p. 12).

[15] Yi Hua Chang and Sandra M. Troian. "Thermocapillary Patterning of Highly Uniform Microarrays by Resonant Wavelength Excitation". In: *Physical Review Applied* 18 (6 Dec. 2022). Testing: contribution, p. 064090. DOI: 10.1103/PhysRevApplied.18.064090 (cit. on pp. 5, 111, 112, 114, 120, 122, 124–126, 128, 130, 132).

[16] Stephen Y Chou and Lei Zhuang. "Lithographically induced self-assembly of periodic polymer micropillar arrays". In: *Journal of Vacuum Science & Technology B: Microelectronics and Nanometer Structures Processing, Measurement, and Phenomena* 17.6 (1999), pp. 3197–3202. DOI: 10.1116/1.590979 (cit. on p. 1).

[17] Stephen Y Chou, Lei Zhuang, and Linjie Guo. "Lithographically induced self-construction of polymer microstructures for resistless patterning". In: *Applied Physics Letters* 75.7 (1999), pp. 1004–1006. DOI: 10.1063/1.124579 (cit. on p. 1).

[18] P.D. Christofides. "Feedback control of the Kuramoto-Sivashinsky equation". In: *Proceedings of the 37th IEEE Conference on Decision and Control (Cat. No.98CH36171)*. Vol. 4. 1998, 4646–4651 vol.4. DOI: 10.1109/CDC.1998.762066 (cit. on p. 144).

[19] Radu Cimpeanu, Susana N Gomes, and Demetrios T Papageorgiou. "Active control of liquid film flows: beyond reduced-order models". In: *Nonlinear Dyn.* (2021), pp. 1–21. DOI: 10.1007/s11071-021-06287-5 (cit. on pp. 143, 146).

[20] Sweden. COMSOL AB Stockholm. *COMSOL Multiphysics® v. 6.0*. URL: www.comsol.com (cit. on pp. 56, 60).

[21] Andrew Corbett and Satish Kumar. "Combined thermal and electrohydrodynamic patterning of thin liquid films". In: *Journal of Engineering Mathematics* 94.1 (2015), pp. 81–96. DOI: 10.1007/s10665-013-9680-3 (cit. on pp. 3, 44).

[22] Richard V Craster and Omar K Matar. "Dynamics and stability of thin liquid films". In: *Reviews of Modern Physics* 81.3 (2009), p. 1131. DOI: 10.1103/revmodphys.81.1131 (cit. on pp. 10, 17, 38, 144).

[23] M. C. Cross and P. C. Hohenberg. "Pattern formation outside of equilibrium". In: *Reviews of Modern Physics* 65 (3 July 1993), pp. 851–1112. DOI: 10.1103/RevModPhys.65.851 (cit. on p. 42).

[24] Michael Cross and Henry Greenside. *Pattern formation and dynamics in nonequilibrium systems*. Cambridge University Press, 2009. DOI: 10.1017/CBO9780511627200 (cit. on pp. 40, 48).

[25] Anton A Darhuber and Sandra M Troian. "Principles of microfluidic actuation by modulation of surface stresses". In: *Annual Review of Fluid Mechanics* 37 (2005), pp. 425–455. DOI: 10.1146/annurev.fluid.36.050802.122052 (cit. on p. 4).

[26] William M. Deen. *Analysis of Transport Phenomena*. Oxford University Press, 1998 (cit. on pp. 10, 13, 14, 16, 188–190).

[27] Aranzazu Del Campo and Eduard Arzt. "Fabrication approaches for generating complex micro-and nanopatterns on polymeric surfaces". In: *Chemical Reviews* 108.3 (2008), pp. 911–945. DOI: 10.1021/cr050018y (cit. on p. 4).

[28] Mathias Dietzel and Sandra M Troian. "Formation of nanopillar arrays in ultrathin viscous films: The critical role of thermocapillary stresses". In: *Physical Review Letters* 103.7 (2009), p. 074501. DOI: 10.1103/physrevlett.103.074501 (cit. on p. 117).

[29] Mathias Dietzel and Sandra M Troian. "Mechanism for spontaneous growth of nanopillar arrays in ultrathin films subject to a thermal gradient". In: *Journal of Applied Physics* 108.7 (2010), p. 074308. DOI: 10.1063/1.3475516 (cit. on pp. 29, 31, 44, 117).

[30] Mathias Dietzel and Sandra M Troian. "Thermocapillary Patterning of Nanoscale Polymer Films". In: *MRS Proceedings* 1179 (2009), 1179–BB08–02. DOI: 10.1557/PROC-1179-BB08-02 (cit. on p. 4).

[31] Javier A Diez, Alejandro G González, and Lou Kondic. "On the breakup of fluid rivulets". In: *Physics of Fluids* 21.8 (2009), p. 082105. DOI: 10.1063/1.3211248 (cit. on p. 94).

[32] Miguel A Durán-Olivencia, Rishabh S Gvalani, Serafim Kalliadasis, and Grigorios A Pavliotis. "Instability, rupture and fluctuations in thin liquid films: Theory and computations". In: *Journal of Statistical Physics* 174.3 (2019), pp. 579–604. DOI: 10.1007/s10955-018-2200-0 (cit. on p. 55).

[33] Thomas Erneux and Stephen H Davis. "Nonlinear rupture of free films". In: *Physics of Fluids A: Fluid Dynamics* 5.5 (1993), pp. 1117–1122. DOI: 10.1063/1.858597 (cit. on pp. 67, 112, 114).

[34] Ran Eshel, Valeri Frumkin, Matan Nice, Omer Luria, Boris Ferdman, Nadav Opatovski, Khaled Gommed, Maxim Shusteff, Yoav Shechtman, and Moran Bercovici. "Programmable thermocapillary shaping of thin liquid films". In: *Flow* 2 (2022), E27. DOI: 10.1017/flo.2022.17 (cit. on pp. 118, 142, 144, 146).

[35] Richard P Feynman, Robert B Leighton, and Matthew Sands. *The Feynman Lectures on Physics*. The New Millennium Edition. Basic Books, 2011. URL: https://www.feynmanlectures.caltech.edu/ (cit. on p. 189).

[36] Kevin R Fiedler, Euan McLeod, and Sandra M Troian. "Differential colorimetry measurements of fluctuation growth in nanofilms exposed to large surface thermal gradients". In: *Journal of Applied Physics* 125.6 (2019), p. 065303. DOI: 10.1063/1.5051456 (cit. on pp. 3, 117).

[37] Kevin R Fiedler and Sandra M Troian. "Early time instability in nanofilms exposed to a large transverse thermal gradient: Improved image and thermal analysis". In: *Journal of Applied Physics* 120.20 (2016), p. 205303. DOI: 10.1063/1.4968575 (cit. on p. 117).

[38] G. Floquet. "Sur les équations différentielles linéaires à coefficients périodiques". In: *Annales scientifiques de l'École normale supérieure* 12 (1883), pp. 47–88. ISSN: 1873-2151. DOI: 10.24033/asens.220 (cit. on p. 48).

[39] Bengt Fornberg. "Generation of finite difference formulas on arbitrarily spaced grids". In: *Mathematics of Computation* 51.184 (1988), pp. 699–706. ISSN: 1088-6842. DOI: 10.1090/s0025-5718-1988-0935077-0 (cit. on p. 51).

[40] Tobias Frohoff-Hülsmann and Uwe Thiele. "Nonreciprocal Cahn-Hilliard Model Emerges as a Universal Amplitude Equation". In: *Phys. Rev. Lett.* 131 (10 Sept. 2023), p. 107201. DOI: 10.1103/PhysRevLett.131.107201 (cit. on p. 43).

[41] Valeri Frumkin, Wenbin Mao, Alexander Alexeev, and Alexander Oron. "Creating localized-droplet train by traveling thermal waves". In: *Physics of Fluids* 26.8 (2014), p. 082108. DOI: 10.1063/1.4892657 (cit. on p. 118).

[42] Valeri Frumkin and Alexander Oron. "Liquid film flow along a substrate with an asymmetric topography sustained by the thermocapillary effect". In: *Physics of Fluids* 28.8 (2016), p. 082107. DOI: 10.1063/1.4961032 (cit. on p. 118).

[43] Valeri Frumkin and Alexander Oron. "Thermocapillary flow of a thin liquid film in a confined two-layer system under a hydrophobic plate". In: *Physical Review Fluids* 2 (10 Oct. 2017), p. 104002. DOI: 10.1103/PhysRevFluids.2.104002 (cit. on p. 118).

[44] Nicolas Garnier, Roman O. Grigoriev, and Michael F. Schatz. "Optical Manipulation of Microscale Fluid Flow". In: *Physical Review Letters* 91 (5 July 2003), p. 054501. DOI: 10.1103/PhysRevLett.91.054501 (cit. on p. 143).

[45] K. B. Glasner and T. P. Witelski. "Coarsening dynamics of dewetting films". In: *Physical Review E* 67 (1 Jan. 2003), p. 016302. DOI: 10.1103/PhysRevE.67.016302 (cit. on p. 85).

[46] Pola Goldberg-Oppenheimer, Sumeet Mahajan, and Ullrich Steiner. "Hierarchical Electrohydrodynamic Structures for Surface-Enhanced Raman Scattering". In: *Advanced Materials* 24.23 (2012), OP175–OP180. DOI: 10.1002/adma.201104159 (cit. on p. 4).

[47] Susana N. Gomes, Demetrios T. Papageorgiou, and Grigorios A. Pavliotis. "Stabilizing non-trivial solutions of the generalized Kuramoto–Sivashinsky equation using feedback and optimal control: Lighthill–Thwaites Prize". In: *IMA Journal of Applied Mathematics* 82.1 (Mar. 2016), pp. 158–194. ISSN: 0272-4960. DOI: 10.1093/imamat/hxw011 (cit. on p. 144).

[48] Roman O Grigoriev. "Contact line instability and pattern selection in thermally driven liquid films". In: *Physics of Fluids* 15.6 (2003), pp. 1363–1374. DOI: 10.1063/1.1566958 (cit. on pp. 143, 146).

[49] Roman O Grigoriev. "Control of evaporatively driven instabilities of thin liquid films". In: *Physics of Fluids* 14.6 (2002), pp. 1895–1909. DOI: 10.1063/1.1476304 (cit. on pp. 143, 146).

[50] Günther Grün, Klaus Mecke, and Markus Rauscher. "Thin-film flow influenced by thermal noise". In: *Journal of Statistical Physics* 122.6 (2006), pp. 1261–1291. DOI: 10.1007/s10955-006-9028-8 (cit. on p. 55).

[51] Max D Gunzburger. *Perspectives in flow control and optimization*. SIAM, 2002. DOI: 10.1137/1.9780898718720 (cit. on p. 142).

[52] Jakob Heier, Jan Groenewold, and Ullrich Steiner. "Pattern formation in thin polymer films by spatially modulated electric fields". In: *Soft Matter* 5.20 (2009), pp. 3997–4005. DOI: 10.1039/b906863e (cit. on pp. 3, 62–64, 66).

[53] Oscar A. Holroyd, Radu Cimpeanu, and Susana N. Gomes. *Linear quadratic regulation control for falling liquid films*. 2023. DOI: 10.48550/ARXIV.2301.11379 (cit. on pp. 143, 146).

[54] Christoph Honisch, Te-Sheng Lin, Andreas Heuer, Uwe Thiele, and Svetlana V Gurevich. "Instabilities of layers of deposited molecules on chemically stripe patterned substrates: ridges versus drops". In: *Langmuir* 31.38 (2015), pp. 10618–10631. DOI: 10.1021/acs.langmuir.5b02407 (cit. on pp. 86, 94).

[55] Hong Hu, Hongmiao Tian, Jinyou Shao, Yucheng Ding, Chengbao Jiang, and Hongzhong Liu. "Fabrication of bifocal microlens arrays based on controlled electrohydrodynamic reflowing of pre-patterned polymer". In: *Journal of Micromechanics and Microengineering* 24.9 (2014), p. 095027. DOI: 10.1088/0960-1317/24/9/095027 (cit. on p. 4).

[56] Jaeseok Hwang, Hyunje Park, Jaejong Lee, and Dae Joon Kang. "Parametric scheme for rapid nanopattern replication via electrohydrodynamic instability". In: *RSC Advances* 11.30 (2021), pp. 18152–18161. DOI: 10.1039/d1ra01728d (cit. on p. 62).

[57] Justin C-T Kao, Alexander A Golovin, and Stephen H Davis. "Rupture of thin films with resonant substrate patterning". In: *Journal of Colloid and Interface Science* 303.2 (2006), pp. 532–545. DOI: 10.1016/j.jcis.2006.08.015 (cit. on pp. 67, 82, 111, 114).

[58] Joshua M Katzenstein, Dustin W Janes, Julia D Cushen, Nikhil B Hira, Dana L McGuffin, Nathan A Prisco, and Christopher J Ellison. "Patterning by photochemically directing the Marangoni effect". In: *ACS Macro Letters* 1.10 (2012), pp. 1150–1154. DOI: 10.1021/mz300400p (cit. on p. 3).

[59] Mattew S Keith. "Mathematical Modelling of Electrohydrodynamic Flows". PhD thesis. University of Strathclyde, 2021. DOI: https://doi.org/10.48730/5qbq-wf57 (cit. on p. 187).

[60] Markus Klein and Andreas Prohl. "Optimal control for the thin film equation: Convergence of a multi-parameter approach to track state constraints avoiding degeneracies". In: *Computational Methods in Applied Mathematics* 16.4 (2016), pp. 685–702. DOI: 10.1515/cmam-2016-0025 (cit. on pp. 143, 144, 146, 150).

[61] Ali Malekpour Koupaei, Hadi Nazaripoor, and Mohtada Sadrzadeh. "Electrohydrodynamic patterning of polyethersulfone membranes". In: *Langmuir* 35.37 (2019), pp. 12139–12149. DOI: 10.1021/acs.langmuir.9b01948 (cit. on p. 4).

[62] Cindy Y Lau and William B Russel. "Fundamental limitations on ordered electrohydrodynamic patterning". In: *Macromolecules* 44.19 (2011), pp. 7746–7751. DOI: 10.1021/ma200952u (cit. on pp. 5, 44, 107, 185).

[63] L. Gary Leal. *Advanced Transport Phenomena: Fluid Mechanics and Convective Transport Processes*. Cambridge Series in Chemical Engineering. Cambridge University Press, 2007. DOI: 10.1017/CBO9780511800245 (cit. on pp. 4, 10, 13–15, 17, 21, 38, 188, 189).

[64] You-Jin Lee, Young Wook Kim, Young-Ki Kim, Chang-Jae Yu, Jin Seog Gwag, and Jae-Hoon Kim. "Microlens array fabricated using electrohydrodynamic instability and surface properties". In: *Optics Express* 19.11 (2011), pp. 10673–10678. DOI: 10.1364/oe.19.010673 (cit. on p. 4).

[65] Rui Li, Lanlan Wang, Hongzhong Liu, Weitao Jiang, Yongsheng Shi, Lei Yin, and Yongkai Zhu. "Tunable mirolens array with a large fill-factor: Self-assembly fabrication and electrodrodynamic actuation". In: *Sensors and Actuators A: Physical* 240 (2016), pp. 85–91. DOI: 10.1016/j.sna.2016.01.009 (cit. on p. 4).

[66] Xiangming Li, Hongmiao Tian, Yucheng Ding, Jinyou Shao, and Yuping Wei. "Electrically templated dewetting of a UV-curable prepolymer film for the fabrication of a concave microlens array with well-defined curvature". In: *ACS Applied Materials & Interfaces* 5.20 (2013), pp. 9975–9982. DOI: 10.1021/am402043u (cit. on p. 4).

[67] G Liu, W Yu, H Li, J Gao, David Flynn, Robert W Kay, Scott Cargill, Catherine Tonry, Mayur K Patel, Christopher Bailey, and M P Y Desmulliez. "Microstructure formation in a thick polymer by electrostatic-induced lithography". In: *Journal of Micromechanics and Microengineering* 23.3 (2013), p. 035018. DOI: 10.1088/0960-1317/23/3/035018 (cit. on p. 4).

[68] Davin Lunz. "Minimizing deformation of a thin fluid film driven by fluxes of momentum and heat". In: *Physical Review E* 103 (3 Mar. 2021), p. 033105. DOI: 10.1103/PhysRevE.103.033105 (cit. on pp. 143, 144, 146).

[69] Guowei Lv, Xiaobing Hu, Lu Hao, Hongmiao Tian, Jinyou Shao, and Demei Yu. "Facile Fabrication of a Flexible Patterned Film with Diverse Micro-/Nanostructures via Electrohydrodynamic Patterning". In: *Industrial & Engineering Chemistry Research* (2020). DOI: 10.1021/acs.iecr.0c04908 (cit. on p. 4).

[70] Oleksiy Lyutakov, Ivan Hüttel, Václav Prajzler, Vítězslav Jeřábek, Alexander Jančárek, Vladimír Hnatowicz, and Václav Švorčík. "Pattern formation in PMMA film induced by electric field". In: *Journal of Polymer Science, Part B: Polymer Physics* 47.12 (2009), pp. 1131–1135. DOI: 10.1002/polb.21718 (cit. on p. 4).

[71] Oleksiy Lyutakov, Jiří Tuma, Václav Prajzler, Ivan Huttel, Vladimír Hnatowicz, and Václav Švorčík. "Preparation of rib channel waveguides on polymer in electric field". In: *Thin Solid Films* 519.4 (2010), pp. 1452–1457. DOI: 10.1016/j.tsf.2010.08.019 (cit. on p. 4).

[72] Sumeet Mahajan, Tanya Hutter, Ullrich Steiner, and Pola Goldberg Oppenheimer. "Tunable microstructured surface-enhanced Raman scattering substrates via electrohydrodynamic lithography". In: *Journal of Physical Chemistry Letters* 4.23 (2013), pp. 4153–4159. DOI: 10.1021/jz4018688 (cit. on p. 4).

[73] James E. Mark. *Polymer Data Handbook*. Oxford University Press, 1999 (cit. on p. 12).

[74] Euan McLeod, Yu Liu, and Sandra M Troian. "Experimental verification of the formation mechanism for pillar arrays in nanofilms subject to large thermal gradients". In: *Physical Review Letters* 106.17 (2011), p. 175501. DOI: 10.1103/physrevlett.106.175501 (cit. on p. 117).

[75] Euan McLeod and Sandra M Troian. "One step non-contact fabrication of polymer microlens arrays by thermocapillary lithography". In: *CLEO: Science and Innovations*. Optical Society of America. 2011, p. CML3. DOI: 10.1364/cleo_si.2011.cml3 (cit. on p. 4).

[76] Vladimir S Mitlin. "Dewetting of solid surface: Analogy with spinodal decomposition". In: *Journal of Colloid and Interface Science* 156.2 (1993), pp. 491–497. DOI: 10.1006/jcis.1993.1142 (cit. on p. 26).

[77] Patrick Kofod Mogensen and Asbjørn Nilsen Riseth. "Optim: A mathematical optimization package for Julia". In: *Journal of Open Source Software* 3.24 (2018). DOI: 10.21105/joss.00615 (cit. on p. 159).

[78] Ali Mohammadtabar, Hadi Nazaripoor, Adham Riad, Arman Hemmati, and Mohtada Sadrzadeh. "A numerical study for thermocapillary induced patterning of thin liquid films". In: *Physics of Fluids* 32.2 (2020), p. 024106. DOI: 10.1063/1.5134460 (cit. on p. 118).

[79] Hadi Nazaripoor, M. R. Flynn, Charles R. Koch, and Mohtada Sadrzadeh. "Thermally induced interfacial instabilities and pattern formation in confined liquid nanofilms". In: *Physical Review E* 98.4 (2018), p. 043106. DOI: 10.1103/physreve.98.043106 (cit. on p. 117).

[80] Hadi Nazaripoor, Charles R Koch, and Mohtada Sadrzadeh. "Enhanced electrically induced micropatterning of confined thin liquid films: Thermocapillary role and its limitations". In: *Industrial & Engineering Chemistry Research* 56.38 (2017), pp. 10678–10688. DOI: 10.1021/acs.iecr.7b02814 (cit. on pp. 117, 141).

[81] Hadi Nazaripoor, Charles R Koch, and Mohtada Sadrzadeh. "Ordered high aspect ratio nanopillar formation based on electrical and thermal reflowing of prepatterned thin films". In: *Journal of Colloid and Interface Science* 530 (2018), pp. 312–320. DOI: 10.1016/j.jcis.2018.06.080 (cit. on p. 117).

[82] Hadi Nazaripoor, Charles R Koch, Mohtada Sadrzadeh, and Subir Bhattacharjee. "Thermo-electrohydrodynamic patterning in nanofilms". In: *Langmuir* 32.23 (2016), pp. 5776–5786. DOI: 10.1021/acs.langmuir.6b01810 (cit. on pp. 117, 141).

[83] Jorge Nocedal and Stephen Wright. *Numerical optimization*. Springer New York, 2006. ISBN: 9780387303031. DOI: 10.1007/978-0-387-40065-5 (cit. on p. 159).

[84] AC Or, RE Kelly, Luca Cortelezzi, and Jason L Speyer. "Control of long-wavelength Marangoni–Bénard convection". In: *Journal of Fluid Mechanics* 387 (1999), pp. 321–341. DOI: 10.1017/s0022112099004607 (cit. on pp. 143, 146).

[85] Alexander Oron, Stephen H Davis, and S George Bankoff. "Long-scale evolution of thin liquid films". In: *Reviews of Modern Physics* 69.3 (1997), p. 931. DOI: 10.1103/revmodphys.69.931 (cit. on pp. 7, 10, 17, 18, 22, 26, 29, 32, 62, 144).

[86] Hyunje Park, Jaeseok Hwang, Jaejong Lee, and Dae Joon Kang. "Rapid Electrohydrodynamic-Driven Pattern Replication over a Large Area via Ultrahigh Voltage Pulses". In: *ACS Nano* 17.22 (2023). PMID: 37939012, pp. 22456–22466. DOI: 10.1021/acsnano.3c05413 (cit. on pp. 62, 107, 108).

[87] Hyunje Park, Jaeseok Hwang, Tae Hyeong Lee, Jaejong Lee, and Dae Joon Kang. "Fog Collection Based on Secondary Electrohydrodynamic-Induced Hybrid Structures with Anisotropic Hydrophilicity". In: *ACS Applied Materials & Interfaces* (2021). DOI: 10.1021/acsami.1c04761 (cit. on p. 4).

[88] Leonid M Pismen and Boris Y Rubinstein. "Computer tools for bifurcation analysis: general approach with application to dynamical and distributed systems". In: *International Journal of Bifurcation and Chaos* 9.06 (1999), pp. 983–1008. DOI: 10.1142/s0218127499000717 (cit. on pp. 111–114).

[89] T. Podgorski, J.-M. Flesselles, and L. Limat. "Corners, Cusps, and Pearls in Running Drops". In: *Physical Review Letters* 87.3 (June 2001), p. 036102. ISSN: 1079-7114. DOI: 10.1103/physrevlett.87.036102 (cit. on p. 1).

[90] Christopher Rackauckas and Qing Nie. "Differentialequations.jl – a performant and feature-rich ecosystem for solving differential equations in Julia". In: *Journal of Open Research Software* 5.1 (2017). DOI: 10.5334/jors.151 (cit. on p. 53).

[91] Lord Rayleigh. "On the instability of jets". In: *Proceedings of the London mathematical society* 1.1 (1878), pp. 4–13. DOI: 10.1112/plms/s1-10.1.4 (cit. on p. 94).

[92] Hermann Riecke. "Methods of Nonlinear Analysis 412". In: (July 2008). URL: https://www.researchgate.net/publication/228688534_Methods_of_Nonlinear_Analysis_412 (cit. on p. 57).

[93] BY Rubinstein and AM Leshansky. "Rupture of thin liquid films: Generalization of weakly nonlinear theory". In: *Physical Review E* 83.3 (2011), p. 031603. DOI: 10.1103/physreve.83.031603 (cit. on p. 114).

[94] Thomas L Saaty. *Modern Nonlinear Equations*. McGraw-Hill, 1967 (cit. on p. 151).

[95] Anna E Samoilova and Alexander Nepomnyashchy. "Controlling of longwave oscillatory Marangoni patterns on a rhombic lattice". In: *Mathematical Modelling of Natural Phenomena* 16 (2021), p. 1. DOI: 10.1051/mmnp/2020054 (cit. on pp. 143, 146).

[96] Anna E Samoilova and Alexander Nepomnyashchy. "Feedback control of Marangoni convection in a thin film heated from below". In: *Journal of Fluid Mechanics* 876 (2019), pp. 573–590. DOI: 10.1017/jfm.2019.578 (cit. on pp. 143, 146).

[97] Anna E Samoilova and Alexander Nepomnyashchy. "Longitudinal modulation of Marangoni wave patterns in thin film heated from below: Instabilities and control". In: *Frontiers in Applied Mathematics and Statistics* 7 (2021), p. 697332. DOI: 10.3389/fams.2021.697332 (cit. on pp. 143, 146).

[98] Anna E Samoilova and Alexander Nepomnyashchy. "Nonlinear feedback control of Marangoni wave patterns in a thin film heated from below". In: *Physica D: Nonlinear Phenomena* 412 (2020), p. 132627. DOI: 10.1016/j.physd.2020.132627 (cit. on pp. 143, 146).

[99] DA Saville. "Electrohydrodynamics: the Taylor-Melcher leaky dielectric model". In: *Annual Review of Fluid Mechanics* 29.1 (1997), pp. 27–64. DOI: 10.1146/annurev.fluid.29.1.27 (cit. on p. 33).

[100] Erik Schäffer, S Harkema, R Blossey, and Ullrich Steiner. "Temperature-gradient–induced instability in polymer films". In: *Europhysics Letters* 60.2 (2002), p. 255. DOI: 10.1209/epl/i2002-00344-9 (cit. on pp. 1, 117).

[101] Erik Schäffer, Stephan Harkema, Monique Roerdink, Ralf Blossey, and Ullrich Steiner. "Morphological instability of a confined polymer film in a thermal gradient". In: *Macromolecules* 36.5 (2003), pp. 1645–1655. DOI: 10.1021/ma021080p (cit. on p. 117).

[102] Erik Schäffer, Stephan Harkema, Monique Roerdink, Ralf Blossey, and Ullrich Steiner. "Thermomechanical lithography: pattern replication using a temperature gradient driven instability". In: *Advanced Materials* 15.6 (2003), pp. 514–517. DOI: 10.1002/adma.200390119 (cit. on p. 117).

[103] Erik Schäffer, Thomas Thurn-Albrecht, Thomas P Russell, and Ullrich Steiner. "Electrically induced structure formation and pattern transfer". In: *Nature* 403.6772 (2000), pp. 874–877. DOI: 10.1038/35002540 (cit. on pp. 1, 61).

[104] Erik Schäffer, Thomas Thurn-Albrecht, Thomas P Russell, and Ullrich Steiner. "Electrohydrodynamic instabilities in polymer films". In: *Europhysics Letters* 53.4 (2001), p. 518. DOI: 10.1209/epl/i2001-00183-2 (cit. on pp. 3, 44, 61).

[105] R. Seemann, S. Herminghaus, and K. Jacobs. "Dewetting Patterns and Molecular Forces: A Reconciliation". In: *Physical Review Letters* 86 (24 June 2001), pp. 5534–5537. DOI: 10.1103/PhysRevLett.86.5534 (cit. on p. 12).

[106] Mathieu Sellier. "Inverse problems in free surface flows: a review". In: *Acta Mechanica* 227.3 (2016), pp. 913–935. DOI: 10.1007/s00707-015-1477-1 (cit. on p. 142).

[107] Mathieu Sellier and Satyananda Panda. "Beating capillarity in thin film flows". In: *International Journal for Numerical Methods in Fluids* 63.4 (2010), pp. 431–448. DOI: 10.1002/fld.2086 (cit. on pp. 142, 146).

[108] Lawrence F Shampine. "Solving 0 = F(t, y(t), y'(t)) in Matlab". In: *Journal of Numerical Mathematics* 10.4 (2002), pp. 291–310. DOI: 10.1515/jnma.2002.291 (cit. on p. 53).

[109] Suraj Shankar, Vidya Raju, and L Mahadevan. "Optimal transport and control of active drops". In: *Proceedings of the National Academy of Sciences* 119.35 (2022), e2121985119. DOI: 10.1073/pnas.2121985119 (cit. on pp. 143, 146, 150).

[110] Roghayeh Shiri, Leonie Schmeller, Dirk Peschka, Ralf Seemann, and Barbara Wagner. "Impact of noise on spinodal dewetting of liquid-liquid films". In: *Communications Physics* 6.1 (2023), p. 109. DOI: 10.1038/s42005-023-01208-x (cit. on p. 54).

[111] Fenhong Song, Yankui Liu, Tingting Zhang, Jing Fan, and Qingzhen Yang. "Marangoni flow of thin liquid film underneath a topographical plate". In: *Case Studies in Thermal Engineering* 35 (2022), p. 102094. DOI: 10.1016/j.csite.2022.102094 (cit. on p. 118).

[112] Samanvaya Srivastava, P Dinesh Sankar Reddy, Cindy Wang, Dipankar Bandyopadhyay, and Ashutosh Sharma. "Electric field induced microstructures in thin films on physicochemically heterogeneous and patterned substrates". In: *J. Chem. Phys* 132.17 (2010), p. 174703. DOI: 10.1063/1.3400653 (cit. on p. 62).

[113] Steven K Stanley, Christopher J Ellison, and Roger T Bonnecaze. "Control of Marangoni-driven patterning by an optimized distribution of surface energy". In: *Journal of Applied Physics* 127.6 (2020), p. 065304. DOI: 10.1063/1.5132360 (cit. on pp. 143, 146, 150).

[114] Geoffrey Ingram Taylor. "Disintegration of water drops in an electric field". In: *Proceedings of the Royal Society of London. Series A. Mathematical and Physical Sciences* 280.1382 (July 1964), pp. 383–397. ISSN: 2053-9169. DOI: 10.1098/rspa.1964.0151 (cit. on p. 3).

[115] Geoffrey Ingram Taylor. "Electrically driven jets". In: *Proceedings of the Royal Society of London. A. Mathematical and Physical Sciences* 313.1515 (1969), pp. 453–475. DOI: 10.1098/rspa.1969.0205 (cit. on p. 3).

[116] Uwe Thiele. "Recent advances in and future challenges for mesoscopic hydrodynamic modelling of complex wetting". In: *Colloids and Surfaces A: Physicochemical and Engineering Aspects* 553 (2018), pp. 487–495. DOI: 10.1016/j.colsurfa.2018.05.049 (cit. on p. 27).

[117] Uwe Thiele, Lutz Brusch, Michael Bestehorn, and Markus Bär. "Modelling thin-film dewetting on structured substrates and templates: Bifurcation analysis and numerical simulations". In: *The European Physical Journal E: Soft Matter and Biological Physics* 11.3 (2003), pp. 255–271. DOI: 10.1140/epje/i2003-10019-5 (cit. on pp. 72, 94).

[118] Alice B Thompson, Susana N Gomes, Grigorios A Pavliotis, and Demetrios T Papageorgiou. "Stabilising falling liquid film flows using feedback control". In: *Physics of Fluids* 28.1 (2016), p. 012107. DOI: 10.1063/1.4938761 (cit. on pp. 143, 146).

[119] Ruben J Tomlin, Susana N Gomes, Grigorios A Pavliotis, and Demetrios T Papageorgiou. "Optimal control of thin liquid films and transverse mode effects". In: *SIAM Journal on Applied Dynamical Systems* 18.1 (2019), pp. 117–149. DOI: 10.1137/18m1193906 (cit. on p. 144).

[120] Fredi Tröltzsch. *Optimal Control of Partial Differential Equations: Theory, Methods and Applications*. Vol. 112. American Mathematical Soc., 2010. DOI: 10.1090/gsm/112 (cit. on pp. 150, 151).

[121] Dmitri Tseluiko and Demetrios T Papageorgiou. "Nonlinear dynamics of electrified thin liquid films". In: *SIAM Journal on Applied Mathematics* 67.5 (2007), pp. 1310–1329. DOI: 10.1137/060663532 (cit. on p. 38).

[122] Lesley-Anne Turner, Sandra Downes, Ernie Hill, and Ian Kinloch. "Investigating the suitability of electrohydrodynamic lithography for the fabrication of cell substrates". In: *Journal of Materials Science* 49.11 (2014), pp. 4045–4057. DOI: 10.1007/s10853-013-7971-8 (cit. on p. 4).

[123] Hannes Uecker. *Numerical Continuation and Bifurcation in Nonlinear PDEs*. SIAM, 2021. DOI: 10.1137/1.9781611976618 (cit. on pp. 52, 57, 59).

[124] Osamu Urakawa, Stephen F Swallen, MD Ediger, and Ernst D von Meerwall. "Self-diffusion and viscosity of low molecular weight polystyrene over a wide temperature range". In: *Macromolecules* 37.4 (2004), pp. 1558–1564. DOI: 10.1021/ma0352025 (cit. on p. 12).

[125] Dirk Willem Van Krevelen and Klaas Te Nijenhuis. *Properties of Polymers: Their Correlation with Chemical Structure; their Numerical Estimation and Prediction from Additive Group Contributions*. 4th ed. Elsevier, 2009. ISBN: 978-0-08-054819-7. URL: https://www.sciencedirect.com/book/9780080548197/properties-of-polymers (cit. on p. 12).

[126] Romain Veltz. *BifurcationKit.jl*. July 2020. URL: https://hal.archives-ouvertes.fr/hal-02902346 (cit. on pp. 59, 72, 123).

[127] Ruhi Verma, Ashutosh Sharma, Kajari Kargupta, and Jaita Bhaumik. "Electric field induced instability and pattern formation in thin liquid films". In: *Langmuir* 21.8 (2005), pp. 3710–3721. DOI: 10.1021/la0472100 (cit. on p. 62).

[128] Nicoleta E Voicu, Stephan Harkema, and Ullrich Steiner. "Electric-Field-Induced Pattern Morphologies in Thin Liquid Films". In: *Advanced Functional Materials* 16.7 (2006), pp. 926–934. DOI: 10.1002/adfm.200500470 (cit. on p. 3).

[129] P. W. Voorhees. "The theory of Ostwald ripening". In: *Journal of Statistical Physics* 38.1–2 (Jan. 1985), pp. 231–252. ISSN: 1572-9613. DOI: 10.1007/bf01017860 (cit. on p. 85).

[130] Alexander W. Wray, Radu Cimpeanu, and Susana N. Gomes. "Electrostatic control of the Navier-Stokes equations for thin films". In: *Physical Review Fluids* 7 (12 Dec. 2022), p. L122001. DOI: 10.1103/physrevfluids.7.l122001 (cit. on pp. 143, 144, 146, 185).

[131] Ning Wu, Michail E. Kavousanakis, and William B. Russel. "Coarsening in the electrohydrodynamic patterning of thin polymer films". In: *Physical Review E* 81 (2 Feb. 2010), p. 026306. DOI: 10.1103/PhysRevE.81.026306 (cit. on pp. 62, 76, 85).

[132] Ning Wu, Leonard F Pease, and William B Russel. "Electric-field-induced patterns in thin polymer films: weakly nonlinear and fully nonlinear evolution". In: *Langmuir* 21.26 (2005), pp. 12290–12302. DOI: 10.1021/la052099z (cit. on pp. 39, 61, 62).

[133] Ning Wu and William B Russel. "Electrohydrodynamic instability of dielectric bilayers: Kinetics and thermodynamics". In: *Industrial & Engineering Chemistry Research* 45.16 (2006), pp. 5455–5465. DOI: 10.1021/ie0510876 (cit. on p. 62).

[134] Ning Wu and William B Russel. "Micro-and nano-patterns created via electrohydrodynamic instabilities". In: *Nano Today* 4.2 (2009), pp. 180–192. DOI: 10.1016/j.nantod.2009.02.002 (cit. on p. 61).

[135] Longjian Xue and Yanchun Han. "Pattern formation by dewetting of polymer thin film". In: *Progress in Polymer Science* 36.2 (2011), pp. 269–293. DOI: 10.1016/j.progpolymsci.2010.07.004 (cit. on p. 4).

[136] Qingzhen Yang, Ben Q Li, and Yucheng Ding. "A numerical study of nanoscale electrohydrodynamic patterning in a liquid film". In: *Soft Matter* 9.12 (2013), pp. 3412–3423. DOI: 10.1039/c3sm27239g (cit. on pp. 62–64, 66, 80).

[137] Qingzhen Yang, Ben Q Li, Yucheng Ding, and Jinyou Shao. "Steady state of electrohydrodynamic patterning of micro/nanostructures on thin polymer films". In: *Industrial & Engineering Chemistry Research* 53.32 (2014), pp. 12720–12728. DOI: 10.1021/ie502288a (cit. on pp. 62–64, 80).

[138] Qingzhen Yang, Ben Q Li, Xuemeng Lv, Fenhong Song, Yankui Liu, and Feng Xu. "Mathematical modelling of thermocapillary patterning in thin liquid film: an equilibrium study". In: *Journal of Fluid Mechanics* 919 (2021). DOI: 10.1017/jfm.2021.407 (cit. on pp. 32, 118, 124).

[139] Qingzhen Yang, Ben Q Li, Hongmiao Tian, Xiangming Li, Jinyou Shao, Xiaoliang Chen, and Feng Xu. "Deformation Hysteresis of Electrohydrodynamic Patterning on a Thin Polymer Film". In: *ACS Applied Materials & Interfaces* 8.27 (2016), pp. 17668–17675. DOI: 10.1021/acsami.6b04192 (cit. on pp. 62–64, 78, 80).

[140] Qingzhen Yang, Yankui Liu, Xinmiao Jia, Tingting Zhang, and Fenhong Song. "Numerical Study of the Thermocapillary Instability in a Thin Liquid-Air Film". In: *Physics of Fluids* (2022). DOI: 10.1063/5.0109313 (cit. on p. 118).

[141] Qingzhen Yang, Yankui Liu, Xinmiao Jia, Tingting Zhang, Hongmiao Tian, Jing Fan, Quange Xu, and Fenhong Song. "Phase-field numerical study on the dynamic process of thermocapillary patterning". In: *Physical Review E* 106 (1 July 2022), p. 015111. DOI: 10.1103/PhysRevE.106.015111 (cit. on p. 118).

[142] Hak Koon Yeoh, Qi Xu, and Osman A Basaran. "Equilibrium shapes and stability of a liquid film subjected to a nonuniform electric field". In: *Physics of Fluids* 19.11 (2007), p. 114111. DOI: 10.1063/1.2798806 (cit. on pp. 62–64, 66).

[143] Yixin Zhang, James E. Sprittles, and Duncan A. Lockerby. "Molecular simulation of thin liquid films: Thermal fluctuations and instability". In: *Physical Review E* 100 (2 Aug. 2019), p. 023108. DOI: 10.1103/PhysRevE.100.023108 (cit. on p. 55).

[144] Zhong Zheng and Howard A Stone. "The influence of boundaries on gravity currents and thin films: Drainage, confinement, convergence, and deformation effects". In: *Annual Review of Fluid Mechanics* 54 (2022), pp. 27–56. DOI: 10.1146/annurev-fluid-030121-025957 (cit. on p. 1).

[145] Chengzhe Zhou. "Collection of Solved Nonlinear Problems for Remote Shaping and Patterning of Liquid Structures on Flat and Curved Substrates by Electric and Thermal Fields". PhD Thesis. California Institute of Technology, 2020. URL: https://resolver.caltech.edu/CaltechTHESIS:12092019-191651654 (cit. on p. 144).

[146] Chengzhe Zhou and Sandra M Troian. "Self-similar cuspidal formation By run-away thermocapillary forces in thin liquid films". In: *New Journal of Physics* 21.1 (2019), p. 013018. DOI: 10.1088/1367-2630/aaf51d (cit. on pp. 31, 117).